Novel solutions for piezogeneration enhancement in GaN nanowires

Tanbir Kaur Sodhi

To cite this version:

Tanbir Kaur Sodhi. Novel solutions for piezogeneration enhancement in GaN nanowires. Micro and nanotechnologies/Microelectronics. Université Paris-Saclay, 2022. English. NNT : 2022UPAST116 . tel-03865436

Novel solutions for piezogeneration enhancement in GaN nanowires

Nouvelles solutions pour accroître les propriétés de piézogénération des nanofils de GaN

Thèse de doctorat de l'université Paris-Saclay

École doctorale n° 575 : electrical, optical, bio : physics and engineering (EOBE)
Spécialité de doctorat : Sciences des matériaux
Graduate School : Sciences de l'ingénierie et des systèmes. Référent : Faculté des sciences d'Orsay

Thèse préparée dans l'unité de recherche **Centre de Nanosciences et de Nanotechnologies** (Université Paris-Saclay, CNRS), sous la direction de **Noëlle LEBEAU GOGNEAU**, Directrice de recherche (C2N), et le co-encadrement de **Frédéric HOUZÉ**, Chargé de recherche (GeePs)

Thèse soutenue à Paris-Saclay, le 26 Septembre 2022, par

Tanbir Kaur SODHI

Composition du Jury

Guylaine POULIN-VITTRANT DR2, Université de Tours (GREMAN)	Présidente
Gustavo ARDILA Maître de conférences (HDR), INP Grenoble	Rapporteur et Examinateur
Brice GAUTIER Professeur des universités, INSA Lyon	Rapporteur et Examinateur
Vincent SALLET Chargé de recherche, Université Paris-Saclay (GEMaC)	Examinateur
Christophe DURAND Maître de conférence, CEA Grenoble	Examinateur
Noëlle LEBEAU GOGNEAU DR, CNRS, Université Paris-Saclay	Directrice de thèse

THESE DE DOCTORAT

NNT : 2022UPAST116

université PARIS-SACLAY
DOCTORAL SCHOOL
Electrical, Optical, Bio:
Physics and Engineering
(EOBE)

Titre : Nouvelles solutions pour accroître les propriétés de piézogénération des nanofils de GaN

Mots clés : Nanofils III-nitrures, AFM-Résiscope, Piézo-générateurs, Récupération d’énergie

Résumé : Au cours des dernières années, les nanofils (NFs) de GaN sont apparus comme de très bons candidats pour la récupération d'énergie aux petites échelles. Leurs grandes propriétés mécaniques et piézoélectriques leur confèrent la capacité de convertir efficacement les énergies vibratoires et mécaniques ambiantes en une énergie électrique, et ainsi de développer une nouvelle génération de générateurs piézoélectriques ultra-compacts, efficaces et autonomes pour assister ou alimenter des micro-dispositifs. Malgré la démonstration de premiers piézo-générateurs prometteurs à base de ces NFs, il est encore aujourd'hui indispensable d'augmenter la capacité de piézo-conversion de ces nouveaux systèmes. L'exploration de nouvelles solutions pour l’amélioration de leurs performances est l'axe de recherche de cette thèse. Dans ce travail, l'épitaxie par jets moléculaires assistée par plasma est utilisée pour développer des NFs de GaN intrinsèquement dopés de type p et présentant une grande qualité cristalline. Grâce à un outil de nano-caractérisation basé sur le microscope à force atomique équipé du module électrique Resiscope spécifiquement adapté pour réaliser des mesures de piézo-conversion, la réponse piézoélectrique des NFs est étudiée en fonction des solutions considérées. L'efficacité de la génération piézoélectrique des NFs est fortement affectée par le circuit externe. Pour la première fois aux échelles nanométriques, nous démontrons expérimentalement son influence. Les limites du protocole établi dans la communauté pour juger de la capacité de génération de ces nanostructures 1D sont abordées et des solutions sont proposées.

L'efficacité de génération piézoélectrique des NFs est également profondément affectée par les charges de surface, qui sont fortement prononcées dans les NFs de GaN caractérisés par des diamètres inférieurs à 100 nm. Nous démontrons que ces charges de surface peuvent être avantageuses pour les applications piézoélectriques car elles offrent la possibilité d'ajuster la concentration de porteurs de charge libres en fonction du diamètre des NFs. Ainsi, nous établissons expérimentalement qu'en présence de charges de surface, l'efficacité de couplage électromécanique des nanofils de GaN augmente jusqu'à 43,4 % pour des diamètres compris entre 45 et 60 nm. Les mesures piézoélectriques sur des NFs de GaN et des NFs cœur/coquille de GaN/Al2O3 sont également effectuées. La réduction de la densité de charge de surface en présence de la coquille d’Al2O3 se traduit par une dégrade la réponse piézoélectrique des NFs, confirmant ainsi l'importance des charges de surface pour améliorer la réponse piézoélectrique de ces derniers. Enfin, en tirant parti de ces solutions, des tensions de sortie pouvant atteindre jusqu'à 520 mV par NF ont été mesurées, établissant un nouvel état de l'art, selon le protocole de mesure couramment utilisé, pour les nanostructures piézoélectriques 1D.

universite
PARIS-SACLAY

DOCTORAL SCHOOL
Electrical, Optical, Bio:
Physics and Engineering
(EOBE)

Title : Novel solutions for piezogeneration enhancement in GaN nanowires

Keywords : III-Nitride Nanowires, AFM-Resiscope, Piezogenerators, Energy harvesting

Abstract : In the last decade, GaN nanowires (NWs) have emerged as promising candidates in the field of small-scale energy harvesting. Their superior mechanical and piezoelectric properties confers to them the ability to effectively convert the ambient vibrational and mechanical energies into electrical energy, and thus develop a new generation of ultra-compact, high-efficient and self-sustainable piezoelectric generators to assist or power microelectronic devices. Despite the demonstration of first promising NW-based piezo-generators, it is today indispensable to further increase the piezo-conversion capacity of these new harvesters. The exploration of novel solutions to enhance their performances is the research axis of this thesis. Here, plasma-assisted molecular beam epitaxy (PA-MBE) is employed to grow intrinsically p-doped GaN NWs with high crystalline quality. Thanks to a nano-characterization tool based on atomic force microscope equipped with the Resiscope electric module specifically adapted for piezoelectric conversion measurements, the piezoelectric response of NWs is investigated as a function of the explored solutions. The piezo-generation efficiency of the NWs is strongly affected by the external circuit. For the first time in the nanoscale regime we experimentally demonstrate its influence on the piezo-generation efficiency of the NWs. The limitations of the formerly established protocol to judge the piezo-generation capacity of 1D-nanostructures are addressed and solutions are proposed.

The piezo-generation efficiency of the NWs is also deeply affected by the surface charges, which are strongly pronounced in sub-100 nm wide GaN NWs. We demonstrate that these surface charges can be advantageous for piezoelectric applications as they offer the possibility to tune the free charge carrier concentration as a function of NW diameter. Thus, we establish experimentally that in the presence of surface charges, the electromechanical coupling efficiency of GaN NWs increases up to 43.4 % for diameters in the range of 45-60 nm. The piezoelectric measurements on GaN and GaN/Al2O3 core-shell NWs are also performed. The reduction of surface charge density by the Al2O3 shell results in a degradation of the piezoelectric response of the NWs. These results confirm the importance of the surface charges for improving the piezo-response of GaN NWs. Finally, by taking advantage of these solutions, output voltages reaching up to 520 mV per NW have been measured, stating a new-state-of-the-art, in the commonly used protocol, for 1D piezoelectric nanostructures.

ੴ

La fin du désert se cache peut-être derrière chaque dune

Et dis-toi que tu pourras compter sur nous le temps que ça dure

Quand tu as le désert à traverser, il y a rien à faire, sauf d'avancer

Rien à faire sauf d'avancer.

Orelsan, Cyril Léon et Stéphane Gable.

Acknowledgements

When I was writing my thesis, I used to often gaze at this empty page containing just the title ‘acknowledgements’ to motivate myself to persevere so that one day I would finally be able to scribe on this empty page. My friends, that day has finally come and now I will take a couple of humble bows in front of all those who have supported me in this journey and shone light when paths got darker.

My first and foremost bow to my beloved parents. Mom, I love you and I could never have made it if you had not decided to take a stand for me in front of the entire family. You are my rock above God and I am sure that even God doesn’t mind! Dear dad, thank you for putting your trust in me and letting me leave India (I know it was hard for you). I hope I’ve made you proud. Thank you both for the education that you’ve provided me and supported me financially even when times were difficult.

I thought I’d already cried enough but…here it comes again! But I don’t mind them as tears of joy have their own charm. So with blurry eyes, I continue…

My second bow to the power trio - Noëlle Gogneau, Frédéric Houzé and Pascal Chrétien, which makes my supervisors. Noëlle, thank you for this opportunity to work amongst the best minds and for all the curve balls that you’ve served me over the last four years. I’ve had a very intense learning experience with our discussions and experiments and I sincerely thank you for that. Frédéric, you told me that I’d have a good luck when I got stung by a bee on my face on the Integration day at GeePs (I still have a photo with one cheek slightly bigger than the other)…and indeed, I feel lucky to have had the chance to spend moments of conviviality over a glass of wine as well as hundreds of hours spent on scientific discussions with you. Thank you for bringing me butter loaded sablés from Bretagne every year (they were imperative for late-night data analysis).

Pascal, a very special thanks to you for fabricating such a marvellous measurement set-up and training me very diligently on it. Thank you for your dedication and countless hours of work in your workshop (filled with secrets that no one should know!). Without your simplified explanations, I’d be lost in the complexity of your electrical circuits. Thank you for feeding me information every single day, until I dreamt of them. Besides work, you’ve been there to listen and offer your guidance during rough times and for your *sagesse,* you definitely deserve the title of Maître Yoda.

My third bow to our dearest MBE engineer Laurent Travers and his pretty little hammer that would fix all MBE-related issues just with a couple of soft blows or just by simply talking to the machine! What would we do without you! Thank you for keeping the MBE up and running and for your funny anecdotes. My next bow is to the C2N cleanroom engineers- Christophe Dupuis, Stéphane Guillet, Fabien Bayle, David Bouville, Alan Durnez, François Maillard, Xavier Lafosse, Xavier Leroux, Abdelmounaim Harouri, Etienne Herth…for helping me analyse and process my samples but also for motivating me.

A Victorian style curtsy to my wonderful colleagues at C2N and GeePs. JC Harmand, Maria Tchernycheva, Martina Morassi and Aristide Lemaître for their guidance and support. Nuño, thank you for making my journey unexpectedly colourful with countless emotions, laughter and fights. Thank you for being a true friend. Dear Anton, thank you for switching off the light so that I could see the RHEED pattern, for your insightful suggestions and remarks on my chapters, always motivating me to improve. My officemates, Jules and Amaury for co-founding *#Teamchubby* and for a positive work environment. Mario, Marina, Linh, Stéfano, Tiphaine, Arup, Mathieu, Paul, Camille, Jean-Michel, Raffaele, Adel, Sleiman, Guillaume, Paul, Khadim, Charles, Koffi, Ana, Aurore, Sylvain…thank you for the warmth that made me miss my family a little bit less.

Once again, I bow to the jury members – Gustavo Ardila, Brice Gautier, Guylaine Poulin-Vittrant, Vincent Sallet and Christophe Durand, for accepting to be a part of my Phd defense and for evaluating my research work.

And lastly, warm hugs to Andréa Soto, Cyril Léon and Stéphane Gable, for making everything simpler (professionally and personally). Thank you for believing in me and carrying me forth when I had no strength left. Extended hugs to Bhavya Agarwal and Prachi Attri for feeding me when I was in the crazy writing phase, and for always cheering me up.

Thank you all for making a dream come true.

Contents

Contents

Introduction

Today, from the simple exchange of an e-mail to advanced computing solutions, passing through health, energy, food, education and security, we rely on the use of information and communication technology (ICT) devices and systems. The ever-increasing smart objects (smartphones, connected watches, smart refrigerator, connected thermostat, voice assistance, medical implants, System Health Monitoring, pressure sensors, energy harvesters…) also known as 'Internet of things' (IoTs) have become an indispensable part of our daily lives and has transformed the society by establishing a fully mobile and globally connected networking system. This technological feat has been made possible by the integration of numerous transistors and electronic components in a dense integrated circuit (IC) as predicted by Moore's law [1].

To this date, micro-devices have become plethoric and cover a large spectrum including personal electronics, biomedical implants, sensors, actuators, nomad electronics… However, their utilisation has led to a drastic increase in the demand of energy supply at times when we are running out of natural resources. Until now, batteries and micro-batteries remain the principal energy source to power the micro-systems. Despite the numerous studies led by the scientific community to increase their performances, their lower lifetimes present a real challenge to the autonomy of the micro-devices. In addition to that, in biological systems or remote environments, battery replacements are extremely challenging and costly. Finally, their integration to micro-nano-systems is very complex and can result in increasing their size or weight, hence limiting the device efficiency and usability.

The recent developments in micro-nano-fabrication processes have permitted the miniaturisation of the micro-devices and thus their demand for energy consumption (to mW or even µW) has significantly reduced. This technological advancement has opened new portals for the self-sustainable micro-systems such as ambient energy harvesters to assist or completely replace the batteries. The greatest advantage of using ambient energy sources is that they are renewable unlike the energy obtained from the fossil fuels. This solution also offers the possibility to supply micro-devices working in environment with restricted or without electrical grid infrastructure.

Various renewable energy sources are found in our environment, out of which the most frequently used forms include:

1. ***Solar energy***: Highly developed solar technologies such as photovoltaics (PV) and concentrating solar-thermal power (CSP) are used to harness the solar radiation and convert it into electricity or stored for later use. It is considered as one of the most efficient form of energy harvesting solutions and is primarily used in very large power plants. Today, solar panels are commercialised in all sizes and thus small-scale solar energy systems can be integrated into homes with the installation of rooftop solar panels. Mini solar panels are used to power small appliances such as pocket calculators, watches, wearable devices, radios ..., which require low power. However, their functional capacity is dependent on their direct exposure to the Sun. Hence, solar energy is not the most adapted solution to power micro-devices, especially in remote environments, and present some limitation in term of integration.

2. ***Thermal energy:*** Thermoelectric energy generator (TEG) are used to convert heat energy into electrical energy using the thermoelectric phenomenon defined by the transfer of temperature change into electric power via temperature gradient. TEGs generally have a higher lifetime due to the lack of mobile components. But they are characterised with a very low conversion efficiency rate (5% - 8%) and require specific environmental conditions.

3. ***Radio-frequency (RF) electromagnetic radiation (EMR):*** RF EMR is the transfer of energy by radio waves in the frequency range between 100 kHz to 300 GHz. In our surroundings, this energy is emitted from TV signals, wireless radio networks, cell phone towers…which can be converted using high-gain antennas into DC voltage. The converted energy (several tens of µW) can be used to power IoTs or low-power micro-devices.

4. ***Mechanical and vibrational energies:*** These energies present the advantage of being ubiquitous and present at all times and are highly suitable for small-scale energy scavenging. Such energies can originate from bodily or vehicular movements, acoustic waves, flux of fluids or friction between two surfaces and can be converted into electrical energy via electrostatic systems, electromagnetic systems or piezoelectric systems.

Concerning the systems acting as transducers to convert mechanical energy into electrical energy, an electrostatic converter is often used at micro-scale. These converters have a variable capacitor structure, which generates charges from the relative motion of the electrodes (capacitor plates). Hence, a continuous motion is requisite for current generation. Electromagnetic systems generate current due to the motion between a magnet and a conductive coil (Faraday's effect). Due to the presence of mobile structures, their integration in micro-device is highly challenging.

Piezoelectric generators are based on the conversion of a mechanical deformation or vibrations into an electrical polarization as a result of the direct piezoelectric effect. Quartz and Lead zirconate titanate (PZT) are the most frequently used piezoelectric materials in the industry. The most common examples of piezoelectric devices around us include the butane lighters, wristwatches, intruder alarms, fire alarms, acoustic guitars… However, conventional piezoelectric materials have a high Young's modulus which makes them extremely stiff and incompatible to harvest mechanical energies present in our surrounding environment. In addition, their size is not compatible with strong dimensional constraints for integration in micro-devices.

Thanks to the development in the field of nanotechnology, especially in material synthesis and in micro-nano-fabrication, a new generation of piezoelectric energy generators integrating nanomaterials has appeared in the last decade. Amongst these nanomaterials, 1D-nanostructures, have gained attention due to their remarkable properties. Contrary to their bulk or 2D counterparts, they present higher mechanical and piezoelectric properties. They also present the advantage of being more sensitive to small scale energy scavenging. These properties thus confer to the 1D-nanostructures fundamental characteristics to improve the conversion efficiency of the transducers and thus offer the possibility to fabricate high-efficient and ultra-compact energy generators.

This thesis focuses on the enhancement of the piezo-generation capacity of GaN NWs for the overall enhancement of the efficiencies of piezo-generators based on these 1D-nanostructures. In order to achieve this goal, my thesis work is structured in three axes, from the first-hand knowledge of the synthesis techniques of GaN NWs, to their piezo-electrical characterisation and a deep understanding of the mechanisms in play at nanoscale. Based on this approach, novel solutions are explored towards the improvement of the conversion efficiency of the GaN NWs.

The first chapter of this manuscript presents an overview of the piezoelectricity principle, a brief discussion of the different piezoelectric materials, especially, GaN, which is the principal material used in this PhD project. In addition, the state-of-the-art of the piezoelectric conversion properties of single nanowires and piezo-generators are discussed.

The second chapter begins with a general introduction of the plasma-assisted molecular beam epitaxy technique, used for the synthesis of GaN NWs, investigated in this project. The main growth mechanisms, growth kinetics, and the Compact12 MBE machine at C2N cleanroom facility are detailed. In the following part, the two main characterization techniques, the scanning electron microscope and especially, the AFM-based techniques equipped with a home-made adapted Resiscope module, are presented. The latter has been rigorously used during the full course of my thesis for the piezoelectric characterization of single GaN NWs. Finally, the growth mechanism employed for the synthesis of GaN NWs is detailed along with a novel approach to control the NW morphology for piezoelectric applications.

Although, the performances of the final piezo-nanogenerator devices firstly depend on the piezo-conversion capacity of the GaN NW based active layer, the measuring circuit used to harvest the piezo-generated energies is of equal importance. In **chapter 3**, we investigate the influence of the load resistance of the electronics on the output voltage and the power generated by the GaN NWs. While in the nanogenerator research field, it is generally accepted that the resistance of the nanogenerator, R_g, (*i.e.,* the sum of contact resistance (R_c), Schottky diode resistance (R_S) and NW resistance (R_{NW})) is negligible, we demonstrate its significant influence on the measurements, with especially its dynamic evolution as a function of the load resistance and applied constant normal force. We also emphasize on the limitations of the formerly established protocol to judge the piezo-generation capacity of 1D-nanostructures. Solutions are proposed at the end of this chapter to overcome these limitations.

To enhance the piezo-electric response of the GaN NWs, another solution consists in taking into account their specific properties at the nanometric scale. In **chapter 4**, we propose to take advantage of the surface charge effects, which are strongly pronounced in our sub-100 nm wide GaN NWs, for the enhancement of their piezo-conversion capacity. Based on two different approaches, we demonstrate that the surface charges offer the possibility to tune the free charge carrier concentration within the NW volume, and thus reduce the screening of the piezo-charges, as a function of the NW diameter or the NW’s immediate environment. Then, by well choosing the NWs characteristics, we establish the advantageous role of the surface charges for piezoelectric applications. In this way, we have demonstrated that our intrinsically p-doped GaN NWs with an optimal diameter can generate output voltages reaching up to 520 mV per NW. This result settles the new state-of-the-art for 1D piezoelectric nanostructures tested via AFM-based systems, following the commonly used measurement protocol. Moreover, this value exceeds the ones generated by ZnO NWs, which remain the most widely investigated nanostructures for the development of piezoelectric energy harvesters, so far.

Finally, this manuscript ends with a general conclusion and some perspectives, opening the way towards future developments.

[1] G. E. Moore, ‘Cramming more components onto integrated circuits’, vol. 38, no. 8, p. 6, 1965.

Chapter 1

Concept of piezo-generation in 1D-nanostructres

Contents

1.1. Introduction to piezoelectricity

We can define piezoelectricity as the ability of certain materials, termed as piezoelectric materials, to acquire an electrical polarisation under the effect of an applied mechanical stress (direct piezoelectric effect). Such materials also exhibit an inverse piezoelectric effect and undergo deformation when an external electric field is applied to them (reverse piezoelectric effect).

1.1.1. Historical overview of piezoelectricity

Prof. Carolus Linnaeus and Prof. Franz Aepinus first observed in the mid-18th century that certain materials such as crystals and some ceramics produce electric charges under a temperature change. Rather unsuccessful attempts to further investigate this phenomenon were made by René Haüy and Prof. Antoine-César Becquerel. The first fundamental research in the field of piezoelectricity was done by Prof. Jacques Curie and Prof. Pierre Curie in the year 1880 [1]. The Curie brothers observed an interesting phenomenon while working with pyroelectric crystals such as quartz, cane sugar, topaz, tourmaline and Rochelle salt. They demonstrated that an applied load (tension or compression) generated an output voltage of opposite polarity (phenomenon illustrated in Fig. 1).

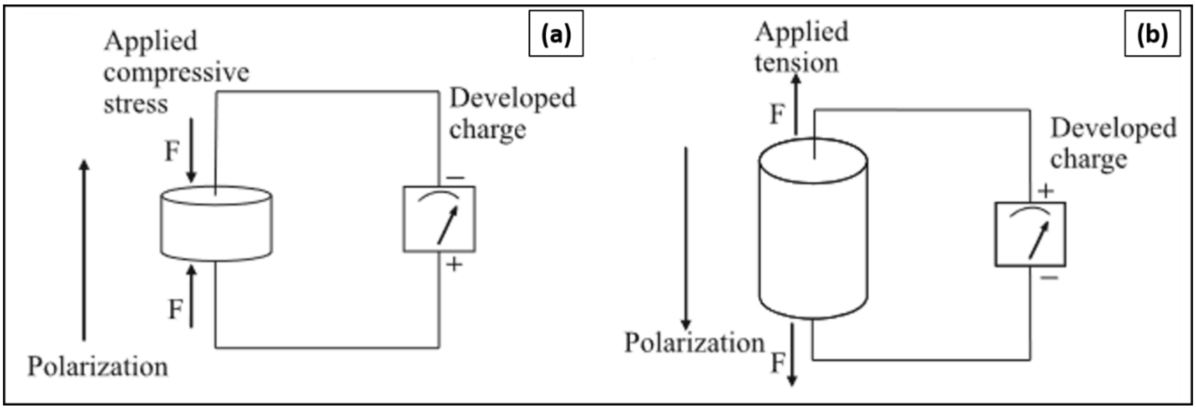

Figure 1. (Image taken from [2]). Direct piezo-effect in a piezoelectric material: (a) under compression; and (b) under tension.

It was Prof. Wilhelm Gottlieb Hankel in 1881 who proposed the term ‘piezoelectricity’ from the Greek word ‘*piezein*’ to distinguish this effect from similar phenomenon such as ‘contact electricity’.

Later in the same year, the concept of inverse piezoelectricity, i.e. the deformation of certain crystals due to an applied electric field, was predicted by Prof. Gabriel Lipmann from the mathematical deductions of the fundamental thermodynamic principles.

Jacques and Pierre Curie soon designed experiments to confirm the converse effect. They experimentally showed that when a piezoelectric crystal is subjected to an electric field, it lengthened or shortened depending on the polarity of the applied field [3], as shown in Fig. 2.

The role of crystal orientations on piezoelectricity was demonstrated by Prof. Voldemar Voigt in 1910. His textbook on physical crystallography thoroughly explained the piezoelectric effect in different crystal classes.

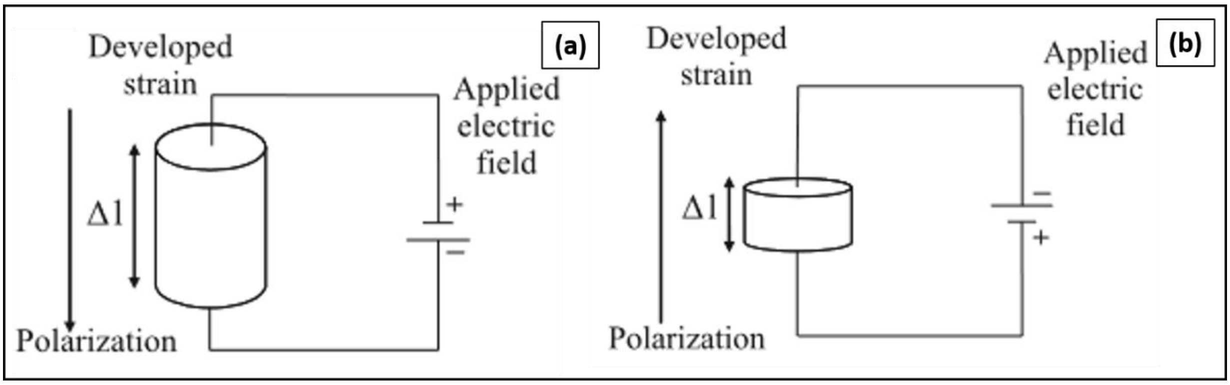

Figure 2. (Image taken from [2]). Inverse piezo-effect in a piezoelectric material: (a) under positive polarisation; and (b) under positive polarisation.

The first industrial applications of piezoelectric materials were only developed during the World War I. Prof. Paul Langevin in 1917 used quartz crystal as a resonator for ultrasound sources in SONAR. The latter was used to detect submarines through echolocation. During the WWII, United States, Japan and the Soviet Union separately led dedicated research work to develop synthetic materials with piezoelectric properties 100 times higher than the natural piezoelectric materials. The ease in manufacturing high quality piezoelectric ceramics thus led to a boost in the development of piezoelectric devices [2].

In 1945, the discovery of barium titanate ($BaTiO_3$) as a ferroelectric material put the focus of investigation on perovskite materials of a stable nature. This marked the beginning of the modern era of man-made piezo-ceramics and piezoelectricity.

Between the years 1945-1965, tailoring of piezoelectric materials for specific applications started taking place. Piezo-ceramics based on the $BaTiO_3$ and the lead zirconate family led to the development of military grade equipment, such as acoustic wave devices, ultrasound speakers, microphones, hydrophones... and pressure sensors.

In the time period 1965-1980, Japan became the hub for the development of new piezoelectric applications (smoke alarms, television remote controls, intrusion alarms, high frequency signal filtering device …) and manufacturing processes. This commercial success in Japan, led investors and industries from all over the globe to successfully develop piezo-ceramic products.

Today, several piezoelectric polymers and nanostructures are the centre of intense research in the field of sensors, robotics, LEDs, energy harvesting to power wearable technology, biomedical devices…

1.1.2. Piezoelectric effect in crystals

Piezoelectric effect is manifested in certain crystals only under two conditions. Firstly, each unit cell of the crystal structure must be composed of at least two different elements (difference of electronegativity) linked via ionic bonds. And secondly, they must lack a centre of symmetry (inversion symmetry). In the state of equilibrium (no load or electric field), the charge centres of the positive and the negative ions in the unit cell of the crystal are overlapping and the net dipole moment of the crystal is zero (Fig. 3a). Here, we do not consider the spontaneous polarisation effect demonstrated by certain piezoelectric crystals, which will be discussed shortly in this Chapter.

When an external deformation is applied, the geometry of the atomic structure of the crystal changes. The charge centres of the positive and the negative ions do not overlap anymore and a net electric dipole is generated in each unit cell (Fig. 3b).

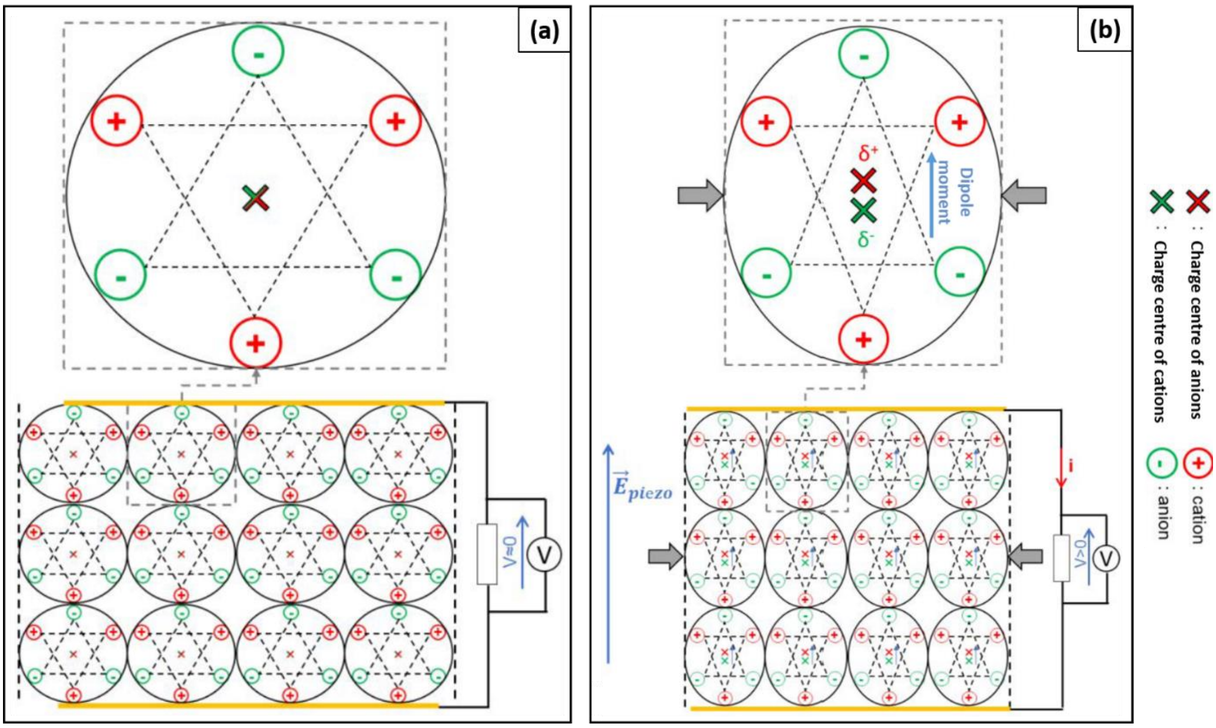

Figure 3. (Image taken from [4]). Schematic representation of a piezoelectric material (a) at rest; and (b) under external deformation. The positive and the negative charges represent the cations and the anions linked via an ionic bond. δ^+ and δ^- represent the positive and the negative charge centres, respectively.

The sum of the dipole moment of each unit cell results in a macroscopic polarisation of the crystal, termed as the piezoelectric polarisation (also called piezo-polarisation) and is oriented along a specific crystal axis. As a result, the opposite faces of the crystal possess an electric potential of inverse sign, which results in the generation of an output voltage when connected via an external circuit. The electrons/holes in the circuit will try to compensate the piezoelectric potential on the opposite faces until an equilibrium is attained anew. In this condition of *equilibrium* of crystal under an external stress, the measured potential is zero. The charges accumulated at the crystal surfaces flow back in the circuit when the external load is removed and an output voltage of opposite sign is detected. Hence, a piezoelectric crystal behaves as a transducer and converts mechanical energy into electrical energy via cyclic compressions-relaxations.

1.1.3. Piezoelectric materials

Piezoelectric materials can be found in the nature or synthetically developed. The natural piezoelectric materials are crystals of quartz, topaz, tourmaline, Rochelle salt and organic substances such as wood, silk, bone etc. The man-made piezoelectric materials consist of quartz analogs, ceramics, polymers, composites and single crystal semiconductors of group III-V and II-VI of the periodic table. The ensemble of these materials have been classified into 32 crystal classes, out of which 21 are non-centrosymmetric and only 20 have piezoelectric properties (Fig. 4).

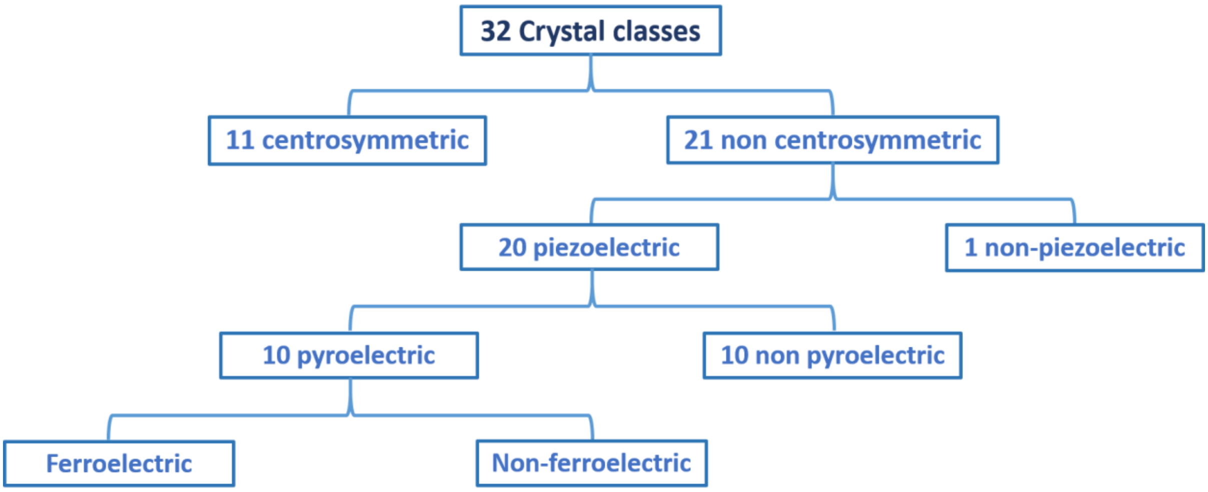

Figure 4: Grouping of crystal classes showing different categories of piezoelectric materials.

Amongst these 20 piezoelectric crystal classes, 10 are polar, i.e. they are characterised by a 'spontaneous polarisation' within the materials in the absence of any applied mechanical stress. These polar materials are classified as ***Pyroelectric*** materials which are very sensitive to temperature fluctuations. Amongst them, we find another family of materials in which the spontaneous polarisation can be modified or even inversed via the application of an external electric field. These materials are categorised as ***ferroelectric*** materials and contain domain walls with dipole moments in different directions. The latter could be aligned via electric poling of the material in order to create a net macroscopic polarization in the crystal. However, these crystals exhibit ferroelectric properties only when the temperatures are within a certain regime fixed by the Curie temperature (T_C). Above T_C, the ferroelectric materials become ***para-electric*** with a cubic symmetry and lose their spontaneous polarisation. This process is completely reversible and the materials re-become ferroelectric once the temperature falls below the T_C.

The remaining 10 classes consist of ***non pyroelectric*** materials. They are non-polar and exhibit piezoelectric properties only under the influence of an externally applied mechanical deformation.

Here, we provide a brief overview of some of the frequently used piezoelectric materials.

1. **Piezo-ceramics**: These generally belong to the family of perovskites, with the crystal structure ABO_3, where A is a larger metal ion linked via covalent or ionic bonds to a smaller atom B and oxygen atoms. Piezo-ceramics are made from fine powders of component metal oxides in defined proportions and heated to make a uniform power. They are then mixed with an organic binder and solidified into a dense crystalline structure at high pressure and temperature without passing through the liquid phase. Ceramics could be crystalline, semi-crystalline or even amorphous. Only crystalline ceramics exhibit piezoelectric properties. $BaTiO_3$, $PbTiO_3$, PZT, $KNbO_3$, $LiNbO_3$, $LiTaO_3$ … are some examples of man-made piezo-ceramics. At temperatures below the Curie point, these perovskite materials exhibit a tetragonal or rhombohedral symmetry and are also ferroelectric in nature.

2. **Polymers**: Polymers are covalently bonded macromolecular structures, which are formed by a linkage of smaller repeating units called monomers. Piezoelectric polymers gained attention after the discovery of piezoelectric effects in Polyvinylidene fluoride (PVDF), demonstrated by Prof. Heiji Kawai in 1969 [5]. Polymers can be sub-categorised into 3 classes:

    a) *Massive piezoelectric polymers*: These polymers can be semi-crystalline or amorphous. Amongst the most used polymers in the industry, we find copolymers of PVDF (poly-vinylidene fluoride-trifluoroethylene and tetrafluoroethylene), Parylene-C, polyamides, liquid-crystal polymers, polyureas and biopolymers such as keratin. These polymers exhibit macroscopic polarisation when electrically poled at high temperatures using external electric fields. The high temperatures allow the polymeric chains to reorganise easily under the influence of the electric field.

    b) *Cellular polymers or electrets*: These polymers are generally based on PVDF (polar polymers) and its copolymers, out of which polypropylene is the most popular. Electrets are insulating by nature and carry fixed charges which are implanted externally. Each polymeric cell consists of gas pockets which gets ionised under the influence of an external electric field. As a result, charges of opposite sign appear on the surface of the polymer and an electric dipole is formed. Only under these conditions, such polymers exhibit piezoelectric properties.

    c) *Composite polymers*: These polymers integrate inorganic piezoelectric nano-materials such as microparticles, microfibers… immersed in an electrically passive flexible matrix and exhibit piezoelectric properties depending upon its constituents.

3. **Single-crystal semiconductors:** These are essentially the semiconductors of the II-VI and the III-V groups of the periodic table. The latter being employed in this thesis, will be detailed in the following section, especially GaN. The oxides of group II and group III-nitrides generally crystallize in a zinc-blende (cubic) or Wurtzite (hexagonal) structure. In zinc blende crystals, all covalent bonds have identical bond lengths and angles, resulting in zero dipole moment in the unit cell. Only Wurtzite structures exhibit piezoelectric properties due to the absence of an inversion symmetry (non-coincidence of the positives and negatives charges at equilibrium). Moreover, due to the difference of electronegativity of the group III and the group V elements, the electron cloud of the ionic bonds gets attracted to the most electronegative atom. This results in an inherent and permanent electrostatic dipole moment, giving rise to a spontaneous polarisation (P_{SP}) in the crystals. The spontaneous polarisation in III-N materials can be computed theoretically using ab-initio methods [6]. It has been reported that the P_{SP} values of III-N materials (GaN, AlN and InN) are 30% higher compared to the classic ferroelectric piezo-ceramics such as $BaTiO_3$ [7].

1.2. Properties of Gallium nitride (GaN)

Gallium nitride (GaN) is a direct bandgap semiconductor of the III-V group of the periodic table. In this section, we describe the properties of GaN, which is the principal material studied in this thesis.

1.2.1. Crystallographic structure

Like all III-nitride semiconductors, GaN can crystallise in three phases, namely, the *Wurtzite* (Wz, Fig. 5a), *Zinc-blende* (ZB, Fig. 5b) and *rock salt* (Fig. 5c). The Wurtzite phase is hexagonal and has a thermodynamically stable structure while Zinc-blende and rock salt phases have cubic-face-centred lattices. The ZB structure has been stabilised by epitaxial growth for III-V materials such as GaN and InN [8]. However, the rock salt phase can be obtained only under extreme pressure conditions and thus cannot be produced with any kind of epitaxial growth method [8].

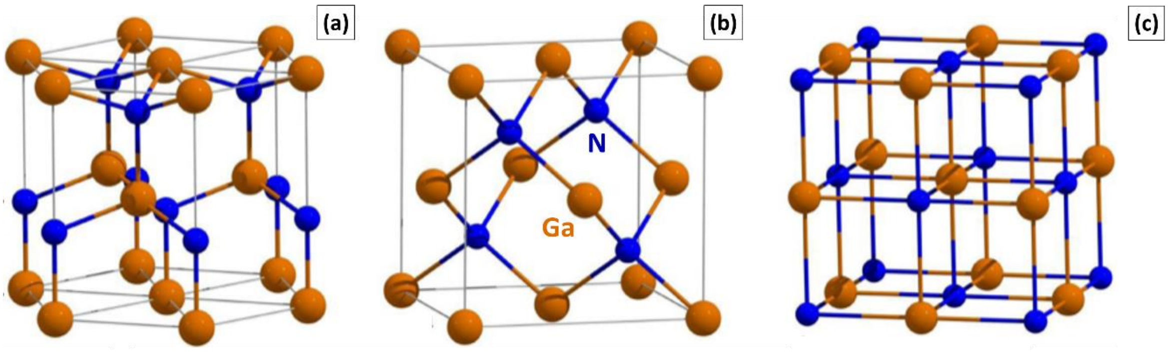

Figure 5. (Image taken from [9]). 3D representations of the crystalline phases of III-N materials, (a) Wurtzite (Wz), (b) Zinc-blende (ZB) and (c) Rock-salt. The basal and the axial lattice parameters are given by 'a' and 'c'; 'u' represents the internal parameter.

In this manuscript, only the Wurtzite phase of GaN has been considered. A unit cell of this phase is shown in Fig. 6 in which each Ga-atom is linked to 4 N atoms and consequently each N-atom is connected to 4 Ga atoms. It is depicted by two lattice parameters, the basal plane lattice parameter 'a' and the axial lattice parameter 'c'. These parameters are also used to describe the in-plane and out-of-plane deformations and lattice mismatches in epitaxial growths. The interatomic distance is usually represented by the internal parameter 'u' (anion-cation bond length divided by c).

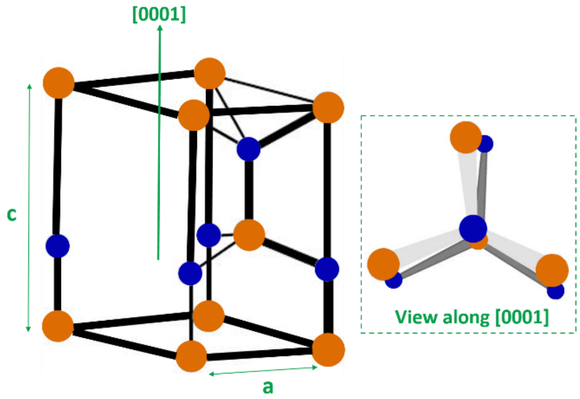

Figure 6. Unit cell of GaN in the Wurtzite phase. A stick and ball representation (in the square) indicating the projection of Wurtzite phase in the [0001] direction.

The values of GaN lattice parameters ‘a’ and ‘c’ are 3.189 Å and 5.186 Å, respectively, for hexagonal Wz structure. For an ideal Wz structure, the values of axial ratio ‘c/a’ and internal parameter ‘u’ are 1.633 and 0.375, respectively. However, in reality, the reported axial ratio for Wz structure is 1.626, which deviates from the ideal value [10]. This leads to a small distortion of the tetrahedral angles formed by Ga and N atoms.

Also, the Wz structure is composed of closely packed diatomic planes and has an ABABA… sequence in the (0001) basal plane, also called the c-axis. The positive direction of the c-axis ([0001]) is defined from Ga to N-atoms by convention.

Due to this packing sequence, Wz structures lack an inversion symmetry perpendicular to the c-axis and thus the [0001] and [000-1] directions are not equivalent. The surfaces could either terminate with Ga-atoms or N-atoms resulting in two different surface polarities (Fig. 7). GaN has a metal-polarity (or Ga-polarity) when the termination layer is made of Ga atoms (growth takes place along [0001] direction). Correspondingly, N-polar surfaces have a nitrogen termination (growth takes place along [$000\bar{1}$] direction). The polarity of Wz structures is an important factor as it affects the surface morphologies, the optical properties and the growth kinetics by directly affecting the diffusivity of atoms on the surface as well as their incorporation into the epitaxial layers [11]–[17].

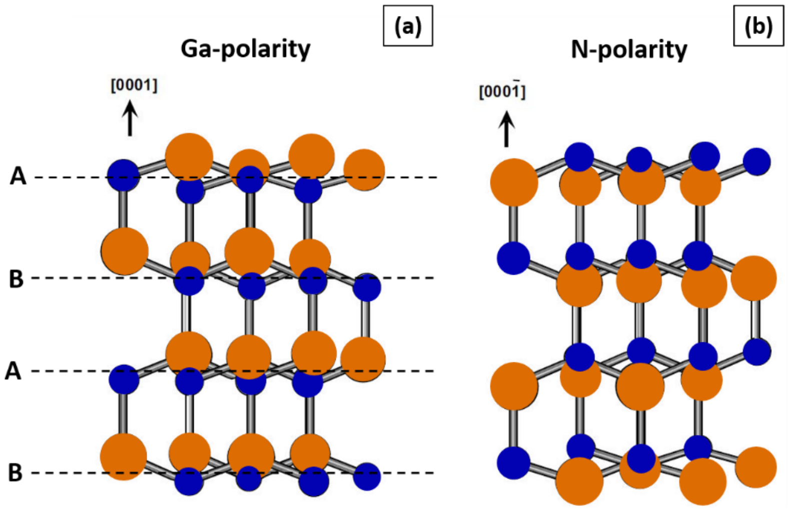

Figure 7. Wurtzite structure of GaN with (a) Ga-polarity and (b) N-polarity. The ABABA…stacking sequence of the Wz phase is also represented.

1.2.2. Mechanical characteristics

The mechanical properties of the Wurtzite crystalline structures are defined by a rank 4 tensor, called the elasticity tensor or the stiffness tensor, $\bar{\bar{C}}$. The relationship between the stresses and strains to the deformation of the material could thus be linked by the elasticity tensor via generalisation of Hooke’s law. The linear relationship is given as follows:

$$\sigma_{ij} = \sum_{kl} C_{ijkl}\, \mathcal{E}_{kl} \qquad (1)$$

where, σ_{ij} and $\mathcal{E}_{kl}$ are the stress and the deformation vectors, and C_{ijkl} are the components of the elasticity matrix. Taking into account the hexagonal symmetry of the Wurtzite structure of GaN, the elasticity coefficients can be represented in thefollowing matrix form:

$$C_{ijkl} = \begin{bmatrix} C_{1111} & C_{1122} & C_{1133} & 0 & 0 & 0 \\ C_{1122} & C_{1111} & C_{1133} & 0 & 0 & 0 \\ C_{1133} & C_{3322} & C_{3333} & 0 & 0 & 0 \\ 0 & 0 & 0 & C_{2323} & 0 & 0 \\ 0 & 0 & 0 & 0 & C_{2323} & 0 \\ 0 & 0 & 0 & 0 & 0 & C_{1212} \end{bmatrix} \qquad (2)$$

The coefficient C_{1212} is given by $\frac{(C_{1111} - C_{1122})}{2}$, while the other 5 coefficents are independent. Using Voigt's contracted notations where (11) = 1, (22) = 2, (33) = 3, (23) = (32) = 4, (13) = 5, and (12) = (21) = 6, the 4th rank tensorial form of C_{ijkl} reduces to $C_{\alpha\beta}$ with (ij) = α and (kl) = β.

$$C_{\alpha\beta} = \begin{bmatrix} C_{11} & C_{12} & C_{13} & 0 & 0 & 0 \\ C_{12} & C_{11} & C_{13} & 0 & 0 & 0 \\ C_{13} & C_{23} & C_{33} & 0 & 0 & 0 \\ 0 & 0 & 0 & C_{44} & 0 & 0 \\ 0 & 0 & 0 & 0 & C_{44} & 0 \\ 0 & 0 & 0 & 0 & 0 & C_{66} \end{bmatrix} \qquad (3)$$

Here, C_{11} and C_{33} represent the elastic coefficients of the solid when the applied strain is perpendicular to the in-plane and out-of-plane, respectively. On the contrary, C_{13} and C_{12} correspond to the coefficients when the applied strain is parallel to the respective crystal faces (shear strain). Lastly, C_{44} and C_{66} represent the mechanical behaviour of the crystal subjected to torsion.

Tables 1 and 2 recapitulate the theoretical as well as experimentally determined elastic coefficients of Wz GaN.

Table1. Elastic coefficients $C_{\alpha\beta}$ (GPa) of GaN crystal in Wurtzite phase obtained theoretically via first-principles calculation.

C_{11}	C_{12}	C_{13}	C_{33}	C_{44}	C_{66}	***References***
396	144	64	476	91	126	[18]
350	140	104	376	101	115	[19]
367	135	103	405	95	116	[20]
334	132	99	372	86	101	[21]

Table 2. Experimentally obtained values of elastic coefficients $C_{\alpha\beta}$ (GPa) of Wurtzite GaN.

C_{11}	C_{12}	C_{13}	C_{33}	C_{44}	C_{66}	**References**
390 ± 15	145 ± 20	106 ± 20	398 ± 20	105 ± 20	123 ± 10	[22]
359.4	129.2	92.0	389.9	98.0	115.1	[23]
296 ± 18	130 ± 11	158 ± 6	267 ± 18	24.1 ± 2	83 ± 4	[24]
374	106	70	379	101	134	[25]
365 ± 2	135 ± 4	114 ± 16	381 ± 1	109 ± 3	115 ± 1	[26]
377	160	114	209	81.4	109	[27]
370	145	110	390	90	113	[28]

1.2.3. Piezoelectric properties

As mentioned earlier, piezoelectric semiconductors of the III-V group exhibits an internal polarisation in the Wurtzite phase of the crystal structure. This is due to the lack of an inversion symmetry of the structure as well as to the difference in the electronegativity of the constituting anions and cations. This polarisation is called the spontaneous polarisation (P_{SP}) and exists inherently in the structure even when no deformation is applied. In GaN crystal, the direction of P_{SP} is from N-atoms to Ga-atoms, by convention. Thus for Ga-polar GaN, P_{SP} is oriented antiparallel to the principal growth direction [0001] (Fig. 8a), while for N-polar GaN, P_{SP} is aligned parallel to the growth direction $[000\bar{1}]$ (Fig. 8b). P_{SP} of GaN is of the order of -0.029 C/m^{-2} [10].

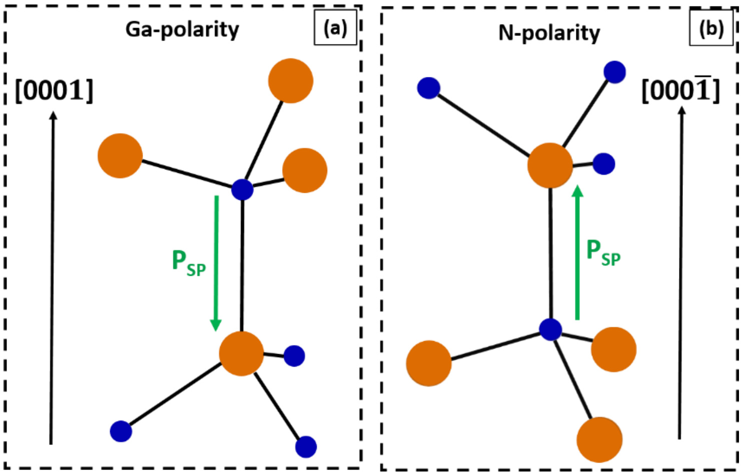

Figure 8. Stick and ball representation of the orientation of spontaneous polarisation (P_{SP}) in (a) Ga-polar and (b) N-polar, GaN structure.

Under an external deformation, a piezoelectric polarisation (P_{PZ}) appears in Wz crystalline structures. The P_{PZ} can thus be defined in terms of the applied strain '$\mathcal{E}$' or the received stress 'σ' as follows:

$$P_i = \sum_{j=1}^{3}\sum_{k=1}^{3} e_{ijk}\ \mathcal{E}_{jk} \qquad (4)$$

and,

$$P_i = \sum_{j=1}^{3}\sum_{k=1}^{3} d_{ijk}\ \sigma_{jk} \tag{5}$$

The matrix representations of the piezo-coefficients e_{ijk} and d_{ijk} in Voigt's notation are given by e_{ij} and d_{ij}:

$$e_{ij} = \begin{bmatrix} 0 & 0 & 0 & 0 & e_{15} & 0 \\ 0 & 0 & 0 & e_{15} & 0 & 0 \\ e_{31} & e_{31} & e_{33} & 0 & 0 & 0 \end{bmatrix} \tag{6}$$

and,

$$d_{ij} = \begin{bmatrix} 0 & 0 & 0 & 0 & d_{15} & 0 \\ 0 & 0 & 0 & d_{15} & 0 & 0 \\ d_{31} & d_{31} & d_{33} & 0 & 0 & 0 \end{bmatrix} \tag{7}$$

The 6 non-zero piezoelectric coefficients found in the literature are reported in Table 3 for GaN in Wz phase.

Table3. Piezo-electric coefficients e_{ij} (C/m^2) and d_{ij} (pm/V) of GaN crystal.

e_{15}	e_{31}	e_{33}	References	d_{15}	d_{31}	d_{33}	References
0.10	0.17	0.29	[23]	-	-	2.13 ± 0.05	[29]
-0.30	-0.36	1.00	[30]	3.1 ± 0.2	-	-	[31]
-	-0.49	0.73	[10]	-	-	2.0 ± 0.1	[32]
-0.33	-0.33	0.65	[33]	-	-1.4 ± 0.1	2.8 ± 0.1	[34]

1.2.4. Optical properties

GaN is a direct band gap semiconductor like all III-nitride materials, i.e. the conduction band minima and the valence band maxima are localised at the same point 'Γ' in the k-space in the first Brillouin zone. III-nitride materials are highly sought after in optoelectronic applications as they offer the possibility to tune the direct bandgap over a wide range of wavelengths. From the deep ultraviolet range (360 nm for GaN and 210 nm for AlN), these semiconductors cover the entire visible spectrum to the near infrared (InN at 1900 nm) (Fig. 9) [35] .

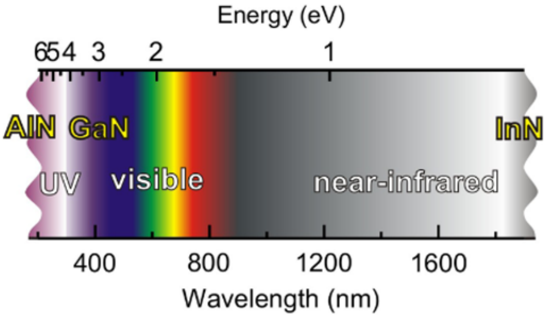

Figure 9. (Image taken from [35]). Optical spectrum showing the coverage of III-nitride semiconductors with a wide wavelength range from deep ultraviolet to the near-infrared range.

The band gap energies (E_g) of semiconductors vary as a function of temperature 'T' [36]. This dependence is given by the Varshni-law as follows:

$$E_g = E_0 - \frac{\alpha T^2}{(T + \beta)} \tag{8}$$

where, E_0 is the band gap energy at 0 K and α (meV/K) and β (K) are Varshni parameters. The first measurement of the temperature dependent energy gap in Wurtzite GaN was performed by Monemar in 1974 [37], [38]. The direct bandgap energy (E_g) of GaN is calculated to be 3.4 eV at 300 K [8]. Here, the bandgap (E_0) of GaN is 3.51 eV [37] and the Varshni constants are 0.909 meV/K and 830 K, respectively [39]. Fig. 10 shows the energy band diagram versus the lattice constants of the most important binary semiconductors at 300 K.

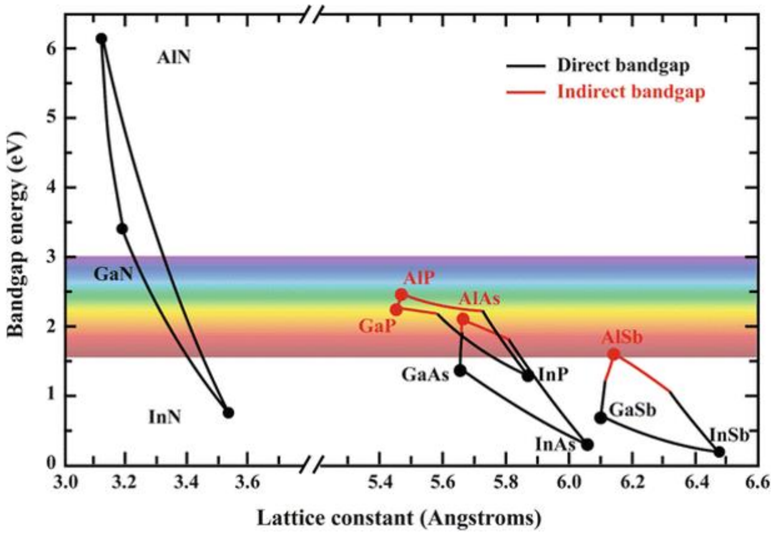

Figure 10. (Image taken from [40]). Bandgap energy diagram of binary semiconductors versus the lattice parameters at 300 K. The III-nitrides have a direct bandgap with GaN located at 3.4 eV. GaN falls in the visible spectrum as also indicated.

1.3. Introduction to the concept of piezoelectric generation in nanowires

1.3.1. Motivation to use 1D-nanostructures

With the first demonstration of piezoelectric conversion from ZnO NWs by Prof. Z.L. Wang in 2006 [41], 1D-nanostructures, such as nanorods, nanowires (NWs), nanowhiskers, nanofibers… have emerged as promising candidates for developing compact and efficient piezoelectric generators.

Because of their defect-free crystalline structures, their nanometer scale dimensions and their large surface-to-volume ratio, 1D-nanostructures demonstrate exalted properties with respect to their bulk and 2D-film counterparts as described below:

1. Thanks to their high crystalline quality, 1D-nanostructures present a higher degree of elastic deformation resulting in a higher resistance to fracture [42] and hence a longer device lifetime.

2. Their high aspect ratios confers to them a high flexibility. They are thus deformable under very small forces in the nN to pN range [43].
3. Due to the scaling of the nanostructures (especially having diameters below 100 nm), exalted piezoelectric coefficients were reported for several materials, such as ZnO [44]–[46], PZT [47], PVDF [48], GaN [49]–[51]… Concerning the GaN NWs, a six-fold increment in the piezoelectric coefficients is reported [49]. *Table 4* summarizes the piezoelectric coefficient (d_{33}) of the respective materials in 1D and bulk/thin films.

Table 4. Piezoelectric d_{33} coefficients of 1D nanostructures w.r.t their bulk/thin films counterparts.

Material	**Type of 1D-nanostructures**	**d_{33} in 1D (pm/V) or (pC/N)**	**d_{33} in bulk state / thin films (pm/V) or (pC/N)**
GaN	Nanowires [49]	12.4 – 13.2	2.8 – 3.7 [34] 2 [32] 2.7 [52] 2.13 [29]
ZnO	Nanopillars [45]	14.3 – 26.7	9.93 [44] 12.4 [53]
	Nanobelts [44]	7.5	
	Nanorods [46]	0.4 – 9.5	
PZT	Nanofibers [47]	127	300 – 1000 [54] 60 – 130 [48]
	Nanoribbons [48]	54.2 - 101	
PVDF	Nanowires [55]	-6.5	-25 [48], [56]
PVDF-TrFE	Nanowires [55]	-8.5	-17 – -38 [57] -38 [48]
$BaTiO_3$	Nanowires [58]	43	190 [59] 260 - 454 [60]–[64]*
PMN-PT	Nanofibers [65]	50	2000 – 3000 [48]

*d_{33} values with doping.

4. Due to their nanometer scale diameters, 1D-nanostructures are characterized by enhanced surface charge effects (SCE), which induces a modulation of the free charge carrier concentration into the NW volume due to the surface fermi level pinning (SFLP). This phenomenon can lead to a modification of their piezoelectric response. Recent studies have demonstrated that SCE is strongly predominant in ZnO and GaN NWs and can present an advantage for enhancing the piezoelectric response of the NWs, as theoretically demonstrated by [66], [67].
5. 1D-nanostructures also exhibit novel characteristics, non-existing or non-expressed at micrometric scale. For instance, an enhanced collection of piezo-charges due to the ‘Schottky nano-contact’ formed between the NW top and the electrode of collect has been reported [68].

1.3.2. Techniques to characterise piezoelectric properties of 1D nanostructures

Piezoelectric coefficients (d_{ij}) are amongst the most important parameters to define the piezoelectric properties of a material. For bulk materials and thin films, standard measurement methods have long been established to quantify these coefficients via direct as well as inverse piezoelectric effects [69]. These methods include piezoelectric resonance [70], interferometry [71], Berlincourt method [72], [73], nano-indentation [74], [75]... However, they cannot be employed to characterise the piezoelectric properties of 1D-nanostructures, as they are not specific to their dimensions.

Piezoelectric conversion (direct piezoelectric effect) is another key parameter, characteristic of the piezoelectric properties of the material. Once again, classical techniques to measure the direct piezoelectric response of bulk and 2D materials are not applicable to 1D nanostructures [76]–[78]. Moreover, no commercial techniques are available, thus driving the community to develop new nano-characterization tools.

Up-to-date, two non-destructive characterisation tools such as conductive atomic force microscopy and in-situ scanning/transmission electron microscopes (SEM/TEM) are used to evaluate the performance of the 1D piezoelectric nanostructures. Here, we provide a brief overview of these two methods.

a) Atomic force microscopy (AFM)

Measurement of indirect piezoelectric effect

AFM is one of the most important extension of scanning tunnelling microscope (STM) which was developed in 1986 by Binnig et al. [79]. In order to access the piezoelectric coefficients of 1D-nanostructures, a commercial scanning probe microscope (SPM) mode is used. The latter is called ***piezoresponse force microscopy (PFM),*** which is based on the standard AFM setup in the contact mode with an electrically conductive cantilever and AFM tip. Fig. 11a shows the schematic representation of the PFM setup. On applying an external alternating bias between the tip and the bottom electrode, strains are produced in the piezoelectric sample due to the *inverse piezoelectric effect.* These strains cause a vertical and lateral deflection of the cantilever which are measured using the position sensitive photodetector (PSD) using lock-in (L.I.) amplifiers [80].

This technique was firstly employed to measure the piezoelectric coefficients of ZnO nanobelts by Zhao et al. in 2004 [44]. Since then, it has been used to investigate the indirect piezoelectric response of various 1D-nanostructures such as $LiNbO_3$ NWs [81], Sb_2S_3 NWs [82], PVDF/GOF nanofibers [83], PMN-PT nanofibers [65], $BNTiO_3$ nanofibers [84], $BaTiO_3$ NWs [58], GaN NWs [51]… However, this method does not provide any spatial resolution of the piezoelectric coefficients (d_{ij}) as only single-point measurements are performed to minimise damage to the nanostructures.

To alleviate this issue, a non-destructive PFM (ND-PFM) technique can be adopted [85] (Fig. 11b). This technique uses the so-called ''DataCube'' mode to induce a periodic oscillation of the cantilever at a high frequency ranging from 0.25 kHz – 1 kHz. The oscillating tip performs an xy-raster scanning of the surface with intermittent contacts, while an alternating voltage is continuously applied between the sample and the tip. The material is strained at each contact resulting in the cantilever deflection. The latter is detected using a virtual L.I. system with high-speed data capturing. This technique has been successfully used on soft polymeric NWs and hard ceramic NWs, which previously could not be measured via conventional PFM [85], as well as very recently on ZnO NWs [86].

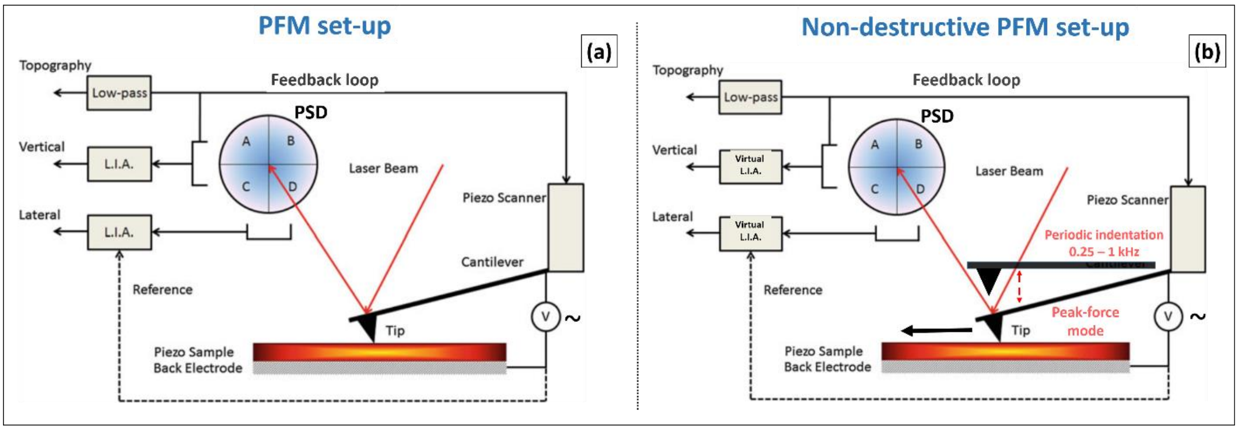

Figure 11. (Images adapted from [80]). Schematic representations of (a) PFM setup and (b) non-destructive PFM (ND-PFM).

Measurement of direct piezoelectric effect

Due to the unavailability of commercial systems to measure the direct piezoelectric effect in 1D nanostructures, *home-made* systems comprising an ***AFM with an electric module*** are used. This technique combines the nanometer scale resolution of the AFM with the real-time electrical measurements to simultaneously obtain topographic and electrical cartographies. The first demonstration of such a system was done by the team of Prof. Z. L. Wang in 2006 to measure the piezoelectric response of ZnO NWs [41]. Only a handful of teams in the world have such ''home-made'' AFM systems with necessary electrical modifications to study the piezoelectric conversion properties of 1D-nanostructures.

Based on these 'home-made' AFM systems, three configurations have been reported in the literature [41], [87]–[89].

Bending in scanning configuration

In this configuration (Fig. 12a), the conductive AFM tip laterally scans the arrays of vertically aligned nanostructures in the contact mode. Each nanostructure is individually deformed (the outer side is stretched and the inner side undergoes compression) with a convoluted lateral scanning force and an applied constant normal force (CNF). A piezoelectric field is thus created in the core of the nanostructure due to the direct piezoelectric effect. The generated electrical signal is harvested by the conductive AFM tip and is measured across an external resistor. Depending on the polarity of the nanostructure, their doping type and the positioning of the AFM tip on the surface, the Schottky contact formed between the AFM tip and the top of the NW could be forward or reversed biased [90]. This technique has also been employed to establish the piezo-generation mechanism in nanostructures (detailed in section 1.3.3).

Apart from the team of Prof. Wang [41], this technique has also been adapted by our team at the laboratory GeePs, where an AFM setup has been equipped with a state-of-the-art home-made electric module developed by Pascal Chrétien, known as ***Resiscope*** [91]. This system has been rigorously employed in this thesis and will be further discussed in Chapter 2.

Bending in horizontal configuration

This specific configuration was developed at IMEP-LaHC in Grenoble by the team of L. Montes, M. Mouis and G. Ardila in 2011 to carry out piezoelectric measurements on GaN and GaN/AlN/GaN NWs [88]. Using Ag-glue, the sample is vertically fixed on a metal support and thus, an Ohmic contact is established at the substrate/NW interface. Piezo-electrical measurements via this method are carried out in two-steps. Firstly, high-resolution topographic images are recorded in the tapping mode of the AFM for NW localisation. And then, in the second part, the AFM mode is switched from tapping to force-modulation mode (approach-withdrawal mode). In this configuration, a very precise local deformation is applied on the selected NW (as illustrated in Fig. 12b). The collection method of generated electric signals is the same as in scanning configuration via the conductive AFM tip, which makes a Schottky contact at the AFM tip/NW interface. However, as the tip is always in contact with the stretched side of the nanostructure, a careful consideration of the piezo-potential distribution is required for a forward-biased Schottky contact.

Axial compression configuration

In the previously described scanning configuration where the AFM tip induces a lateral bending of the NW with a convoluted force (convolution of CNF and lateral scanning force), it is extremely difficult to correlate the mechanical and the piezoelectrical properties of the nanostructures. To alleviate this issue, direct piezoelectric measurements using an AFM, equipped with an advanced electric module was recently proposed by our team [89]. This module was operated in an AFM mode inspired by the 'pulsed force mode', which is a low frequency non-resonant mode primarily developed to perform local mechanical measurements [92]. In this technique, the conductive AFM tip interacts with the surface only intermittently with a well-controlled and purely axial force. The nanostructure is thus deformed under pure axial compression, as shown in Fig. 12c. With this new configuration, a direct correlation of the NW axial deformation with its piezoelectric response is obtained, which makes possible the establishment of the electromechanical coupling coefficient of GaN NWs [89].

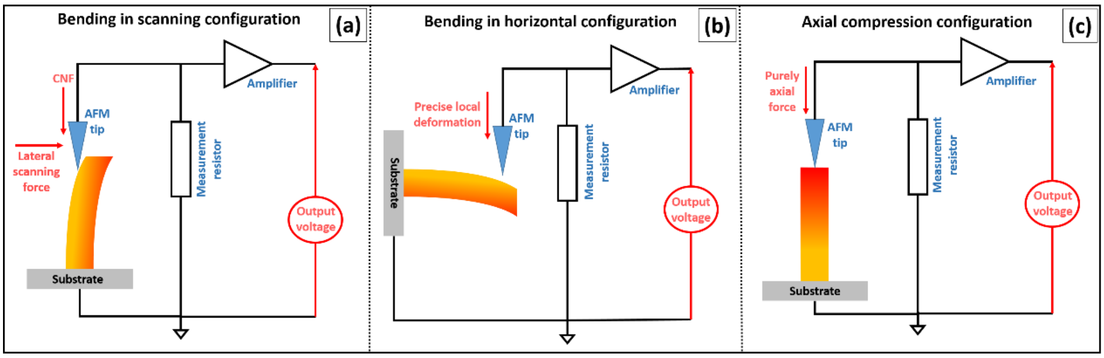

Figure 12. Schematic representations of the three AFM configurations used to measure the piezoelectric conversion properties of NWS: (a) scanning configuration, (b) horizontal configuration and (c) newly developed intermittent configuration.

b) Scanning electron microscope (SEM)/ Transmission electron microscope (TEM)

1D-nanostructures have emerged as the building blocks of next-generation micro/nano devices. This highlights the need to understand their structural, mechanical, electrical and electromechanical properties at an atomic level. Hence, these last years, new methodology, based on existing equipment, have been adapted to perform piezoelectric measurements on nano-objects.

Thanks to the development of micromanipulators and multifunctional sample holders, in-situ characterisation tools such as SEM and TEM have been used to study the aforementioned properties of 1D-nanomaterials [93]–[97]. The spatial and temporal resolution of SEM/TEM coupled with their analytical capabilities allow real time measurements of current and voltage as the nanostructure is deformed. Hence a correlation between the applied force and the piezoelectric response can be established in real-time.

The advantages of TEM have been combined with other approaches such as electromechanical resonance to calculate the elastic modulus of ZnO [98] and GaN NWs [99]. Fig. 13a shows the tensile tests performed in SEM on a single InAs NW to obtain the Young's modulus as well as its fracture strength [100].

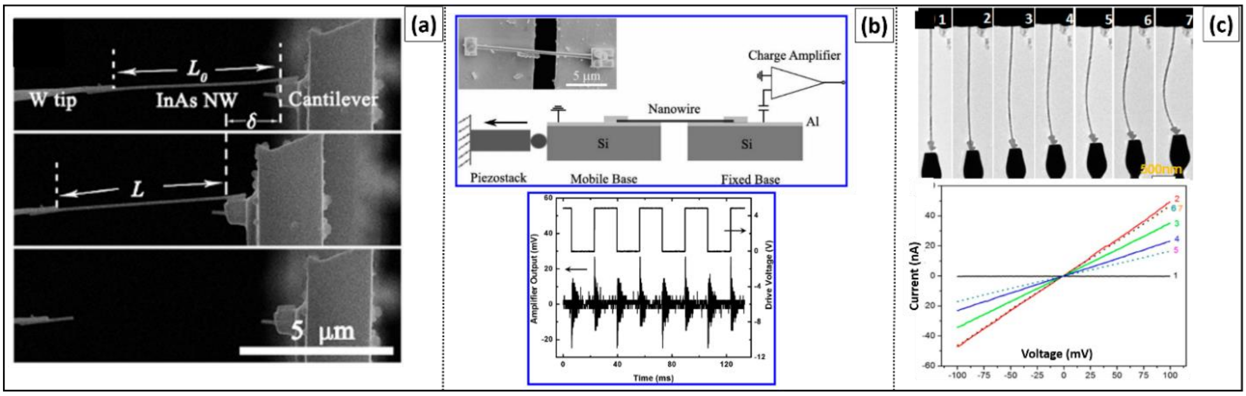

Figure 13. (Images taken from [100]–[102]). In-situ SEM/TEM characterisations of (a) tensile strength of single InAs NW, (b) schematic representation of the mechanical stage to induce periodic stretching in an individual BaTiO$_3$ NW and the measured output signal from the charge amplifier; and (c) deformation and I-V measurements performed on individually clasped InAs NWs with a Wurtzite structure.

Using a loading platform with a fixed and a mobile base inside a SEM, an individual $BaTiO_3$ NW was stretched and the generated piezoelectric charges were detected from the charge amplifier (Fig. 13b) [101]. Electromechanical characteristics of InAs NWs were also studied in an STM-TEM probing system [102] (Fig. 13c).

1.3.3. Piezoelectric generation mechanism in GaN NWs

The polarity of the NWs plays a crucial role in defining the orientation of the spontaneous polarization as well as the piezoelectric one. Our GaN NWs are characterized by an N-polarity with nitrogen atoms as surface terminations. The anionic polarity of GaN NWs has already been demonstrated by KOH etching in previous studies by our team [103], [104]. The hydroxide ions etch the Ga atoms but at the same time they are repelled by the electronegativity of the nitrogen dangling bonds. As a result, the Ga-polar surfaces are conserved while the N-polar surfaces undergo a change in their morphology and become tilted with {10-1-1} planes [103].

The total polarization inside the volume of the NW consists of the sum of the inherent spontaneous polarisation (P_{SP}) and the piezo-polarisation (P_{PZ}) created as result of an external applied force. P_{SP}, which originates due to the non-zero net dipole moment along the c-axis, is aligned parallel to the (000-1) for our N-polar GaN NWs. The orientation of P_{PZ}, which appears under NW deformation, is driven both by the P_{SP} orientation (and thus the material polarity) and the type of deformation applied. Hence, for N-polar GaN NWs, P_{PZ} is oriented parallel to the P_{SP} as well as the growth direction under purely axial stretching, while it is oriented anti-parallel to both P_{SP} and the growth direction under pure axial compression. A strong negative piezo-potential is thus created at the NW summit under extension while under compression a piezo-potential of opposite sign is observed. This phenomenon is clearly illustrated in Fig. 14 (b-c).

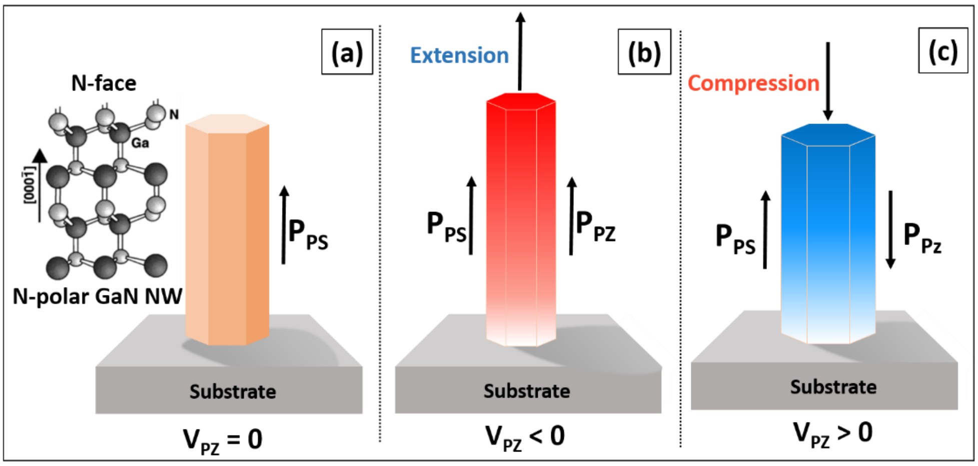

Figure 14: (a) The atomic arrangement of N-polar GaN NW with its schematic representation. The P_{SP} is aligned parallel to the (000-1) growth direction for N-polar GaN NWs. For such NWs, (b) under axial stretching, P_{PZ} is oriented parallel to P_{SP} with a negative piezo-potential distribution, and (c) under axial compression, P_{PZ} is oriented anti-parallel to P_{SP} with a positive piezo-potential distribution.

The piezo-generation mechanism in N-polar GaN NWs was established by Gogneau et al. [90] based on the previous studies performed by Su et al. [105] on N-polar GaN nanorods and by Z.L. Wang on ZnO NWs [41]. The authors demonstrated that the mechanism depends crucially on the NW polarity and its doping type. Thanks to an AFM equipped with an electric module, the authors carefully correlated the NW morphologies and their piezoelectric responses.

While scanning in contact mode the AFM tip induces a lateral bending of the NWs. As a result, an asymmetric strain field is created inside the NW with the external part of the NW (stretched side) having a positive strain, and the inner part (compressed side) having a negative strain, as shown in Fig. 15a. In response to this strain field and due to the piezoelectric properties of the GaN, a piezoelectric polarisation is created inside the volume of the NW. In the case of bended N-polar GaN NWs, the P_{PZ} is oriented parallel to the P_{SP} (parallel to the growth direction) on the extended side of the NW, while it is anti-parallel to the P_{SP} (anti-parallel to the growth direction) on the compressed side of the NW (Fig. 15b). Due to this specific orientation, the potential evolves between V_S^- to V_S^+ from the stretched side to the compressed one of the NW (Fig. 15c).

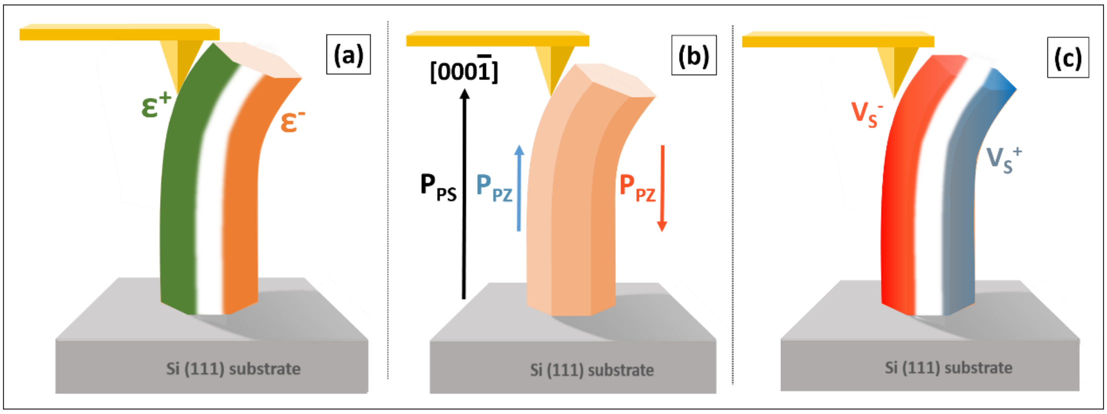

Figure 15. (a) The outer side of the GaN NW is stretched (positive strain) whereas the internal side undergoes compression (negative strain) when an external force is applied by the AFM tip; (b) The orientation of the P_{PZ} of an N-polar GaN NW on the stretched and the compressed side; (c) Potential distribution in N-polar GaN NWs.

These piezo-potentials induces the generation of an output voltage, which is harvested through the conductive AFM tip, and measured across an external resistor. The AFM tip forms a Schottky contact with the top of the NWs (metal-semiconductor contact) as the work-function of the metal tip is higher than GaN electron affinity (4.1 eV). An Ohmic contact is established at the the NW-substrate interface [106] allowing to maintain the neutrality of the external circuit. However, due to the variation in the potential distribution inside the NWs, the Schottky contact presents two different behaviours. It can either be forward biased or reversed biased depending on which NW side (and thus piezo-potential) the AFM tip is in contact with, and on the NW doping type.

In the case of our ***n-type doped N-polar GaN NWs***, the majority charge carriers are electrons which tend to screen the V_S^+ created at the compressed side of the NW, while on the stretched side a strong V_S^- leads to the flow of electrons from the NW to the electrode of collect, resulting in a negative voltage peak which is detected across the measurement resistor. The flow of electrons is maintained until all the ionic charges are neutralized in the volume of the NW, resulting in the decrease of V_S^- and V_S^+. For the collection of piezo-charges via the AFM tip, the Schottky contact is forward biased only when the AFM tip is in contact with the stretched side of the NW (given that, $\Delta V = V_m - V_S^- > 0$, where V_m is the potential of the metal and is approximately zero) [90]. Or in other words, when the AFM tip is in contact with the negative piezo-potential created inside the NW, as we can observe in Fig. 16a.

On the other hand, for ***p-type doped N-polar GaN NWs***, the Schottky barrier is forward biased (given that, $\Delta V = V_m - V_S^+ < 0$) when the AFM tip is in contact with the compressed side of the NWs [90]. A positive output voltage peak is thus obtained when the AFM tip is in contact with the positive piezo-potential as shown in Fig. 16b.

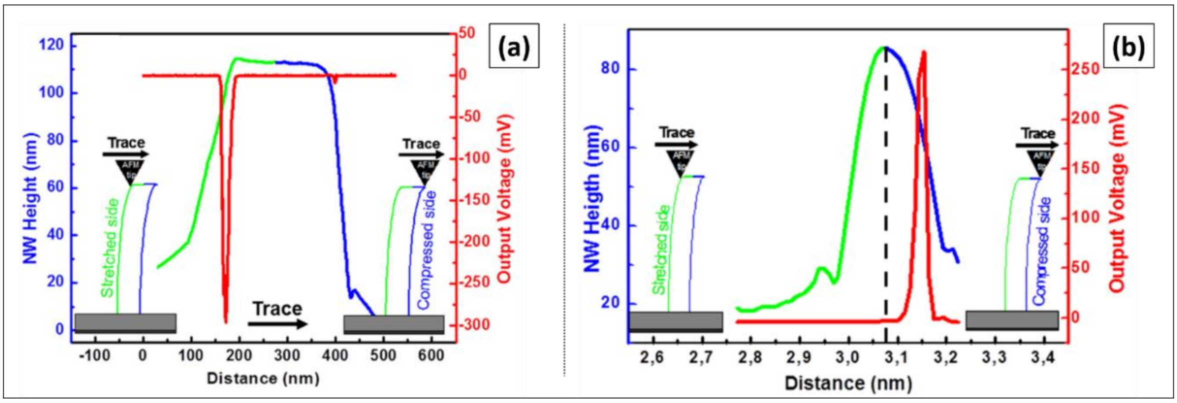

Figure 16. Images taken from [90] and [107]. Superimposition of the topography profile and the output voltage response for N-polar GaN NWs with (a) n-type doping and (b) p-type doping. The Schottky is forward biased when AFM tip is in contact only with the stretched side of the NW for n-type doping, while for p-type doping in the NWs, the Schottky is forward biased when AFM tip is in contact only with the compressed side of the NW.

An opposite rectifying behaviour of the Schottky diode is observed for ZnO, as detailed by Wang and Song [41] and Lin et al [108]. Contrary to GaN NWs with an anion-polarity, ZnO NWs are characterised with a metal-polarity [109], [110], as the surface terminates with Zn^{2+} atoms. Consequently, the P_{SP} is oriented anti-parallel to the growth direction and the piezo-potential evolves from V_S^+ to V_S^- from the stretched side to the compressed side of the NW. In this case, for n-doped ZnO NWs as represented in Fig. 17, the Schottky diode is positively (forward) biased when the AFM tip enters in contact with the compressed side (negative piezo-potential) of the NW and thus allows the output voltage harvesting. While it is negatively (reversed) biased at the stretched side (positive piezo-potential) of the NW and consequently no output voltage is obtained.

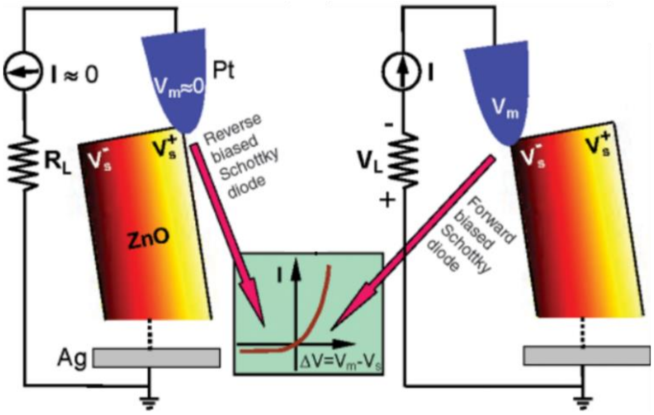

Figure 17. Image taken from [41]. Forward and reversed biased Schottky rectifying behaviour of an n-type ZnO NW.

1.3.4. Impact of Schottky diode on energy harvesting at nanometer scale: Origin of Schottky nano-contacts

The collection of generated piezo-charges in the volume of the NW is governed by the Schottky contact formed between the conductive AFM tip and the top of the NW, as already described in the previous section. In order to take full advantage of the piezo-generation capacity of the NWs for the development of high efficient NW-based devices, it is essential to investigate the harvesting efficiency of the Schottky diode and carefully consider its behaviour in the nanoscale regime.

In 2017, Jamond et al. established the impact of the Schottky diode on the energy harvesting efficiency in n-doped GaN NWs using an AFM equipped with the modified Resiscope [68]. Three distinct conductive AFM tips, (p-doped diamond tip, PtSi tip and PtIr tip) were used in this study. As their respective work functions ($W_{\text{p-doped diamond}}$ = 5.21 eV, W_{PtSi} = 5.03 eV and W_{PtIr} = 5.13 eV) are higher than the electron affinity of GaN (4.1 eV), all three tips formed a Schottky contact with the GaN NWs.

The evolution of the piezoelectric response of the same population of NWs as a function of applied CNF was individually recorded with each AFM tip. Under similar scanning conditions, the GaN NWs systematically generate an equivalent piezoelectric potential and thus the O.V. collected via the different AFM tips is expected to be equivalent as well. However, a dispersion in the obtained O.V. values was observed (Fig. 18) which indicated a strong influence of the nature of the Schottky contact established with individual AFM tips.

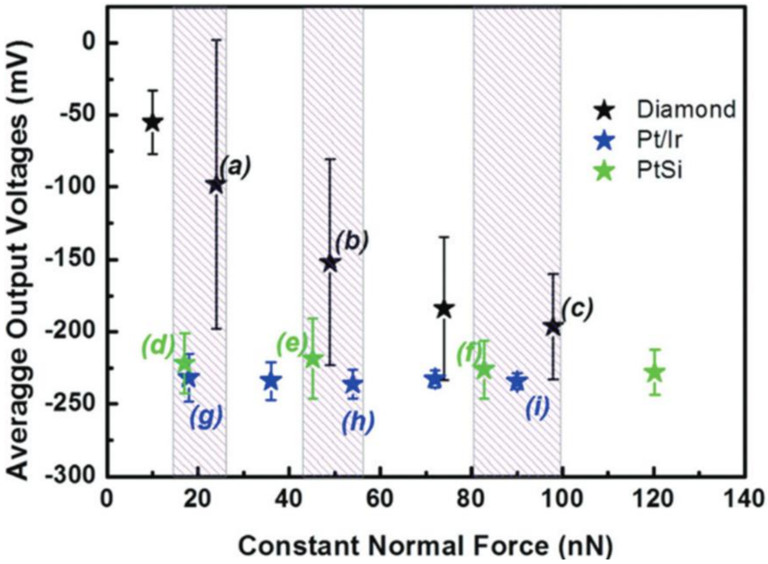

Figure 18. (Image taken from [68]). Average output voltage as a function of CNF individually collected via a p-doped diamond tip, PtIr tip and PtSi tip.

Irrespective of the applied CNF, the Pt-based AFM tips demonstrated a higher collection efficiency (about 2.4 times) as compared to the p-type diamond tip. Based on the classical description of the Schottky diode (barrier height is directly related to the band bending), the diamond-GaN contact presents the highest Schottky barrier height (SBH = 1.11 eV). It is thus coherence with its lowest collection capacity. However, a non-classical behaviour was observed for the Pt-based AFM tips, where the best collection was demonstrated by the PtIr tip despite its higher SBH (1.03 eV) than the PtSi tip (0.93 eV). This irregularity was also reported experimentally by Y.S.Zhou [43], [111].

To better understand the origin of this irregularity, I-V measurements at different CNFs were performed. The bias voltage evolved between -3.5 V and 3.5 V and a diode-like rectifying behaviour was observed for the three Schottky contacts (Fig. 19 (a-c)). Fig. 19d presents the specific configuration of the Schottky contact formed between the AFM tip and the GaN NW. Here the bias is applied via the substrate contrary to the AFM tip (through which the current is collected) and thus a negative representation of the diode characteristics is obtained [68].

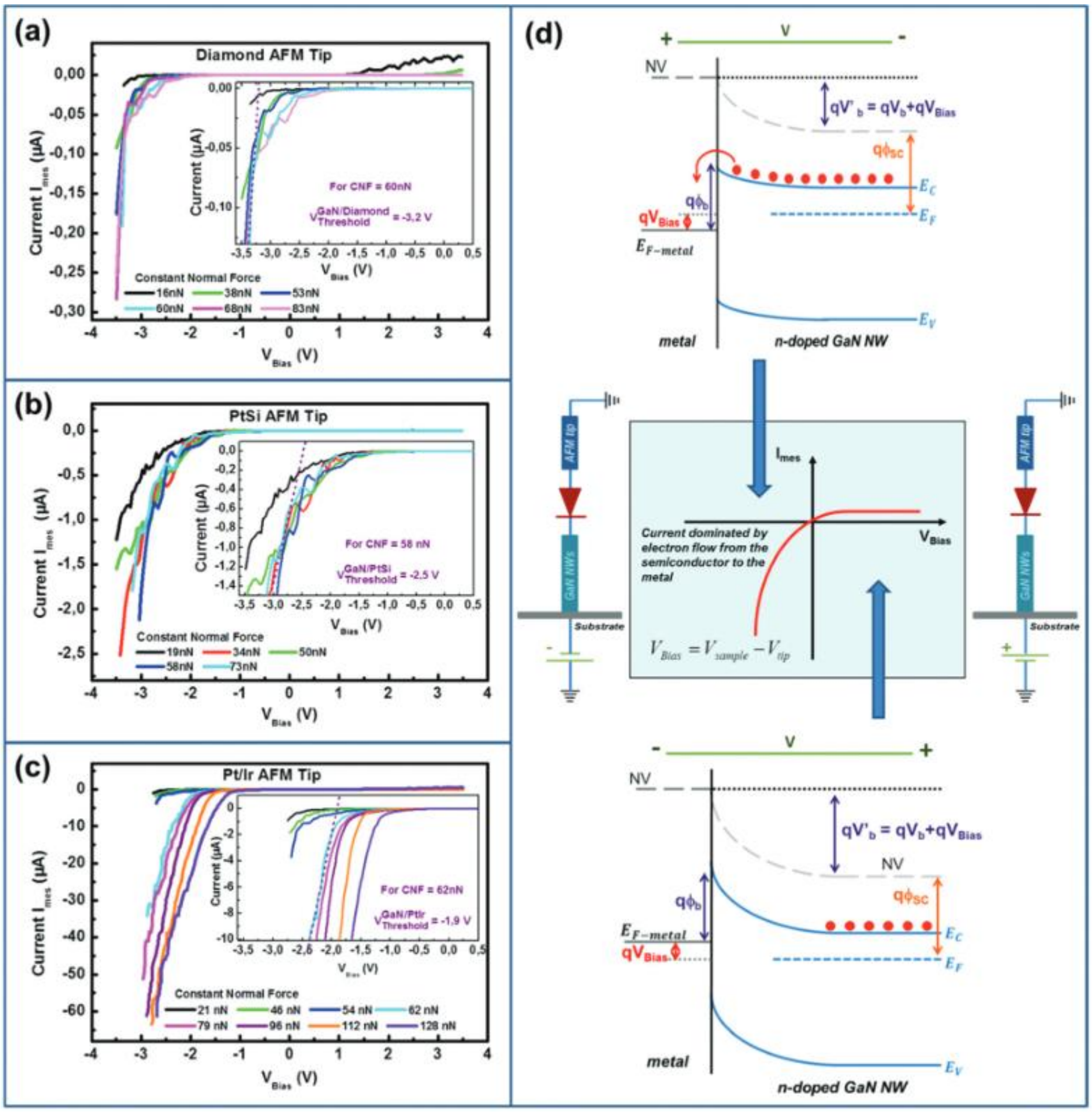

Figure 19. (Image taken from [68]). I-V characteristics measured for (a) p-doped diamond tip, (b) PtSi tip and (c) PtIr tip. (d) The specific configuration of the measurement set-up in which the bias is applied via the substrate and current collection occurs via the AFM tip.

Firstly, these I-V curves permitted to establish the threshold values of applied force '$F_{threshold}$' below which the Schottky contact is unstable, which is demonstrated by the low current obtained for smaller force values in Fig. 19 (a-c). An unstable Schottky contact can lead to a poor collection efficiency. The force range of the measured threshold values however depended on the AFM tip shape (16 nN < $F_{Diamond}$ < 38 nN, 19 nN < F_{PtSi} < 34 nN and 54 nN < F_{PtIr} < 62 nN): larger (sharper) the tip, easier (more difficult) it becomes to establish a stable contact [68], [112].

Secondly, it was demonstrated that the classical Schottky model is not applicable to the NWs and thus the nanometer scale description of the Schottky contacts, called *'Schottky nano-contacts'* was established.

The evolution of the measured threshold voltages '$V_{threshold}$' for each tip-GaN Schottky contact deviated from the expected classical behaviour: $(V_{threshold})_{diamond} > (V_{threshold})_{PtIr} > (V_{threshold})_{PtSi}$. This deviation was marked by the inversion of $V_{threshold}$ for PtSi (-2.5 V) > $V_{threshold}$ for PtIr (-1.9 V) and led to the consideration of the interface dimensions in the nanoscale regime. The contact surface of the Schottky diode formed by the three AFM tips was calculated using an approximation of the Hertz theory [113]. Fig. 20 shows that the calculated contact radius is of the order of a few nanometers, which is smaller than the depletion width inside the NWs (20-80 nm depending on the doping) [114]–[116]. This concluded that the conventional description of the Schottky contact cannot be applied in the case of 1D-nanostructures.

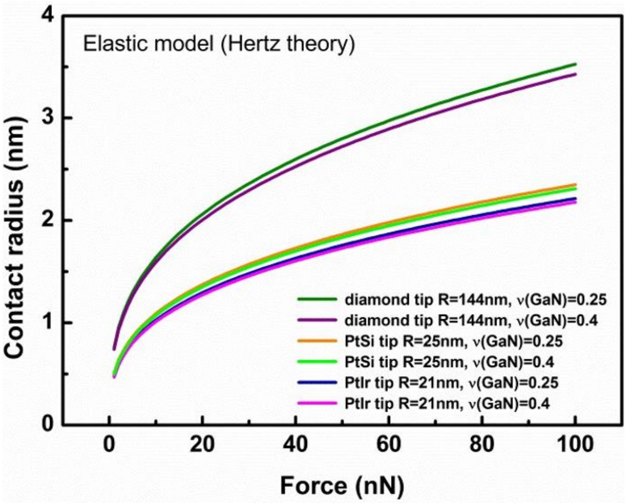

Figure 20. (Image taken from [68]). Evolution of the contact radius as a function of force (nN) for each AFM tip.

Therefore, in the case of nano-contacts, the SBH becomes a function of the diode size: a thinning of the barrier height occurs with the reduction in the diode size and tunnelling effect becomes dominant [117], [118]. The contact radius (measured by SEM) of PtIr tip, being smaller (21 nm) than PtSi tip (25 nm) and diamond tip (144 nm), led to a better collection efficiency. This nanometer scale behaviour of the Schottky diode thus justified the higher O.V. harvesting with the PtIr AFM tip (Fig. 18).

Thirdly, the increase of the current (I_{mes}) with the increase of CNF was attributed to the piezotronic effect. The latter is defined as the modulation of the electric transport of the charge carriers as a result of the strain-induced piezoelectric potential (or piezo-charges) in any piezoelectric material along the polar direction [119], [120]. As the applied force increases, the GaN NW deformation also increases, which results in the augmentation of the piezoelectric potential inside the NWs. The latter induces a thinning of the SBH at the NW-tip interface [121]–[123] and a higher conduction is achieved (as can be seen from the I-V curves).

Finally, using the Cheung-Cheung method [124] and the thermionic emission theory [125], the effective SBH of the three Schottky diodes were obtained: $\phi_{Diamond} = 0.88 \pm 0.12$ eV, $\phi_{PtSi} = 0.61 \pm 0.14$ eV and $\phi_{PtIr} = 0.38 \pm 0.09$ eV [68]. The theoretical as well as the calculated SBH values are plotted in Fig. 21 for the three tips as a function of the CNF. We can observe that as the diode size decreases, the difference between the theoretical and the experimental values increases, which further confirms the 'nano-contact' effect which dominates in the nanoscale regime.

These results demonstrated that the Schottky diode plays a crucial role in the energy harvesting efficiency, which varies as a function of the diode size. While this important behaviour has been established with conductive AFM tip, it gives important directions for designing efficient piezoelectric generator devices in which the energy is harvested through a Schottky diode.

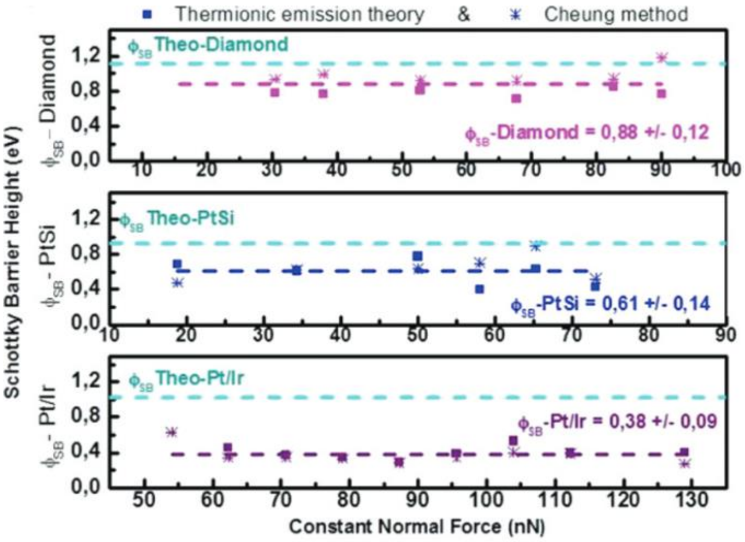

Figure 21. (Image taken from [68]). Theoretical and experimentally measured values of Schottky barrier height for the three diodes.

1.3.5. Piezo-generation in 1D nanostructures and integrated systems: State-of-the-art

To begin with this part, firstly, it is important to define the terms 'nano-generator' and 'piezo-generator' that can lead to confusion. In this manuscript, a nano-generator (NG) refers to the capacity of a single nanowire (NW) to convert the mechanical energy into electrical energy. Whereas, a piezo-generator (PG) is defined as a micro-system integrating arrays of single nanowires embedded in a flexible polymer matrix and generating electricity in response to an external deformation applied simultaneously on the entire active material.

The first demonstration of piezo-generation in 1D nanostructures was made by Prof. Wang in 2006 [41] on vertically oriented single ZnO NWs via AFM in scanning configuration. Since then, piezoelectric properties of several other 1D nanostructures have been investigated such as CdS [126], CdSe [43], PZT [127], $BaTiO_3$ [58], [101], PMN-PT [65], NKN [128]…and III-nitrides NWs such as GaN [87], [88], [107], [129], [130], InN [131], Ga(In)N [132] and AlGaN [133]. Apart from the AFM technique, the piezoelectric generation of 1D nanostructures such as PVDF nanofibers [134], PMN-PT NWs [135], $ZnSO_3$ microbelts [136], CdTe micro/nanowires [137]…has also been studied via energy harvesters consisting of one single nanostructure on a flexible substrate. Using bending cycles, the nanostructures are subjected to a mechanical deformation and the generated energy is collected via external electrodes.

Despite the excellent piezoelectric properties of III-nitrides [10], ZnO NWs remain up-to-date the most used nanostructures for piezo-conversion. In this section, we highlight the piezoelectric responses of III-N materials, studied via AFM in scanning configuration. Output voltages as high as 472 mV per NW [132] were reported in 2018, that established the last state-of-the-art for piezo-generation by 1D-nanostructures. This value exceeded the ones generated by other 1D-nanostructures and especially ZnO NWs [138]–[140].

a) Piezo-electric response analysis of III-N nanostructures using conductive AFM

The first piezo-conversion demonstration of GaN nanorods was done using a commercial AFM system in contact mode by Su et al. [105] in 2007. From the direct correlation between the topography image and the output current image, the piezoelectric response of individual nanorods was obtained. Several sharp peaks of the order of 0.03 nA were measured as could be observed in Fig. 22. The author also established a linear relationship between the scanning speed and the obtained current values. The increase in the current values was attributed to the transfer of kinetic energy into elastic energy of the bended nanorod. This study was amongst the primitive studies performed on III-nitride materials which explained the piezo-generation mechanism taking place inside the nanostructures. In 2010, the group of Prof. Wang [133] studied the piezoelectric responses of different 1D nanostructures based on GaN, AlGaN, InN and AlN via AFM in the scanning configuration (as represented in Fig. 12a). Negative output voltage peaks of 4, 7 and 60 mV were recorded for AlGaN nanocones, GaN nanorods and InN nanocones respectively (Fig. 23). The difference in the piezoelectric responses of the materials was assigned to the variation in their charge-carrier densities, affecting their conductivity. No piezo-generation was observed for AlN nanocones due to their very high resistivity.

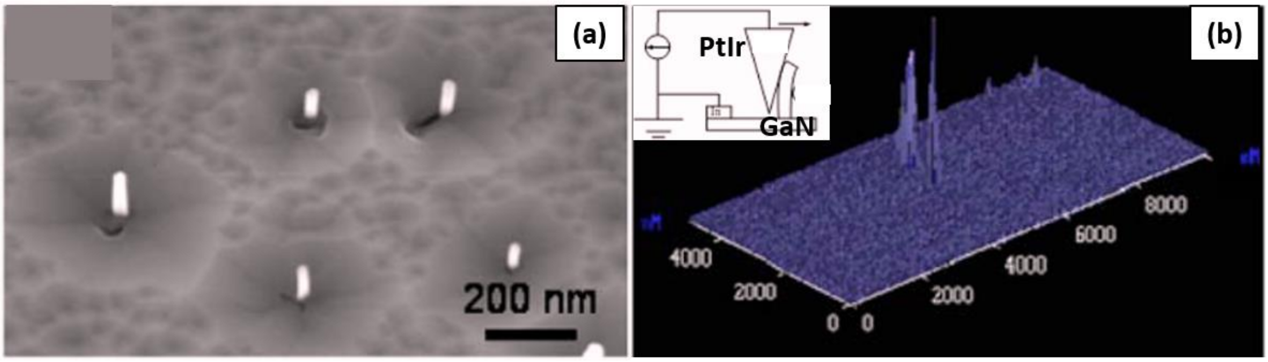

Figure 22. Images taken from [105]. (a) SEM image of the GaN nanorods. (b) The output current image with peaks of the order of 0.03 nA. The schematics of the AFM measurement set-up in the inset.

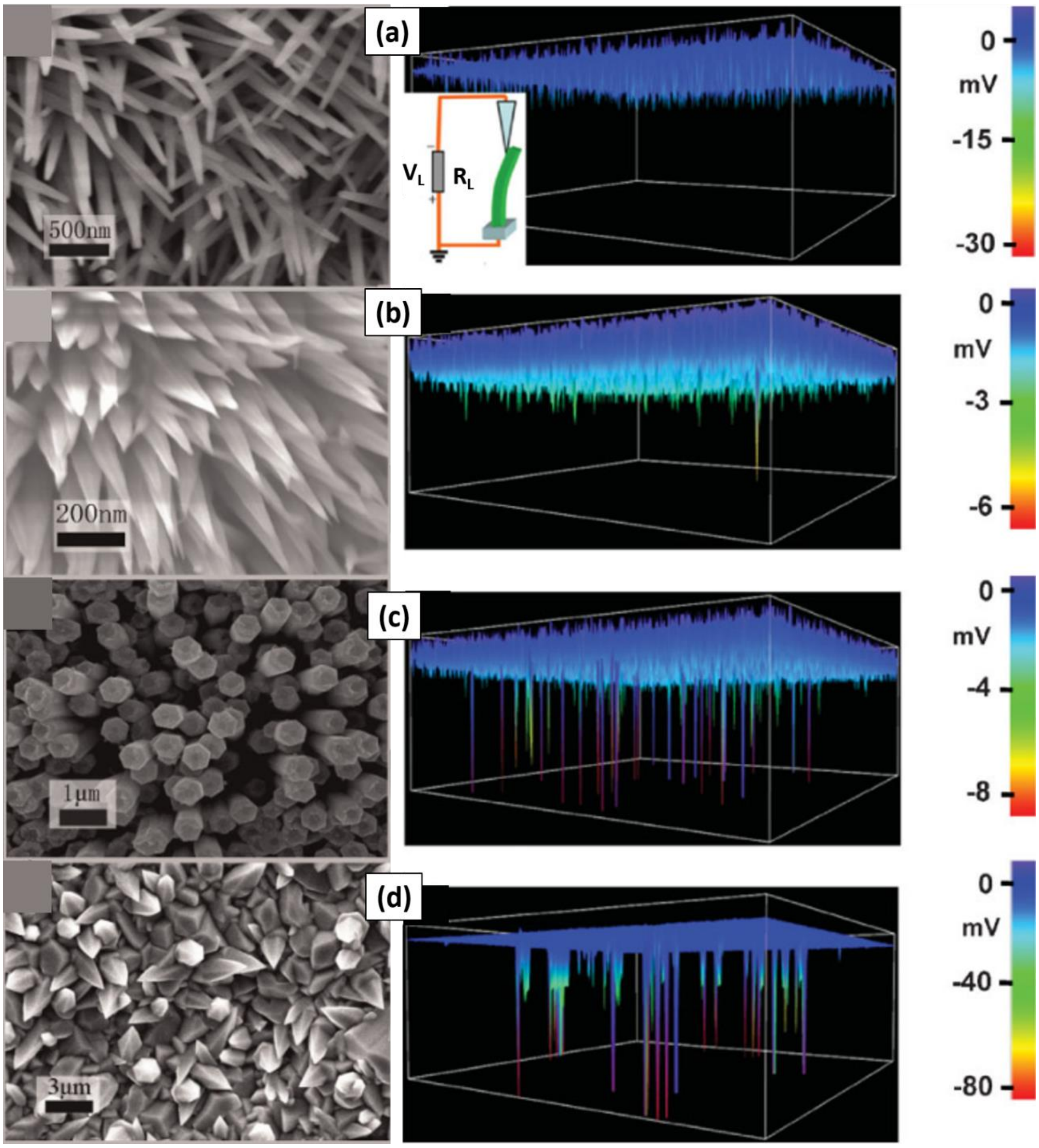

Figure 23. Images taken from [133]. SEM images and 3D representations of the electric maps for (a) AlN nanocones with no generation; (b) AlGaN nanocones with 4 mV of output voltage peaks; (c) GaN nanorods with 7 mV of output voltage peaks and (d) InN nanocones with the highest output voltage peaks of about 60 mV. The employed 'bending in scanning configuration' AFM technique, is shown in the inset.

Huang et al. [131] also employed the scanning configuration of AFM in order to demonstrate the high piezo-generation capacity of InN NWs. A distribution in the piezo-performance of the NWs was observed with about 40 % to 55 % of the obtained output voltages within -1 to -20 mV range and 25 % to 30 % exceeding -100 mV. Some NWs also generated record breaking output voltage peaks of about 1 V as shown in Fig. 24. The stability and reproducibility of the output voltage generated by the NWs was also examined by the author over a period of 4 months.

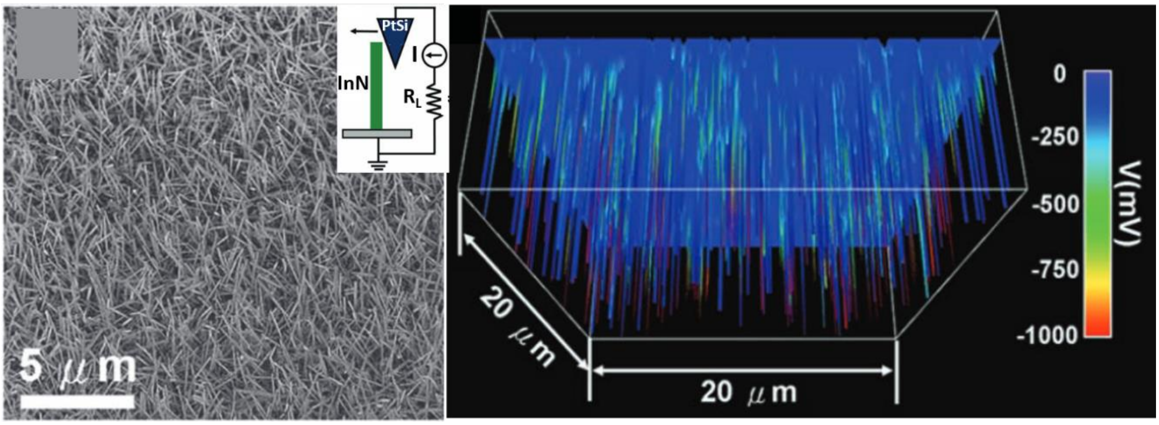

Figure 24. Images taken from [131]. SEM image of the VLS grown InN NWs with the 3D representation of their piezo-response. Output voltage peaks reaching up to 1 V were obtained, which are the highest recorded responses for NGs based on 1D nanostructures. Pt coated Si AFM tip was used to deform the NW as shown in the inset.

Chen et al. in 2012 [130] obtained negative output voltage peaks of about 100 mV from the mechanical solicitation of vertically aligned GaN NWs via conductive AFM tip in scanning mode (Fig. 25), while the highest output voltage could reach up to 300 mV per NW.

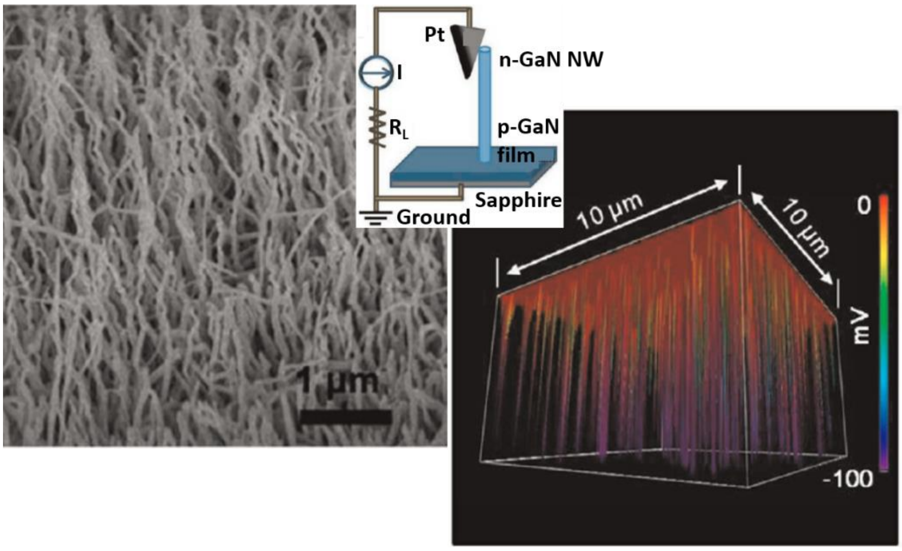

Figure 25. Images taken from [130]. SEM image of the GaN NWs with a unique morphology and the 3D representation of the output voltage map with negative peaks of about 100 mV. Inset shows the AFM schematics.

In order to fully understand and examine the piezoelectric phenomena in III-nitride nanogenerators, Xu et al. [88] employed a unique AFM characterisation technique with a cross-sectional configuration on intrinsic GaN NWs and n-doped GaN-AlN-GaN heterostructures (Fig. 26). This configuration allows the application of a well-controlled force on the selected NW which is localized using its topographic image in tapping mode. Output voltages are observed for both samples once the NW deflection and the generated piezo potentials inside the NWs are sufficiently high to lower the Schottky barrier height. Fig. 27 shows the piezoelectric response of both samples as a function of time, which reduces systematically as the applied force decreases. While GaN NWs generated only up to 17 mV, higher output voltages of the order of 200 mV were obtained for GaN-AlN-GaN NWs under an equivalent applied force of 250 nN ((Figure 27 (c-d)).

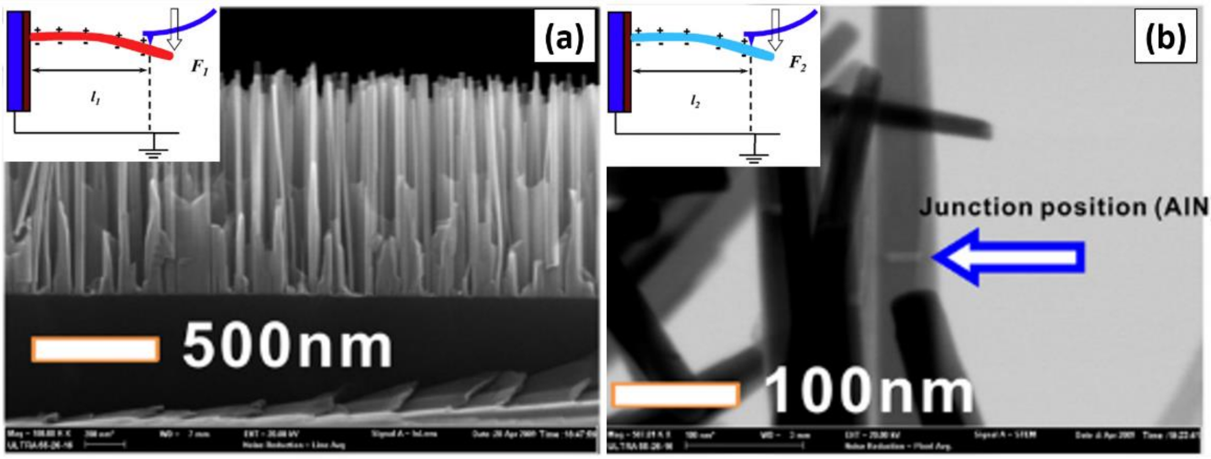

Figure 26. Images taken from [88]. (a) SEM image of GaN NWs and (b) TEM image of GaN NWs with AlN insertion. Downward bending of the NWs shown in the inset of each image. Using the unique cross-sectional AFM technique, a control of NW deflection and force is achieved.

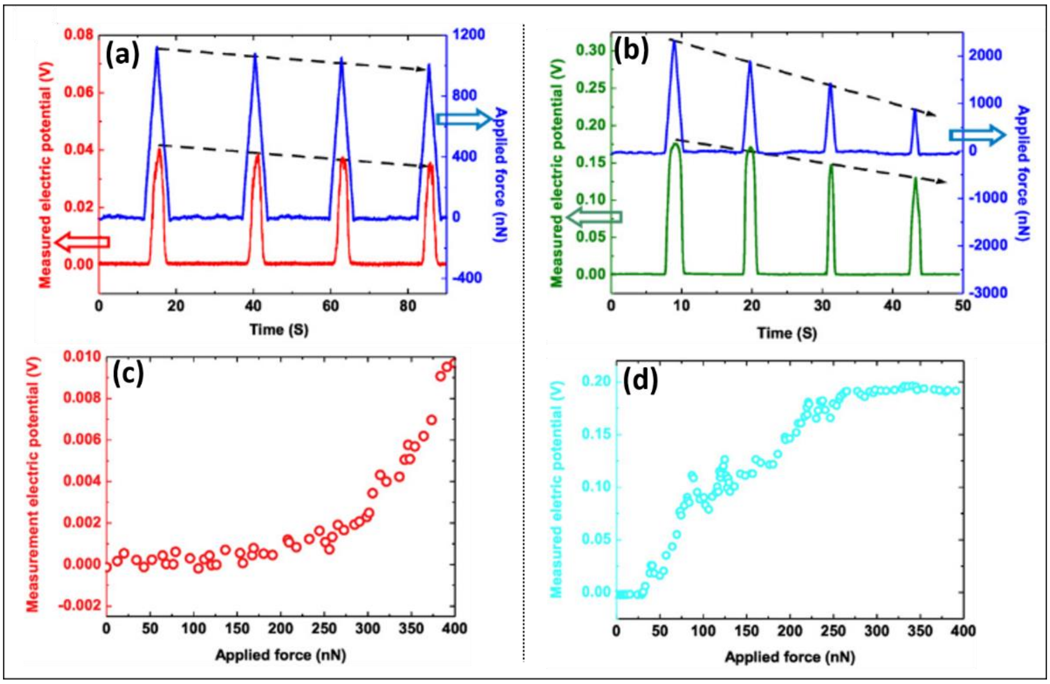

Figure 27. Images taken from [88]. Measured piezoelectric potential as a function of (a) - (b) time and (c)-(d) applied force, for GaN NWs (left) and GaN-AlN-GaN NWs (right). A decrease in the electric potentials is observed with decrease in applied force.

The author also highlighted the stability and reproducibility of the generated electric potentials inside the NWs by applying different deformation rates. Eventually, the authors established the relationship between NW deflection and the corresponding generation for each NW set, as shown in Fig. 28. These curves are composed of three sections. At the beginning of the deflection curve, the measured electric potential is zero. This is the cut-off region in which the generated piezo-potential is not sufficient to overcome the SBH. In the quasi-linear region, the generated piezo-potential is sufficient enough to open the Schottky barrier. As a result, the electric potential increases linearly with the increaseof the deflection. Finally, at the end of the curve, the measured electric potential saturates. In this region, the NW deflection is at its highest and the piezo-potential saturates due to the rotation of the electric dipoles [141].

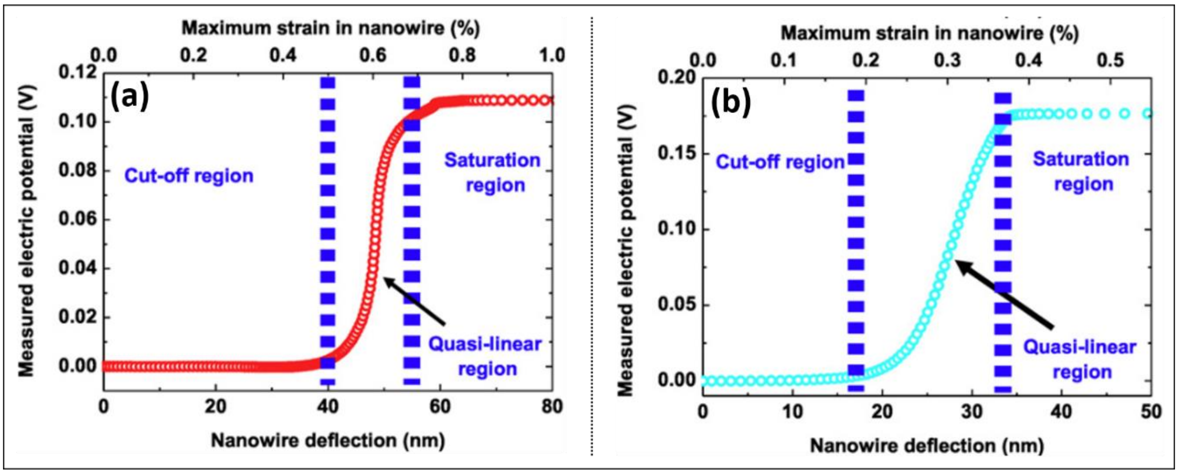

Figure 28. (Images taken from [88]). Relation between the measured electric potential and the nanowire deflection for (a) GaN NWs and (b) GaN-AlN-GaN NWs.

Piezo-conversion efficiencies of PA-MBE grown GaN NWs [87], [107] (Fig. 29 (a-b)) and InGaN/GaN NWs (Fig. 29c) [132] have been demonstrated by our team thanks to the home-made AFM system equipped with the modified Résiscope module [91] working under scanning configuration (illustrated in Fig. 12a). Negative output voltages reaching up to - 443 mV per NW [87] were generated by n-doped GaN NWs, while p-doped GaN NWs generated positive O.V peaks of about 350 mV per NW [107] (Fig. 29 (d-e)). The distribution in the piezo-responses of the NWs was attributed to the dispersion of the NW dimensions resulting from their self-assembled growth mode. Our team has demonstrated the possibility to tune the piezoelectric response of InGaN/GaN NWs as a function of the thickness and position of InGaN insertions in the NW volume. Consequently, a 35 % increment in the piezo-conversion efficiency of InGaN/GaN heterostructured NWs was obtained by positioning the insertions in the top part of the NW (Fig. 29f). This led to a maximum generated O.V. of the order of 470 mV per NW [132]. This enhancement of the piezo-conversion efficiency has been assigned to the higher piezoelectric coefficients of the InGaN in comparison with GaN. These reported output voltages have been the highest obtained piezo-responses (new state-of-the-art established in this thesis) by III-N nanostructures and exceed largely the output voltages obtained by single ZnO NWs [138], [139] with both n-type and p-type doping.

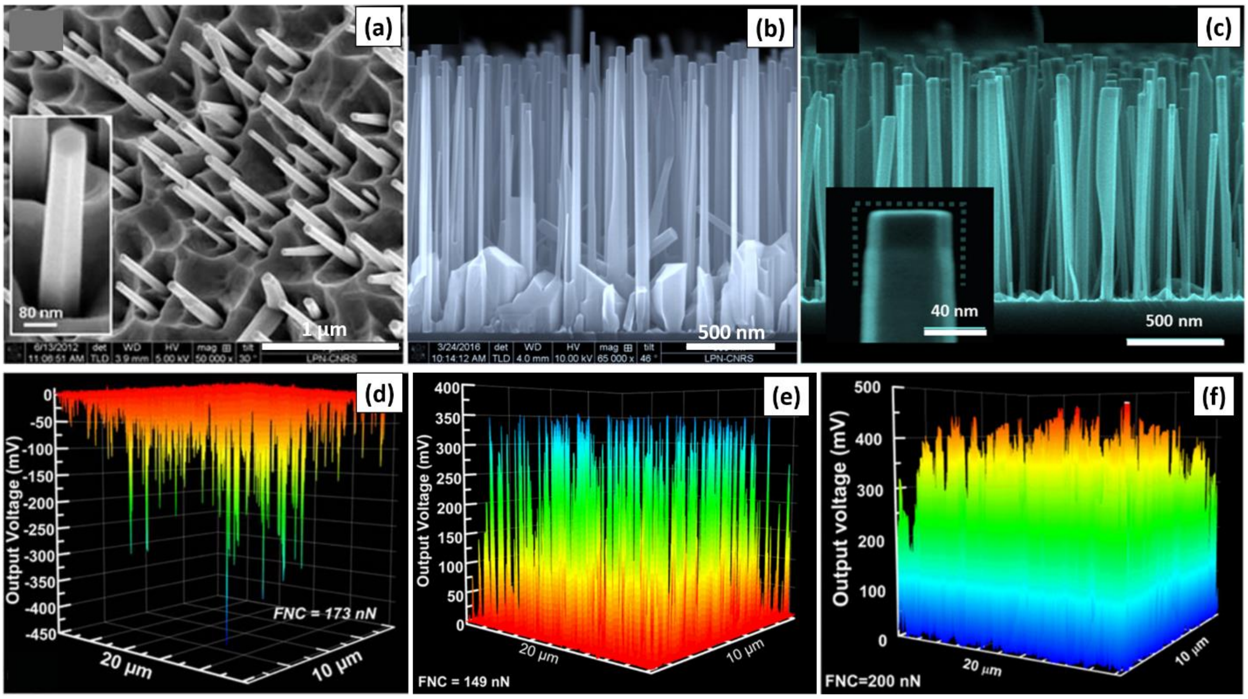

Figure 29. Images taken from [87], [107], [132]. Top images: SEM images of (a) n-doped GaN NWs; (b) p-doped GaN NWs and (c) InGaN/GaN heterostructured NWs with the InGaN insertions located at the NWs top part. Bottom images: 3D representations of output voltages generated by (d) n-doped GaN NWs; (e) p-doped GaN NWs and (f) InGaN/GaN hetero-structured NWs at applied constant normal forces of 173 nN, 149 nN and 200 nN respectively.

Table 5 recapitulates the output voltage values generated by single 1D nanostructures along with their growth techniques and their respective AFM scanning conditions as reported in the literature.

Due to the difference in their dimensions, the nanostructures are expected to have different stiffness values, which is given by their aspect ratios (height/diameter ratio). Hence, the deformation of the nanostructures is not *purely* equivalent for a given force. In addition, their characteristics as dopant type and doping level can play a significant role on the outputs. Finally, the conditions of testing are also differing (applied force, scanning conditions (rate, velocity of the tip), conductive AFM tip used…). We are thus aware that a direct comparison of the piezoelectric performances of the presented nanostructures is not easy. However, amongst all these values, III-nitride based nanostructures having different dimensions and tested under different conditions have nevertheless presented the best results. These 1D-nanostructures offer a promising potential for the development of ultra-compact and high-efficient piezo-energy harvesters working under ambient conditions.

Table 5. Piezoelectric response of 1D nanostructures analysed via conductive AFM.

1D Nanostructures	Growth Method	Height (µm)	Diameter (nm)	AFM deformation type/ AFM tip	CNF (nN)	Output voltage (mV)/R_{load}	Refs.
n- type doped ZnO NWs	Syn. chemistry	1-2	200-300	Scanning/PtSi	5	45/500 MΩ	[138]
n-type doped ZnO NWs	Thermal vapour deposition (TVD)	0.6	25	Scanning/PtSi	5	-10/500 MΩ	[139]
p-type doped ZnO NWs	TVD	0.6	25	Scanning/PtSi	5	90/500 MΩ	[139]
ZnS NWs	TVD	-		Scanning/PtSi	5	2/500 MΩ	[142]
CdS NWs	PVD	1	100	Scanning/PtSi	5	-3	[126]
CdSe NWs	PA-MBE	2-4	60	Scanning/ Ti(5 nm)/Pt(20 nm)	140	-137	[43]
PZT NWs	PLD	0.01-0.022	50	Scanning/PtSi	5	-30/500 MΩ	[127]
GaAs NWs	Syn. chemistry	6	100	Scanning/W_2C coating	-	-	[143]
III-nitride nanostructures							
InN NWs	VLS	5	25-100	Scanning/PtSi	80	-1000	[131]
InN nanocones	CVD	4	700	Scanning/PtSi	5	60/500 MΩ	[133]
AlGaN nanocones	CVD	1	70	Scanning/PtSi	5	4/500 MΩ	[133]
GaN nanorods	CVD	3.5	500	Scanning/PtSi	5	7/500 MΩ	[133]
n-type GaN NWs	MOCVD	10-20	25-70	Scanning/PtSi	5	- 350/500 MΩ	[129]
n-type GaN NWs	MOCVD	3	50	Scanning/PtSi	80	-300/500 MΩ	[130]
n-type GaN NWs	MBE	-	25-30	Horizontal AFM /PtIr	250	150/100 MΩ	[88]
n-type GaN-AlN-GaN NWs	MBE	-	25-30	Horizontal AFM /PtIr	250	200/100 MΩ	[88]
n-type GaN NWs	PA-MBE	0.35- 0.75	60-100	Scanning/diamond tip	173	-473/1 GΩ	[87]
p-type GaN NWs	PA-MBE	0.88-1.2	25-65	Scanning/PtIr	149	350/1 GΩ	[107]
p-type InGaN/GaN NWs	PA-MBE	1-1.1	30-70	Scanning/PtSi	200	472/1 GΩ	[132]

b) Piezogeneration in integrated microsystems: Piezogenerators

From the first demonstration of the piezoelectric generation by single ZnO NWs [41], then defining for the first time the concept of a nanogenerator, up-to this date, many other 1D-nanostructures have demonstrated their potentiality for piezo-conversion. Very early, the first piezo-generators integrating 1D-nanostructures appeared. Over the years, and owing to the thorough understanding of the piezo-generation mechanism in single 1D nanostructures, the design of integrated systems has greatly evolved. Despite the strong potential of III-N NWs, their integration in piezoelectric generators remains very limited compared to ZnO NWs-based piezo-generators.

Piezoelectric generators based on ZnO nanostructures

The first piezo-generator (PG), demonstrated by Prof. Wang in 2007 [144], was based on vertically oriented ZnO NWs with a zig-zag top electrode. Ultrasonic waves were used to induce vibrations in this electrode, which further deformed the ZnO NWs in contact (Fig. 31a). An output voltage of the order of 0.7 mV was generated. In 2008, Xu et al. [145] demonstrated that the generation capacity of an integrated system, based on the same zig-zag top electrode design, could be enhanced by stacking several layers of NWs. Using ultrasonic waves to induce deformation in a four-layer integrated PG based on ZnO NWs (Fig. 31b), an output voltage of 62 mV, corresponding to a power density of 0.11 µW/cm^2 was obtained. A new design of PG, based on the zig-zag electrode motion was presented by Qin et al. [146] in 2008. The system consisted of two microfibers with compact vertically oriented ZnO NWs entangled around each other as shown in Fig. 31c. A mutual deformation of the ZnO NWs was achieved by stretching the microfibers. ZnO NWs of one of the fibers were coated with gold in order to play the role of electrode harvesting the outputs. Based on this design, an output voltage of 1-3 mV was recorded.

These first PGs have demonstrated the feasibility of the harvesters. However, they are difficult to fabricate and present low conversion efficiencies.

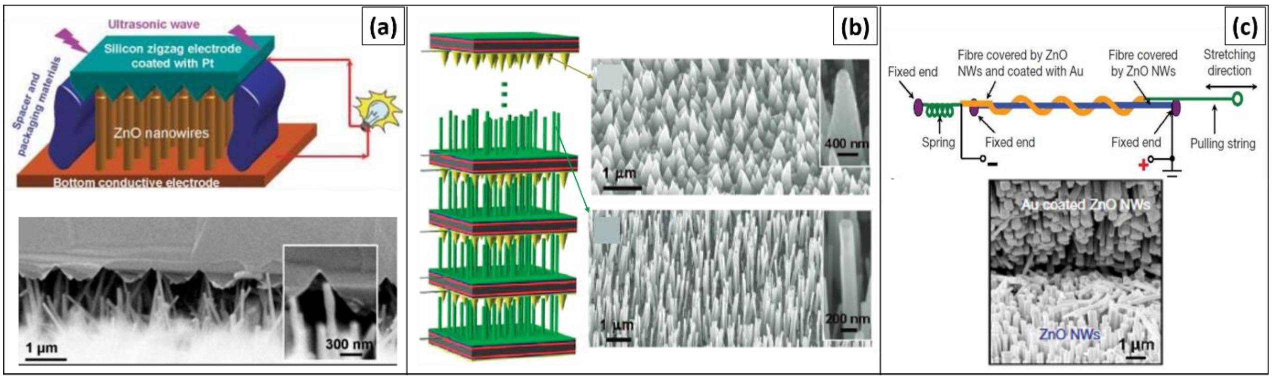

Figure 31. Images taken from [144]–[146]. SEM images and schematic representations of ZnO NWs based first piezo-generators with (a) vertically oriented NWs with a zig-zag PtSi top electrode; (b) 4 layered PG stacked on top of each other. The top electrode consists of ZnO nanotips and is similar to the zig-zag configuration of Z.L. Wang [144]. Both these PGs are deformed using ultrasonic waves; (c) PG with 2 intertwined microfibers consisting of compact ZnO NWs deformed by stretching. ZnO NWs of one of the fibres with Au coating serve as an electrode as it brushes against the second fibre when stretched.

Other designs of PGs based on 1D-nanostructures have been presented in the last decade with two main configurations, namely the vertically integrated nanogenerators (VINGs) (Fig. 32a) and the laterally integrated nanogenerators (LINGs) (Fig. 32b).

The fabrication of LINGs require the transfer or deposition of the nanostructures on a flexible host substrate. Cyclic loading and unloading cycles are then used to laterally deform the active layer integrating the nanostructures [147]–[151].

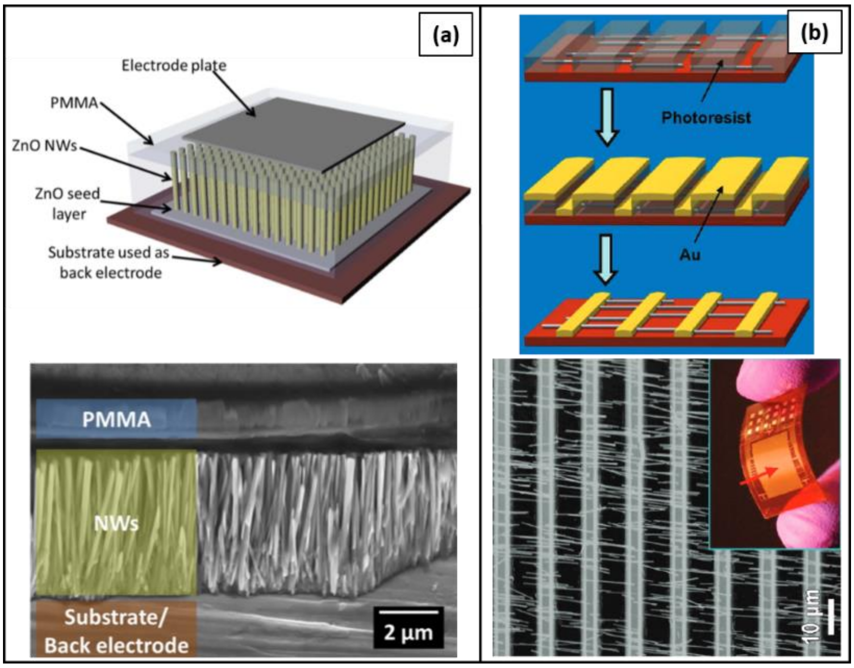

Figure 32. (a) Image taken from [152]. Vertically integrated nanogenerator (VING) based on ZnO NWs; (b) Image taken from [151]. Laterally integrated nanogenerator (LING) based on ZnO NWs.

VINGs are the most frequently studied PGs in the literature, with two sub-configurations, deciding the collection method of the generated piezo-energies. VINGs could either have a Schottky configuration, where the top electrode collecting the outputs is directly in contact with the nanostructures [147], [153]; or a capacitive configuration, where the top electrode is in contact with the matrix embedding the nanostructures [152], [154]–[156]. In addition, some VING structures have been designed on flexible substrates [157]–[163]. Fig. 33 recapitulates these three types of VING devices.

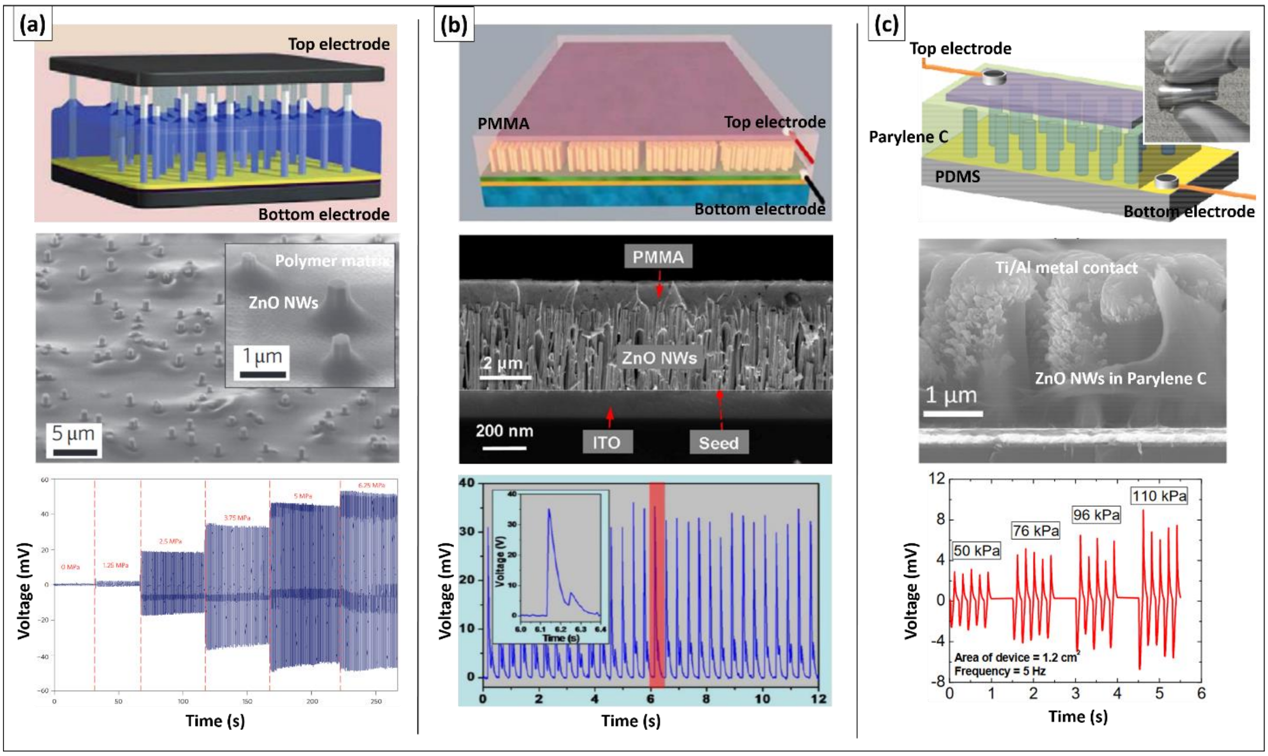

Figure 33. (Images taken from [147], [156], [163]). Schematic illustrations and SEM images of ZnO NWs based VINGs (a) with a Schottky configuration, (b) with a capacitive configuration and (c) on a flexible substrate. The piezoelectric response of the devices under external deformation is also shown.

The capacitive configuration offers an easier fabrication approach than the Schottky one and hence is the most used configuration in PGs. Depending on the final model of the VING prototypes, they can be mechanically deformed either using ultrasonic waves [153], [164], impact by hand/foot movement [156], [165]–[167] or mechanical systems such as shakers, actuators or linear motors [147], [152], [154], [161], [168].

VINGs and LINGs based on ZnO NWs have reported power densities up to several hundred mW/cm^3 [156], [169] and have demonstrated the powering of micro-nano devices, such as pH or chemical sensors, LEDs, digital watches…[151], [170]–[175].

Piezo-generators based on III-nitride nanostructures

Despite the very promising piezoelectric responses of III-nitrides nanowires (refer to *Table 1*), only a handful of PG prototypes have been demonstrated. The very first III-N NWs based LING device was developed by Lin et al. [176] in 2011. The PG device consists of layers of GaN NWs encapsulated in PMMA and sandwiched between two Cr/Au electrodes. This prototype demonstrated the generation of an output voltage of about 1.2 V as shown in Fig. 34a. The power density of the device was estimated to be about 0.16 mW/cm^3. In 2016, Liu et al. developed VING devices integrating InN NWs with non-intentional doping and p-type dopants, and tested them using a mechanical shaker. The output voltage/current was recorded to be 55 mV/211 nA for device based on intrinsic NWs and 85 mV/80 nA for PG based on p-doped NWs generated (Fig. 34b). From these values, the author estimated a three times higher power generation by PG integrating p-doped InN NWs than the intrinsic one [177].

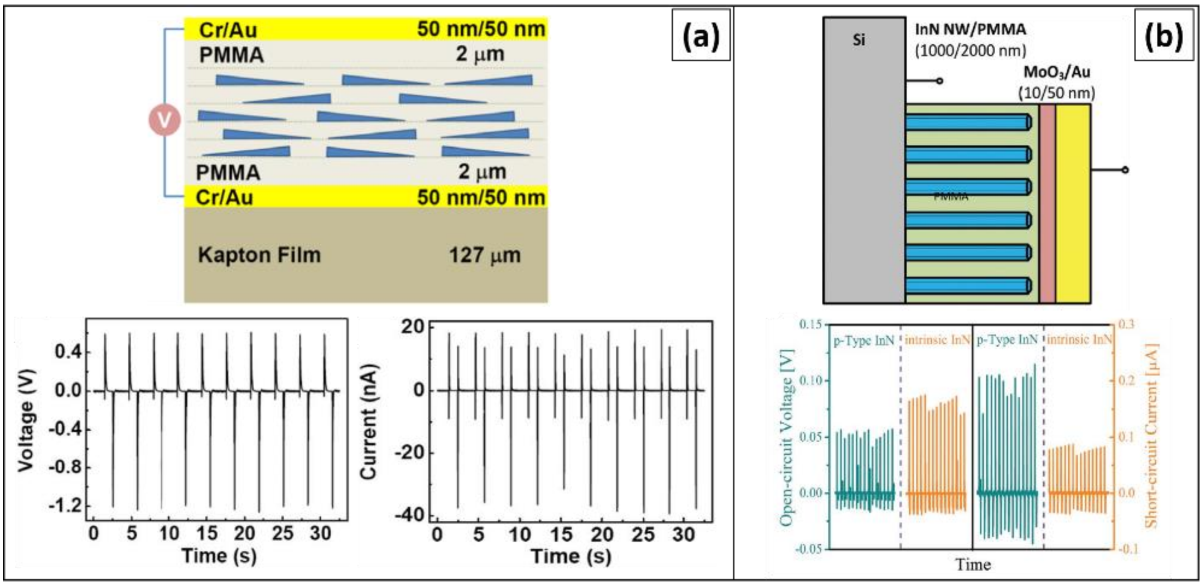

Figure 34. Representation and piezoelectric response of III-nitride nanostructures based PGs. (a) (Image taken from [176]). First LING device based on GaN NWs. (b) (Image taken from [177]). VING device based on p-doped and non-intentionally doped InN NWs.

The first GaN NWs based high efficiency VING was developed by Jamond et al. [104] in 2016 at C2N. Fig. 35a shows the final device working under laterally bended using an actuator. Due to the difference in the thickness of the active layer (1 µm) as compared to that of the substrate (about 300 µm), a lateral stretching of the device occurs applying a uniform axial compression on the GaN NWs (see Jamond et al. [104]). The active media generates a maximum O.V. of 200 mV, which corresponds to a maximum output power density of 12.7 mW/cm^3 for a large number of compressive cycles in the 1-6 Hz applied frequency range. In 2018, L. Lu et al. [178] developed another GaN NWs based VING prototype working under direct compression. A soft matrix was chosen to encapsulate the NWs, in order to allow a maximum deformation of the piezoelectric nanostructures (Fig. 35b). This device was tested using deformation frequencies in the range of 1 Hz to 2 kHz via a shaker head and an output power density of 35 mW/cm^3 was estimated.

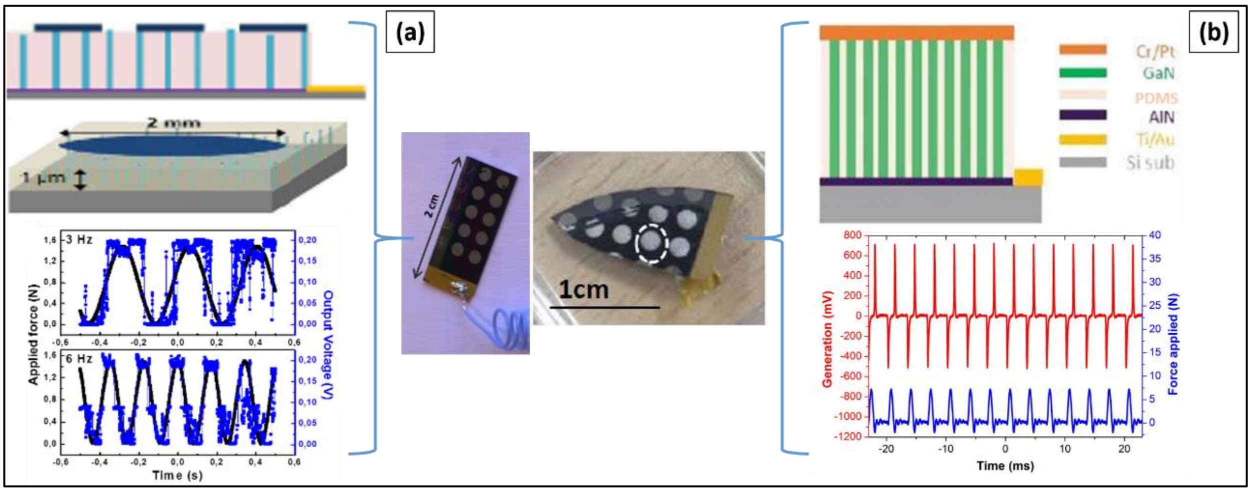

Figure 35. Representation and piezoelectric response of PGs based on GaN NWs fabricated at C2N. (a) Image taken from [107]; (b) Image taken from [178]. The images of the final PG prototypes also shown.

More recently, new designs of VINGs integrating GaN NWs based with axial heterojunctions (Fig. 36a) and core-shell structures on flexible substrates (Fig. 36(b-c)) have been developed by Johar et al. [179], [180] and Waseem et al. [167], [172], [181]. These PGs have demonstrated their capacity for supplying power densities as high as several tens of µW/cm^2.

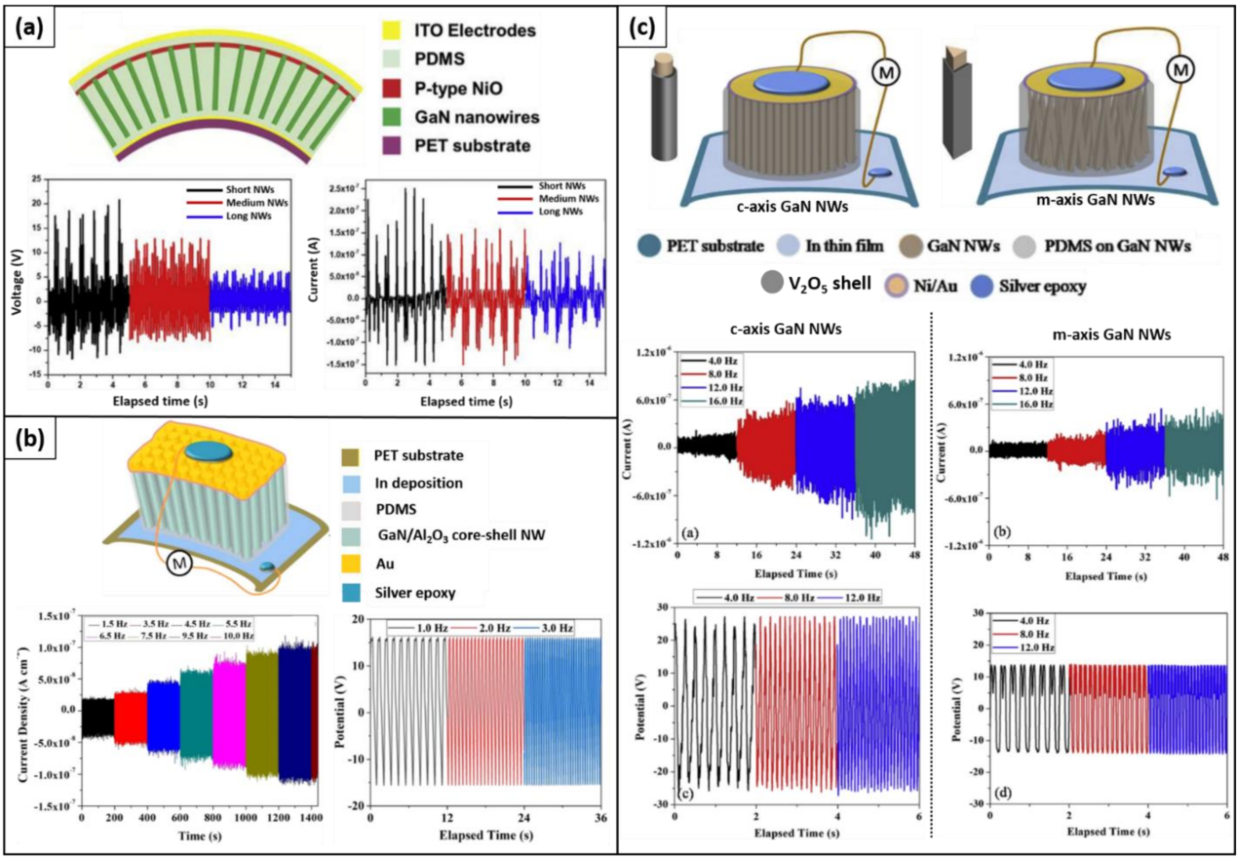

Figure 36. (Images taken from [172], [179], [181]). Schematic representations and the piezoelectric responses of new-generation VING devices based on GaN NWs.

Table 6 recapitulates the piezoelectric performances of PGs based on 1D nanostructures. The devices have been tested under different conditions depending upon their respective configurations. We note here that for the quasi totality of them, the testing conditions remains far from the real conditions found in the environment.

Table 6. Piezoelectric performances of PGs based on 1D nanostructures.

PGs based on 1D Nanostructures	Deformation	Output Voltage/ Current	Current density	Power density	R_{load}	References
Ferroelectric PGs						
PDMS-$KNbO_3$ nanorods composite on flexible substrate	Flexion (0.33 Hz, 0.38%)	3.2 V/67.5 nA	9.3 nA/cm^2	-	-	[182]
PDMS-LiNbO3 NWs composite on flexible substrate	Compression (0.8 Hz)	0.4 V/6.3 nA	-	-	-	[183]
PDMS -PMN-PT NWs comosite	Compression (5 Hz)	7.8 V/2.29 nA	4.58 µA/cm^2	-	-	[184]
Horizonatlly aligned PZT nanofibres	Compression (8Hz)	1.63 V	-	-	6 MΩ	[149]
Horizontally aligned PVDF nanofibres	Flexion (2 Hz)	30 mV/3 nA	-	-	15 GΩ	[134]
Nanoporous PVDF	Acoustic waves (88.9-100 dB)	2.6 V/0.6 µA	-	0.17 mW/cm^3	-	[164]
ZnO NWs based PGs						
Vertically aligned ZnO NWs	Palm movement	58 V/134 µA	-	0.78 W/cm^3	-	[156]
Vertically aligned ZnO NWs	20 Hz actuator	22 mV/-32 mV	5.5 nA/cm^2/ 8 nA/cm^2	288 nW/cm^3	1 MΩ	[154]
Vertically aligned ZnO NWs (2 layers)	0.12 % strain at 3.56% s^{-1}	10 V/ 0.6 µA	1 mA/ cm^3	10 mW/cm^3	-	[185]
ZnO NWs VING	Compression (5 N)	0.29 V	-	85 µW/cm^3	1 MΩ	[152]
ZnO NW-parylene nanocomposite	Compression (13 N, 5 Hz)	10V/ 0.5 µA	0.11 µA/cm^2	-	10 MΩ	[161]
III-nitride based PGs						
Vertically aligned p-type InN NWs	Compression (3 Hz, 2ms^{-2})	55 mV/ 211 nA	-	0.012 µW/cm^2	1 KΩ	[177]
Horizontally integrated GaN NWs	Flexion	1.2 V/ 40 nA	0.16 µA/cm^2	-	-	[176]
Vertically aligned GaN NWs	Compression (3-6 Hz)	200 mV	-	12.7 mW/cm^3	1 MΩ	[107]
Vertically aligned GaN NWs	Compression (300 Hz)	1.2 V	-	22.1 mW/cm^3	1 MΩ	[178]
p-n NiO/GaN NWs	Flexion (7 Hz)	20.8 V/ 253 nA	-	-	-	[179]
GaN/V_2O_5 core-shell NWs	Flexion (4 Hz)	27 V/ 850 nA	-	-	-	[181]
Vertical GaN NWs on Graphene coated Cu foil	Flexion (8 Hz)	19.7 V	1.9 mA/cm^2	39 µW/cm^{-2}	250 GΩ	[180]
GaN/Al_2O_3 core-shell NWs VING	Flexion (1-10 Hz)	7.3 V/ 71 nA	100 nA/cm^2	-	100 MΩ	[172]
GaN:Mg/ZnO Coaxial NWs	Flexion (10 Hz)	66 V/ 40 µA	170 µW/cm^2	-	2.5 MΩ	[167]

1.4. Objectives

In the context of small-scale ambient energy harvesting for powering micro-nano devices (sensors, biological implants…), 1D-nanostructures such as III-nitride NWs, are excellent candidates. However, the current challenge involves the development of a new generation of ultra-compact piezo-generators for the self-sufficient functionality of the micro-devices without increasing their size and weight. This requires a higher piezo-conversion efficiency per unit surface area of the active layer while complying with the dimensional limitations of the device. Recent studies presented in this Chapter have shown that the insertions of hetero-structures can strongly enhance the piezo-generation efficiency of GaN NWs. Nevertheless, it remains insufficient in response to the ambient deformations. In this thesis, we propose new solutions to further enhance and optimise the conversion efficiency of piezoelectric transducers based on III-nitride NWs.

REFERENCES

[1] J. Curie and P. Curie, ‘Développement par compression de l’électricité polaire dans les cristaux hémièdres à faces inclinées’, *bulmi*, vol. 3, no. 4, pp. 90–93, 1880, doi: 10.3406/bulmi.1880.1564.

[2] P. Dineva, D. Gross, R. Müller, and T. Rangelov, *Dynamic Fracture of Piezoelectric Materials*, vol. 212. Cham: Springer International Publishing, 2014. doi: 10.1007/978-3-319-03961-9.

[3] J. Curie and P. Curie, ‘Contractions et dilatations produites par des tensions électriques dans les cristaux hémièdres à faces inclinées’, *Compt. Rend*, vol. 93, pp. 1137–1140, 1881.

[4] N. Jamond, ‘Des nanofils Nitrure à la génération piézoélectrique’, p. 164.

[5] H. Kawai, ‘The Piezoelectricity of Poly (vinylidene Fluoride)’, *Jpn. J. Appl. Phys.*, vol. 8, no. 7, p. 975, Jul. 1969, doi: 10.1143/JJAP.8.975.

[6] S. Yu. Karpov, ‘Spontaneous polarization in III-nitride materials: crystallographic revision’, *Phys. Status Solidi (c)*, vol. 7, no. 7–8, pp. 1841–1843, May 2010, doi: 10.1002/pssc.200983414.

[7] J. S. Speck and S. F. Chichibu, ‘Nonpolar and Semipolar Group III Nitride-Based Materials’, *MRS Bull.*, vol. 34, no. 5, pp. 304–312, May 2009, doi: 10.1557/mrs2009.91.

[8] H. Morkoç, *Handbook of Nitride Semiconductors and Devices, Materials Properties, Physics and Growth*. John Wiley & Sons, 2009.

[9] T. Wonglakhon and D. Zahn, ‘Interaction potentials for modelling GaN precipitation and solid state polymorphism’, *J. Phys.: Condens. Matter*, vol. 32, no. 20, p. 205401, May 2020, doi: 10.1088/1361-648X/ab6cbe.

[10] F. Bernardini, V. Fiorentini, and D. Vanderbilt, ‘Spontaneous polarization and piezoelectric constants of III-V nitrides’, *Phys. Rev. B*, vol. 56, no. 16, pp. R10024–R10027, Oct. 1997, doi: 10.1103/PhysRevB.56.R10024.

[11] F. A. Ponce, D. P. Bour, W. T. Young, M. Saunders, and J. W. Steeds, ‘Determination of lattice polarity for growth of GaN bulk single crystals and epitaxial layers’, *Appl. Phys. Lett.*, vol. 69, no. 3, pp. 337–339, Jul. 1996, doi: 10.1063/1.118052.

[12] Z. Liliental-Weber *et al.*, ‘Structural characterization of bulk GaN crystals grown under high hydrostatic pressure’, *JEM*, vol. 25, no. 9, pp. 1545–1550, Sep. 1996, doi: 10.1007/BF02655397.

[13] T. Sasaki and T. Matsuoka, ‘Substrate-polarity dependence of metal-organic vapor-phase epitaxy-grown GaN on SiC’, *Journal of Applied Physics*, vol. 64, no. 9, pp. 4531–4535, Nov. 1988, doi: 10.1063/1.341281.

[14] E. Monroy *et al.*, ‘Growth kinetics of N-face polarity GaN by plasma-assisted molecular-beam epitaxy’, *Appl. Phys. Lett.*, vol. 84, no. 18, pp. 3684–3686, May 2004, doi: 10.1063/1.1739511.

[15] R. Held *et al.*, ‘Structure and composition of GaN(0001) A and B surfaces’, *Journal of Applied Physics*, vol. 85, no. 11, pp. 7697–7704, Jun. 1999, doi: 10.1063/1.370574.

[16] R. M. Feenstra, J. E. Northrup, and J. Neugebauer, ‘Review of Structure of Bare and Adsorbate-Covered GaN(0001) Surfaces’, *MRS Internet j. nitride semicond. res.*, vol. 7, p. e3, 2002, doi: 10.1557/S1092578300000296.

[17] N. Gogneau, E. Sarigiannidou, E. Monroy, S. Monnoye, H. Mank, and B. Daudin, ‘Surfactant effect of gallium during the growth of GaN on AlN(0001^{-}) by plasma-assisted molecular beam epitaxy’, *Appl. Phys. Lett.*, vol. 85, no. 8, pp. 1421–1423, Aug. 2004, doi: 10.1063/1.1782264.

[18] K. Kim, W. R. L. Lambrecht, and B. Segall, ‘Electronic structure of GaN with strain and phonon distortions’, *Phys. Rev. B*, vol. 50, no. 3, pp. 1502–1505, Jul. 1994, doi: 10.1103/PhysRevB.50.1502.

[19] K. Shimada, T. Sota, and K. Suzuki, ‘First-principles study on electronic and elastic properties of BN, AlN, and GaN’, *Journal of Applied Physics*, vol. 84, no. 9, pp. 4951–4958, Nov. 1998, doi: 10.1063/1.368739.

[20] A. F. Wright, ‘Elastic properties of zinc-blende and wurtzite AlN, GaN, and InN’, *Journal of Applied Physics*, vol. 82, no. 6, pp. 2833–2839, Sep. 1997, doi: 10.1063/1.366114.

[21] Y. Duan, J. Li, S.-S. Li, and J.-B. Xia, ‘Elasticity, band-gap bowing, and polarization of AlxGa1−xN alloys’, *Journal of Applied Physics*, vol. 103, no. 2, p. 023705, Jan. 2008, doi: 10.1063/1.2831486.

[22] A. Polian, M. Grimsditch, and I. Grzegory, ‘Elastic constants of gallium nitride’, *Journal of Applied Physics*, vol. 79, no. 6, pp. 3343–3344, Mar. 1996, doi: 10.1063/1.361236.

[23] N. Nakamura, H. Ogi, and M. Hirao, ‘Elastic, anelastic, and piezoelectric coefficients of GaN’, *Journal of Applied Physics*, vol. 111, no. 1, p. 013509, Jan. 2012, doi: 10.1063/1.3674271.

[24] V. A. Savastenko and A. U. Sheleg, ‘Study of the elastic properties of gallium nitride’, *Phys. Stat. Sol. (a)*, vol. 48, no. 2, pp. K135–K139, Aug. 1978, doi: 10.1002/pssa.2210480253.

[25] Y. Takagi, M. Ahart, T. Azuhata, T. Sota, K. Suzuki, and S. Nakamura, ‘Brillouin scattering study in the GaN epitaxial layer’, *Physica B: Condensed Matter*, vol. 219–220, pp. 547–549, Apr. 1996, doi: 10.1016/0921-4526(95)00807-1.

[26] M. Yamaguchi *et al.*, ‘Brillouin scattering study of gallium nitride: elastic stiffness constants’, *J. Phys.: Condens. Matter*, vol. 9, no. 1, pp. 241–248, Jan. 1997, doi: 10.1088/0953-8984/9/1/025.

[27] R. B. Schwarz, K. Khachaturyan, and E. R. Weber, ‘Elastic moduli of gallium nitride’, *Appl. Phys. Lett.*, vol. 70, no. 9, pp. 1122–1124, Mar. 1997, doi: 10.1063/1.118503.

[28] C. Deger *et al.*, 'Sound velocity of AlxGa1−xN thin films obtained by surface acoustic-wave measurements', *Appl. Phys. Lett.*, vol. 72, no. 19, pp. 2400–2402, May 1998, doi: 10.1063/1.121368.

[29] C. M. Lueng *et al.*, 'Piezoelectric coefficient of GaN measured by laser interferometry', *Journal of Non-Crystalline Solids*, vol. 254, no. 1–3, pp. 123–127, Sep. 1999, doi: 10.1016/S0022-3093(99)00383-X.

[30] A. D. Bykhovski, B. L. Gelmont, and M. S. Shur, 'Elastic strain relaxation and piezoeffect in GaN-AlN, GaN-AlGaN and GaN-InGaN superlattices', *Journal of Applied Physics*, vol. 81, no. 9, pp. 6332–6338, May 1997, doi: 10.1063/1.364368.

[31] S. Muensit, E. M. Goldys, and I. L. Guy, 'Shear piezoelectric coefficients of gallium nitride and aluminum nitride', *Appl. Phys. Lett.*, vol. 75, no. 25, pp. 3965–3967, Dec. 1999, doi: 10.1063/1.125508.

[32] S. Muensit and I. L. Guy, 'The piezoelectric coefficient of gallium nitride thin films', *Appl. Phys. Lett.*, vol. 72, no. 15, pp. 1896–1898, Apr. 1998, doi: 10.1063/1.121219.

[33] M. A. Littlejohn, J. R. Hauser, and T. H. Glisson, 'Monte Carlo calculation of the velocity-field relationship for gallium nitride', *Appl. Phys. Lett.*, vol. 26, no. 11, pp. 625–627, Jun. 1975, doi: 10.1063/1.88002.

[34] I. L. Guy, S. Muensit, and E. M. Goldys, 'Extensional piezoelectric coefficients of gallium nitride and aluminum nitride', *Appl. Phys. Lett.*, vol. 75, no. 26, pp. 4133–4135, Dec. 1999, doi: 10.1063/1.125560.

[35] S. Arafin, X. Liu, and Z. Mi, 'Review of recent progress of III-nitride nanowire lasers', *J. Nanophoton*, vol. 7, no. 1, p. 074599, Sep. 2013, doi: 10.1117/1.JNP.7.074599.

[36] Y. P. Varshni, 'Temperature dependence of the energy gap in semiconductors', *Physica*, vol. 34, no. 1, pp. 149–154, Jan. 1967, doi: 10.1016/0031-8914(67)90062-6.

[37] B. Monemar, 'Fundamental energy gap of GaN from photoluminescence excitation spectra', *Phys. Rev. B*, vol. 10, no. 2, pp. 676–681, Jul. 1974, doi: 10.1103/PhysRevB.10.676.

[38] O. Lagerstedt and B. Monemar, 'Luminescence in epitaxial GaN : Cd', *Journal of Applied Physics*, vol. 45, no. 5, pp. 2266–2272, May 1974, doi: 10.1063/1.1663574.

[39] I. Vurgaftman, J. R. Meyer, and L. R. Ram-Mohan, 'Band parameters for III–V compound semiconductors and their alloys', *Journal of Applied Physics*, vol. 89, no. 11, pp. 5815–5875, Jun. 2001, doi: 10.1063/1.1368156.

[40] M. D. Al-Amri, M. El-Gomati, and M. S. Zubairy, Eds., *Optics in Our Time*. Cham: Springer International Publishing, 2016. doi: 10.1007/978-3-319-31903-2.

[41] Z. L. Wang and J. Song, 'Piezoelectric Nanogenerators Based on Zinc Oxide Nanowire Arrays', *Science*, vol. 312, no. 5771, pp. 242–246, Apr. 2006, doi: 10.1126/science.1124005.

[42] P. Yang, R. Yan, and M. Fardy, 'Semiconductor Nanowire: What's Next?', *Nano Lett.*, vol. 10, no. 5, pp. 1529–1536, May 2010, doi: 10.1021/nl100665r.

[43] Y. S. Zhou *et al.*, 'Vertically Aligned CdSe Nanowire Arrays for Energy Harvesting and Piezotronic Devices', *ACS Nano*, vol. 6, no. 7, pp. 6478–6482, Jul. 2012, doi: 10.1021/nn3022074.

[44] M.-H. Zhao, Z.-L. Wang, and S. X. Mao, 'Piezoelectric Characterization of Individual Zinc Oxide Nanobelt Probed by Piezoresponse Force Microscope', *Nano Lett.*, vol. 4, no. 4, pp. 587–590, Apr. 2004, doi: 10.1021/nl035198a.

[45] H. J. Fan *et al.*, 'Template-Assisted Large-Scale Ordered Arrays of ZnO Pillars for Optical and Piezoelectric Applications', *Small*, vol. 2, no. 4, pp. 561–568, 2006, doi: 10.1002/smll.200500331.

[46] D. A. Scrymgeour and J. W. P. Hsu, 'Correlated Piezoelectric and Electrical Properties in Individual ZnO Nanorods', *Nano Lett.*, vol. 8, no. 8, p. 6, 2008.

[47] R. Steinhausen *et al.*, 'Properties of fine scale piezoelectric PZT fibers with different Zr content', *Journal of the European Ceramic Society*, vol. 21, no. 10–11, pp. 1459–1462, Jan. 2001, doi: 10.1016/S0955-2219(01)00041-3.

[48] Y. Qi and M. C. McAlpine, 'Nanotechnology-enabled flexible and biocompatible energy harvesting', *Energy Environ. Sci.*, vol. 3, no. 9, p. 1275, 2010, doi: 10.1039/c0ee00137f.

[49] M. Minary-Jolandan, R. A. Bernal, I. Kuljanishvili, V. Parpoil, and H. D. Espinosa, 'Individual GaN Nanowires Exhibit Strong Piezoelectricity in 3D', *Nano Lett.*, vol. 12, no. 2, pp. 970–976, Feb. 2012, doi: 10.1021/nl204043y.

[50] R. Agrawal and H. D. Espinosa, 'Giant Piezoelectric Size Effects in Zinc Oxide and Gallium Nitride Nanowires. A First Principles Investigation', *Nano Lett.*, vol. 11, no. 2, pp. 786–790, Feb. 2011, doi: 10.1021/nl104004d.

[51] M. Minary-Jolandan, R. A. Bernal, and H. D. Espinosa, 'Strong piezoelectricity in individual GaN nanowires', *MRS Communications*, vol. 1, no. 1, pp. 45–48, Nov. 2011, doi: 10.1557/mrc.2011.14.

[52] F. Bernardini and V. Fiorentini, 'First-principles calculation of the piezoelectric tensor d↓↓ of III–V nitrides', *Appl. Phys. Lett.*, vol. 80, no. 22, pp. 4145–4147, Jun. 2002, doi: 10.1063/1.1482796.

[53] J. A. Christman, H. Maiwa, S.-H. Kim, A. I. Kingon, and R. J. Nemanich, 'Piezoelectric Measurements with Atomic Force Microscopy', *MRS Proc.*, vol. 541, p. 617, 1998, doi: 10.1557/PROC-541-617.

[54] T. R. Shrout and S. J. Zhang, 'Lead-free piezoelectric ceramics: Alternatives for PZT?', *J Electroceram*, vol. 19, no. 1, pp. 113–126, Oct. 2007, doi: 10.1007/s10832-007-9047-0.

[55] V. Cauda, S. Stassi, K. Bejtka, and G. Canavese, 'Nanoconfinement: an Effective Way to Enhance PVDF Piezoelectric Properties', *ACS Appl. Mater. Interfaces*, vol. 5, no. 13, pp. 6430–6437, Jul. 2013, doi: 10.1021/am4016878.

[56] T. R. Dargaville, M. Celina, J. W. Martin, and B. A. Banks, 'Evaluation of piezoelectric PVDF polymers for use in space environments. II. Effects of atomic oxygen and vacuum UV exposure', *J. Polym. Sci. B Polym. Phys.*, vol. 43, no. 18, pp. 2503–2513, Sep. 2005, doi: 10.1002/polb.20549.

[57] K. Omote, H. Ohigashi, and K. Koga, 'Temperature dependence of elastic, dielectric, and piezoelectric properties of "single crystalline'' films of vinylidene fluoride trifluoroethylene copolymer', *Journal of Applied Physics*, vol. 81, no. 6, pp. 2760–2769, Mar. 1997, doi: 10.1063/1.364300.

[58] Z. Zhou, H. Tang, and H. A. Sodano, 'Vertically Aligned Arrays of BaTiO $_3$ Nanowires', *ACS Appl. Mater. Interfaces*, vol. 5, no. 22, pp. 11894–11899, Nov. 2013, doi: 10.1021/am403587q.

[59] H. Jaffe, 'Piezoelectric Ceramics', *J American Ceramic Society*, vol. 41, no. 11, pp. 494–498, Nov. 1958, doi: 10.1111/j.1151-2916.1958.tb12903.x.

[60] T. Kimura, Q. Dong, S. Yin, T. Hashimoto, A. Sasaki, and T. Sato, 'Synthesis and piezoelectric properties of Li-doped BaTiO3 by a solvothermal approach', *Journal of the European Ceramic Society*, vol. 33, no. 5, pp. 1009–1015, May 2013, doi: 10.1016/j.jeurceramsoc.2012.11.007.

[61] L.-F. Zhu, B.-P. Zhang, and W.-G. Yang, 'Enhancing piezoelectric coefficient d33 in LiF-doped BaTiO3 ceramics by optimizing excess Ba content', *Materials Research Bulletin*, vol. 52, pp. 158–161, Apr. 2014, doi: 10.1016/j.materresbull.2014.01.018.

[62] W.-G. Yang, B.-P. Zhang, N. Ma, and L. Zhao, 'High piezoelectric properties of BaTiO3–xLiF ceramics sintered at low temperatures', *Journal of the European Ceramic Society*, vol. 32, no. 4, pp. 899–904, Apr. 2012, doi: 10.1016/j.jeurceramsoc.2011.10.054.

[63] L.-F. Zhu, B.-P. Zhang, W.-G. Yang, N. Ma, X.-K. Zhao, and L. Zhao, 'High piezoelectric properties of (Ba,Ca)TiO3-0.04LiF ceramics sintered at a low temperature', *J Electroceram*, vol. 30, no. 1–2, pp. 24–29, Apr. 2013, doi: 10.1007/s10832-012-9701-z.

[64] M. Chen *et al.*, 'Y 2 O 3 -modified Ba(Ti 0.96 Sn 0.04)O 3 ceramics with improved piezoelectricity and raised Curie temperature', *Materials Research Bulletin*, vol. 59, pp. 305–310, Nov. 2014, doi: 10.1016/j.materresbull.2014.07.040.

[65] S. Xu, G. Poirier, and N. Yao, 'Fabrication and piezoelectric property of PMN-PT nanofibers', *Nano Energy*, vol. 1, no. 4, pp. 602–607, Jul. 2012, doi: 10.1016/j.nanoen.2012.03.011.

[66] R. Tao, M. Mouis, and G. Ardila, 'Unveiling the Influence of Surface Fermi Level Pinning on the Piezoelectric Response of Semiconducting Nanowires', *Adv. Electron. Mater.*, vol. 4, no. 1, p. 1700299, Jan. 2018, doi: 10.1002/aelm.201700299.

[67] A. J. L. Lopez Garcia, M. Mouis, V. Consonni, and G. Ardila, 'Dimensional Roadmap for Maximizing the Piezoelectrical Response of ZnO Nanowire-Based Transducers: Impact of Growth Method', *Nanomaterials*, vol. 11, no. 4, p. 941, Apr. 2021, doi: 10.3390/nano11040941.

[68] N. Jamond *et al.*, 'Energy harvesting efficiency in GaN nanowire-based nanogenerators: the critical influence of the Schottky nanocontact', *Nanoscale*, vol. 9, no. 13, pp. 4610–4619, 2017, doi: 10.1039/C7NR00647K.

[69] J.-M. Liu, B. Pan, H. L. W. Chan, S. N. Zhu, Y. Y. Zhu, and Z. G. Liu, 'Piezoelectric coefficient measurement of piezoelectric thin films: an overview', *Materials Chemistry and Physics*, vol. 75, no. 1–3, pp. 12–18, Apr. 2002, doi: 10.1016/S0254-0584(02)00023-8.

[70] M. G. Cain and M. Stewart, 'Piezoelectric Resonance', in *Characterisation of Ferroelectric Bulk Materials and Thin Films*, vol. 2, M. G. Cain, Ed. Dordrecht: Springer Netherlands, 2014, pp. 15–35. doi: 10.1007/978-1-4020-9311-1_2.

[71] Z. Huang and G. Leighton, 'Interferometry for Piezoelectric Materials and Thin Films', in *Characterisation of Ferroelectric Bulk Materials and Thin Films*, vol. 2, M. G. Cain, Ed. Dordrecht: Springer Netherlands, 2014, pp. 87–113. doi: 10.1007/978-1-4020-9311-1_5.

[72] D. Berlincourt and H. H. A. Krueger, 'Domain Processes in Lead Titanate Zirconate and Barium Titanate Ceramics', *Journal of Applied Physics*, vol. 30, no. 11, pp. 1804–1810, Nov. 1959, doi: 10.1063/1.1735059.

[73] M. Stewart and M. G. Cain, 'Direct Piezoelectric Measurement: The Berlincourt Method', in *Characterisation of Ferroelectric Bulk Materials and Thin Films*, vol. 2, M. G. Cain, Ed. Dordrecht: Springer Netherlands, 2014, pp. 37–64. doi: 10.1007/978-1-4020-9311-1_3.

[74] C. Chima-Okereke, M. J. Reece, and M. G. Cain, 'Indentation Stiffness Analysis of Ferroelectric Thin Films', in *Characterisation of Ferroelectric Bulk Materials and Thin Films*, vol. 2, M. G. Cain, Ed. Dordrecht: Springer Netherlands, 2014, pp. 221–231. doi: 10.1007/978-1-4020-9311-1_9.

[75] C. Chima-Okereke, A. J. Bushby, M. J. Reece, R. W. Whatmore, and Q. Zhang, 'Experimental, analytical, and finite element analyses of nanoindentation of multilayer PZT/Pt/SiO $_2$ thin film systems on silicon wafers', *J. Mater. Res.*, vol. 21, no. 2, pp. 409–419, Feb. 2006, doi: 10.1557/jmr.2006.0047.

[76] M. Safaei, H. A. Sodano, and S. R. Anton, 'A review of energy harvesting using piezoelectric materials: state-of-the-art a decade later (2008–2018)', *Smart Mater. Struct.*, vol. 28, no. 11, p. 113001, Nov. 2019, doi: 10.1088/1361-665X/ab36e4.

[77] C. Keawboonchuay and T. G. Engel, 'Electrical power generation characteristics of piezoelectric generator under quasi-static and dynamic stress conditions', *IEEE Trans. Ultrason., Ferroelect., Freq. Contr.*, vol. 50, no. 10, pp. 1377–1382, Oct. 2003, doi: 10.1109/TUFFC.2003.1244755.

[78] Chao-Nan Xu, M. Akiyama, K. Nonaka, and T. Watanabe, 'Electrical power generation characteristics of PZT piezoelectric ceramics', *IEEE Trans. Ultrason., Ferroelect., Freq. Contr.*, vol. 45, no. 4, pp. 1065–1070, Jul. 1998, doi: 10.1109/58.710589.

[79] G. Binnig, C. F. Quate, and Ch. Gerber, 'Atomic Force Microscope', *Phys. Rev. Lett.*, vol. 56, no. 9, pp. 930–933, Mar. 1986, doi: 10.1103/PhysRevLett.56.930.

[80] S. Lepadatu and M. G. Cain, 'Piezoresponse Force Micropscopy', in *Characterisation of Ferroelectric Bulk Materials and Thin Films*, vol. 2, M. G. Cain, Ed. Dordrecht: Springer Netherlands, 2014, pp. 191–219. doi: 10.1007/978-1-4020-9311-1_8.

[81] Z. Chen *et al.*, 'Piezoelectric properties of rhombic LiNbO3 nanowires', *RSC Adv.*, vol. 2, no. 19, p. 7380, 2012, doi: 10.1039/c2ra20237a.

[82] J. Varghese, S. Barth, L. Keeney, R. W. Whatmore, and J. D. Holmes, 'Nanoscale Ferroelectric and Piezoelectric Properties of Sb_2S_3 Nanowire Arrays', *Nano Lett.*, vol. 12, no. 2, pp. 868–872, Feb. 2012, doi: 10.1021/nl2039106.

[83] A. Gebrekrstos, G. Madras, and S. Bose, 'Piezoelectric Response in Electrospun Poly(vinylidene fluoride) Fibers Containing Fluoro-Doped Graphene Derivatives', *ACS Omega*, vol. 3, no. 5, pp. 5317–5326, May 2018, doi: 10.1021/acsomega.8b00237.

[84] M. B. Ghasemian, Q. Lin, E. Adabifiroozjaei, F. Wang, D. Chu, and D. Wang, 'Morphology control and large piezoresponse of hydrothermally synthesized lead-free piezoelectric $(Bi_{0.5}Na_{0.5})TiO_3$ nanofibres', *RSC Adv.*, vol. 7, no. 25, pp. 15020–15026, 2017, doi: 10.1039/C7RA01293D.

[85] Y. Calahorra, M. Smith, A. Datta, H. Benisty, and S. Kar-Narayan, 'Mapping piezoelectric response in nanomaterials using a dedicated non-destructive scanning probe technique', *Nanoscale*, vol. 9, no. 48, pp. 19290–19297, 2017, doi: 10.1039/C7NR06714C.

[86] A. J. L. Garcia *et al.*, 'Size and Semiconducting Effects on the Piezoelectric Performances of ZnO Nanowires Grown onto Gravure-Printed Seed Layers on Flexible Substrates', *Nanoenergy Advances*, vol. 2, no. 2, pp. 197–209, May 2022, doi: 10.3390/nanoenergyadv2020008.

[87] N. Gogneau *et al.*, 'GaN nanowires for piezoelectric generators: GaN nanowires for piezoelectric generators', *Phys. Status Solidi RRL*, vol. 8, no. 5, pp. 414–419, May 2014, doi: 10.1002/pssr.201409105.

[88] X. Xu *et al.*, 'An improved AFM cross-sectional method for piezoelectric nanostructures properties investigation: application to GaN nanowires', *Nanotechnology*, vol. 22, no. 10, p. 105704, Mar. 2011, doi: 10.1088/0957-4484/22/10/105704.

[89] N. Gogneau *et al.*, 'Electromechanical conversion efficiency of GaN NWs: critical influence of the NW stiffness, the Schottky nano-contact and the surface charge effects', *Nanoscale*, vol. 14, no. 13, pp. 4965–4976, 2022, doi: 10.1039/D1NR07863A.

[90] N. Gogneau *et al.*, 'Impact of the GaN nanowire polarity on energy harvesting', *Appl. Phys. Lett.*, vol. 104, no. 21, p. 213105, May 2014, doi: 10.1063/1.4880101.

[91] 'Schneegans O, Chrétien P and Houzé F 2011 French Patent Specification FR 10 01940 International PCT WO 2011/ 138738'

[92] A. Vecchiola *et al.*, 'Wide range local resistance imaging on fragile materials by conducting probe atomic force microscopy in intermittent contact mode', *Appl. Phys. Lett.*, vol. 108, no. 24, p. 243101, Jun. 2016, doi: 10.1063/1.4953870.

[93] J. Y. Huang, H. Zheng, S. X. Mao, Q. Li, and G. T. Wang, 'In Situ Nanomechanics of GaN Nanowires', *Nano Lett.*, vol. 11, no. 4, pp. 1618–1622, Apr. 2011, doi: 10.1021/nl200002x.

[94] H. D. Espinosa, R. A. Bernal, and T. Filleter, 'In Situ TEM Electromechanical Testing of Nanowires and Nanotubes', *Small*, vol. 8, no. 21, pp. 3233–3252, Nov. 2012, doi: 10.1002/smll.201200342.

[95] R. Erdélyi *et al.*, 'In-situ mechanical characterization of wurtzite InAs nanowires', *Solid State Communications*, vol. 152, no. 19, pp. 1829–1833, Oct. 2012, doi: 10.1016/j.ssc.2012.07.005.

[96] Z. Y. Ning *et al.*, '*In situ* multiproperty measurements of individual nanomaterials in SEM and correlation with their atomic structures', *Nanotechnology*, vol. 25, no. 27, p. 275703, Jul. 2014, doi: 10.1088/0957-4484/25/27/275703.

[97] K. H. Liu, W. L. Wang, Z. Xu, L. Liao, X. D. Bai, and E. G. Wang, '*In situ* probing mechanical properties of individual tungsten oxide nanowires directly grown on tungsten tips inside transmission electron microscope', *Appl. Phys. Lett.*, vol. 89, no. 22, p. 221908, Nov. 2006, doi: 10.1063/1.2397547.

[98] C. Q. Chen, Y. Shi, Y. S. Zhang, J. Zhu, and Y. J. Yan, 'Size Dependence of Young's Modulus in ZnO Nanowires', *Phys. Rev. Lett.*, vol. 96, no. 7, p. 075505, Feb. 2006, doi: 10.1103/PhysRevLett.96.075505.

[99] C.-Y. Nam, P. Jaroenapibal, D. Tham, D. E. Luzzi, S. Evoy, and J. E. Fischer, 'Diameter-Dependent Electromechanical Properties of GaN Nanowires', *Nano Lett.*, vol. 6, no. 2, pp. 153–158, Feb. 2006, doi: 10.1021/nl051860m.

[100] X. Li *et al.*, ‘Mechanical properties of individual InAs nanowires studied by tensile tests’, *Appl. Phys. Lett.*, vol. 104, no. 10, p. 103110, Mar. 2014, doi: 10.1063/1.4868133.

[101] Z. Wang, J. Hu, A. P. Suryavanshi, K. Yum, and M.-F. Yu, ‘Voltage Generation from Individual BaTiO $_3$ Nanowires under Periodic Tensile Mechanical Load’, *Nano Lett.*, vol. 7, no. 10, pp. 2966–2969, Oct. 2007, doi: 10.1021/nl070814e.

[102] K. Zheng *et al.*, ‘Orientation Dependence of Electromechanical Characteristics of Defect-free InAs Nanowires’, *Nano Lett.*, vol. 16, no. 3, pp. 1787–1793, Mar. 2016, doi: 10.1021/acs.nanolett.5b04842.

[103] L. Largeau, E. Galopin, N. Gogneau, L. Travers, F. Glas, and J.-C. Harmand, ‘N-Polar GaN Nanowires Seeded by Al Droplets on Si(111)’, *Crystal Growth & Design*, vol. 12, no. 6, pp. 2724–2729, Jun. 2012, doi: 10.1021/cg300212d.

[104] N. Jamond *et al.*, ‘Piezo-generator integrating a vertical array of GaN nanowires’, *Nanotechnology*, vol. 27, no. 32, p. 325403, Aug. 2016, doi: 10.1088/0957-4484/27/32/325403.

[105] W. S. Su, Y. F. Chen, C. L. Hsiao, and L. W. Tu, ‘Generation of electricity in GaN nanorods induced by piezoelectric effect’, *Appl. Phys. Lett.*, vol. 90, no. 6, p. 063110, Feb. 2007, doi: 10.1063/1.2472539.

[106] G. Jacopin *et al.*, ‘Interplay of the photovoltaic and photoconductive operation modes in visible-blind photodetectors based on axial p-i-n junction GaN nanowires’, *Appl. Phys. Lett.*, vol. 104, no. 2, p. 023116, Jan. 2014, doi: 10.1063/1.4860968.

[107] N. Jamond *et al.*, ‘Piezo-generator integrating a vertical array of GaN nanowires’, *Nanotechnology*, vol. 27, no. 32, p. 325403, 2016.

[108] S. S. Lin, J. H. Song, Y. F. Lu, and Z. L. Wang, ‘Identifying individual n- and p-type ZnO nanowires by the output voltage sign of piezoelectric nanogenerator’, *Nanotechnology*, vol. 20, no. 36, p. 365703, Sep. 2009, doi: 10.1088/0957-4484/20/36/365703.

[109] Z. L. Wang, ‘The new field of nanopiezotronics’, *Materials Today*, vol. 10, no. 5, pp. 20–28, May 2007, doi: 10.1016/S1369-7021(07)70076-7.

[110] Z. L. Wang, X. Y. Kong, and J. M. Zuo, ‘Induced Growth of Asymmetric Nanocantilever Arrays on Polar Surfaces’, *Phys. Rev. Lett.*, vol. 91, no. 18, p. 185502, Oct. 2003, doi: 10.1103/PhysRevLett.91.185502.

[111] Y. S. Zhou *et al.*, ‘Nano-Newton Transverse Force Sensor Using a Vertical GaN Nanowire based on the Piezotronic Effect’, *Adv. Mater.*, vol. 25, no. 6, pp. 883–888, Feb. 2013, doi: 10.1002/adma.201203263.

[112] W. I. Park, G.-C. Yi, J.-W. Kim, and S.-M. Park, ‘Schottky nanocontacts on ZnO nanorod arrays’, *Appl. Phys. Lett.*, vol. 82, no. 24, pp. 4358–4360, Jun. 2003, doi: 10.1063/1.1584089.

[113] K. L. Johnson, *Contact Mechanics*, 1st ed. Cambridge University Press, 1985. doi: 10.1017/CBO9781139171731.

[114] B. S. Simpkins, M. A. Mastro, C. R. Eddy, and P. E. Pehrsson, ‘Surface depletion effects in semiconducting nanowires’, *Journal of Applied Physics*, vol. 103, no. 10, p. 104313, May 2008, doi: 10.1063/1.2932072.

[115] R. Calarco, T. Stoica, O. Brandt, and L. Geelhaar, ‘Surface-induced effects in GaN nanowires’, *J. Mater. Res.*, vol. 26, no. 17, pp. 2157–2168, Sep. 2011, doi: 10.1557/jmr.2011.211.

[116] P. Tchoulfian, F. Donatini, F. Levy, A. Dussaigne, P. Ferret, and J. Pernot, ‘Direct Imaging of p–n Junction in Core–Shell GaN Wires’, *Nano Lett.*, vol. 14, no. 6, pp. 3491–3498, Jun. 2014, doi: 10.1021/nl5010493.

[117] G. D. J. Smit, S. Rogge, and T. M. Klapwijk, ‘Enhanced tunneling across nanometer-scale metal–semiconductor interfaces’, *Appl. Phys. Lett.*, vol. 80, no. 14, pp. 2568–2570, Apr. 2002, doi: 10.1063/1.1467980.

[118] G. D. J. Smit, S. Rogge, and T. M. Klapwijk, ‘Scaling of nano-Schottky-diodes’, *Appl. Phys. Lett.*, vol. 81, no. 20, pp. 3852–3854, Nov. 2002, doi: 10.1063/1.1521251.

[119] X. Wang, R. Yu, W. Peng, W. Wu, S. Li, and Z. L. Wang, ‘Temperature Dependence of the Piezotronic and Piezophototronic Effects in *a* -axis GaN Nanobelts’, *Adv. Mater.*, vol. 27, no. 48, pp. 8067–8074, Dec. 2015, doi: 10.1002/adma.201504534.

[120] X. Wang *et al.*, ‘Piezotronic Effect Modulated Heterojunction Electron Gas in AlGaN/AlN/GaN Heterostructure Microwire’, *Adv. Mater.*, vol. 28, no. 33, pp. 7234–7242, Sep. 2016, doi: 10.1002/adma.201601721.

[121] R. Yu *et al.*, ‘Piezotronic Effect on the Transport Properties of GaN Nanobelts for Active Flexible Electronics’, *Adv. Mater.*, vol. 24, no. 26, pp. 3532–3537, Jul. 2012, doi: 10.1002/adma.201201020.

[122] R. Yu *et al.*, ‘Enhanced performance of GaN nanobelt-based photodetectors by means of piezotronic effects’, *Nano Res.*, vol. 6, no. 10, pp. 758–766, Oct. 2013, doi: 10.1007/s12274-013-0354-2.

[123] P. Keil, T. Frömling, A. Klein, J. Rödel, and N. Novak, ‘Piezotronic effect at Schottky barrier of a metal-ZnO single crystal interface’, *Journal of Applied Physics*, vol. 121, no. 15, p. 155701, Apr. 2017, doi: 10.1063/1.4981243.

[124] S. K. Cheung and N. W. Cheung, ‘Extraction of Schottky diode parameters from forward current-voltage characteristics’, *Appl. Phys. Lett.*, vol. 49, no. 2, pp. 85–87, Jul. 1986, doi: 10.1063/1.97359.

[125] ‘Frontmatter’, in *Semiconductor Material and Device Characterization*, Hoboken, NJ, USA: John Wiley & Sons, Inc., 2005, pp. i–xv. doi: 10.1002/0471749095.fmatter.

[126] Y.-F. Lin, J. Song, Y. Ding, S.-Y. Lu, and Z. L. Wang, ‘Piezoelectric nanogenerator using CdS nanowires’, *Appl. Phys. Lett.*, vol. 92, no. 2, p. 022105, Jan. 2008, doi: 10.1063/1.2831901.

[127] C.-Y. Chen *et al.*, 'Electricity generation based on vertically aligned PbZr0.2Ti0.8O3 nanowire arrays', *Nano Energy*, vol. 1, no. 3, pp. 424–428, May 2012, doi: 10.1016/j.nanoen.2012.01.003.

[128] M.-G. Kang *et al.*, 'Enhanced piezoelectric properties of vertically aligned single-crystalline NKN nano-rod arrays', *Sci Rep*, vol. 5, no. 1, p. 10151, Sep. 2015, doi: 10.1038/srep10151.

[129] C.-T. Huang *et al.*, 'GaN Nanowire Arrays for High-Output Nanogenerators', *J. Am. Chem. Soc.*, vol. 132, no. 13, pp. 4766–4771, Apr. 2010, doi: 10.1021/ja909863a.

[130] C.-Y. Chen *et al.*, 'Gallium Nitride Nanowire Based Nanogenerators and Light-Emitting Diodes', *ACS Nano*, vol. 6, no. 6, pp. 5687–5692, Jun. 2012, doi: 10.1021/nn301814w.

[131] C.-T. Huang *et al.*, 'Single-InN-Nanowire Nanogenerator with Upto 1 V Output Voltage', *Adv. Mater.*, vol. 22, no. 36, pp. 4008–4013, Sep. 2010, doi: 10.1002/adma.201000981.

[132] N. Jegenyes *et al.*, 'High piezoelectric conversion properties of axial InGaN/GaN nanowires', *Nanomaterials*, vol. 8, no. 6, p. 367, 2018.

[133] X. Wang, J. Song, F. Zhang, C. He, Z. Hu, and Z. Wang, 'Electricity Generation based on One-Dimensional Group-III Nitride Nanomaterials', *Adv. Mater.*, vol. 22, no. 19, pp. 2155–2158, Mar. 2010, doi: 10.1002/adma.200903442.

[134] C. Chang, V. H. Tran, J. Wang, Y.-K. Fuh, and L. Lin, 'Direct-Write Piezoelectric Polymeric Nanogenerator with High Energy Conversion Efficiency', *Nano Lett.*, vol. 10, no. 2, pp. 726–731, Feb. 2010, doi: 10.1021/nl9040719.

[135] B. Moorthy *et al.*, 'Piezoelectric energy harvesting from a PMN–PT single nanowire', *RSC Adv.*, vol. 7, no. 1, pp. 260–265, 2017, doi: 10.1039/C6RA24688E.

[136] J. M. Wu, C. Xu, Y. Zhang, and Z. L. Wang, 'Lead-Free Nanogenerator Made from Single ZnSnO$_3$ Microbelt', *ACS Nano*, vol. 6, no. 5, pp. 4335–4340, May 2012, doi: 10.1021/nn300951d.

[137] T.-C. Hou *et al.*, 'Nanogenerator based on zinc blende CdTe micro/nanowires', *Nano Energy*, vol. 2, no. 3, pp. 387–393, May 2013, doi: 10.1016/j.nanoen.2012.11.004.

[138] P. X. Gao, J. Song, J. Liu, and Z. L. Wang, 'Nanowire Piezoelectric Nanogenerators on Plastic Substrates as Flexible Power Sources for Nanodevices', *Adv. Mater.*, vol. 19, no. 1, pp. 67–72, Jan. 2007, doi: 10.1002/adma.200601162.

[139] M.-P. Lu *et al.*, 'Piezoelectric Nanogenerator Using p-Type ZnO Nanowire Arrays', *Nano Lett.*, vol. 9, no. 3, pp. 1223–1227, Mar. 2009, doi: 10.1021/nl900115y.

[140] M. Riaz, J. Song, O. Nur, Z. L. Wang, and M. Willander, 'Study of the Piezoelectric Power Generation of ZnO Nanowire Arrays Grown by Different Methods', *Adv. Funct. Mater.*, vol. 21, no. 4, pp. 628–633, Feb. 2011, doi: 10.1002/adfm.201001203.

[141] D. J. Leo, *Engineering analysis of smart material systems*. Hoboken, N.J: John Wiley & Sons, 2007.

[142] M.-Y. Lu, J. Song, M.-P. Lu, C.-Y. Lee, L.-J. Chen, and Z. L. Wang, 'ZnO−ZnS Heterojunction and ZnS Nanowire Arrays for Electricity Generation', *ACS Nano*, vol. 3, no. 2, pp. 357–362, Feb. 2009, doi: 10.1021/nn800804r.

[143] P. A. Alekseev *et al.*, 'Piezoelectric Current Generation in Wurtzite GaAs Nanowires', *Phys. Status Solidi RRL*, vol. 12, no. 1, p. 1700358, Jan. 2018, doi: 10.1002/pssr.201700358.

[144] X. Wang, J. Song, J. Liu, and Z. L. Wang, 'Direct-Current Nanogenerator Driven by Ultrasonic Waves', *Science*, vol. 316, no. 5821, pp. 102–105, Apr. 2007, doi: 10.1126/science.1139366.

[145] S. Xu, Y. Wei, J. Liu, R. Yang, and Z. L. Wang, 'Integrated Multilayer Nanogenerator Fabricated Using Paired Nanotip-to-Nanowire Brushes', *Nano Lett.*, vol. 8, no. 11, pp. 4027–4032, Nov. 2008, doi: 10.1021/nl8027813.

[146] Y. Qin, X. Wang, and Z. L. Wang, 'Microfibre–nanowire hybrid structure for energy scavenging', *Nature*, vol. 451, no. 7180, pp. 809–813, Feb. 2008, doi: 10.1038/nature06601.

[147] S. Xu, Y. Qin, C. Xu, Y. Wei, R. Yang, and Z. L. Wang, 'Self-powered nanowire devices', *Nature Nanotech*, vol. 5, no. 5, pp. 366–373, May 2010, doi: 10.1038/nnano.2010.46.

[148] L. Serairi, L. Gu, Y. Qin, Y. Lu, P. Basset, and Y. Leprince-Wang, 'Flexible piezoelectric nanogenerators based on PVDF-TrFE nanofibers', *Eur. Phys. J. Appl. Phys.*, vol. 80, no. 3, p. 30901, Dec. 2017, doi: 10.1051/epjap/2017170288.

[149] X. Chen, S. Xu, N. Yao, and Y. Shi, '1.6 V Nanogenerator for Mechanical Energy Harvesting Using PZT Nanofibers', *Nano Lett.*, vol. 10, no. 6, pp. 2133–2137, Jun. 2010, doi: 10.1021/nl100812k.

[150] X. Chen *et al.*, 'A Stretchable and Transparent Nanocomposite Nanogenerator for Self-Powered Physiological Monitoring', *ACS Appl. Mater. Interfaces*, vol. 9, no. 48, pp. 42200–42209, Dec. 2017, doi: 10.1021/acsami.7b13767.

[151] G. Zhu, R. Yang, S. Wang, and Z. L. Wang, 'Flexible High-Output Nanogenerator Based on Lateral ZnO Nanowire Array', *Nano Lett.*, vol. 10, no. 8, pp. 3151–3155, Aug. 2010, doi: 10.1021/nl101973h.

[152] R. Tao *et al.*, 'Performance of ZnO based piezo-generators under controlled compression', *Semicond. Sci. Technol.*, vol. 32, no. 6, p. 064003, Jun. 2017, doi: 10.1088/1361-6641/aa691f.

[153] S. N. Cha *et al.*, 'Sound-Driven Piezoelectric Nanowire-Based Nanogenerators', *Adv. Mater.*, vol. 22, no. 42, pp. 4726–4730, Nov. 2010, doi: 10.1002/adma.201001169.

[154] C. Opoku *et al.*, 'Fabrication of ZnO Nanowire Based Piezoelectric Generators and Related Structures', *Physics Procedia*, vol. 70, pp. 858–862, 2015, doi: 10.1016/j.phpro.2015.08.176.

[155] R. Hinchet, S. Lee, G. Ardila, L. Montès, M. Mouis, and Z. L. Wang, ‘Performance Optimization of Vertical Nanowire-based Piezoelectric Nanogenerators’, *Adv. Funct. Mater.*, vol. 24, no. 7, pp. 971–977, Feb. 2014, doi: 10.1002/adfm.201302157.

[156] G. Zhu, A. C. Wang, Y. Liu, Y. Zhou, and Z. L. Wang, ‘Functional Electrical Stimulation by Nanogenerator with 58 V Output Voltage’, *Nano Lett.*, vol. 12, no. 6, pp. 3086–3090, Jun. 2012, doi: 10.1021/nl300972f.

[157] S.-H. Shin, Y.-H. Kim, M. H. Lee, J.-Y. Jung, J. H. Seol, and J. Nah, ‘Lithium-Doped Zinc Oxide Nanowires–Polymer Composite for High Performance Flexible Piezoelectric Nanogenerator’, *ACS Nano*, vol. 8, no. 10, pp. 10844–10850, Oct. 2014, doi: 10.1021/nn5046568.

[158] S. Stassi, V. Cauda, C. Ottone, A. Chiodoni, C. F. Pirri, and G. Canavese, ‘Flexible piezoelectric energy nanogenerator based on ZnO nanotubes hosted in a polycarbonate membrane’, *Nano Energy*, vol. 13, pp. 474–481, Apr. 2015, doi: 10.1016/j.nanoen.2015.03.024.

[159] Q. Liao, Z. Zhang, X. Zhang, M. Mohr, Y. Zhang, and H.-J. Fecht, ‘Flexible piezoelectric nanogenerators based on a fiber/ZnO nanowires/paper hybrid structure for energy harvesting’, *Nano Res.*, vol. 7, no. 6, pp. 917–928, Jun. 2014, doi: 10.1007/s12274-014-0453-8.

[160] S. Lee *et al.*, ‘Solution-processed Ag-doped ZnO nanowires grown on flexible polyester for nanogenerator applications’, *Nanoscale*, vol. 5, no. 20, p. 9609, 2013, doi: 10.1039/c3nr03402j.

[161] A. S. Dahiya *et al.*, ‘Zinc oxide nanowire-parylene nanocomposite based stretchable piezoelectric nanogenerators for self-powered wearable electronics’, *J. Phys.: Conf. Ser.*, vol. 1052, p. 012028, Jul. 2018, doi: 10.1088/1742-6596/1052/1/012028.

[162] L. Zhou, ‘Piezoelectric nanogenerators with high performance against harsh conditions based on tunable N doped 4H-SiC nanowire arrays’, *Nano Energy*, p. 10, 2021.

[163] A. S. Dahiya, F. Morini, S. Boubenia, K. Nadaud, D. Alquier, and G. Poulin-Vittrant, ‘Organic/Inorganic Hybrid Stretchable Piezoelectric Nanogenerators for Self-Powered Wearable Electronics’, *Advanced Materials Technologies*, vol. 3, no. 2, p. 1700249, 2018, doi: 10.1002/admt.201700249.

[164] S. Cha *et al.*, ‘Porous PVDF As Effective Sonic Wave Driven Nanogenerators’, *Nano Lett.*, vol. 11, no. 12, pp. 5142–5147, Dec. 2011, doi: 10.1021/nl202208n.

[165] Z. L. Wang *et al.*, ‘Lateral nanowire/nanobelt based nanogenerators, piezotronics and piezo-phototronics’, *Materials Science and Engineering: R: Reports*, vol. 70, no. 3–6, pp. 320–329, Nov. 2010, doi: 10.1016/j.mser.2010.06.015.

[166] Z. Chen *et al.*, ‘Flexible Piezoelectric-Induced Pressure Sensors for Static Measurements Based on Nanowires/Graphene Heterostructures’, *ACS Nano*, vol. 11, no. 5, pp. 4507–4513, May 2017, doi: 10.1021/acsnano.6b08027.

[167] A. Waseem *et al.*, ‘Enhanced performance of a flexible and wearable piezoelectric nanogenerator using semi-insulating GaN:Mg/ZnO coaxial nanowires’, *Nano Energy*, vol. 90, p. 106552, Dec. 2021, doi: 10.1016/j.nanoen.2021.106552.

[168] L. Lu *et al.*, ‘Nitride Nanowires: From Rigid to Flexible Piezo-generators’, *J. Phys.: Conf. Ser.*, vol. 773, p. 012010, Nov. 2016, doi: 10.1088/1742-6596/773/1/012010.

[169] Y. Hu, L. Lin, Y. Zhang, and Z. L. Wang, ‘Replacing a Battery by a Nanogenerator with 20 V Output’, *Adv. Mater.*, vol. 24, no. 1, pp. 110–114, Jan. 2012, doi: 10.1002/adma.201103727.

[170] A. T. Le, M. Ahmadipour, and S.-Y. Pung, ‘A review on ZnO-based piezoelectric nanogenerators: Synthesis, characterization techniques, performance enhancement and applications’, *Journal of Alloys and Compounds*, vol. 844, p. 156172, Dec. 2020, doi: 10.1016/j.jallcom.2020.156172.

[171] Z. Li, Q. Zheng, Z. L. Wang, and Z. Li, ‘Nanogenerator-Based Self-Powered Sensors for Wearable and Implantable Electronics’, *Research*, vol. 2020, pp. 1–25, Mar. 2020, doi: 10.34133/2020/8710686.

[172] A. Waseem *et al.*, ‘GaN/Al2O3 core-shell nanowire based flexible and stable piezoelectric energy harvester’, *Journal of Alloys and Compounds*, vol. 860, p. 158545, Apr. 2021, doi: 10.1016/j.jallcom.2020.158545.

[173] S. K. Ghosh and D. Mandal, ‘Efficient natural piezoelectric nanogenerator: Electricity generation from fish swim bladder’, *Nano Energy*, vol. 28, pp. 356–365, Oct. 2016, doi: 10.1016/j.nanoen.2016.08.030.

[174] V. Vivekananthan, N. R. Alluri, Y. Purusothaman, A. Chandrasekhar, S. Selvarajan, and S.-J. Kim, ‘Biocompatible Collagen Nanofibrils: An Approach for Sustainable Energy Harvesting and Battery-Free Humidity Sensor Applications’, *ACS Appl. Mater. Interfaces*, vol. 10, no. 22, pp. 18650–18656, Jun. 2018, doi: 10.1021/acsami.8b02915.

[175] S. Ye *et al.*, ‘High-performance piezoelectric nanogenerator based on microstructured P(VDF-TrFE)/BNNTs composite for energy harvesting and radiation protection in space’, *Nano Energy*, vol. 60, pp. 701–714, Jun. 2019, doi: 10.1016/j.nanoen.2019.03.096.

[176] L. Lin *et al.*, ‘High output nanogenerator based on assembly of GaN nanowires’, *Nanotechnology*, vol. 22, no. 47, p. 475401, Nov. 2011, doi: 10.1088/0957-4484/22/47/475401.

[177] G. Liu *et al.*, 'Nanogenerators based on vertically aligned InN nanowires', *Nanoscale*, vol. 8, no. 4, pp. 2097–2106, 2016, doi: 10.1039/C5NR06841J.

[178] L. Lu, 'Nanofils piézoélectriques de nitrure pour la récupération d'énergie et la détection de pression', These de doctorat, Université Paris-Saclay (ComUE), 2018. Accessed: Oct. 13, 2021. [Online]. Available: http://www.theses.fr/2018SACLS436

[179] M. A. Johar *et al.*, 'Facile growth of high aspect ratio c-axis GaN nanowires and their application as flexible p-n NiO/GaN piezoelectric nanogenerators', *Acta Materialia*, vol. 161, pp. 237–245, Dec. 2018, doi: 10.1016/j.actamat.2018.09.030.

[180] M. A. Johar *et al.*, 'Highly Durable Piezoelectric Nanogenerator by Heteroepitaxy of GaN Nanowires on Cu Foil for Enhanced Output Using Ambient Actuation Sources', *Adv. Energy Mater.*, vol. 10, no. 47, p. 2002608, Dec. 2020, doi: 10.1002/aenm.202002608.

[181] A. Waseem *et al.*, 'Effect of crystal orientation of GaN/V2O5 core-shell nanowires on piezoelectric nanogenerators', *Nano Energy*, vol. 60, pp. 413–423, Jun. 2019, doi: 10.1016/j.nanoen.2019.03.075.

[182] J. H. Jung *et al.*, 'Lead-free KNbO $_3$ ferroelectric nanorod based flexible nanogenerators and capacitors', *Nanotechnology*, vol. 23, no. 37, p. 375401, Sep. 2012, doi: 10.1088/0957-4484/23/37/375401.

[183] B. K. Yun *et al.*, 'Lead-free LiNbO3 nanowire-based nanocomposite for piezoelectric power generation', *Nanoscale Res Lett*, vol. 9, no. 1, p. 4, Dec. 2014, doi: 10.1186/1556-276X-9-4.

[184] S. Xu, Y. Yeh, G. Poirier, M. C. McAlpine, R. A. Register, and N. Yao, 'Flexible Piezoelectric PMN–PT Nanowire-Based Nanocomposite and Device', *Nano Lett.*, vol. 13, no. 6, pp. 2393–2398, Jun. 2013, doi: 10.1021/nl400169t.

[185] Y. Hu, Y. Zhang, C. Xu, L. Lin, R. L. Snyder, and Z. L. Wang, 'Self-Powered System with Wireless Data Transmission', *Nano Lett.*, vol. 11, no. 6, pp. 2572–2577, Jun. 2011, doi: 10.1021/nl201505c.

Chapter 2

Growth of GaN nanowires via plasma-assisted molecular beam epitaxy and characterisation techniques

Contents

This chapter is dedicated to the techniques used during my PhD project in order to synthesize and characterize the GaN NWs. The molecular beam epitaxy technique is introduced with a brief description of the growth kinetics and the various epitaxial growth modes. The Compact12 plasma assisted MBE (PA-MBE) machine used at C2N is detailed. The scanning electron microscope (SEM) is the first characterization technique described. This technique has served as the 'go-to' technology for morphological characterisation of our NWs. Further in this characterization section, we detail the atomic force microscopy technique which is the primary characterisation method used in this thesis for the study of the piezoelectric properties of GaN NWs. Finally, we present the growth mechanism of the self-assembled GaN NWs using PA-MBE. A novel way to control the NW density, as well as the influence of dopants on the NW morphology are presented.

2.1. Molecular beam epitaxy (MBE)

The term *'epitaxy'* comes from Greek where *epi* means 'above' and *taxis* means 'an ordered manner'. Thus epitaxy is defined as the deposition of a crystalline overlayer that has a well-defined orientation with respect to the substrate crystal.

Depending on the different ways of delivering the constituents of the growth towards the substrate, the epitaxial techniques can be roughly categorised into three groups: Liquid-phase epitaxy (LPE) refers to the epitaxial mode in which the contituents are deposited on the substrate from a liquid phase (a solution or a melt); Vapor-phase epitaxy (VPE) involves the delivery of the precursors as vapour to the substrate; and finally, Molecular beam epitaxy (MBE) has a ballistic projection of the atoms/molecules of the participating species towards the substrate in an ultra-high vacuum (UHV) environment.

MBE technique was first employed at Plessey labs by Bruce Joyce and coworkers in the year 1960 to grow monocrystalline thin films of Si using molecular beams of silane on a heated Si substrate [1]. A high crystallinity of the grown sample was observed as a result of the collision-free deposition of the species on the substrate under UHV conditions. This demonstration led to the advancement of the MBE technology over the years with its extension to other classes of compounds such as III-V, II-VI and III-nitride materials.

MBE systems are often equipped with in-situ characterisation tools. The reflective high energy electron diffraction (RHEED), allowing a real-time monitoring of the surface reconstruction and growth modes at an atomic level, is the most widespread.

An MBE system offers several advantages:

- Ultra-High Vacuum (UHV) conditions, necessary to avoid beam scattering and to reduce impurity incorporation. These conditions allow the grower to use in situ characterization techniques, such as RHEED, X-ray photoemission spectroscopy, mass spectrometry…
- Relatively low substrate temperatures which prohibit the interdiffusion of species and other thermally activated processes, especially while growing nanostructures with different compositions.

- Fairly low growth rates (0.2 – 1 ML/sec) ensures surface smoothness via migration of species and a thickness control with sub-monolyer precision.

Thus, MBE presents itself as a highly sophisticated, well-controlled growth technique for synthesising materials (particularly group III-V semiconductor compounds) with very high crystalline quality and high purity.

2.1.1. Growth kinetics

In an MBE system, elements of high purity are heated up in the Knudsen cells above their fusion temperatures to evaporate the materials, which are then directed towards the heated substrate. Thanks to the UHV environment, a collision-free arrival of the atoms on the substrate is ensured. Atoms arriving at the substrate surface may undergo **adsorption** to the surface, **surface diffusion**, **incorporation** into the crystal lattice, decomposition and **thermal desorption** processes, as schematized in Fig. 1.

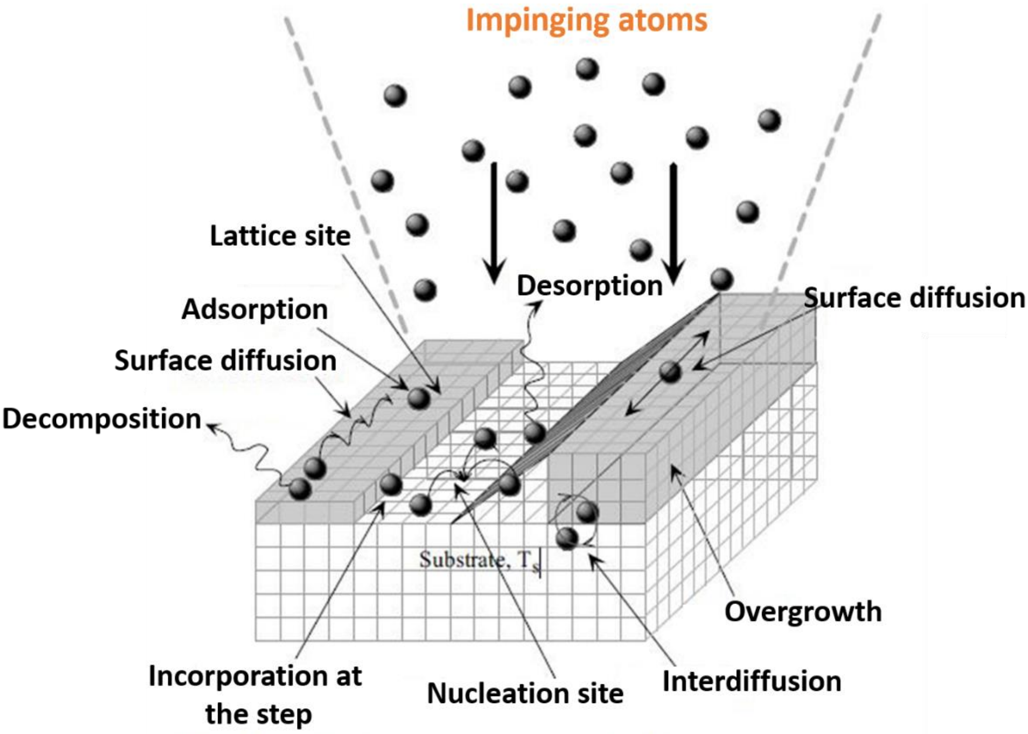

Figure 1. (Image take from [2]). Surface processes during the MBE growth.

In MBE, the growth is principally governed by the surface kinetics. The competing pathways dominating the growth depend on the substrate characteristics (presence of dangling bonds, kinks, steps..), impinging flux rate and strongly on the temperature of the substrate. For instance, at low temperatures, atoms stick where they land without arranging properly, leading to a poor crystal quality. By contrast, at high temperatures, atoms will desorb fastely from the surface, leading to low growth rates along with a poor crystal quality. It is only for an appropriate intermediate temperature range (depending on the material under growth and the impinging atom flux) that the atoms will have sufficient energy to diffuse and be incorporated, resulting in the growth of a high crystalline film/heterostructures.

2.1.2. Epitaxial Growth modes

In homo-epitaxy, an overlayer is grown on a substrate of the same material. By contrast, in hetero-epitaxy, the substrate and the deposited material are different. In the latter case, lattice mismatching often exists between the crystal and the host substrate. Depending on the lattice parameters of the two materials and the interfacial surface energy, the hetero-epitaxial growths could follow one of the following growth models (Fig. 2):

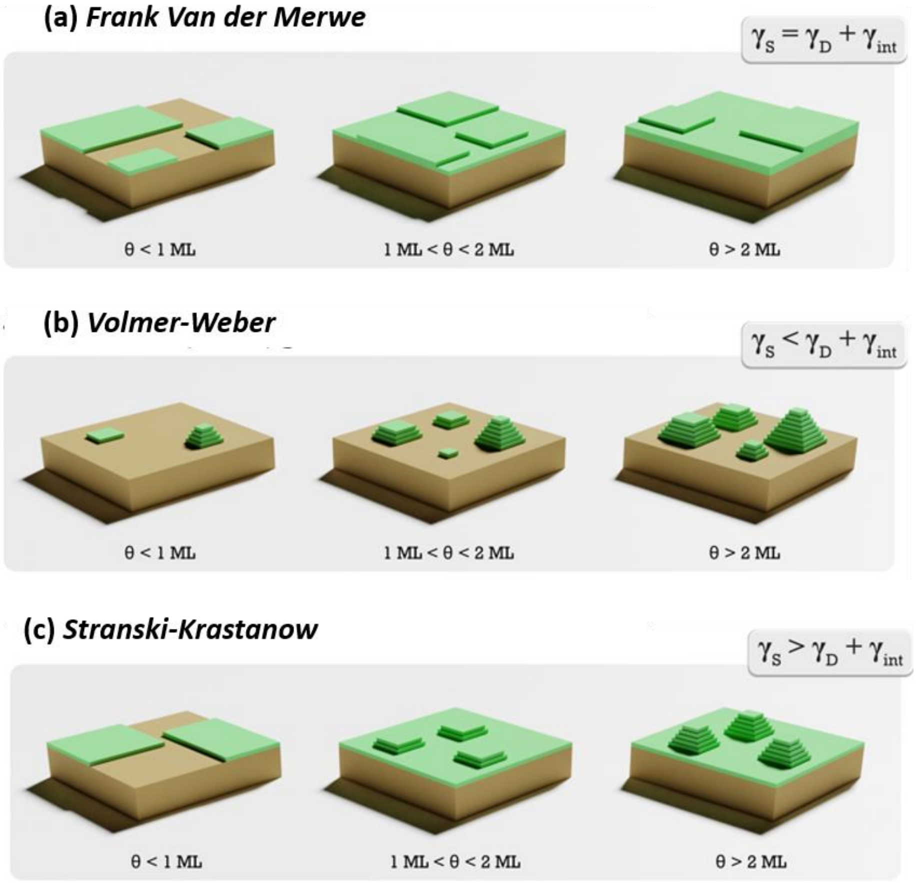

Figure 2. Schematic illustration of the three hetero-epitaxial growth modes: (a) the Frank- Van der Merwe growth mode, (b) the Volmer-Weber growth mode and (c) the Stranski-Krastanov growth mode.

a) Frank Van der Merwe growth mode

The Frank Van der Merwe growth mode [3], also known as the layer by layer growth mode (Fig. 2a), is a 2D growth process. This growth mechanism takes place in systems with small lattice mismatch or small surface energy. High crystalline quality epitaxial layers can be obtained via the nucleation of 2D islands or on substrates having atomic steps (vicinal surfaces), where the impinging atomic flux gets incorporated. These sites are energetically favourable and a lateral expansion of the surface (step-flow growth) takes place. The layer-by-layer growth is favoured if the substrate's surface energy (γ_S) is equal to the sum of the epitaxial layers (γ_D) and the interfacial energy (γ_{int}) [2]. The 2D growth continues until a critical thickness of the layers ($\theta_{\textbf{critical}}$) is reached and then the strain energy is released through plastic relaxation via the formation of dislocations.

b) Volmer-Weber growth mode

The Volmer-Weber growth mode [4] occurs typically for highly mismatched systems [5]. 3D island formation takes place by the nucleation of *'islands'* directly on the surface of the substrate without the formation of any 2D-layer (Fig. 2b) [6]. This type of growth is mostly encountered while depositing metals on insulating substrates. In this growth mode, the substrate's surface energy (γ_S) is lower than the sum of the epitaxial layers (γ_D) and the interfacial energy (γ_{int}).

c) Stranski-Krastanow growth mode

The Stranski-Krastanow growth mode [7] is an intermediary growth mode. At the beginning, the growth follows the Frank Van der Merwe growth mechanism with the formation of few monolayers thick 2D-layer. This layer, also termed as the wetting layer, presents a lattice parameter equivalent to the one of the underlaying substate or layer. As this layer grows, the underlying strain also increases. At the critical value of the layer thickness ($\theta_{\mathbf{critical}}$), the formation of 3D islands takes place in order to release the in-built strain. Here, the substrate's surface energy (γ_S) is higher than the sum of the epitaxial layers (γ_D) and the interfacial energy (γ_{int}). Fig. 2c represents the schematic diagram showing the growth mechanism. In this heteroepitaxial growth mode, the critical thickness ($\theta_{\mathbf{critical}}$) defines the limit between the 2D growth and the onset of the 3D morphology [5].

Fig. 3 gives an account of the dependence of $\theta_{\mathbf{critical}}$ on the lattice mismatch of the system for each growth mode. As the lattice mismatch increases, the critical thickness decreases.

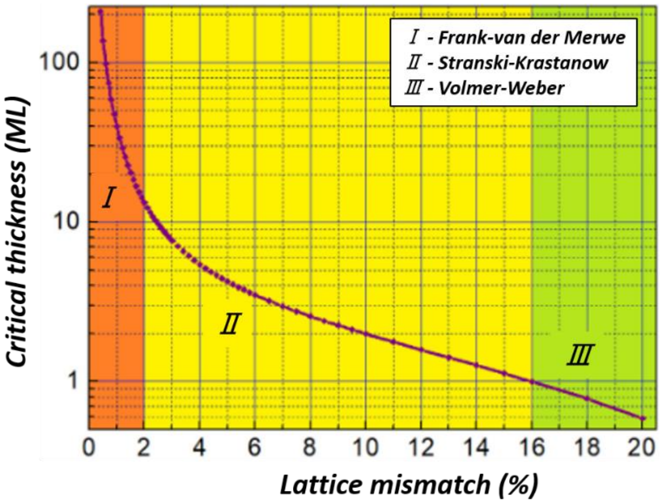

Figure 3. (Image taken from [5]). Critical thickness as a function of lattice mismatch.

2.1.3. Compact-12 plasma-assisted MBE (PA-MBE) at C2N

In this thesis, a Riber *Compact-12* (C12) MBE system assisted with a nitrogen-plasma cell has been used for the growth of GaN nanowires on Si (111) substrate. An UHV of the order of 10^{-11} Torr is achieved using a cryogenic pump. The machine C12 is entirely dedicated to the growth of III-nitride materials. It is equipped with 5 Knudsen effusion cells, oriented towards the substrate with an angle of 35° in order to maximise the fluxes reaching the substrate. Our system has Ga, Al and In as the three principal element sources, and Si for an n-type doping and Mg for a p-type doping constitute the two dopant-elements. By adjusting the cell temperatures, the flux of the elements can be controlled. The flux of the group–III elements is measured using a retractable gauge, which is placed directly below the substrate.

The active nitrogen species are supplied by a plasma cell. This nitrogen source excites and dissociates the gaseous N_2 injected in the PBN (Boron nitride) cavity with a 13.56 MHz radio frequency (RF) electromagnetic wave. The flux of the active nitrogen species (monoatomic nitrogen) can be varied by changing the flux of the injected gaseous N_2 using the mass-flow meter and the RF pulse power. However, it is not possible to measure the flux of the monoatomic nitrogen with the help of the gauge like the group-III elements. It is primarily because of the very high chamber pressure (of the order of 10^{-6} to 10^{-5} Torr) when the plasma cell is working. And secondly because of the very low flux of the monoatomic nitrogen species, as less than 1 % of the diatomic nitrogen is dissociated. An alternative way to measure the nitrogen flux consists in calibrating the growth rate of 2D-GaN layer, using the RHEED oscillations (*cf.* section 2.1.3 (b) of this chapter).

The growth is performed on Si (111) substrate. The substrate is mounted facing downwards on a molybdenum holder called the 'molyblock' in the direction of the effusion cells. For the growth of III-N NWs, our MBE system is equipped with a high temperature substrate heater, which can be maintained at 850 °C for several hours in continuity and can sustain flash temperatures of about 1000 °C. A thermocouple and an optical pyrometer are used to monitor the substrate temperature. To increase the homogeneity of the material deposition, the substrate is set to rotation during the growth.

Finally, our MBE system is equipped with an *in-situ* RHEED characterisation technique allowing us to monitor the growth process in real-time. Fig. 4 presents our MBE machine.

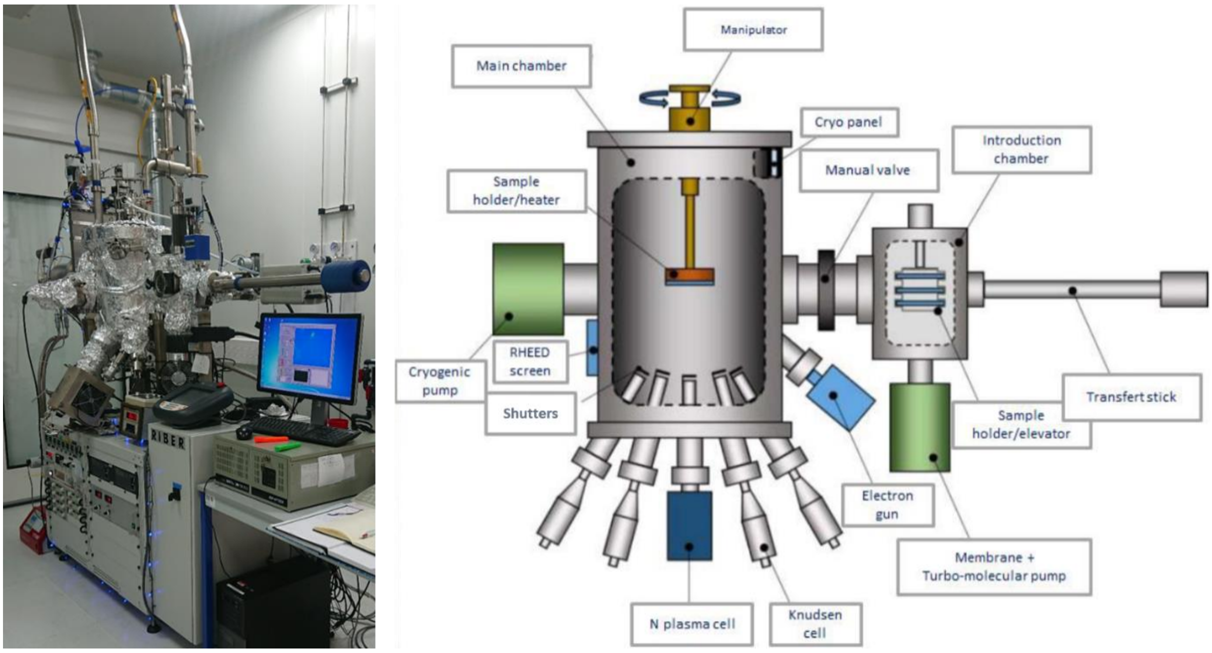

Figure 4. (Left) RIBER C12 PA-MBE machine at C2N; (Right) a schematic representation of the epitaxy machine with the introduction chamber and the growth chamber.

The impinging atomic flux as well as the substrate temperature are two important parameters that govern the epitaxial growths. To ensure a run-to-run reproducibility of the growths, calibration of atomic flux and substrate temperature were performed before each growth.

a) Temperature calibrations via (7×7) reconstruction of the Si (111)

As described earlier, the different physical processes (diffusion, adsorption, decomposition, desorption…) occurring at the surface of the substrate during the growth are temperature dependent. In our case, substrate temperature highly influences the nucleation process and the NWs morphology. Hence, a good control of the substrate temperature is a prerequisite which can be monitored either using a thermocouple or an optical pyrometer.

In our MBE system, the thermocouple is placed very far from the substrate and thus the temperature measurements are not effective. To overcome this problem, we rely on the indirect temperature measurements performed by the optical pyrometer, which collects the infrared radiations emitted by the substrate. In C12 MBE system, the pyrometer is oriented perpendicularly towards the surface to maximise the radiation detection. However, this method is very sensitive to the transparency of the pyrometer window through which the thermal radiations are detected. A progressive coating of the pyrometer window occurs over time and the temperature measurements become less accurate. Therefore, a systematic correction of the temperatures recorded via the pyrometer is required before every growth process. To achieve this correction, we take advantage of the (7x7) reconstruction of the Si (111) substrate used to synthesis the NWs.

A temperature-dependent phenomenon: the (7 × 7) surface reconstruction of Si (111) is known to disappear at temperatures equal and above 830 °C [8] and serves as a *marker* for pyrometer calibrations. This temperature is very close to the ones used for the growth of GaN NWs in this thesis (790 – 810 °C), which makes this calibration method very reliable over a longer time period.

For the purpose of temperature calibration, the sample is first degassed at 850 °C for 15 minutes in order to remove the remaining traces of oxide from the surface. Then, the temperature is decreased to 810-820 °C by adjusting the substrate heating power to see the appearance of the (7 × 7) reconstruction (Fig. 5a). This atomic rearrangement occurs in order to minimise the surface energy [9] and has a 7 times higher periodicity than the volume of the crystal. Fig. 6 shows the atomic arrangements of the reconstructed (7 × 7) unit cell.

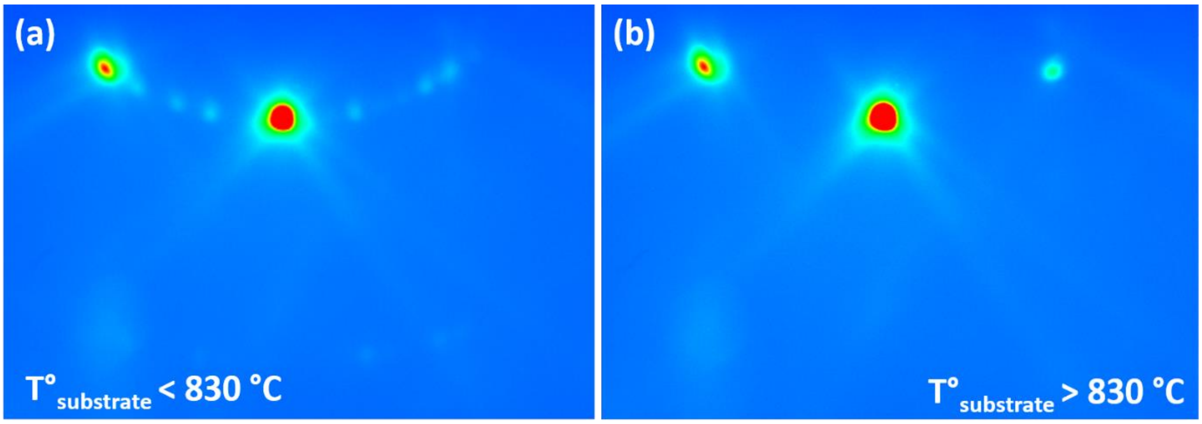

Figure 5. (a) (7×7) Si (111) reconstruction at temperatures below 830 °C; and (b) (1×1) Si (111) surface symmetry for a surface temperature equal to or above 830 °C.

The substrate power is then increased in small steps until the (7 × 7) reconstruction disappears completely due to increased thermal agitation. The surface temperature at which only the (1× 1) Si (111) surface symmetry (Fig. 5b) is visible corresponds to 830°C. The drift in the temperature read by the pyrometer is then corrected with respect to this temperature and the growth temperature is adjusted by the calculated ΔT_{pyro}.

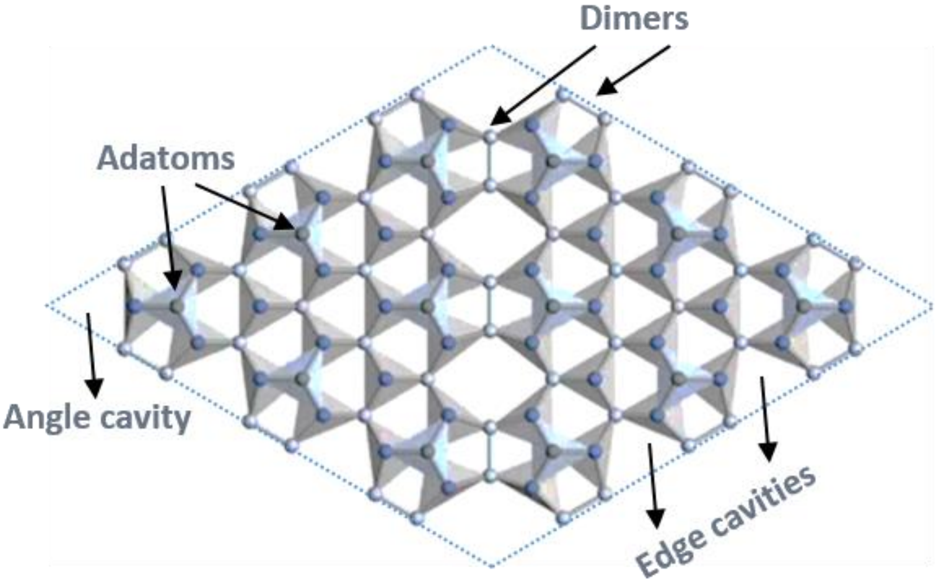

Figure 6. Atomic arrangement of the (7×7) unit cell after surface reconstruction.

b) Growth rate and flux calibrations: RHEED oscillations

As previously discussed, the flux of active nitrogen species cannot be measured by the gauge flux. This flux is therefore indirectly quantified through the calibration of the GaN growth rate performed by growing a 2D layer of GaN on a GaN template (4 µm thick GaN layer grown by MOVPE on a sapphire substrate) at a temperature of 730°C, where the decomposition/desorption processes are quasi in-effective. This homo-epitaxial growth occurs layer-by-layer, and thus, the intensity variation of the specular RHEED spot is directly related to the growth of subsequent monolayers (Fig. 7a).

In the beginning, when the surface is formed by a complete monolayer, the surface roughness is negligible and the spectral spot intensity is maximum. When a new layer is under construction, the roughness of the surface starts to increase, which induces a decrease of the RHEED spot intensity. When the surface is half completed (θ = 0.5 ML) the surface roughness is at its maximum and consequently, the RHEED spot intensity is at its minimum. This is due to the formation of large number of 3D islands resulting in a higher scattering of the impinging electrons. With the completion of one monolayer (θ = 1 ML), the roughness reaches its minimum, leading to the maximum specular intensity due to the increased reflectance of the electrons. One complete RHEED oscillation corresponds to the growth of one monolayer. Hence the growth rate *'V'* can be measured in-situ by counting the number of oscillations (n) as a function of time '*t*' using the following relationship:

$$V = \frac{n}{t_n}$$

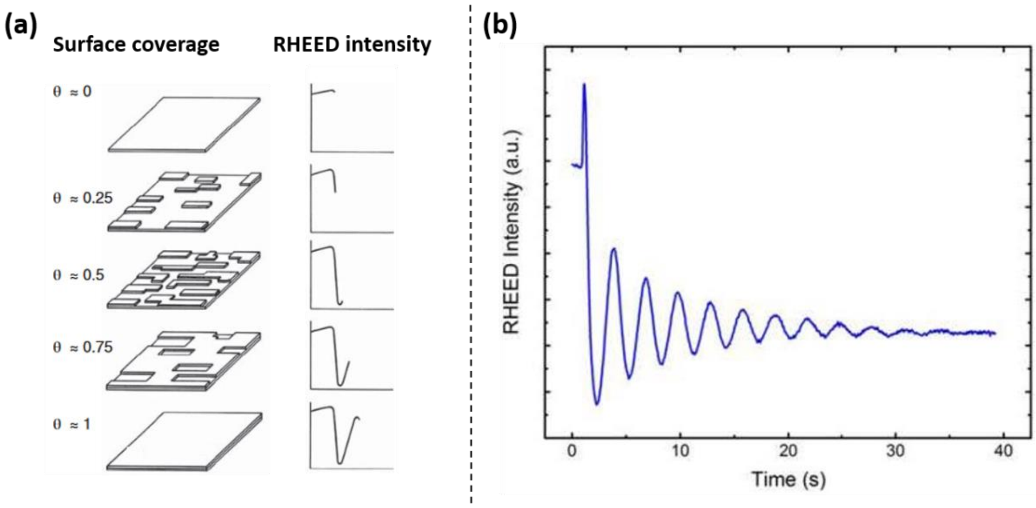

Figure 7. (Images taken from [10], [11]). (a) RHEED intensity variation as a function of the surface roughness; and (b) The growth rate is calculated from the number of RHEED oscillations per unit time.

To quantify the flux of the active monoatomic N species, the 2D growth of GaN is performed at fixed plasma cell conditions (N_2 flux and power supply), while varying the Ga flux (controlled via the cell temperature). As schematised in Fig. 8, under N-rich conditions (V/III flux ratio > 1), the growth rate is limited by the Ga elements. The growth rate thus increases with the increase of the Ga cell temperature, until the stoichiometric conditions are achieved. Here, the flux of Ga is equal to the flux of N (V/III = 1). Further increase in the Ga flux results in Ga-rich conditions (V/III < 1). Here, the growth rate is limited by the N-elements and saturates, since the flux of nitrogen remains unchanged. Therefore, for the given plasma conditions (nitrogen gas flow rate in sccm, RF power), the nitrogen flux is equal to that of Ga at the stoichiometric condition.

In this thesis, a V/III flux ratio of 1.36 (N-rich condition) and growth rates of 0.7 ML/sec as well as 0.48 ML/sec have been used for the growth of GaN NWs.

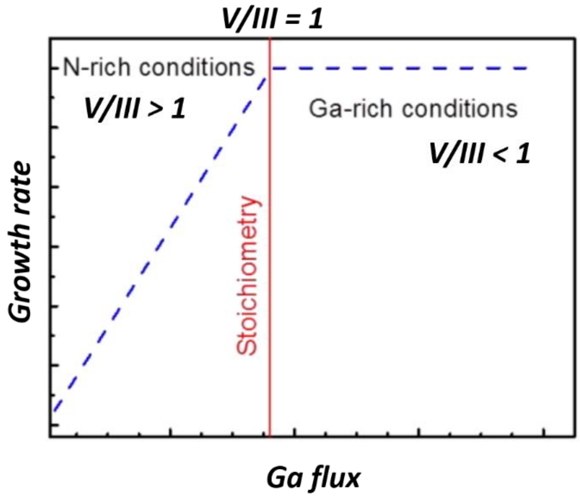

Figure 8. Evolution of growth rate as a function of the Ga flux. The red line defines the stoichiometric condition, which marks the transition from N-rich regime to Ga-rich regime.

2.2. Characterisation techniques

In this section, I present the two most frequently used characterisation tools/techniques during my thesis.

2.2.1. Scanning electron microscope (SEM)

The NW morphology strongly depends on the growth conditions. But it can also be influenced by the evolution of the growth conditions in time. In order to control their morphology, a systematic characterisation was done using a high-resolution scanning electron microscope (SEM) after each growth. This technique provides information about the NWs characteristics (density, height, diameter, general surface morphology), which also helps the MBE user to adjust the growth diagram (explained in section 2.3.1) accordingly, to assure the reproducibility of NW morphology.

Scanning electron microscope (SEM) is one of the most versatile instrument for material characterisation at a research level as well as in the industry. The history of SEM dates back to the 1930’s when Max Knoll first established the physical laws explaining the basic principles of SEM [12]. In 1940, Von Ardenne proposed the first model describing the electron scattering inside a material [13]. In 1965, the investigations of Sir Charles Oatley and his Ph.D. students at Cambridge led to the development of commercial models of SEM [14], [15]. Primarily developed to surpass the limitations of an optical microscope (resolution limit of about 2000 Å), today, SEM is the go-to technique to analyse the material’s topography, morphology, crystallographic orientation as well as its chemical composition. It is the fastest technique to obtain high quality images with great precision and a sub-nanometer resolution.

a) Configuration of a SEM

SEM consists of a microscope column kept under UHV conditions (10^{-10} to 10^{-11} Torr) and a specimen chamber with vacuum of the order of 10^{-5} to 10^{-7} Torr. Fig. 9b presents the internal configuration of the column consisting of the major components enlisted below:

- a source (electron gun) of the electrons, which are accelerated down the column with high energy (0-30 keV);
- a series of electromagnetic lenses (condensers and objective) to control the diameter of the electron beam and to focus it on the specimen;
- a series of apertures to exclude scattered electrons and control spherical aberrations;
- scanning coils in the objective lens to allow xy scanning of the specimen and correct stigmatism;
- specimen chamber with electron detectors.

In this thesis, high-resolved SEM fabricated by Field Electron and Ion Company (FEI), Magellan 400 L (Fig. 9a) and Verios G4 HP (Fig. 9c), were used for morphological characterisation of GaN NWs.

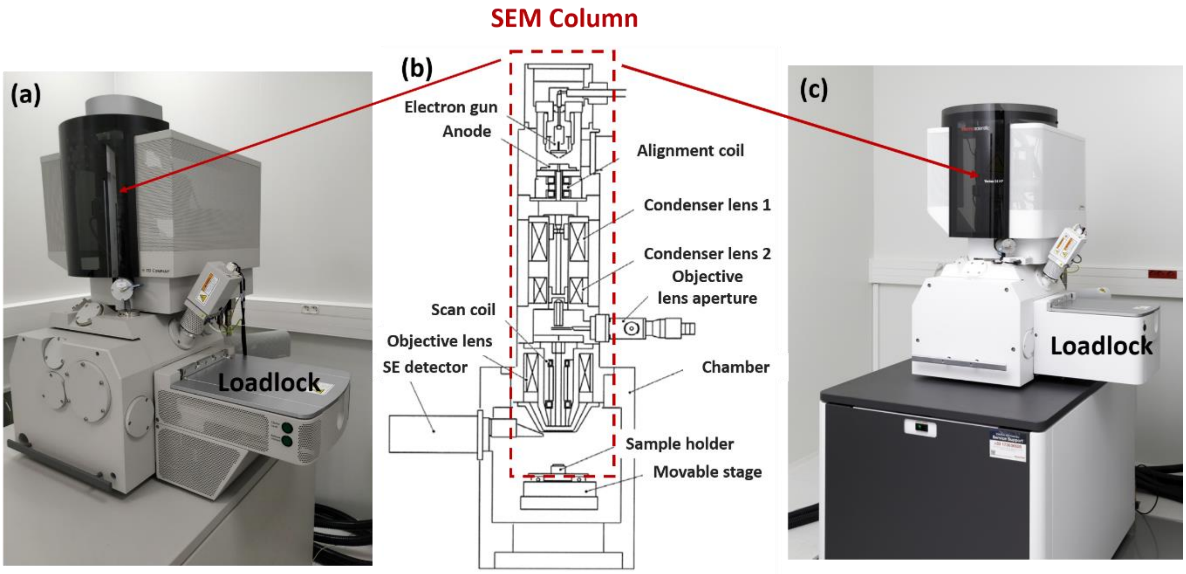

Figure 9. (a) FEI Magellan 400 L and (c) Verios G4 HP SEM systems at C2N cleanroom facility. (b) Schematics of the microscope column with major components.

b) Working principle: electron-sample interactions

SEM is based on the principle of the detection of particles/radiations emitted from a sample as a result of its interaction with highly energetic electrons, projected by the electron gun. These electrons are also known as the ‘primary electrons’. As the primary electrons hit the sample, they penetrate into it to a certain volume called the interaction volume. The shape and depth of this volume depend on the accelerating voltage as well as the atomic number of the specimen. In this zone, the interactions occur through elastic or inelastic mechanisms resulting in different by-products (backscattered electrons, secondary electrons, Auger electrons and a variety of X-rays), which can be used for imaging as well to do an in-depth sample characterisation. Fig. 10 presents a schematic representation of different regions of the interaction volume and the respective signals emitted from each region.

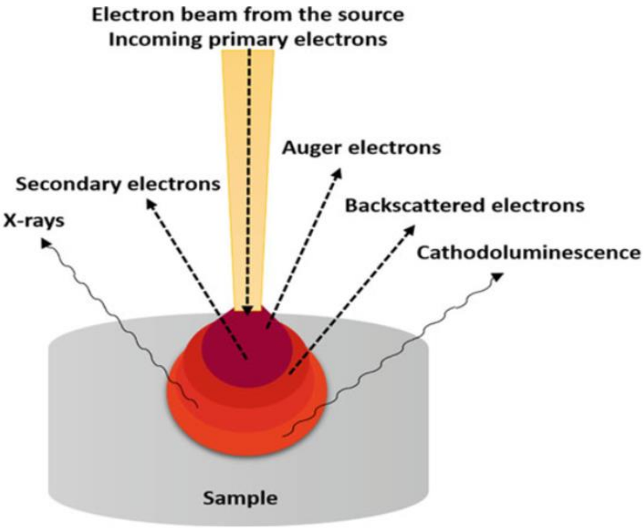

Figure 10. (Image taken from [16]). Illustration of the interaction volume within the sample and the signals resulting from the electron-sample interaction.

Here, a small overview of the nature of interactions and the corresponding reaction products is given:

<u>Elastic interactions</u>

In these interactions, the primary electrons undergo a directional change in the presence of the positively charged nuclei of the specimen's atoms. This phenomenon is known as the Rutherford scattering, and the incident electrons are emitted out of the sample without any loss of energy. If the scattering angle is wider than 90°, the emitted electrons are known as *Backscattered electrons* (BSE) (Fig. 11). BSE can have single or multiple interaction events before being detected, and can penetrate to a non-negligible depth within the sample. The percentage of incident electrons re-emitted by the sample (BSE yield) is highly dependent on the atomic number (Z) of its constituting elements. For instance, BSE yield is only 6 % for Carbon which is a lighter element as compared to Tungsten or Gold with about 50 % BSE yield [17]. Therefore, BSE are used for composition analysis of the material with high contrast SEM images (elements with high Z appear brighter).

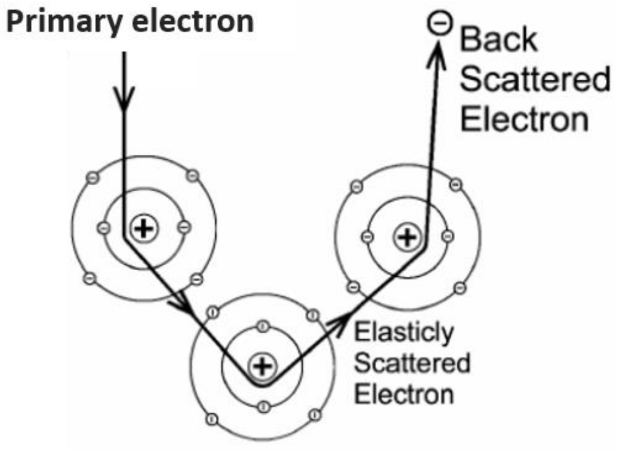

Figure 11. The primary electron (1° e$^-$) undergoes elastic scattering on interacting with the atomic nuclei and is emitted out of the sample as backscattered electrons.

Inelastic interactions

In these interactions, the energy of the primary electrons is not conserved and a significant amount is spent to excite and eject the loosely bound electrons in the outer shells of the atom. These expulsed electrons are called *Secondary electrons (SE)* and carry less than 50 eV of energy. This inelastic process is described in Fig. 12a. These electrons are emitted from a distance of only a few nm from the sample's surface and therefore, high-resolution topography images can be obtained by the detection of SE.

Inner core electrons are more tightly bound but can nevertheless be ejected on interacting with the primary electrons. In such conditions, a hole is created in the inner electronic orbital. If this vacancy is filled by another electron from a higher orbital, a radiative process takes place by the emission of *X-rays* characteristic of that electronic shell (Fig. 12b), which varies from one specimen to another. By the detection of these characteristic X-rays, information about the orbital transition in the specimen can be obtained. In addition, some lower energy X-rays can also be produced by *bremsstrahlung method* in which the primary electrons undergo deceleration due to a repulsive interaction with the atomic electrons and lose energy as photons (few eV).

Another inelastic electron-material interaction can also occur if instead of emitting X-rays, the transition energy is used to ionise the outer shell electron (Fig. 12c). This electron is then ejected as an *Auger electron* and has a very low energy. These electrons are principally used for surface analysis.

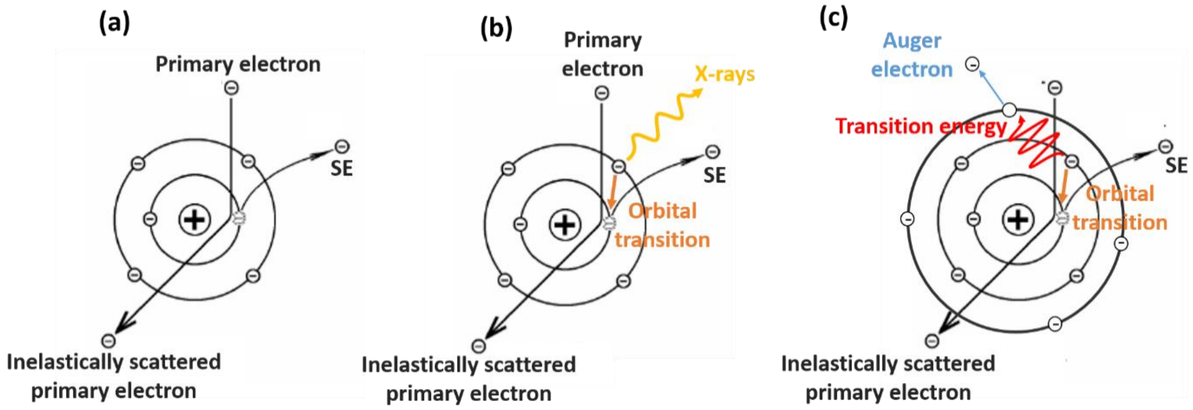

Figure 4. Different inelastic interactions leading to the creation of (a) secondary electrons, (b) characteristic X-rays and (c) Auger electrons.

In some materials, by the ejection of photons in the UV, visible or infrared spectrum, *Cathodoluminiscence* can occurs. Only selective microscopes are equipped with detectors to investigate the luminescence characteristics of the samples.

2.2.2. Introduction to atomic force microscopy (AFM)

Atomic force microscope or AFM was introduced by Binnig et al. in 1986 to investigate the surfaces of insulators as well as conductors on an atomic level [18]. As such, it has rapidly become a reference instrument in the family of local probe microscopes, which measures the interaction between a nanoscale tip and the surface. Historically, this technique combined the principles of a scanning tunnelling microscope to measure interaction forces as small as 10^{-18} N, and the stylus profilometer to obtain 3D surface images [19]–[21]. Then very quickly the measurement of the interaction forces was operated optically (see principle described below). The first commercial AFM system was developed by Digital Instruments in 1989. Today, AFM is one of the most frequently used tools in academic research laboratories, but also for industrial R&D purposes in the field of microelectronics, molecular and cell biology, medicine, energy storage and energy generation, micro-nano devices.

AFM is a high resolution and non-destructive (when using suitable mode) scanning probe microscopy technique. It is used to visualise and generate topographic maps of a variety of surfaces including polymers, glass, ceramics, composites, biological samples… at a scale ranging from below 1 nanometer to tens of µm. AFM is capable of imaging specimens with a horizontal and vertical resolution down to a fraction of a nanometer. In association with specific add-ons, the AFM technique can be extended to perform localised electrical, mechanical, magnetic, piezoelectric and other characterisations on a wide range of materials (electrically conductive, insulating, opaque, transparent, soft, viscous, liquid and more).

a) Set-up and operation principle

The experimental set-up of the AFM mainly consists of the following components:

- A probing tip, known as the AFM tip, attached at the end of a spring beam, called the cantilever, as shown in Fig. 13

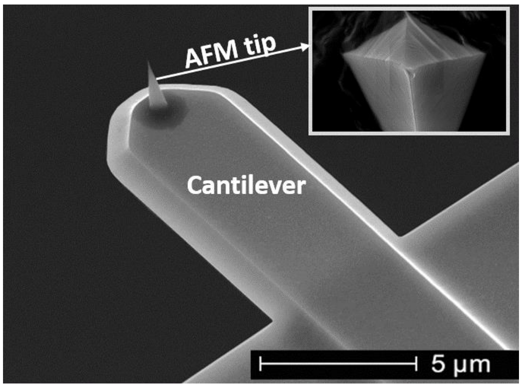

Figure 13. SEM image showing the flexible cantilever and the AFM tip attached at its end. A zoomed-in SEM image of the tip is shown in the inset.

- An “optical lever” consisting of a laser diode and a photodetector (with split photodiodes);
- A feedback loop to control the deflection of the cantilever according to a selected set-point;
- A piezoelectric tube (AFM scanner) to ensure movements in x, y and z directions for a 3D scanning of the surface;
- A conversion system for graphical visualisation of the acquired data in the form of an image.

The schematic diagram of an AFM set-up is shown in Fig. 14.

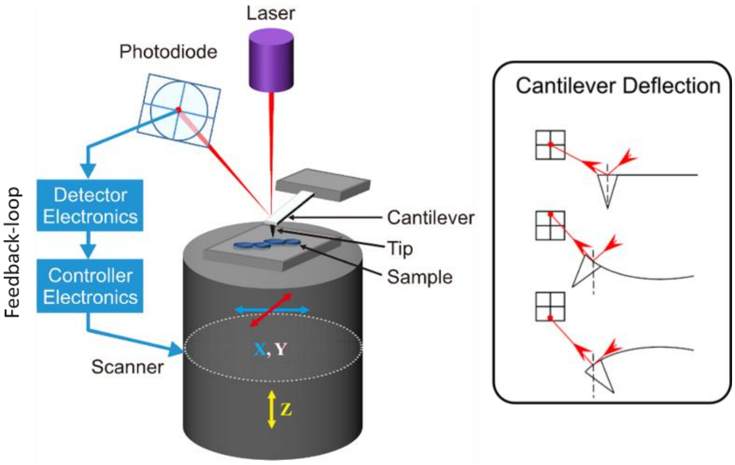

Figure 14. (Image adapted from [22]). Schematic illustration of the AFM set-up. The laser spot displaces on the position-sensitive photodetector as a function of the cantilever bending.

The AFM technique takes advantage of the interactions of the sharp probing tip with the sample surface. These interactions give rise to either attractive or repulsive forces and consequently lead to the cantilever deflection, which can be measured using the optical beam deflection (OBD) method. To realise such measurements, a laser beam is reflected on the backside of the cantilever and then directed onto a photodetector. This four-quadrant photoelectric sensor detects vertical or lateral movements of the laser spot and thus provides information on the deflection or torsion of the cantilever. The measured signals are then transmitted to the feedback loop to act on the AFM scanner and maintain a selected setpoint.

In Fig. 14, the sample stage is moved relative to the fixed tip holder as well as the photodetector. This is the configuration that I've used in this thesis at laboratory GeePs with the Bruker Multimode 8-HR AFM system (Fig. 15). Note that the reverse configuration can also be found, in which the tip and the optical detector move.

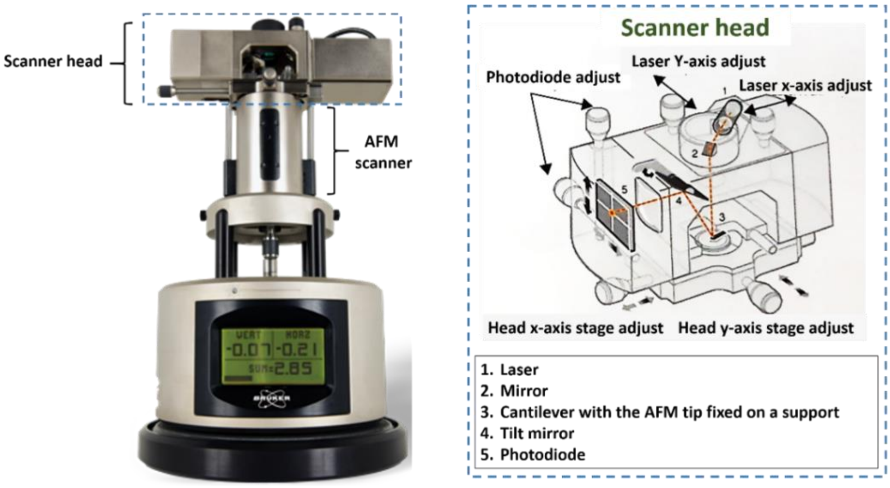

Figure 15. Bruker Multimode 8-HR system at GeePs. The main components of the scanner head are shown in the schematic representation

Cantilever calibrations

Commercially available cantilevers are generally fabricated from silicon or silicon nitride using photolithography techniques and are available in different dimensions. They can have a rectangular or a 'V' type shape, and are chosen according to the sample to be characterised. The cantilever dimensions strongly influence the sensitivity and the spring constant of the AFM measurements. Therefore, prior to each measurement series, a calibration of the cantilever is performed by calculating its spring constant '*k*' (nN/nm) by using the 'thermal tuning method' [23]–[25]. The force applied by the AFM tip on the sample is then calculated as a function of the relative vertical displacement (or deflection) 'Δz' (nm) using the following equation:

$$F = k \times \Delta z \qquad (1)$$

b) Tip-sample interaction and modes of operation

AFM tips generally present a pyramidal or a conical form. Their radius of curvature can range from a few tens of nm to a few hundred nm and they might have a variety of coatings. Due to their finite dimensions and respective shapes, one must take into account the tip-surface "convolution" effect. Irrespective of the coating material, this effect is manifested by the fact that the shape of the surface motifs cannot be accurately resolved and is one of the main limitations of the lateral resolution of the AFM technique. Fig. 16a presents different scenarios of the tip-surface convolution and the topographic information obtained based on the tip geometry. Here, tip 1, being the sharpest, follows the grooves and protrusions on the sample surface, as illustrated by the green profile. This tip thus truly reflects the surface topography (shown in dashed lines here). It could be considered as the ideal probe to scan such surfaces. The tip 2 faces restrictions due to its specific form and consequently induces modifications of the topological characteristics of the surface, as illustrated by the red profile. Finally, the tip 3 represents a tip with a radius of curvature having undergone a change due to some local damage. It leads to artefacts, hence "*falsifying the data*" as illustrated by the blue profile.

This suggests that the AFM tip must be chosen carefully depending on the application of interest as well as the sample morphology. In our case, the tips, which met the various requirements in terms of lever stiffness, tip radius and coating, were pyramidal shaped tips (having distinct triangular facets and radius of curvature comparable to the NW diameter). Concerning the GaN NWs, they are characterised with hexagonal facets. The recorded topological mappings are therefore the result of a complex convolution of the interaction between the pyramid-shaped tip and the NW facets which, together in the contact mode, generate the triangular patterns shown in Fig. 16b.

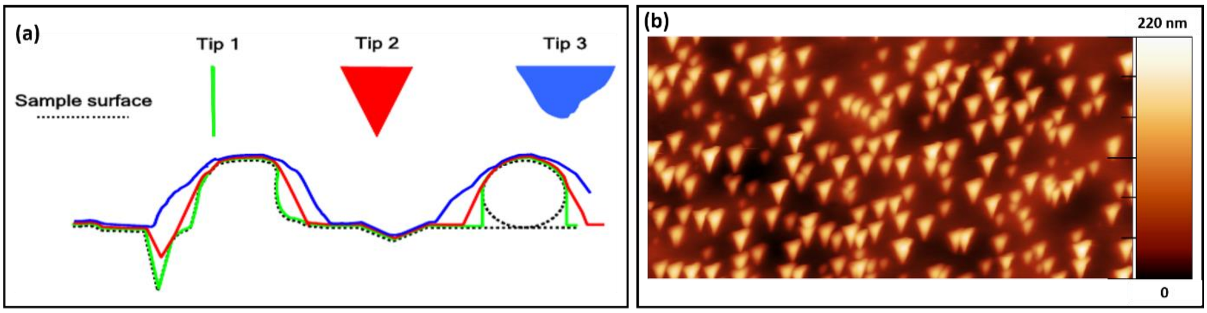

Figure 16. (a) Schematic diagram showing the tip-surface convolution. (b) Topography of GaN NWs using a pyramidal AFM tip.

Force-distance curves

Now let's take a closer look at the interactive forces between the tip and the sample surface, which could either be attractive or repulsive in nature. It is convenient to represent the global tip/surface interaction using a Lennard-Jones type potential (Eq. 2), in which the interaction is attractive at a long range (predominance of Van der Waals forces) and repulsive at very short ranges (non-penetrability of the electronic clouds of both surfaces):

$$U\,(r) = -\frac{A}{r^6} + \frac{B}{r^{12}} \tag{2}$$

where, '*r*' is the tip-sample distance and *A* and *B* are constants whose values depend on the types of atoms [26], [27]. For an interaction between two atoms of a solid, A~ 10^{-77} Jm^6 and B ~ 10^{-134} Jm^{12} [28]. Using Eq. 2, we can calculate the forces of interaction:

$$F\,(r) = -\left(\frac{dU}{dr}\right) \tag{3}$$

Fig. 17 represents the schematic illustration of a force-distance curve, which has been divided into the attractive forces' regime ($F < 0$) and the repulsive forces regime ($F > 0$).

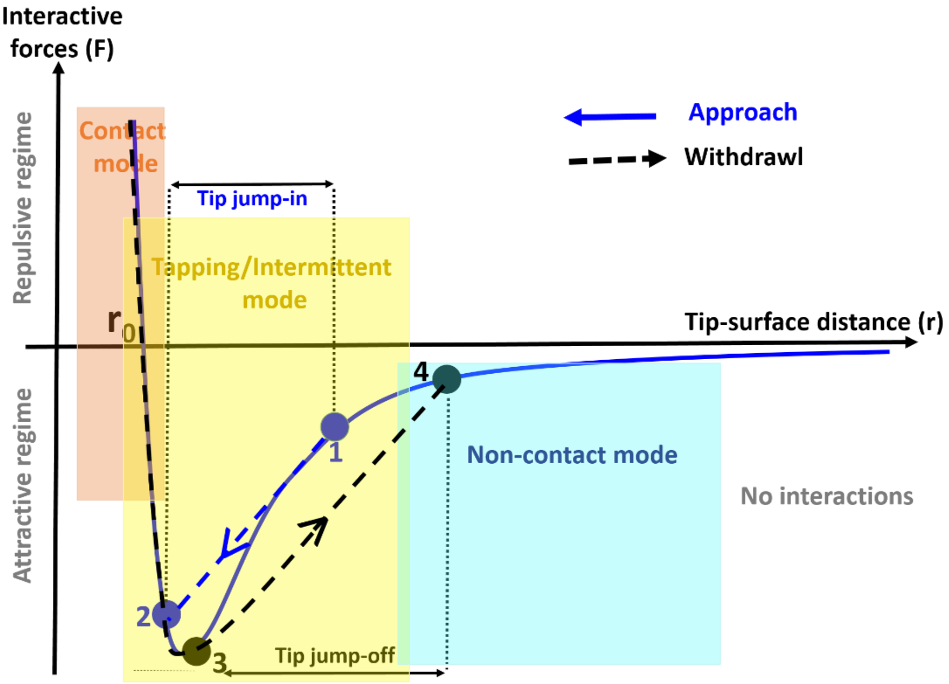

Figure 17. Schematic representation of the force-distance curve to illustrate the tip-surface interaction. Depending on the tip-surface distance, different AFM modes have been represented.

At the beginning, when the cantilever is far from the surface (high tip-surface distance), no interaction occurs and the cantilever deflection is zero. While approaching the surface, the tip feels an increasing attractive force and jumps-in towards the sample surface (from point 1 to 2) as soon as the force gradient becomes equivalent to the spring constant 'k' of the cantilever. Until here, attractive forces, such as the Van der Walls forces and capillary forces are pre-dominant.

Below the balance point of attractive and repulsive forces (at r_0), the repulsive Coulomb force dominates due to the close-interaction of the respective electron clouds. Then the force increases until a given deflection setpoint is reached. Reversing the tip/cantilever movement, in the ideal case of no adhesion, the same path would be followed until the tip jumps-off of the surface. In practice, the trajectory remains in the prolongation of the characteristic line of the contact as long as the pull-out force exerted by the cantilever does not exceed the adhesion force (as shown by the dashed line). The cantilever then returns to a slightly deflected position on the right-hand side of the curve (from point 3 to 4).

Depending on these regimes, different modes of AFM can be defined.

c) Frequently used AFM modes

Contact mode

This imaging mode is the most often used modes of the AFM, which operates in the repulsive force regime (the interactive Coulomb forces of the order of 10^{-9} N) [29], [30]. Here, the tip is brought into contact with the sample surface until the deflection/force pre-set by the user is achieved. Once in contact, the tip scans the sample in a xy raster pattern. The cantilever deflection is maintained constant by the feedback loop, which adjusts the z-scanner for each xy coordinate. The change in the z-height corresponds to the sample height and high-resolution topographic images are obtained. However, this mode is harmful for soft, brittle or weakly anchored samples samples, because of the perpetual tip-surface contact. Moreover, a lateral force arises while scanning the samples, which could drag the soft materials along and can even bring damages to the tip.

Tapping mode

To avoid friction issues related to the contact mode while imaging sensitive samples, oscillating modes, such as the tapping mode were developed. In this mode, a quite stiff cantilever oscillates near its resonance frequency (in the range of 100 - 300 kHz) in a swing-like motion and establishes a brief contact with the surface at the bottom of each swing. As a result of the interactive forces, the frequency, phase and the amplitude of oscillation changes, which may then be adjusted using the feedback loop. In this most commonly used operating mode, the amplitude of the oscillation (about 100 nm) is kept constant by the movement of the z-piezo. This dynamic scanning mode allows a gentler topographic imaging of soft samples by reducing the tip-surface contact time. Moreover, lateral force effects are highly reduced in this mode as most of the lateral movement of the tip takes place when it is not in contact with the surface. In this thesis, tapping mode was used to measure the height of the NWs partially encapsulated in a polymer matrix (as explained in Chapter 3 and 4).

Intermittent mode

Due to the furtive tip-surface contact established at high frequency in the above-described tapping mode, the quantification of the applied force is very difficult. In order to resolve this issue, intermittent mode was developed. This is a highly lower frequency (typically 10^2 – 10^3 Hz) dynamic mode. In our case, we use the Peak-force intermittent mode (Bruker), where a sinusoidal oscillation is introduced to the z-piezo at a frequency between 100 Hz and 2 kHz. The oscillation amplitude is maintained using the feedback loop to alternate between contact and non-contact in each cycle. This mode ensures the scanning of delicate samples with a well-controlled force. Due to the low-frequency actuation of this mode, real-time characterisation of the mechanical properties of the samples can also be performed amongst other properties.

Non-contact mode

This mode is historically the main of oscillating modes or dynamic modes. The cantilever is oscillated at its resonance frequency above the sample surface so that the distance between the tip-sample is in the range of 10 Å – 100 Å. Here, the interactive forces (substantially weak attractive Van der Walls forces) are of the order of 10^{-12} N and the amplitude of oscillations is typically a few nanometers (< 10nm) [31]–[33]. The variations in the interactive forces can cause a change in the oscillation amplitude (or frequency) of the cantilever, which is kept constant by the z-movement of the piezotube. This mode is a non-destructive scanning mode as the tip doesn't come in contact with the surface at any moment and is highly suitable for imaging biological samples, organic thin films…

d) AFM equipped with the electrical mode 'Resiscope'

During my thesis, I've used the Bruker Multimode 8-HR AFM system (Fig. 3) equipped with an electric module, called Resiscope [34], to perform electrical measurements on single GaN NWs. Commercially available since 2011, this module was initially developed to perform localised resistance measurements in the range of 10^2 – 10^{12} Ω, as well as I-V characteristics. For these measurements, an external potential is applied via the substrate. Fig. 18 presents the schematic diagram explaining the general principle of the Resiscope module.

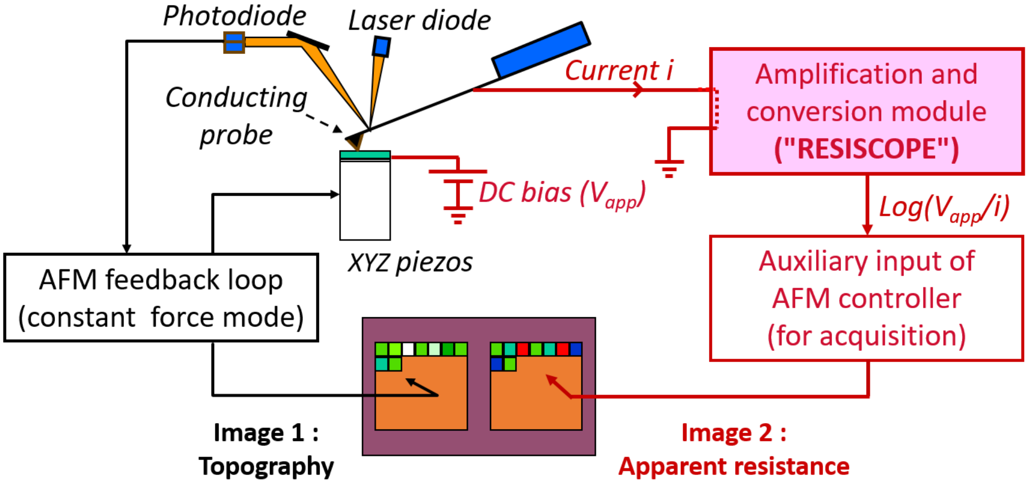

Figure 18. (Courtesy of GeePs) Schematic illustration of the general principal of an AFM equipped with the Resiscope module. Real-time measurements of topography and resistance are performed simultaneously.

In order to perform direct piezoelectric measurements on our 1D-nanostructures, the Resiscope module has been specifically adapted by Pascal Chrétien from the laboratory GeePs. The modifications have been performed in order to carry out investigations of the piezoelectric properties of the NWs similarly to the method used by Wang and Song [35]. In this configuration, an Ohmic contact is formed between the NWs and the substrate [36], while the conductive AFM tip in contact with the NW top forms a Schottky barrier that ensures the collection of piezo-generated charges [37]. Finally, no external bias is applied and the recorded output signals across an external load resistor (R_{load}) are solely generated by the NWs being deformed by the AFM tip [38]–[40].

Two deformation modes have been used during my PhD project:

Bending in scanning configuration

Piezoelectric measurements on GaN NWs have been performed under bending deformation. In this configuration, as previously explained in Chapter 1, the AFM tip is brought in contact with the surface and scans over the GaN NW arrays. The force applied by the conductive tip (resulting from the convolution of the CNF and the scanning force) on the NW induces its lateral bending. In response to its elastic deformation and due to its piezoelectric properties (principle explained in Chapter 1), the NW generates an output voltage which is harvested through the Schottky diode. Fig. 19a schematizes this configuration.

Axial compression configuration

In this mode, the AFM tip interacts with the surface in an intermittent manner, inspired by the so-called 'pulsed force mode' (PFM),which is a low frequency non-resonant mode originally developed for local mechanical measurements [41]. The piezoelectric response of individual NWs is achieved under a well-controlled and purely axial force. In this new adaptation, the technique consists in introducing a sinusoidal modulation on the AFM z-piezo at a frequency between 100 Hz and 2 kHz (i.e., far below the cantilever's fundamental resonance), in order to oscillate in close proximity to the probe so that the tip furtively hits the sample surface at each period. Then, the associated adapted Resiscope allows to collect, through the tip/NW Schottky diode, the output voltage generated by the axially deformed NW. Fig. 19b illustrates this second configuration.

Whatever the configuration of our AFM system, topographic and electrical signals are recorded simultaneously. Thus, a direct correlation between the NW morphology and their electromechanical response can be established.

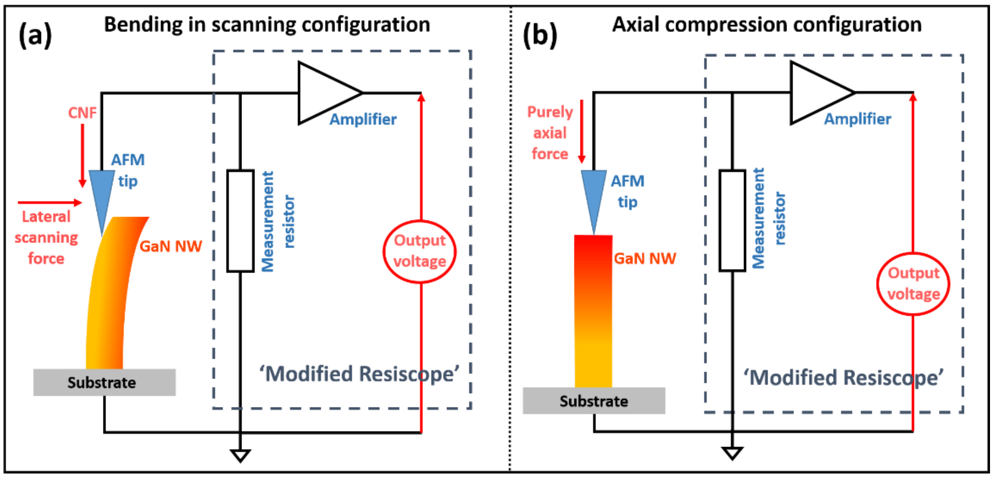

Figure 19. Principle of piezoelectric measurements performed by AFM equipped with the modified Resiscope in (a) bending in scanning configuration and (b) axial compression configuration.

2.3. Auto-catalysed, self-assembled growth of GaN NWs

In this section, we describe the catalyst-free growth of GaN NWs studied in this thesis.

2.3.1. Substrate preparation and growth of the AlN buffer layer

Prior each growth, a chemical cleaning of the Si (111) substrates was systematically performed to eliminate organic residues as well as the native oxide layer. After its introduction in the growth chamber, the substrate was degassed at 850 °C for 15 minutes for its complete de-oxydation. The calibration of the pyrometer was performed after this stage.

All growths have been performed following the procedure described in [42]. Here, prior to the GaN NW growth, a 2.5 nm thin AlN buffer is deposited on Si (111) substrates, allowing a better control of the NW nucleation, density and orientation [42], [43], [44]. In addition, this layer prevents the nitridation of the substrate, which can degrade the conductivity between the NWs and the substrate. The AlN buffer is achieved in a two-step method, as illustrated in Fig. 20.

- The de-oxidised Si (111) substrate is exposed to an aluminium flux of 8 × 10^{-8} Torr for 30 seconds at 620°C, allowing the formation of Al/Si droplets (Fig. 20a). The Al deposition is directly followed by the activation of the nitrogen-plasma cell and in the meantime the Ostwald-ripening of the Al/Si alloyed droplets takes place.
- Once the plasma cell is activated (within 60 seconds), the substrate undergoes a nitridation process for an additional 50 seconds to form the 2.5 nm thick AlN buffer layer.

Following this deposition procedure, the AlN buffer is an incomplete film. It is formed of 3D islands, the so-called *pedestals*. This AlN is characterized by a Nitrogen polarity, which is fixed by the saturation of the dangling bonds of Si atoms by Al adatoms and the formation of Al-Si eutectic bonds [42], [45], [46], as shown in Fig. 20b. Finally, this AlN buffer plays an important role in the growth of GaN NWs by acting as potential nucleation sites. More specifically, at low temperatures (T_{sub} < 780°C), the GaN NWs nucleate at the top of the pedestals, while at T_{sub} > 780 °C, the NWs nucleate at their edges. Consequently, the GaN NWs grown on these pedestals are also characterised by an N-polarity [42].

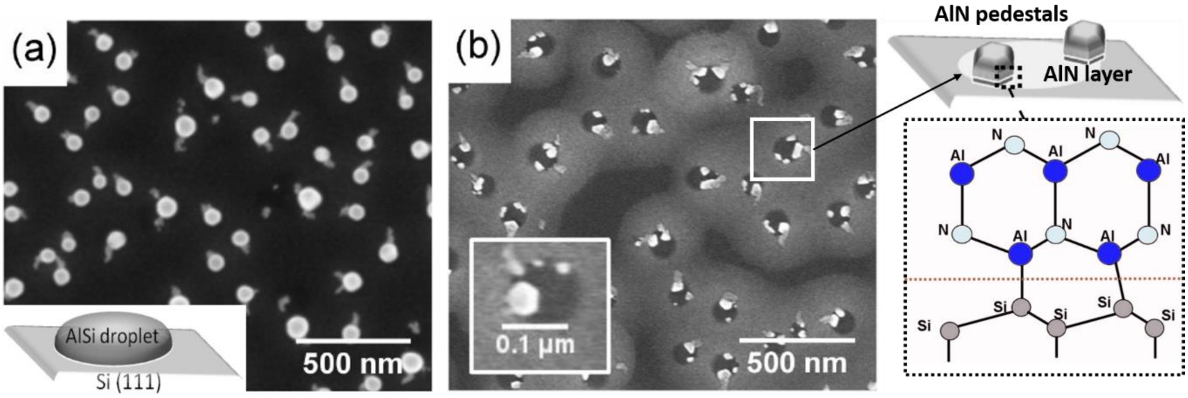

Figure 20. (Images adapted from [42], [45]). (a) SEM image of Al/Si droplets after 40 seconds of Al exposure on Si (111) substrate. A schematic of the droplet formation in the inset. (b) SEM image after 60 seconds of nitridation of the Al exposed substrate. Formation of AlN nanocrystals on thin AlN layer (appears lighter in contrast) is observed. Eutectic Al-Si bond formation fixes the N-polarity of the pedestals as well as the NWs.

From a piezoelectric point of view, the AlN interlayer can act as a barrier preventing the circulation of piezoelectric charges. However, this is not the case. In fact, the exposition of the de-oxidized Si(111) substrate to the Al adatoms leads to the formation of Al–Si eutectic of composition x = 0.126 [47]. Then, during the nitridation of the Al-Si droplet, the Si adatoms are incorporated into the AlN layer, producing an efficient n-type doping, thereby yielding a conductive behavior. This two-step procedure to grow the AlN buffer layer is thus beneficial for piezo-conversion measurements, since an Ohmic contact is formed between the GaN NWs grown on this buffer layer and the substrate [36].

2.3.2. Growth diagram

Once the AlN buffer layer is achieved, the growth conditions are adjusted for the GaN NW growth. The substrate temperature is increased higher than 750 °C and the growth is performed under N-rich rich-conditions (V/III > 1). Depending on the chosen parameters, the NW characteristics can be modified. Fig. 21 shows the reference growth diagram of our PA-MBE machine as a function of temperature and V/III flux ratio for a fixed growth rate of 0.7 ML/sec.

It can be seen that both the decrease in substrate temperature and V/III flux ratio (higher Ga flux) favours the formation of a thick 2D polycrystalline GaN layer interpenetrated between the NW bottoms.

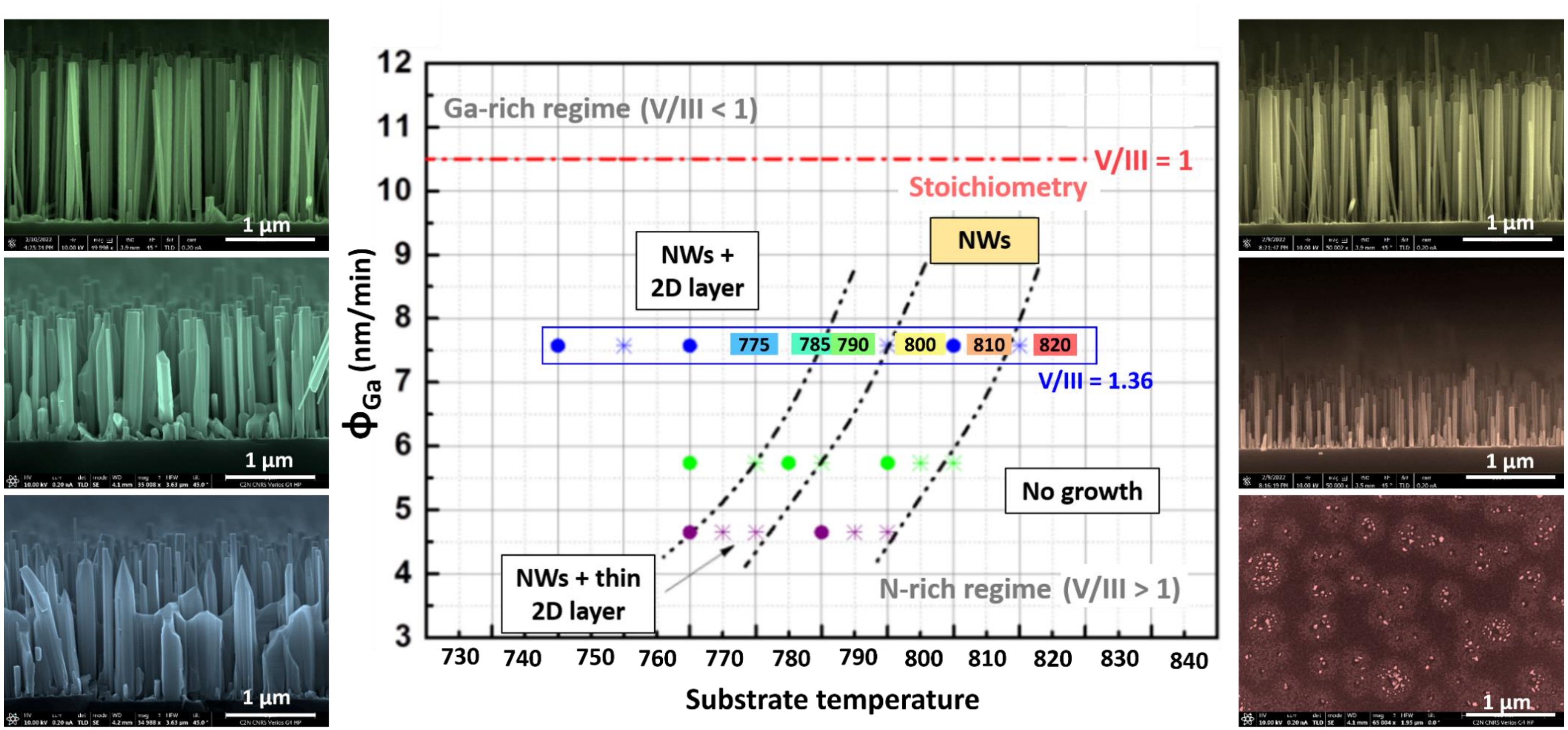

*Figure 21. Growth diagram established for **Compact 12** for epitaxial growth of GaN NWs on AlN/Si (111) substrates. The coloured SEM images describe the NW morphology in each regime at highlighted growth temperatures for a V/III flux ratio of 1.36.*

On increasing the substrate temperature, the 2D layer thickness decreases until it disappears, leaving only the nanowires on the surface (window highlighted in the growth diagram). With further increase in temperature, Ga desorption becomes dominant. The Ga adatoms thus leave the surface before being incorporated to the growth front. Consequently, no NW growth takes place.

The NWs dimensions (height, diameter) and density can be adjusted by varying the growth temperature, the growth rate, the V/III flux ratio and the growth time [48]–[54]. Following this growth procedure, the self-assembled GaN NWs are vertically oriented as shown by the X-ray 2D (10-11) pole figure (Fig. 22a) obtained from Bragg reflections of GaN NWs. Sharp peaks are located at $\phi = 62^\circ$ indicating that the NWs grow spontaneously along the c-axis [55]. They also present a Wurtzite crystalline structure as shown by the TEM diffraction pattern (inset Fig. 22b) and have hexagonal cross-sections (Fig. 22c) delimited by {1010} planes [55].

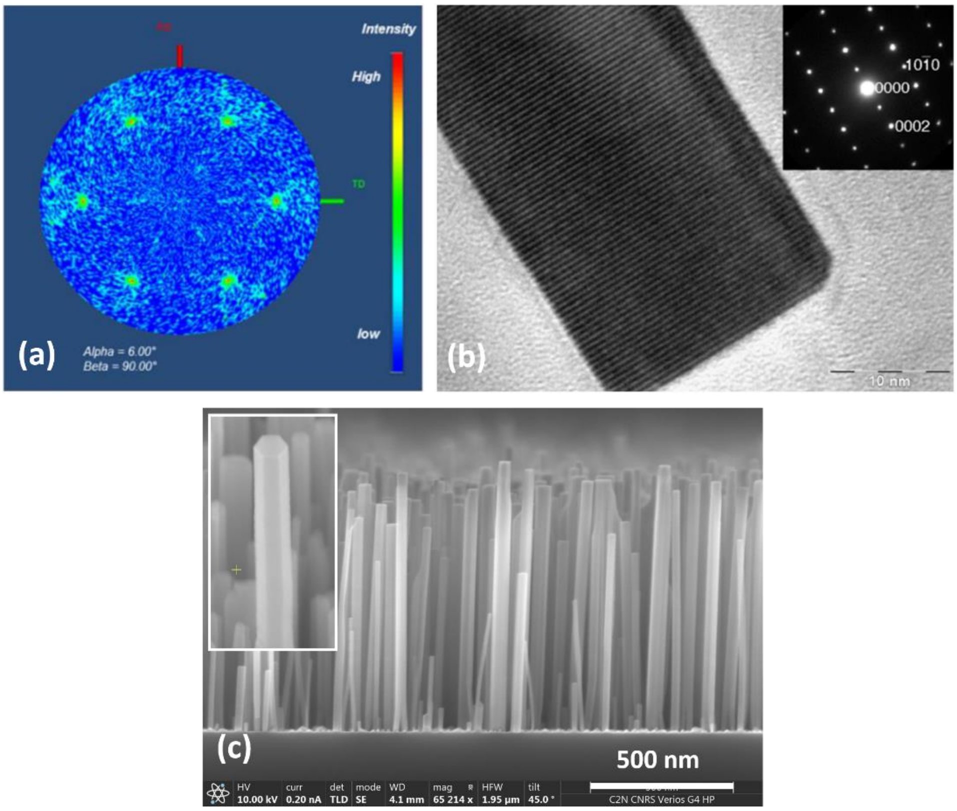

Figure 22. (a) (Image obtained from [56]) Pole figure obtained from the Bragg reflection (10-11) of GaN NWs indicating its orientation along the c-axis. (b) (Image obtained from [48]) High-resolution TEM image of the NW with the corresponding electron diffraction in the inset showing a Wurtzite crystalline structure, and (c) Cross-section view of self-assembled GaN NWs on Si(111) substrate using Compact12 PA-MBE at C2N. Image in the inset shows hexagonal cross-sections of a single NW in tilted view.

2.3.3. Growth mechanism

A certain number of reports can be found in the literature describing the growth of catalyst-free GaN NWs on AlN/Si substrates [44], [51], [57]–[59]. It has been demonstrated that N-rich conditions and high substrate temperatures are crucial for NW growth [51], [60]–[64]. Based on these studies, the GaN NWs growth can be explained by a three-step mechanism as illustrated in Fig. 23.

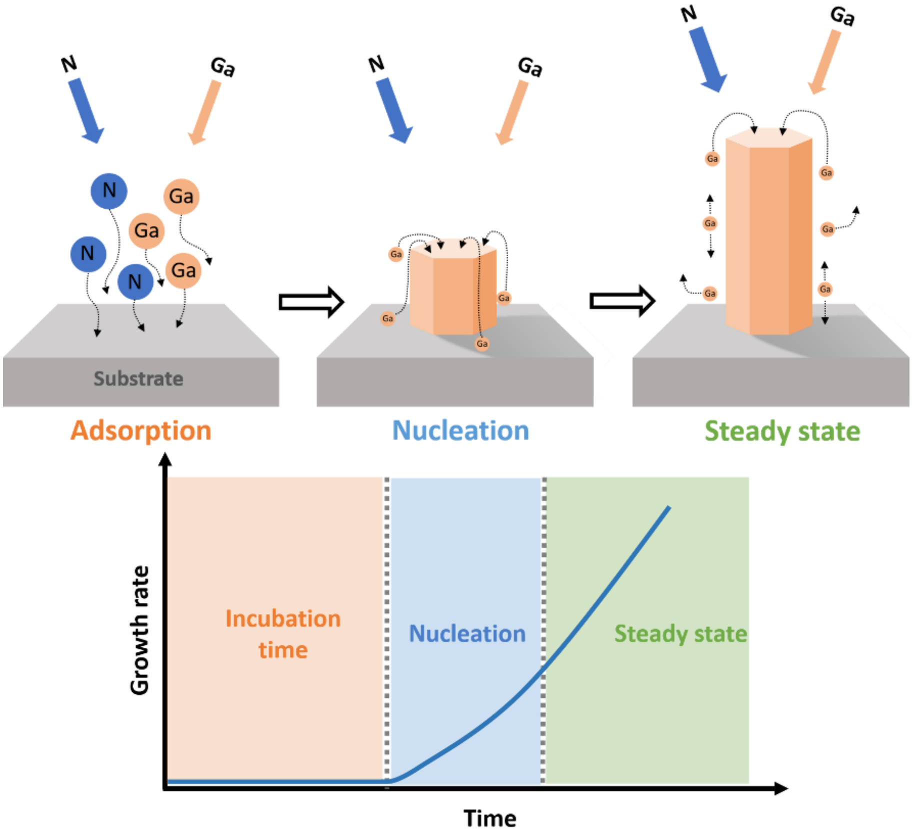

Figure 23. The three-step growth mechanism with the respective incubation period, the first nucleation of nanowires and the steady state corresponding to the axial nanowire growth.

a) Nanowire incubation time

The initialization of the GaN NWs growth does not occur instantaneously with the arrival of the first III- and V-elements on the substrate’s surface. A delay period, the so-called *incubation time*, systematically exists before the NW nucleation. This time of incubation strongly depends on the growth conditions (temperature, V/III ratio, growth rate) as well as on the substrate. In our case, the incubation time on AlN buffer layer is of the order of a few minutes, while it can last longer (tens of minutes or even more than an hour) for GaN NWs grown respectively on Si/SiN [65], silica [66] or Si/SiO$_2$/graphene substrates [67], [68]. The origin of this NW nucleation delay is not yet well understood and remains an open discussion in the epitaxial community.

The incubation period is defined as the time lag between the opening of the shutters of the respective elements, and the moment at which the nucleation of the NWs becomes visible on the fluorescent RHEED screen, i.e., the transition between the straight lines corresponding to the AlN surface (Fig. 24a) to the spotted diffraction pattern of the NWs (Fig. 24b).

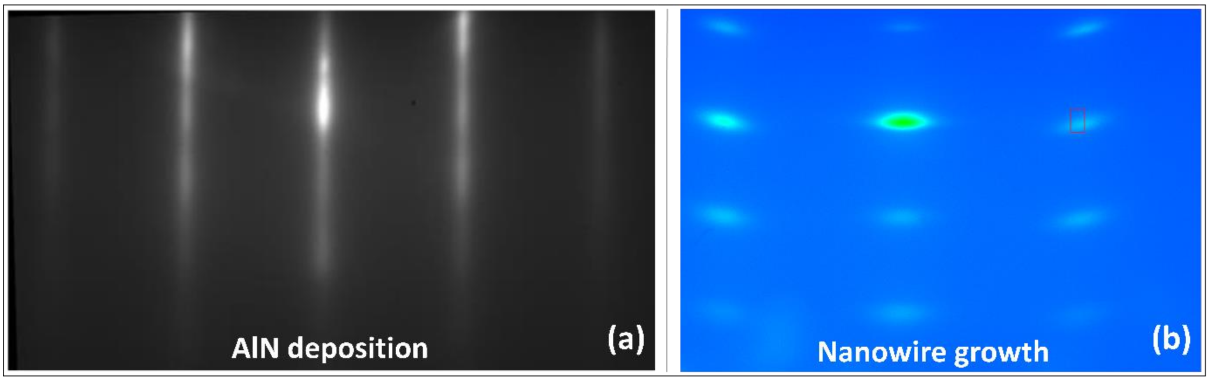

Figure 24. (a) (Image obtained from [69]) Streaky RHEED diffraction pattern corresponding to AlN deposition and (b) (our MBE) spotted RHEED pattern indicating the vertical growth of GaN nanowires, on Si(111) substrate.

b) Nanowire nucleation

The nucleation phase defines the regime during which the NW growth starts at the substrate's surface. During this phase, the effective growth rate of the GaN NWs is accelerated due to the excess of actives species driving the axial growth. In fact, the species arriving on the NW edges, as well as the ones arriving on the substrate have the possibility to migrate to the top of the NWs and thus induce an enhancement of the axial growth. This specific phase lasts until the NW reaches a height longer than the diffusion length of the III-elements, the ones driving the growth rate in N-rich conditions.

The initial stages leading to the nucleation of the NWs are still not clear and currently a topic of discussion. According to R. Songmuang [44] and V. Consonni et al. [58], the 3D islands, suggested to be the NW precursors [57], [70], [71], undergo a shape transitions from spherical to faceted pyramidal (Fig. 25(a-b)) in the elastic regime in order to minimise the built-in strain during the nucleation process. Finally, the pyramids become germs of nanowires with vertical walls (Fig. 25c), through the introduction of dislocations at the GaN/AlN interface.

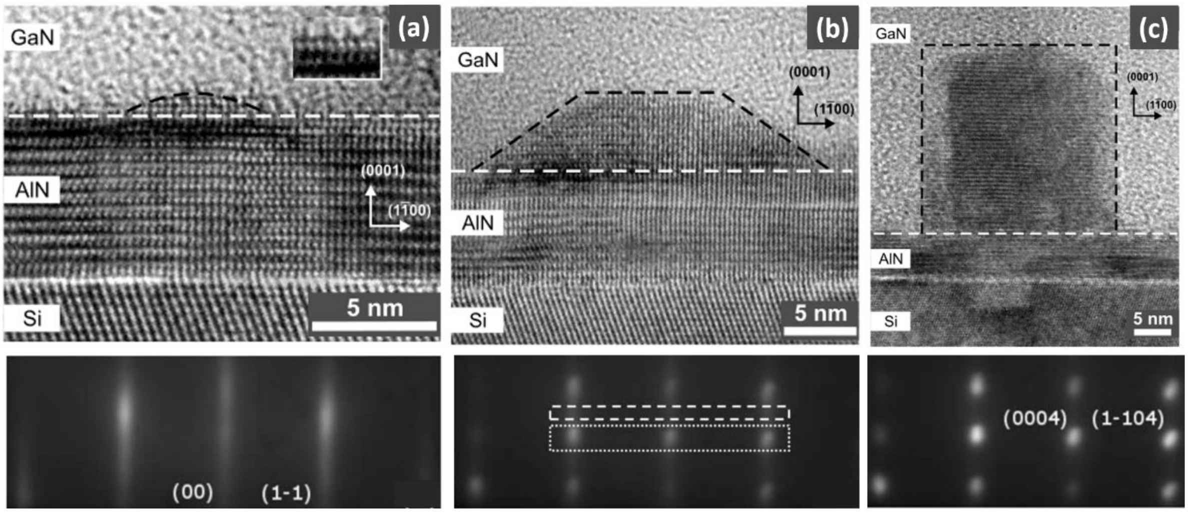

Figure 25. (Images taken from [58]). High-resolution TEM images showing the different shape transitions in the nucleation phase of GaN NWs on AlN/Si (111) substrate. The corresponding RHEED signals evolve from streaks to distinguished spots in this phase.

c) Nanowire elongation

This regime corresponds to the axial growth of the nanowires, which can be addressed by considering the *Diffusion-induced (DI) mechanism* as reported in various studies [44], [52], [72], [73]. When the substrate is exposed to the impinging flux, a small part of the active species is directly incorporated at the apex of the NW. However, the main part is principally adsorbed at the NW edges as well as at the substrate's surface. These adatoms then diffuse along the NW edge, as schematized in Fig. 26, and can participate in the following scenarios:

- Reach the NW top, which is the preferential incorporation site due to a lower kinetic energy barrier [46], [53];
- Get incorporated at the sidewalls leading to a radial growth [74], [75];
- Desorb and eventually be re-absorbed on another NW.

We can note here that at the nanowire growth temperatures (*cf*. Fig. 21), the incorporation rate of Ga adatoms is much higher at the {000-1} face of the GaN (nanowire tops), than at the $\{10\bar{1}0\}$ facets (nanowire edges). Thus, if a Ga adatom, adsorbed at the NW edge, is characterized by a sufficient diffusion length, it will preferentially diffuse along the sidewalls to be incorporated at the top of the nanowire. By contrast, if the distance to join the NW apex is greater than its diffusion length, the adatom will tend to desorb. In these conditions, the axial growth is favored as compared to the radial growth and the NW elongation takes place.

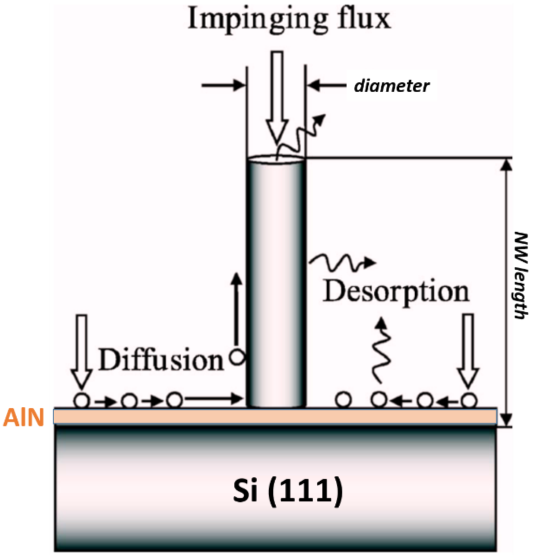

Figure 26. Diffusion-induced mechanism of the axial growth of GaN NWs on AlN/Si (111) substrate.

2.3.4. Optimization of the nanowire characteristics: a two-step growth method

In order to maximize the piezoelectric response of the future devices, the first choice is to orient towards the growth of densely packed NWs without any 2D layer at their bottom. The idea here is to maximize the active material and ensure a maximum deformation in order to collect the maximum piezoelectric response. However, this choice can induce specific issues, which can in turn degrade the piezoelectric response of the device:

- It can be difficult to embed the densely packed NWs in a polymer matrix. In fact, as a function of the *application mode* of the mechanical inputs, the matrix can present a different density. For deformation by bending, a high-density matrix is used but it cannot deeply penetrate between the NW arrays, therefore leading to a partial and non-controlled embedding. For deformation by axial compression, soft matrix are used. However, such matrix can be problematic for the encapsulation of nanostructures longer than 2 µm, due to their low density.
- To maximize the NW density, we often grow them at high temperatures as can be observed from the growth diagram (*cf*. Fig. 21). Thus, the NWs are directly connected to the substrate, without any 2D-layer at their bottom. However, this kind of NWs can present a stronger mechanical fragility compared to the ones with a 2D-layer at their bottom. This fragility can lead to a partial or complete breakage of the NWs at their base, during the deposition of the polymer matrix via the spin-coater. In addition, this fragility is prone to increase with the long-term repetition of the mechanical inputs. Consequently, the electrical contact at the NW/substrate interface might get disrupted, resulting in the degradation of the piezoelectric response of our NW/matrix composite, in time.

To overcome these situations, one solution is to perform the growth at low temperatures to obtain NW arrays with a lower density structure. Another advantage of growing at lower temperatures is the presence of a 2D-GaN layer along with the NWs, which provides a certain rigidity to our piezoelectric material. However, a very thick layer can adversely affect the flexibility of the NWs and hence their piezoelectric response which is a function of their degree of deformation. To keep a low NW density while reducing the residual 2D-layer at the same time, a two-step growth procedure, inspired by [76] has been developed:

- In the first step, the NW growth takes place at low temperatures ranging from 755 °C to 775 °C for several tens of minutes. In this temperatures range, the lateral and axial growth co-exists in a quasi-equivalent proportion, leading to the nucleation of low-density NWs surrounded by a 2D-layer. By initializing the NW growth in these conditions, we take advantage of the mechanical consolidation offered by the 2D-layer to the NWs, by rigidly fixing their bottoms.
- The second step consists of a linear increment of the growth temperature to 790 °C – 795 °C, without closing the shutters or changing the initial flux elements. In these new conditions, the lateral growth is inhibited. As a matter of fact, at high temperatures, the diffusion length of the Ga adatoms increases and the growth is thus continued solely along the c-axis following the previously explained 'diffusion induced mechanism'. This axial growth of GaN NWs is carried out for a few additional hours. In Fig. 27(a-c), we provide a comparison of the NW morphologies between a low-temperature, a high-temperature and the newly developed two-step growth. By performing the growth at high temperatures in the second

phase, we take advantage of the surface kinetics of Ga adatoms for the axial NW growth without further thickening of the 2D-layer.

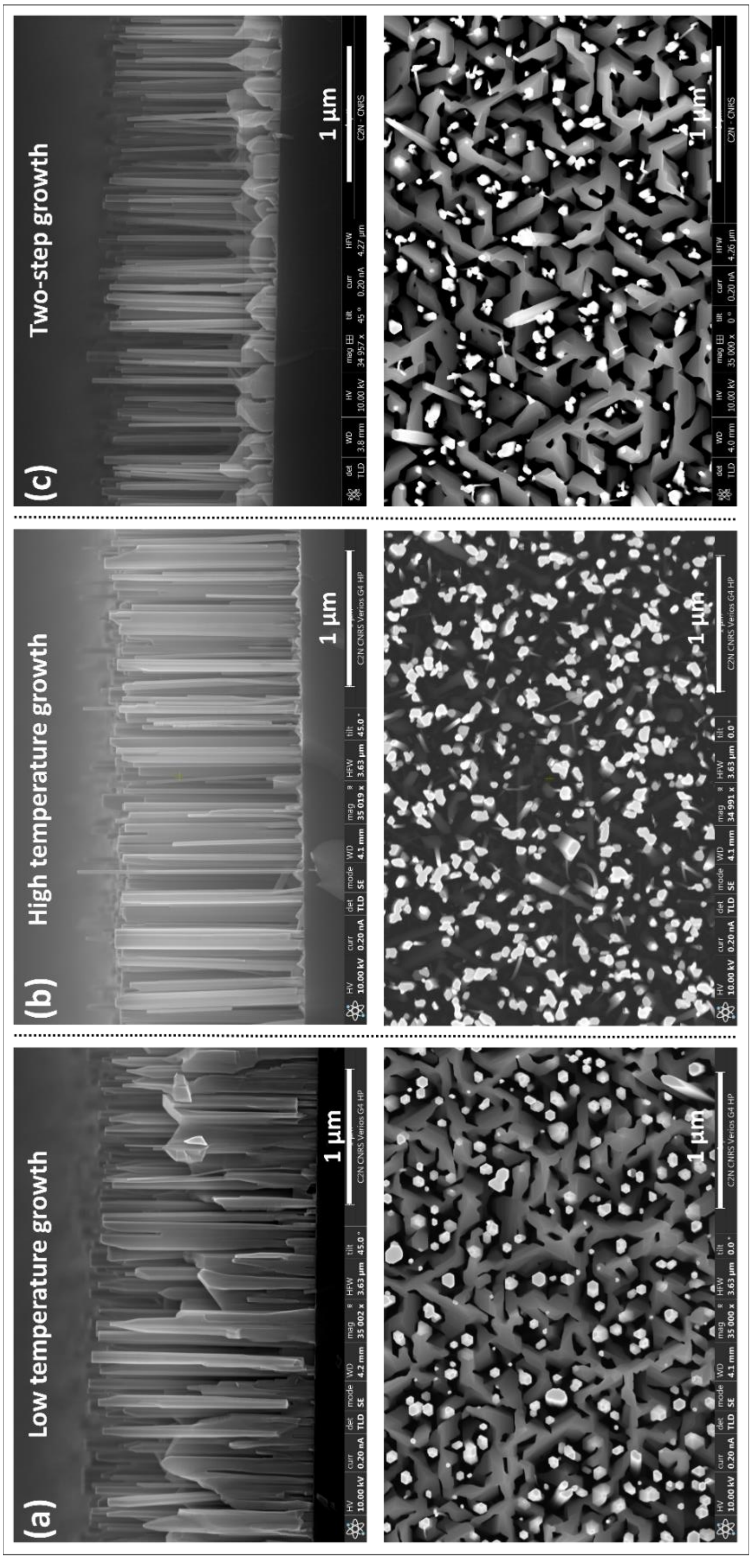

Figure 27. SEM images in (top) cross-section view and (bottom) top-view of as-grown GaN NWs on Si(111) substrates at (a) low temperature, (b) high temperature, and (c) following the two-step growth procedure. The density as well as the thickness of the 2D-GaN layer can be controlled via this technique.

2.3.5. Doping in nanowires

Doping of the piezoelectric NWs is known to be detrimental for their piezo-conversion capacity. In fact, the free charge carriers screen the piezoelectric charges, thus drastically reducing the internal piezoelectric field within the NW volume. Hence, it is essential to decrease the doping levels inside the 1D-nanostructures as argued in [77]–[79]. This argument can be considered for piezoelectric transducers with a capacitive configuration. However, it’s not the case for PZs with a Schottky configuration, the ones we develop in the team. For the latter case, an optimum doping level must be found, taking into account the competition between high resistivity of the material with very low doping, thwarting the free circulation of the charges and therefore inducing a weak piezoelectric response, and the screening effects induced by too much doping [80].

In order to investigate this aspect, we have developed the growth of n-type (Si) and p-type (Mg) doped GaN NWs. The incorporation of dopants affect the growth kinetics of Ga adatoms [81]. As previously reported, an increased Si incorporation results in a decrease of the NW height [81]–[83], without changing their diameter. This is mainly because of the decrease of the sticking coefficient of Ga adatoms in the presence of Si [83]. The diffusion length of the Ga-adatoms is thus reduced and their desorption rate increases, resulting in the diminution of the NW height.

This behaviour has also been observed in our GaN NWs on increasing the Si cell temperature (and thus the Si flux) from 900 °C to 1200 °C. SEM images in cross-section view were analysed to perform height and diameter measurements. The height of the NWs decreases with the increase in Si cell temperature (Fig. 28a). No tapering of the GaN NWs has been observed as reported in [83].

Contrary to Si doping, the sticking coefficient of Ga-adatoms increases in the presence of Mg. The non-polar planes are thus energetically favourable sites due to a decrease in the adsorption energy [83]–[86]. Moreover, the diffusion barrier of Ga-adatoms is reduced conferring to them greater diffusion lengths [84], [87]. As a result, with the increase of Mg-dopants, a radial growth takes place as more and more Ga-adatoms reside on the m-plane. At very high Mg-doping, a NW coalescence can be obtained [84]. In our case, p-type doping of GaN NWs was carried out at Mg cell temperatures of 225 °C, 325°C and 375 °C, respectively. Fig. 28b shows the evolution of GaN nanowires as a function of Mg doping temperatures. At higher Mg cell temperatures, a strong coalescence of the NWs is observed, and the growth becomes un-controllable.

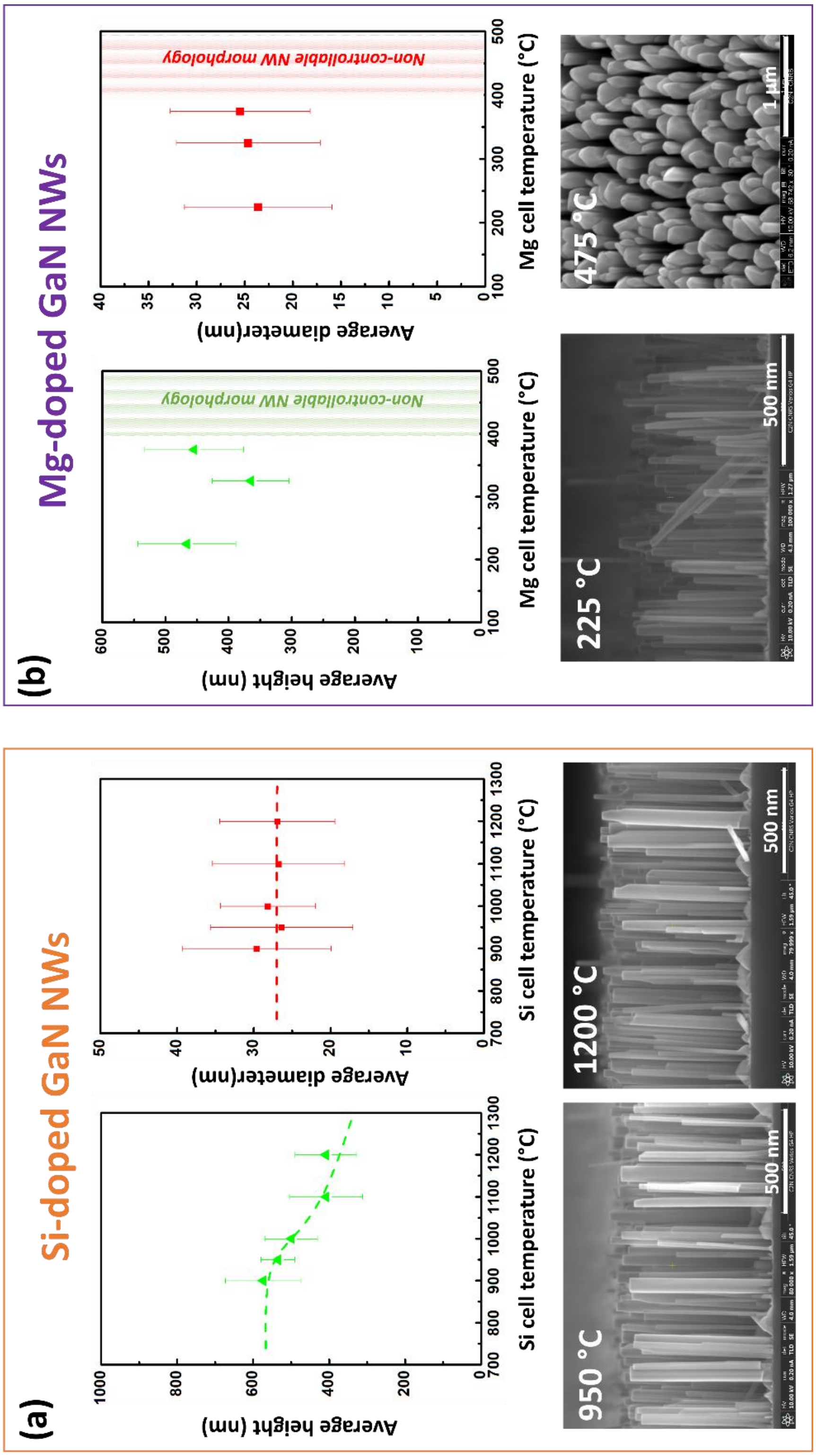

Figure 28. (a) Average GaN NW height decreases with increasing Si doping. (b) Average NW diameter increases due to an increased radial incorporation of Mg adatoms.

A complete series of doped GaN NWs (from highly n- type doped to highly p-type doped, passing through intrinsically doped nanostructures) has been grown following the two-step growth procedure.

The investigation of their piezoelectric responses is under investigation both via the AFM-based technique and device fabrication and testing.

REFERENCES

[1] G. R. Booker and B. A. Joyce, ‘A study of nucleation in chemically grown epitaxial silicon films using molecular beam techniques: II. initial growth behaviour on clean and carbon-contaminated silicon substrates’, *Philosophical Magazine*, vol. 14, no. 128, pp. 301–315, Aug. 1966, doi: 10.1080/14786436608219013.

[2] H. Morkoç, *Handbook of Nitride Semiconductors and Devices, Materials Properties, Physics and Growth*. John Wiley & Sons, 2009.

[3] ‘One-dimensional dislocations. I. Static theory’, *Proc. R. Soc. Lond. A*, vol. 198, no. 1053, pp. 205–216, Aug. 1949, doi: 10.1098/rspa.1949.0095.

[4] M. Volmer and A. Weber, ‘Keimbildung in übersättigten Gebilden’, *Zeitschrift für Physikalische Chemie*, vol. 119U, no. 1, pp. 277–301, Jan. 1926, doi: 10.1515/zpch-1926-11927.

[5] K. A. Lozovoy, A. G. Korotaev, A. P. Kokhanenko, V. V. Dirko, and A. V. Voitsekhovskii, ‘Kinetics of epitaxial formation of nanostructures by Frank–van der Merwe, Volmer–Weber and Stranski–Krastanow growth modes’, *Surface and Coatings Technology*, vol. 384, p. 125289, Feb. 2020, doi: 10.1016/j.surfcoat.2019.125289.

[6] J. E. Prieto and I. Markov, ‘Stranski–Krastanov mechanism of growth and the effect of misfit sign on quantum dots nucleation’, *Surface Science*, vol. 664, pp. 172–184, Oct. 2017, doi: 10.1016/j.susc.2017.05.018.

[7] I. N. Stranski and L. Krastanow, ‘Zur Theorie der orientierten Ausscheidung von Ionenkristallen aufeinander’, *Monatshefte für Chemie*, vol. 71, no. 1, pp. 351–364, Dec. 1937, doi: 10.1007/BF01798103.

[8] W. Telieps and E. Bauer, ‘The (7 × 7) ↔ (1 × 1) phase transition on Si(111)’, *Surface Science*, vol. 162, no. 1–3, pp. 163–168, Oct. 1985, doi: 10.1016/0039-6028(85)90890-8.

[9] K. Cho, A. M. Rappe, and J. Wang, ‘Chapter 4. Semiconductor Surface Studies’, p. 6.

[10] ‘Molecular Beam Epitaxy’, p. 513.

[11] C. Barbier, ‘Epitaxie de GaN sur substrat de graphène’, p. 208.

[12] O. C. Wells and D. C. Joy, ‘The early history and future of the SEM’, *Surf. Interface Anal.*, vol. 38, no. 12–13, pp. 1738–1742, Dec. 2006, doi: 10.1002/sia.2431.

[13] M. B. von Ardenne, *Elektronen-Übermikroskopie*. Berlin, Heidelberg: Springer Berlin Heidelberg, 1940. doi: 10.1007/978-3-642-47348-7.

[14] C. W. Oatley, ‘The early history of the scanning electron microscope’, *Journal of Applied Physics*, vol. 53, no. 2, pp. R1–R13, Feb. 1982, doi: 10.1063/1.331666.

[15] B. C. Breton and C. W. Oatley, Eds., *Sir Charles Oatley and the scanning electron microscope: a tribute published to coincide with the centenary of the birth of Charles William Oatley O.B.E., F.R.S., 14 February 1904 - 11 March 1996*. Amsterdam: Elsevier, 2004.

[16] K. Akhtar, S. A. Khan, S. B. Khan, and A. M. Asiri, ‘Scanning Electron Microscopy: Principle and Applications in Nanomaterials Characterization’, in *Handbook of Materials Characterization*, S. K. Sharma, Ed. Cham: Springer International Publishing, 2018, pp. 113–145. doi: 10.1007/978-3-319-92955-2_4.

[17] W. Zhou, R. P. Apkarian, Z. L. Wang, and D. Joy, ‘Fundamentals of Scanning Electron Microscopy’, p. 40.

[18] G. Binnig, C. F. Quate, and Ch. Gerber, ‘Atomic Force Microscope’, *Phys. Rev. Lett.*, vol. 56, no. 9, pp. 930–933, Mar. 1986, doi: 10.1103/PhysRevLett.56.930.

[19] G. Binnig and H. Rohrer, ‘SCANNING TUNNELING MICROSCOPY’, p. 9.

[20] K. H. Guenther, P. G. Wierer, and J. M. Bennett, ‘Surface roughness measurements of low-scatter mirrors and roughness standards’, *Appl. Opt.*, vol. 23, no. 21, p. 3820, Nov. 1984, doi: 10.1364/AO.23.003820.

[21] J. B. P. Williamson, ‘Paper 17: Microtopography of Surfaces’, *Proceedings of the Institution of Mechanical Engineers, Conference Proceedings*, vol. 182, no. 11, pp. 21–30, Sep. 1967, doi: 10.1243/PIME_CONF_1967_182_300_02.

[22] S.-H. Jung, D. Park, J. H. Park, Y.-M. Kim, and K.-S. Ha, ‘Molecular imaging of membrane proteins and microfilaments using atomic force microscopy’, *Exp Mol Med*, vol. 42, no. 9, p. 597, 2010, doi: 10.3858/emm.2010.42.9.064.

[23] J. L. Hutter and J. Bechhoefer, ‘Calibration of atomic-force microscope tips’, *Review of Scientific Instruments*, vol. 64, no. 7, pp. 1868–1873, Jul. 1993, doi: 10.1063/1.1143970.

[24] J. E. Sader, J. W. M. Chon, and P. Mulvaney, ‘Calibration of rectangular atomic force microscope cantilevers’, *Review of Scientific Instruments*, vol. 70, no. 10, pp. 3967–3969, Oct. 1999, doi: 10.1063/1.1150021.

[25] S. Belikov, J. Alexander, C. Wall, I. Yermolenko, S. Magonov, and I. Malovichko, ‘Thermal tune method for AFM oscillatory resonant imaging in air and liquid’, in *2014 American Control Conference*, Portland, OR, USA, Jun. 2014, pp. 1009–1014. doi: 10.1109/ACC.2014.6859224.

[26] M. C. Piontek and W. H. Roos, ‘Atomic Force Microscopy: An Introduction’, in *Single Molecule Analysis*, vol. 1665, E. J. G. Peterman, Ed. New York, NY: Springer New York, 2018, pp. 243–258. doi: 10.1007/978-1-4939-7271-5_13.

[27] P. J. de Pablo, ‘Introduction to Atomic Force Microscopy’, in *Single Molecule Analysis*, vol. 783, E. J. G. Peterman and G. J. L. Wuite, Eds. Totowa, NJ: Humana Press, 2011, pp. 197–212. doi: 10.1007/978-1-61779-282-3_11.

[28] J. N. Israelachvili, ‘Intermolecular and Surface Forces’, p. 706.

[29] S. K. Das, H. R. Pota, and I. R. Petersen, ‘Intelligent Tracking Control System for Fast Image Scanning of Atomic Force Microscopes’, in *Chaos Modeling and Control Systems Design*, vol. 581, A. T. Azar and S. Vaidyanathan, Eds. Cham: Springer International Publishing, 2015, pp. 351–391. doi: 10.1007/978-3-319-13132-0_14.

[30] C. R. Blanchard, ‘Atomic Force Microscopy’, *Chem. Educator*, vol. 1, no. 5, pp. 1–8, Dec. 1996, doi: 10.1007/s00897960059a.

[31] S. Morita, R. Wiesendanger, and E. Meyer, Eds., *Noncontact Atomic Force Microscopy*. Berlin, Heidelberg: Springer Berlin Heidelberg, 2002. doi: 10.1007/978-3-642-56019-4.

[32] N. Sasaki and M. Tsukada, ‘The Relation between Resonance Curves and Tip-Surface Interaction Potential in Noncontact Atomic-Force Microscopy’, *Jpn. J. Appl. Phys.*, vol. 37, no. Part 2, No. 5A, pp. L533–L535, May 1998, doi: 10.1143/JJAP.37.L533.

[33] R. Pérez, I. Štich, M. C. Payne, and K. Terakura, ‘Surface-tip interactions in noncontact atomic-force microscopy on reactive surfaces: Si(111)’, *Phys. Rev. B*, vol. 58, no. 16, pp. 10835–10849, Oct. 1998, doi: 10.1103/PhysRevB.58.10835.

[34] ‘Schneegans O, Chrétien P and Houzé F 2011 French Patent Specification FR 10 01940 International PCT WO 2011/ 138738’

[35] Z. L. Wang and J. Song, ‘Piezoelectric Nanogenerators Based on Zinc Oxide Nanowire Arrays’, *Science*, vol. 312, no. 5771, pp. 242–246, Apr. 2006, doi: 10.1126/science.1124005.

[36] G. Jacopin *et al.*, ‘Interplay of the photovoltaic and photoconductive operation modes in visible-blind photodetectors based on axial p-i-n junction GaN nanowires’, *Appl. Phys. Lett.*, vol. 104, no. 2, p. 023116, Jan. 2014, doi: 10.1063/1.4860968.

[37] J. Liu *et al.*, ‘Carrier Density and Schottky Barrier on the Performance of DC Nanogenerator’, *Nano Lett.*, vol. 8, no. 1, pp. 328–332, Jan. 2008, doi: 10.1021/nl0728470.

[38] N. Gogneau *et al.*, ‘GaN nanowires for piezoelectric generators: GaN nanowires for piezoelectric generators’, *Phys. Status Solidi RRL*, vol. 8, no. 5, pp. 414–419, May 2014, doi: 10.1002/pssr.201409105.

[39] N. Jegenyes *et al.*, ‘2 High piezoelectric conversion properties of axial 3 InGaN/GaN nanowires’, p. 13, 2018.

[40] N. Jamond *et al.*, ‘Piezo-generator integrating a vertical array of GaN nanowires’, *Nanotechnology*, vol. 27, no. 32, p. 325403, Aug. 2016, doi: 10.1088/0957-4484/27/32/325403.

[41] A. Vecchiola *et al.*, ‘Wide range local resistance imaging on fragile materials by conducting probe atomic force microscopy in intermittent contact mode’, *Appl. Phys. Lett.*, vol. 108, no. 24, p. 243101, Jun. 2016, doi: 10.1063/1.4953870.

[42] L. Largeau, E. Galopin, N. Gogneau, L. Travers, F. Glas, and J.-C. Harmand, ‘N-Polar GaN Nanowires Seeded by Al Droplets on Si(111)’, *Crystal Growth & Design*, vol. 12, no. 6, pp. 2724–2729, Jun. 2012, doi: 10.1021/cg300212d.

[43] M. D. Brubaker *et al.*, ‘Effect of AlN buffer layer properties on the morphology and polarity of GaN nanowires grown by molecular beam epitaxy’, *Journal of Applied Physics*, vol. 110, no. 5, p. 053506, Sep. 2011, doi: 10.1063/1.3633522.

[44] R. Songmuang, O. Landré, and B. Daudin, ‘From nucleation to growth of catalyst-free GaN nanowires on thin AlN buffer layer’, *Appl. Phys. Lett.*, vol. 91, no. 25, p. 251902, Dec. 2007, doi: 10.1063/1.2817941.

[45] S. Dasgupta, F. Wu, J. S. Speck, and U. K. Mishra, ‘Growth of high quality N-polar AlN (000 1 ¯) on Si(111) by plasma assisted molecular beam epitaxy’, *Appl. Phys. Lett.*, p. 4, 2014.

[46] K. Yasutake, A. Takeuchi, H. Kakiuchi, and K. Yoshii, ‘Molecular beam epitaxial growth of AlN single crystalline films on Si (111) using radio- frequency plasma assisted nitrogen radical source’, p. 9.

[47] T. B. Massalski, *Binary Alloy Phase Diagrams*, vol. 1. American Society For Metals, 1986.

[48] M. Tchernycheva *et al.*, ‘Growth of GaN free-standing nanowires by plasma-assisted molecular beam epitaxy: structural and optical characterization’, p. 8, 2007.

[49] D. N. Nath, E. Gür, S. A. Ringel, and S. Rajan, ‘Molecular beam epitaxy of N-polar InGaN’, *Appl. Phys. Lett.*, vol. 97, no. 7, p. 071903, Aug. 2010, doi: 10.1063/1.3478226.

[50] R. Calarco, R. J. Meijers, R. K. Debnath, T. Stoica, E. Sutter, and Hans. Lüth, ‘Nucleation and Growth of GaN Nanowires on Si(111) Performed by Molecular Beam Epitaxy’, *Nano Lett.*, vol. 7, no. 8, pp. 2248–2251, Aug. 2007, doi: 10.1021/nl0707398.

[51] K. A. Bertness, A. Roshko, L. M. Mansfield, T. E. Harvey, and N. A. Sanford, ‘Nucleation conditions for catalyst-free GaN nanowires’, *Journal of Crystal Growth*, vol. 300, no. 1, pp. 94–99, Mar. 2007, doi: 10.1016/j.jcrysgro.2006.10.209.

[52] R. K. Debnath, R. Meijers, T. Richter, T. Stoica, R. Calarco, and H. Lüth, ‘Mechanism of molecular beam epitaxy growth of GaN nanowires on Si(111)’, *Appl. Phys. Lett.*, vol. 90, no. 12, p. 123117, Mar. 2007, doi: 10.1063/1.2715119.

[53] R. Meijers *et al.*, ‘GaN-nanowhiskers: MBE-growth conditions and optical properties’, *Journal of Crystal Growth*, vol. 289, no. 1, pp. 381–386, Mar. 2006, doi: 10.1016/j.jcrysgro.2005.11.117.

[54] J.-K. Tsai *et al.*, 'Effect of N to Ga flux ratio on the GaN surface morphologies grown at high temperature by plasma-assisted molecular-beam epitaxy', *Journal of Applied Physics*, vol. 95, no. 2, pp. 460–465, Jan. 2004, doi: 10.1063/1.1634388.

[55] L. Largeau, D. L. Dheeraj, M. Tchernycheva, G. E. Cirlin, and J. C. Harmand, 'Facet and in-plane crystallographic orientations of GaN nanowires grown on Si(111)', *Nanotechnology*, vol. 19, no. 15, p. 155704, Apr. 2008, doi: 10.1088/0957-4484/19/15/155704.

[56] M. Morassi, 'Growth of InGaN nanowires for photovoltaic and piezoelectric energy harvesting', p. 225.

[57] O. Landré, C. Bougerol, H. Renevier, and B. Daudin, 'Nucleation mechanism of GaN nanowires grown on (111) Si by molecular beam epitaxy', *Nanotechnology*, vol. 20, no. 41, p. 415602, Oct. 2009, doi: 10.1088/0957-4484/20/41/415602.

[58] V. Consonni, M. Knelangen, L. Geelhaar, A. Trampert, and H. Riechert, 'Nucleation mechanisms of epitaxial GaN nanowires: Origin of their self-induced formation and initial radius', *Phys. Rev. B*, vol. 81, no. 8, p. 085310, Feb. 2010, doi: 10.1103/PhysRevB.81.085310.

[59] K. Hestroffer, C. Leclere, V. Cantelli, C. Bougerol, H. Renevier, and B. Daudin, '*In situ* study of self-assembled GaN nanowires nucleation on Si(111) by plasma-assisted molecular beam epitaxy', *Appl. Phys. Lett.*, vol. 100, no. 21, p. 212107, May 2012, doi: 10.1063/1.4721521.

[60] K. A. Bertness, A. Roshko, N. A. Sanford, J. M. Barker, and A. V. Davydov, 'Spontaneously grown GaN and AlGaN nanowires', *Journal of Crystal Growth*, vol. 287, no. 2, pp. 522–527, Jan. 2006, doi: 10.1016/j.jcrysgro.2005.11.079.

[61] E. Calleja *et al.*, 'Luminescence properties and defects in GaN nanocolumns grown by molecular beam epitaxy', *Phys. Rev. B*, vol. 62, no. 24, pp. 16826–16834, Dec. 2000, doi: 10.1103/PhysRevB.62.16826.

[62] K. A. Bertness *et al.*, 'Catalyst-free growth of GaN nanowires', *Journal of Elec Materi*, vol. 35, no. 4, pp. 576–580, Apr. 2006, doi: 10.1007/s11664-006-0102-4.

[63] M. A. Sanchez-Garcia *et al.*, 'The effect of the III/V ratio and substrate temperature on the morphology and properties of GaN- and AlN-layers grown by molecular beam epitaxy on Si(1 1 1)', *Journal of Crystal Growth*, vol. 183, no. 1–2, pp. 23–30, Jan. 1998, doi: 10.1016/S0022-0248(97)00386-2.

[64] J. K. Zettler *et al.*, 'High-Temperature Growth of GaN Nanowires by Molecular Beam Epitaxy: Toward the Material Quality of Bulk GaN', *Crystal Growth & Design*, vol. 15, no. 8, pp. 4104–4109, Aug. 2015, doi: 10.1021/acs.cgd.5b00690.

[65] L. Mancini *et al.*, 'Corrigendum: Optical properties of GaN nanowires grown on chemical vapor deposited-graphene (2019 *Nanotechnology* 30 214005)', *Nanotechnology*, vol. 31, no. 45, p. 459501, Nov. 2020, doi: 10.1088/1361-6528/abaade.

[66] V. Kumaresan *et al.*, 'Self-induced growth of vertical GaN nanowires on silica', *Nanotechnology*, vol. 27, no. 13, p. 135602, Apr. 2016, doi: 10.1088/0957-4484/27/13/135602.

[67] V. Kumaresan *et al.*, 'Epitaxy of GaN Nanowires on Graphene', *Nano Lett.*, vol. 16, no. 8, pp. 4895–4902, Aug. 2016, doi: 10.1021/acs.nanolett.6b01453.

[68] C. Barbier *et al.*, 'In Situ X-ray Diffraction Study of GaN Nucleation on Transferred Graphene', *Crystal Growth & Design*, vol. 20, no. 6, pp. 4013–4019, Jun. 2020, doi: 10.1021/acs.cgd.0c00306.

[69] M. Belloeil, 'Molecular beam epitaxy growth and optical characterization of GaN/AlGaN nanowire heterostructures emitting in the ultraviolet', p. 271.

[70] B. Daudin, F. Widmann, G. Feuillet, Y. Samson, M. Arlery, and J. L. Rouvière, 'Stranski-Krastanov growth mode during the molecular beam epitaxy of highly strained GaN', *Phys. Rev. B*, vol. 56, no. 12, pp. R7069–R7072, Sep. 1997, doi: 10.1103/PhysRevB.56.R7069.

[71] J. Ristic *et al.*, 'On the mechanisms of spontaneous growth of III-nitride nanocolumns by plasma-assisted molecular beam epitaxy', p. 14.

[72] E. Calleja *et al.*, 'Growth of III-nitrides on Si(111) by molecular beam epitaxy Doping, optical, and electrical properties', *Journal of Crystal Growth*, vol. 201–202, pp. 296–317, May 1999, doi: 10.1016/S0022-0248(98)01346-3.

[73] M. Yoshizawa, A. Kikuchi, N. Fujita, K. Kushi, H. Sasamoto, and K. Kishino, 'Self-organization of GaN/Al0.18Ga0.82N multi-layer nano-columns on (0 0 0 1) Al2O3 by RF molecular beam epitaxy for fabricating GaN quantum disks', *Journal of Crystal Growth*, vol. 189–190, pp. 138–141, Jun. 1998, doi: 10.1016/S0022-0248(98)00188-2.

[74] S. Fernández-Garrido *et al.*, 'Self-Regulated Radius of Spontaneously Formed GaN Nanowires in Molecular Beam Epitaxy', *Nano Lett.*, vol. 13, no. 7, pp. 3274–3280, Jul. 2013, doi: 10.1021/nl401483e.

[75] K. A. Bertness, A. Roshko, L. M. Mansfield, T. E. Harvey, and N. A. Sanford, 'Mechanism for spontaneous growth of GaN nanowires with molecular beam epitaxy', *Journal of Crystal Growth*, vol. 310, no. 13, pp. 3154–3158, Jun. 2008, doi: 10.1016/j.jcrysgro.2008.03.033.

[76] S. D. Carnevale, J. Yang, P. J. Phillips, M. J. Mills, and R. C. Myers, 'Three-Dimensional GaN/AlN Nanowire Heterostructures by Separating Nucleation and Growth Processes', *Nano Lett.*, vol. 11, no. 2, pp. 866–871, Feb. 2011, doi: 10.1021/nl104265u.

[77] C.-H. Wang *et al.*, 'Effects of Free Carriers on Piezoelectric Nanogenerators and Piezotronic Devices Made of GaN Nanowire Arrays', *Small*, vol. 10, no. 22, pp. 4718–4725, Nov. 2014, doi: 10.1002/smll.201400768.

[78] C.-H. Wang *et al.*, 'Optimization of the Output Efficiency of GaN Nanowire Piezoelectric Nanogenerators by Tuning the Free Carrier Concentration', *Adv. Energy Mater.*, vol. 4, no. 16, p. 1400392, Nov. 2014, doi: 10.1002/aenm.201400392.

[79] R. Hinchet, S. Lee, G. Ardila, L. Montès, M. Mouis, and Z. L. Wang, 'Performance Optimization of Vertical Nanowire-based Piezoelectric Nanogenerators', *Adv. Funct. Mater.*, vol. 24, no. 7, pp. 971–977, Feb. 2014, doi: 10.1002/adfm.201302157.

[80] X. Li, M. Sun, X. Wei, C. Shan, and Q. Chen, '1D Piezoelectric Material Based Nanogenerators: Methods, Materials and Property Optimization', *Nanomaterials*, vol. 8, no. 4, p. 188, Mar. 2018, doi: 10.3390/nano8040188.

[81] T. Stoica and R. Calarco, 'Doping of III-Nitride Nanowires Grown by Molecular Beam Epitaxy', *IEEE J. Select. Topics Quantum Electron.*, vol. 17, no. 4, pp. 859–868, Jul. 2011, doi: 10.1109/JSTQE.2010.2092416.

[82] T. Richter, H. L. R. Meijers, R. Calarco, and M. Marso, 'Doping Concentration of GaN Nanowires Determined by Opto-Electrical Measurements', *Nano Lett.*, vol. 8, no. 9, pp. 3056–3059, Sep. 2008, doi: 10.1021/nl8014395.

[83] F. Furtmayr *et al.*, 'Nucleation and growth of GaN nanorods on Si (111) surfaces by plasma-assisted molecular beam epitaxy - The influence of Si- and Mg-doping', *Journal of Applied Physics*, vol. 104, no. 3, p. 034309, Aug. 2008, doi: 10.1063/1.2953087.

[84] S. Nayak, R. Kumar, N. Pandey, K. K. Nagaraja, M. Gupta, and S. M. Shivaprasad, 'Enhanced radial growth of Mg doped GaN nanorods: A combined experimental and *first-principles* study', *Journal of Applied Physics*, vol. 123, no. 13, p. 135303, Apr. 2018, doi: 10.1063/1.5024278.

[85] A.-M. Siladie *et al.*, 'Dopant radial inhomogeneity in Mg-doped GaN nanowires', *Nanotechnology*, vol. 29, no. 25, p. 255706, Jun. 2018, doi: 10.1088/1361-6528/aabbd6.

[86] M. McLaurin, T. E. Mates, and J. S. Speck, 'Molecular-beam epitaxy of p-type m-plane GaN', *Appl. Phys. Lett.*, vol. 86, no. 26, p. 262104, Jun. 2005, doi: 10.1063/1.1977204.

[87] L. Lymperakis and J. Neugebauer, 'Large anisotropic adatom kinetics on nonpolar GaN surfaces: Consequences for surface morphologies and nanowire growth', *Phys. Rev. B*, vol. 79, no. 24, p. 241308, Jun. 2009, doi: 10.1103/PhysRevB.79.241308.

Chapter 3

Determining the piezo-conversion capacity of nitride nanowires

“Challenges and limitations of measurement method”

Contents

3.1. Introduction

Thanks to their excellent mechanical properties, higher flexibility and exalted piezoelectric coefficients (as discussed in Chapter 1), 1D-nanostructures are highly sought after nano-objects for fabricating ultra-compact and integratable energy generators for powering micro/nano devices. This potentiality has already been demonstrated by 1D-nanostructures based on ZnO [1], CdS [2], CdSe [3], PZT [4], GaAs [5], III-Nitrides [6]–[11]… having the ability to generate output voltages reaching up to several hundreds of mV. Based on these promising results, piezo-generators (PGs) integrating CdTe micro/nanowires [12], $BaTiO_3$ NWs [13], PMN-PT single NW [14], PVDF nanofibers [15], PZT nanofibers [16], ZnO NWs [17]–[20], GaN NWs [21]–[25]…can also be found in the literature with power densities reaching up to $\mu W/cm^2$ generated under a large range of mechanical actuation techniques[21], [24], [26], [27].

Firstly, the efficiency of piezo-generators (PGs) depends on the capacity of the piezoelectric media (here the NWs) to efficiently convert the mechanical deformation into an electrical signal. Hence, numerous studies have been made in the recent years to understand the piezo-conversion mechanism in the NWs using *in-situ* SEM/TEM techniques [28]–[32], AFM systems equipped with piezo-response module [33]–[36] or homemade piezo-conversion module [11], [37]–[40]. The functionalization [41], [42] and doping level control [43]–[45] have also been studied to improve the piezo-response of the nanostructures.

Secondly, the impedance of the external read-out circuit and the internal PG resistance plays a significant role in the optimisation of their power densities. Despite the strong influence of the load resistance (R_{load}) on the performances of ''classical'' transducers, its effect on the piezo-efficiencies of 1D-nanostructures based PGs has only recently gained attention [46], [47]. A handful of teams have successfully demonstrated that the external circuit impedance is an important limiting factor and have determined optimal R_{load} values corresponding to the maxima of generated powers [26], [48]–[52].

However, only the load resistance is considered, assuming that the internal impedance of the PG is negligible. For PGs presenting the capacitive configuration (*i.e.* the top electrode collecting the piezo-charges is not in direct contact with the NWs) [17], [48], [53], the output signal integrates the NW impedance. Therefore, only the R_{load} of the electronics influences the electrical response of the system. However, this is not the case for PGs with a Schottky configuration (*i.e.* the top electrode harvesting the piezo-charges is directly in contact with the NWs) [21], [54] or for single NWs (nanogenerators, NGs) investigated with AFM system where the AFM tip forms a Schottky contact with the NWs [4], [9], [10], [38]. In this scenario, the Schottky diode plays a critical role. Firstly, we have demonstrated that the classical behaviour of the Schottky diode cannot be applied to NWs [55]. Here, we are in the nanoscale regime, and thus, Schottky nano-contacts must be considered (as described in Chapter 1). Secondly, the NG's impedance is not inherently equivalent to the resistance of the NWs (R_{NW}), but a *minima*.

In this Chapter, we investigate the piezoelectric response of arrays of non-intentionally n-type and p-type doped GaN NWs by using an AFM, which has been specifically adapted to perform piezo-conversion measurements on single vertically oriented NWs. We experimentally establish the dependence of the output voltage (O.V.) signals on the external R_{load} in the nanoscale regime. We also stress on the non-negligible aspect of the nanogenerator's impedance, which is strongly dependent on the NW characteristics. Finally, we establish that the classical method considered here and in the literature permits to judge the piezoelectric conversion efficiency of the NWs, but with certain limitations, which implies the use of more adapted techniques in order to overcome them.

3.2. Experimental section

3.2.1. Synthesis and morphology of GaN nanowires

The growth of non-intentionally n-type and p-type doped GaN NWs (on n-type and p-type doped Si (111) substrates, respectively) has been done using the PA-MBE system (detailed in Chapter 2). Both GaN NW ensembles were grown under active nitrogen conditions with an N/Ga flux ratio of 1.36. Prior the growth of NWs, a thin AlN buffer layer was grown following the procedure described in [56] to achieve a better control of the nanowire nucleation, density and orientation [57]–[59]. Since PA-MBE grown GaN NWs are characterized by an n-type residual doping, the Mg cell was kept at 225 °C during the growth in order to induce a p-type residual doping of GaN NWs.

The morphology of the as-grown GaN NWs was studied using a scanning electron microscope (SEM) as shown in Fig. 1(a-b). The GaN NWs are vertically oriented along the [0001] direction with hexagonal cross-sections delimited by {10-10} planes [60] and exhibit a nitrogen polarity (N-polar) [39], [56]. Due to the self-assembled growth method used to synthesise the NWs, they are characterized by a height distribution while their diameter stays approximatively constant. The dimension of the as-grown NWs have been extracted from the SEM images, both in top and cross-sectional views, and are summarized in Table 1.

Table 1. Average dimensions (heights, diameters and densities) of the non-intentionally n-type and p-type doped GaN NWs measured from SEM images.

GaN NWs	**Height h_1 (nm)**	**Height h_2 (nm)**	**Diameter (nm)**	**Density (NW/cm^2)**
Non-intentionally n-doped	469 ± 118	678 ± 88	88 ± 21	6.8×10^8
Non-intentionally p-doped	553 ± 93	755 ± 85	36 ± 9	3.4×10^9

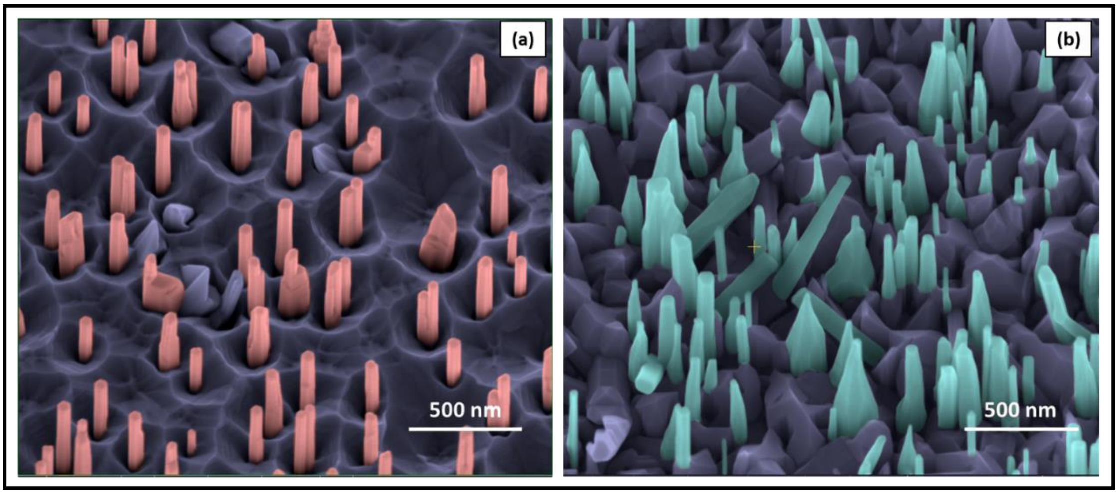

Figure 1. Scanning electron microscope (SEM) images of non-intentionally (a) n-doped and (b) p-doped GaN NWs, grown by PA-MBE.

3.2.2. AFM measurement principle and sample preparation

The GaN NWs have been studied under bending configuration using an AFM equipped with a Resiscope module [61], which has been adapted to realize piezoelectric conversion measurements [9] (Chapter 2_section 2.3.4). As a reminder, in this experimental configuration, no external bias has been applied and the output signals observed across R_{load} are purely generated by the NWs. In addition, this configuration allows a direct correlation of the topography and electrical mappings as they are recorded simultaneously. Thus, a statistical analysis of the piezo-electric response of individual NWs has been made while scanning the NW arrays. A schematic representation of the AFM system and a simplified equivalent electrical circuit are shown in Fig. 2(a-b). By simplified circuit, we mean that the nanogenerator (the NW) and the measurement load are described by purely resistive elements, R_g and R_{load}, respectively. Whereas in reality, there are also capacitive components, which make the analysis more complex due to the shortness of the voltage (peak) generated by each NW and that vary as a function of the NW characteristics (density, morphology, dimensions, doping…).

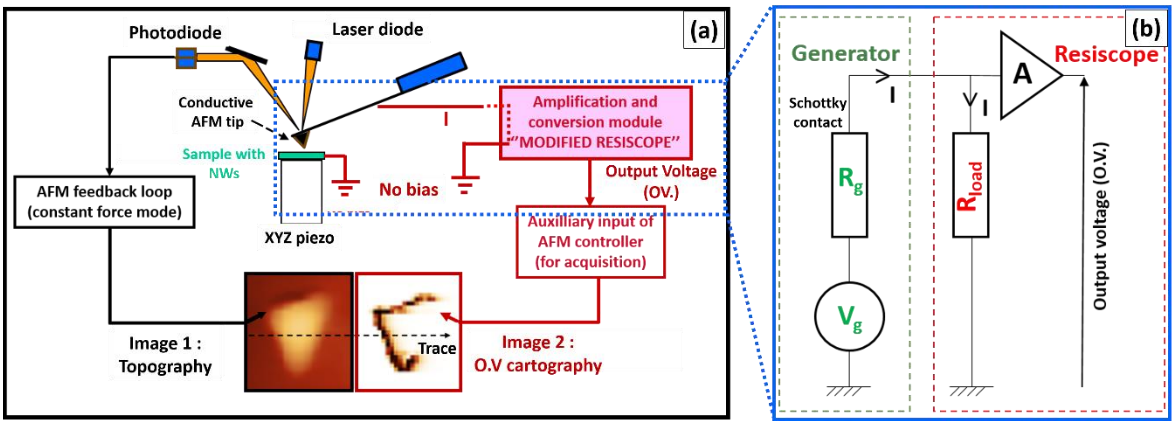

Figure 2. Schematic representation of (a) conductive AFM set-up with the modified Resiscope and (b) simplified electrical circuit representing the nanogenerator (a nanowire) and the modified Resiscope. No external bias is applied during the measurements.

A constant normal force (CNF) is applied via the conductive AFM tip as it scans over the vertically oriented GaN NWs in contact mode. As a result of this mechanical input, a lateral bending of the NW occurs and an electric field is created in the volume of the NW. The generated output voltage is simultaneously harvested via the AFM tip (here a CrPt AFM tip with a spring constant of 2 N/m), which forms a Schottky contact with the NW summit [62], while an Ohmic contact is established at the NW-substrate interface [63]. In order to collect the generated piezo-charges using this technique, a forward-biased Schottky contact is a pre-requisite. This in turn depends on the piezoelectric potential distribution in the NWs which is a characteristic of the NW polarity and the doping type [39]. In N-polar GaN NWs, the piezoelectric potential distribution evolves between V_S^- at the stretched NW facet and V_S^+ at its compressed side [39] (Fig. 3b). Hence, for n-doped GaN NWs, negative O.V. peaks are collected at the stretched side while for a p-type doping, positive O.V. peaks are collected at the compressed side (See chapter 1).

It must be noted that NWs with diameters less than 100 nm are very flexible and thus CNFs of the order of a few tens of nN can fold them towards other neighbouring NWs or even the substrate. This could degrade their piezo-responses due to the predominant leakage of the piezo-charges [9]. Therefore, the NWs are partially embedded in a polymer matrix (Fig. 3a), which does not apply any external strain to the surrounding NWs and provides a mechanical rigidity to the otherwise extremely flexible NWs [9].

AFM in tapping mode has been used to measure the average un-encapsulated heights of the NWs, which was 90 ± 30 nm and 200 ± 50 nm for intrinsically n-doped and p-doped GaN NWs respectively. The diameter of the NWs remain unaffected by the encapsulation.

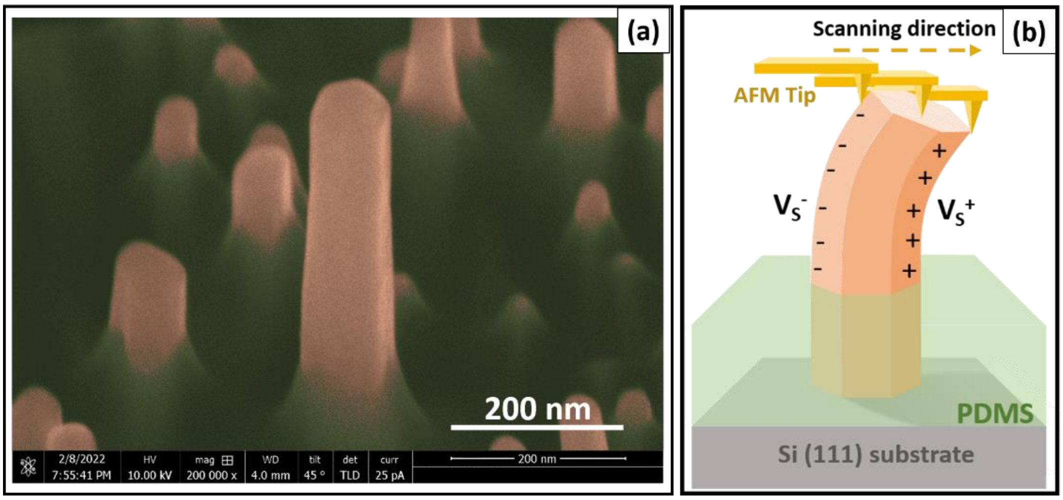

Figure 3. (a) SEM image of GaN NWs partially encapsulated in a flexible PDMS matrix and (b) schematic diagram showing the lateral deformation of a NW due to the externally applied CNF via the AFM tip during scanning. For N-polar GaN NWs, the piezopotential distribution within the NW volume evolves from V_S- to V_S+ from the stretched side to the compressed side of the NW.

3.3. Piezoelectric response of non-intentionally n-type and p-type doped GaN NWs as function of measurement load

The efficiency of piezoelectric generators firstly depends on the capacity of the piezoelectric media (here the NWs) to efficiently convert the mechanical deformation into an electrical signal. Moreover, other parameters inherent to the nanostructure, such as its doping level [43]–[45] and its dimensions [38], [64] also influence their piezo-electric response. In addition, it has been demonstrated that the energy harvesting efficiency is strongly affected by the Schottky nano-contact formed at the NW-AFM tip interface [55].

However, there is another parameter, which is known to play a significant role in the charge collection capacity of the system, namely the readout resistance of the circuit, or the so-called load resistance (R_{load}). In order to take full advantage of the piezo-generation capacity of 1D-nanostructures, it is crucial to study their piezo-conversion properties in the nanoscale regime using an optimised measurement system.

In this section, we focus on the first-ever investigation of the influence of R_{load} on the piezo-response of individual n-type and p-type doped GaN NWs. This type of investigation has already been carried out on piezoelectric devices [26], [48]–[52].

3.3.1. Evolution of output voltages generated by GaN NWs

By using the home-made AFM system equipped with a modified Resiscope in contact mode, O.V. peaks are recorded as a function of CNF varying between 120 nN and 380 nN. A range of R_{load} values from 1 MΩ to 1 GΩ were used for these measurements. Fig. 4 (a-h) presents the 3D mappings of output voltages generated by the two undertaken sets of NWs for two representative CNFs of 160 nN and 330 nN at R_{load} values of 10 MΩ and 1 GΩ. In these mappings, each O.V peak corresponds to the piezo-electric response of a single GaN NW.

The statistical analysis of the electrical maps is performed by extracting the O.V. values generated by individual NWs for each testing condition. These values are then distributed under a histogram and follow a Gaussian fitting within the limits of statistical error. Fig. 5 presents the generated average output voltages as a function of applied CNF for the chosen R_{load} range (1 MΩ to 1 GΩ) for both types of NWs.

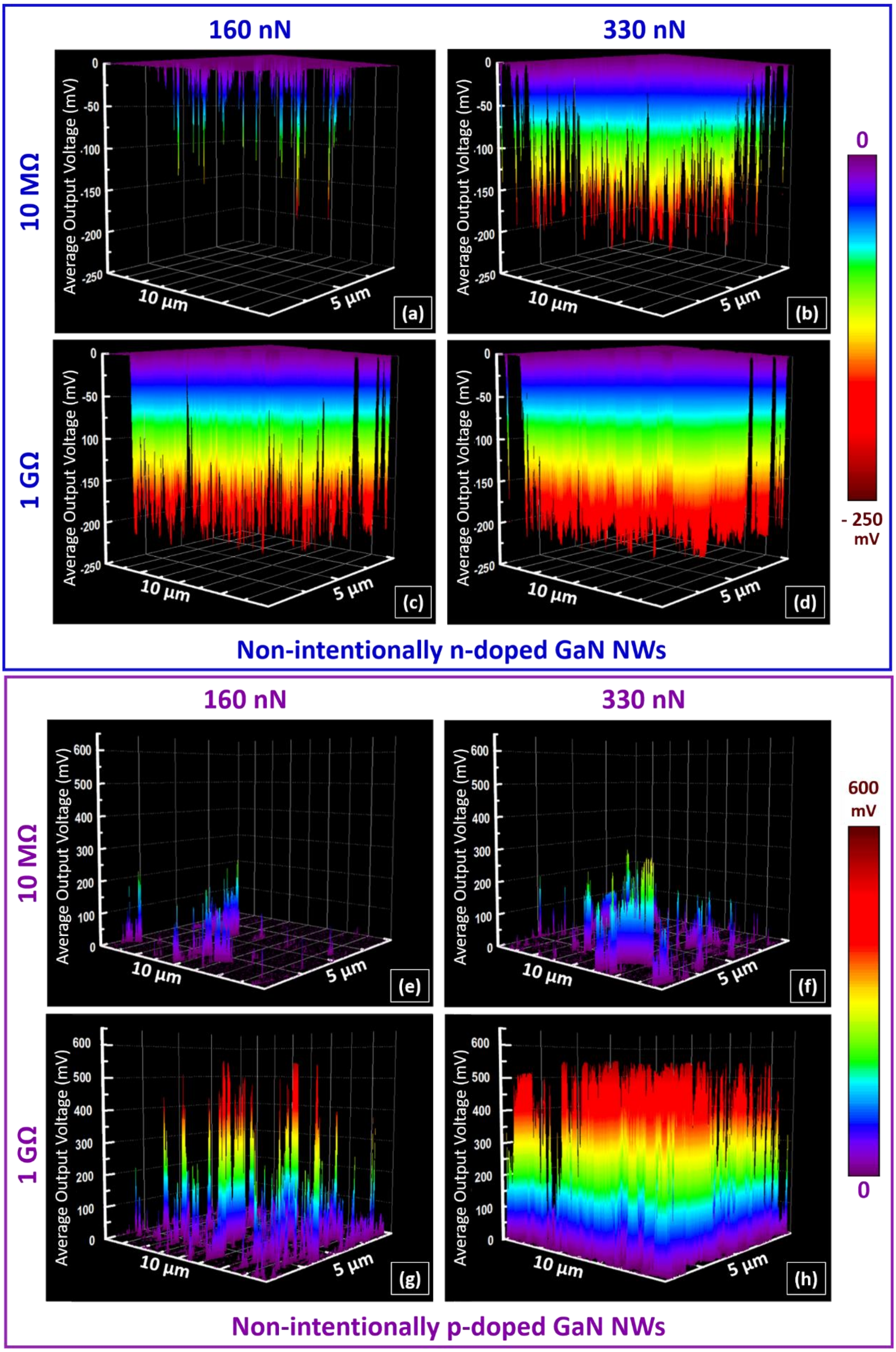

Figure 4. 3D representations of AFM electrical mappings of O.V.s at R_{load} *of 10 MΩ and 1 GΩ and for applied CNFs of 160 nN and 330 nN generated by non-intentionally (a)-(d) n-doped; and (e)-(h) p-doped GaN NWs. An increment of the output voltages is observed with the increase in applied CNF and* R_{load} *values for both types of NWs.*

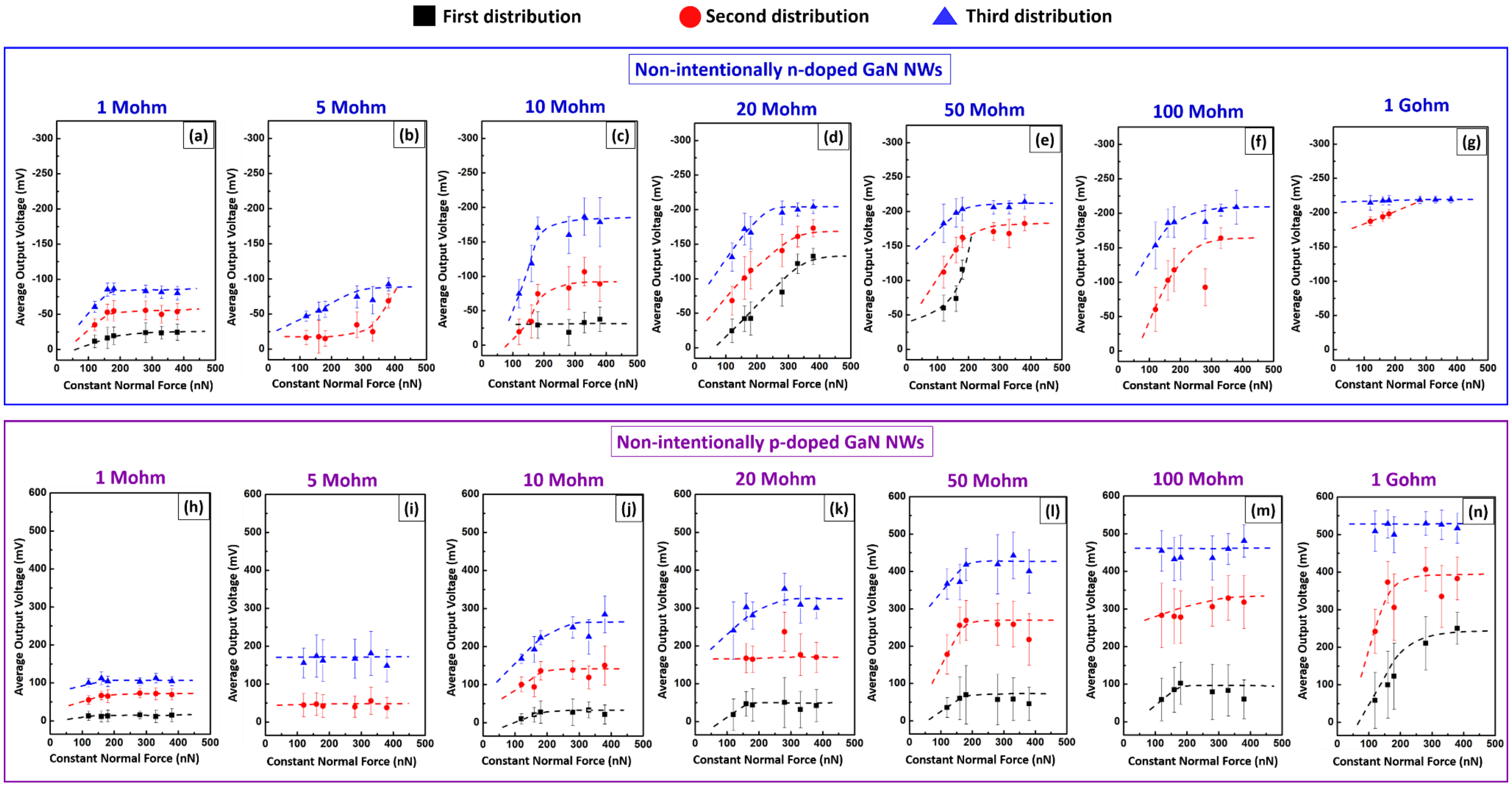

Figure 5. Evolution of the average O.V.s generated by non-intentionally (a–g) n- type doped; and (h-n) p-type doped GaN NWs, as a function of CNF for different R_{load} values.

If we analyse the results from the point of view of the piezoelectric response of the GaN NWs (Fig. 4 and Fig. 5), we observe several *"classical"* behaviours.

Firstly, n-type and p-type doped GaN NWs generate negative and positive O.V. respectively, which is in full agreement with their non-intentional doping obtained with our growth conditions [9], [21], [65].

Secondly, a multi-modal distribution of the average O.V. is observed in all cases. The piezo-response of NWs is directly related to their degree of deformation and thus to their dimensions. Due to the self-assembled growth mode used to synthesis the NWs, they are characterised by a small dispersion in their heights (while their diameters remain unchanged), and thus, have different stiffness values. Consequently, under equivalent external mechanical inputs (here the applied CNF in scanning mode), the NWs exhibit a different deformation rate, leading to a dispersion of their output signals. In our case, the first distribution corresponds to the most rigid set of NWs while the second and third distributions consist of comparatively flexible NWs, as discussed in previously published results [10], [38].

Thirdly, whatever the type of NW doping, an increase of the O.V. with increasing CNF is observed for each distribution. This behaviour is explained by two phenomena: (i) *the direct piezoelectric effect*: as the NW deformation increases, the piezoelectric potential increases, in agreement with experimental reports [9], [11] and theoretical predictions [66]; (ii) *improvement of metal-semiconductor contact stability*: as the force applied by the conductive AFM tip increases, the surface of the contact (through which the O.V. is harvested) increases, leading to a better harvesting efficiency [55], [67]. As for the O.V. saturation phenomena, observed for different CNF values depending on the NW dimensions, it can be explained by a saturation of the internal electric field inside the NWs, resulting from the complete rotation of electric dipoles [11], [68].

Fourthly, the fact that the O.V. generated by p-type doped GaN NWs are systematically higher than the ones generated by n-type doped NWs can be attributed to: (i) the *difference in the un-encapsulated average height of NWs* : the p-doped GaN NWs have an average height higher than the n-doped NWs ($H_{\mathbf{p\text{-}GaN}}$ = 200 ± 50 nm > $H_{\mathbf{n\text{-}GaN}}$ = 90 ± 30 nm). Thus under an equivalent mechanical input, the p-doped GaN NWs generate higher O.V. due to the creation of a stronger internal piezoelectric field; (ii) the *difference in residual doping concentration*: although both sets of GaN NWs present a residual type doping, the level of doping can be mildly different. For a higher residual doping, the concentration of free charge carriers will be slightly higher, inducing a more pronounced screening of the piezoelectric charges and thus a reduction of the piezoelectric response.

Finally, the average O.V. generated by both sets of GaN NWs evolved between several tens and hundreds of mV as detailed in Tables 2 to 8. Despite the doping type in the NWs and the employed R_{load}, the O.V. values either equalize, or exceed those generated by various other single 1D-nanostructures, such as ZnS [69], CdS [2], CdSe [3], CdTe [12], GaAs [5] and ZnO nanowires [70]. Especially, for p-doped GaN NWs, the average values yielded by the AFM system can reach more than 442 ± 62 mV for an R_{load} value of 50 Mohm and up to 529 ± 30 mV at 1 Gohm respectively. These values settle a new state-of-the-art for piezoelectric generation by 1D-nanostructures.

The following tables recapitulate the average O.V. values generated by non-intentionally n-doped and p-doped GaN NWs as a function of CNFs at R_{load} values ranging between 1 MΩ and 1 GΩ.

Table 2. R_{load} = 1 MΩ

	Average O.V. (mV) **Non-intentionally n-doped GaN NWs**			**Average O.V. (mV)** **Non-intentionally p-doped GaN NWs**		
CNF (nN)	1st distribution	2nd distribution	3rd distribution	1st distribution	2nd distribution	3rd distribution
120	-12 ± 9	-35 ± 8	-61 ± 8	13 ± 13	55 ± 11	100 ± 11
160	-16 ± 15	-53 ± 11	-85 ± 9	11 ± 14	67 ± 11	112 ± 17
180	-19 ± 12	-55 ± 14	-86 ± 8	13 ± 15	65 ± 17	104 ± 14
280	-28 ± 14	-56 ± 13	-83 ± 9	15 ± 10	73 ± 12	103 ± 10
330	-24 ± 9	-55 ± 13	-81 ± 9	11 ± 16	71 ± 15	113 ± 13
380	-25 ± 12	-54 ± 12	-80 ± 10	15 ± 17	69 ± 15	104 ± 12

Table 3. R_{load} = 5 MΩ

	Average O.V. (mV) **Non-intentionally n-doped GaN NWs**			**Average O.V. (mV)** **Non-intentionally p-doped GaN NWs**		
CNF (nN)	1st distribution	2nd distribution	3rd distribution	1st distribution	2nd distribution	3rd distribution
120	-	-17 ± 10	-47 ± 7	-	44 ± 31	155 ± 40
160	-	-17 ± 23	-55 ± 12	-	47 ± 30	174 ± 56
180	-	-15 ± 11	-57 ± 11	-	42 ± 30	162 ± 55
280	-	-35 ± 18	-74 ± 16	-	40 ± 28	167 ± 51
330	-	-25 ± 14	-70 ± 19	-	56 ± 36	181 ± 58
380	-	-69 ± 10	-92 ± 9	-	38 ± 27	148 ± 42

Table 4. R_{load} = 10 MΩ

	Average O.V. (mV) **Non-intentionally n-doped GaN NWs**			**Average O.V. (mV)** **Non-intentionally p-doped GaN NWs**		
CNF (nN)	1st distribution	2nd distribution	3rd distribution	1st distribution	2nd distribution	3rd distribution
120	-	-19 ± 18	-75 ± 20	10 ± 13	100 ± 20	168 ± 12
160	-	-34 ± 24	-118 ± 26	20 ± 19	94 ± 26	192 ± 34
180	-29 ± 19	-75 ± 14	-170 ± 16	28 ± 29	136 ± 24	223 ± 19
280	-19 ± 19	-83 ± 31	-160 ± 27	27 ± 35	138 ± 24	250 ± 28
330	-33 ± 15	-107 ± 21	-186 ± 27	33 ± 21	118 ± 30	226 ± 45
380	-37 ± 18	-89 ± 25	-178 ± 35	21 ± 25	150 ± 51	284 ± 48

Table 5. R_{load} *= 20 MΩ*

	Average O.V. (mV) **Non-intentionally n-doped GaN NWs**			**Average O.V. (mV)** **Non-intentionally p-doped GaN NWs**		
CNF (nN)	1st distribution	2nd distribution	3rd distribution	1st distribution	2nd distribution	3rd distribution
120	-24 ± 17	-68 ± 21	-131 ± 21	18 ± 42	-	240 ± 76
160	-42 ± 18	-101 ± 31	-172 ± 23	47 ± 33	168 ± 38	302 ± 37
180	-42 ± 24	-112 ± 27	-167 ± 23	44 ± 43	165 ± 35	280 ± 36
280	-80 ± 20	-141 ± 23	-195 ± 17	50 ± 66	237 ± 51	350 ± 42
330	-122 ± 14	-161 ± 15	-200 ± 9	31 ± 48	177 ± 55	309 ± 49
380	-132 ± 12	-173 ± 13	-204 ± 10	42 ± 42	170 ± 40	300 ± 28

Table 6. R_{load} *= 50 MΩ*

	Average O.V. (mV) **Non-intentionally n-doped GaN NWs**			**Average O.V. (mV)** **Non-intentionally p-doped GaN NWs**		
CNF (nN)	1st distribution	2nd distribution	3rd distribution	1st distribution	2nd distribution	3rd distribution
120	-60 ± 19	-112 ± 23	-183 ± 28	35 ± 27	178 ± 52	367 ± 41
160	-74 ± 18	-144 ± 18	-198 ± 21	60 ± 57	256 ± 49	371 ± 48
180	-116 ± 4	-162 ± 15	-203 ± 17	69 ± 78	269 ± 54	418 ± 43
280	-	-171 ± 13	-206 ± 10	57 ± 68	258 ± 56	419 ± 79
330	-	-168 ± 21	-206 ± 10	58 ± 57	258 ± 61	442 ± 62
380	-	-183 ± 10	-214 ± 11	45 ± 45	218 ± 69	400 ± 59

Table 7. R_{load} *= 100 MΩ*

	Average O.V. (mV) **Non-intentionally n-doped GaN NWs**			**Average O.V. (mV)** **Non-intentionally p-doped GaN NWs**		
CNF (nN)	1st distribution	2nd distribution	3rd distribution	1st distribution	2nd distribution	3rd distribution
120	-	-60 ± 32	-153 ± 34	59 ± 57	283 ± 85	454 ± 54
160	-	-102 ± 29	-186 ± 20	85 ± 59	280 ± 73	432 ± 57
180	-	-118 ± 31	-187 ± 22	102 ± 56	278 ± 70	436 ± 59
280	-	-93 ± 27	-187 ± 25	79 ± 73	306 ± 52	435 ± 59
330	-	-164 ± 15	-204 ± 9	83 ± 68	329 ± 59	459 ± 41
380	-	-	-209 ± 24	60 ± 52	318 ± 70	480 ± 44

Table 8. R_{load} = 1 GΩ

	Average O.V. (mV) **Non-intentionally n-doped GaN NWs**			**Average O.V. (mV)** **Non-intentionally p-doped GaN NWs**		
CNF (nN)	1st distribution	2nd distribution	3rd distribution	1st distribution	2nd distribution	3rd distribution
120	-	-187 ± 6	-214 ± 11	58 ± 75	242 ± 58	509 ± 54
160	-	-194 ± 7	-217 ± 6	100 ± 89	373 ± 55	528 ± 37
180	-	-198 ± 6	-218 ± 7	123 ± 88	306 ± 88	499 ± 48
280	-	-	-218 ± 5	211 ± 71	407 ± 58	529 ± 31
330	-	-	-219 ± 5	-	335 ± 82	526 ± 39
380	-	-	-219 ± 5	250 ± 42	383 ± 57	517 ± 40

If now, the results are analysed from an 'energy-harvesting' point of view, a strong impact of the R_{load} is observed. For a clear illustration of this impact, we have plotted the variation of the average O.V. as a function of the R_{load} for a few representative CNFs (Fig. 6). The dashed lines have been simulated using the least square method to fit the output voltage curves with analytical expressions. The latter have been patterned relative to the response of each nanowire as expressed in Eq. (1), and thus serve as a visual indication of the O.V. evolution.

From the simplified electrical circuit in Fig. 2(b), the O.V. collected at R_{load} for each individual NW '*i*' is given as follows:

$$(O.V.)_i = V_i = \frac{(V_g)_i \times R_{load}}{(R_g)_i + R_{load}} \qquad (1)$$

where, $(V_g)_i$ is the O.V generated by the individual NW '*i*' in "*open-circuit conditions*" (in practice we consider the values for R_{load}=1 GΩ) and $(R_g)_i$ is the internal resistance of the nanogenerator. Once again, this description is simplified because we are thinking in terms of pure resistance and not impedance. With the increase in R_{load}, the O.V. values present an asymptote, while they significantly decrease when the R_{load} becomes presumably smaller than the resistance of the generator itself, hence limiting the measurement efficiency of the electrical system. We want to emphasize here that in the following discussions, only the second and the third distributions have been considered, the first one being too difficult to be measured accurately at low R_{load} values.

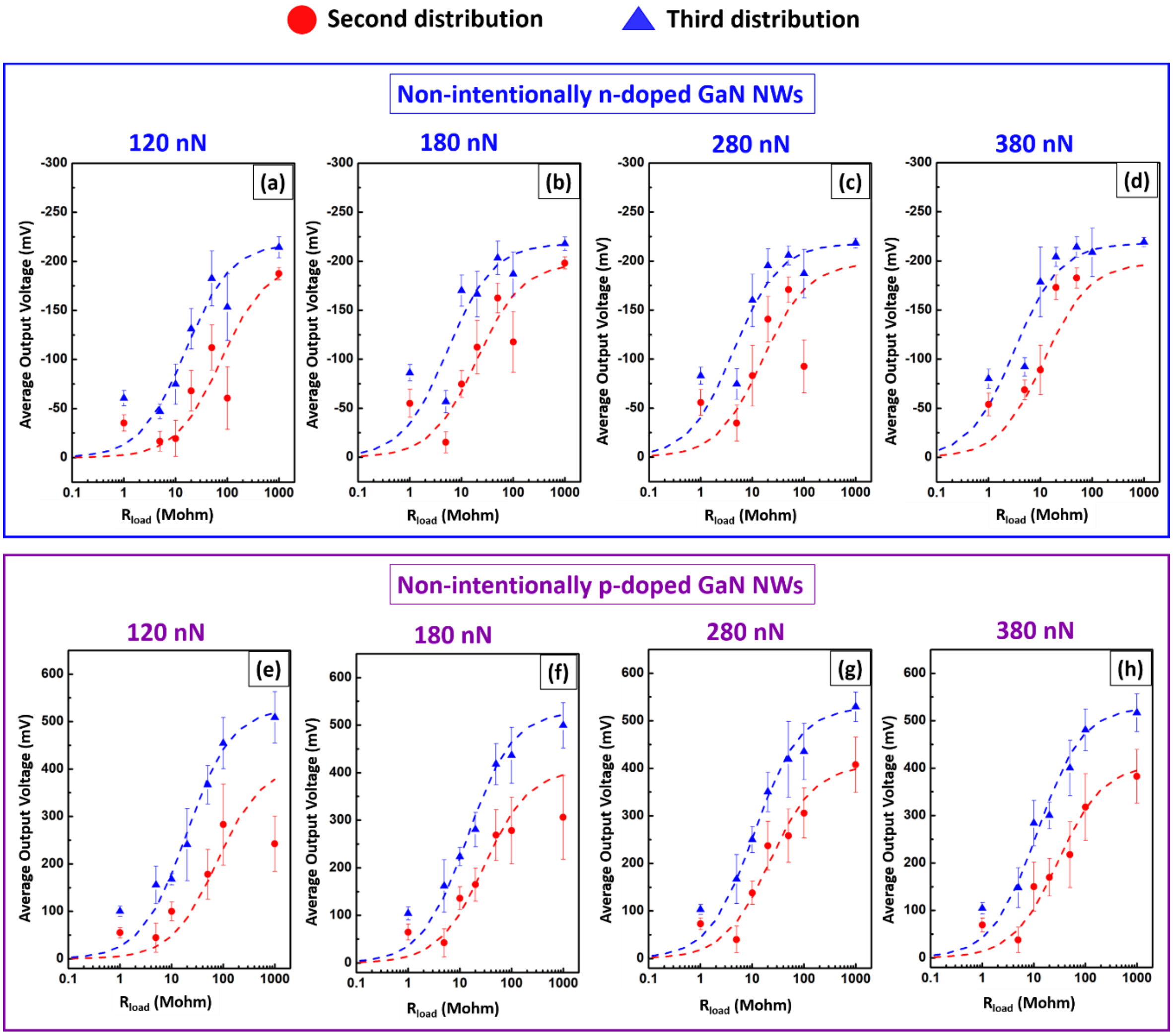

Figure 6. Variation of the average O.V. for the 2nd and the 3rd distributions generated by (a-d) non-intentionally n- type doped and (e-h) non-intentionally p-type doped GaN NWs as a function of R_{load} and for CNF values of 120 nN, 180 nN, 280 nN and 380 nN. The dashed lines have been simulated using least squares method to fit the data with analytical law of the same form as Eq. (1) as a visual indication of the output voltage evolution.

3.3.2. Power generation capacity of GaN NWs

In literature, the piezoelectric efficiencies of 1D-nanostructures are judged by the values of generated output voltages, which are usually measured at resistive loads of 100 MΩ or 500 MΩ of the conductive AFM setup (see Table 1 of Chapter 1). As demonstrated in the previous section, the obtained O.V. values are highly dependent on the selected R_{load} value amongst other parameters inherent to the 1D-nanostructures (material type, morphology…). Therefore, we can presume that the O.V. values found in literature might not be representative of the actual piezo-generation capacities of the corresponding 1D nanostructures. Consequently, a direct comparison of the piezoelectric efficiencies of various 1D nanostructures is challenging.

For micro-systems based on 1-D nanostructures, some authors have proposed the optimisation of the measurement set-up by plotting instantaneous power as a function of a range of R_{load} values [48], [49], [71], [72]. We have tried to do the same for our individual nanowires.

The instantaneous power values are calculated using the following relation:

$$P_i = \frac{V_i^2}{R_{load}} \qquad (2)$$

where V_i is the instantaneous peak voltage generated by individual NW '*i*' across a given R_{load}. On the basis of what has been observed for micro-systems, it is expected that the evolution of P_i as a function of R_{load} is described by a bell-shaped curve as schematically drawn in Fig. 7. In this condition, the maximum read-out power (P_{max}) is obtained only when the applied R_{load} is equivalent to the internal resistance of the system. An optimal value of the external load resistance is thus obtained, which inherently depends upon the characteristics of the (micro or nano) system under study.

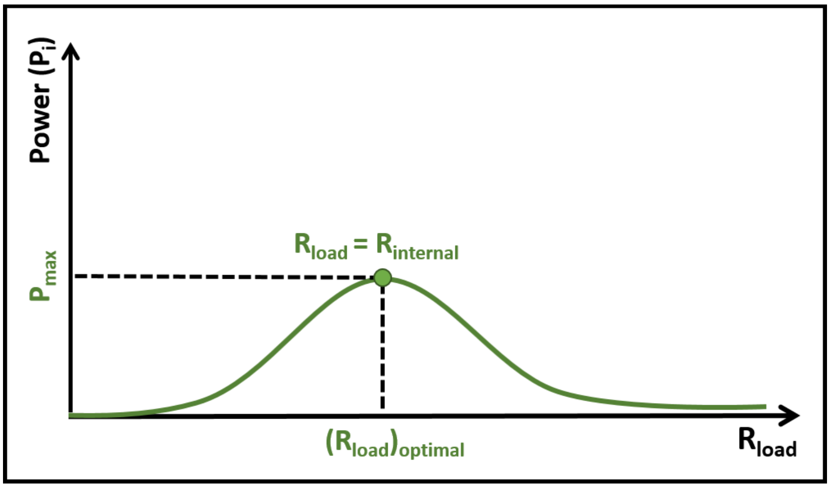

Figure 7. Theoretical representation of the power curve as a function of R_{load}. The maximum of the power curve is obtained when applied R_{load} is equal to internal resistance of the system under study.

We have employed this method to access the actual generation capacity of our NWs at an optimal R_{load} value. With the current AFM configuration used in this study, this method should allow us to obtain the value of generator resistance 'R_g', which is often neglected for NGs in the literature.

Fig. 8 presents the calculated power curves as a function of R_{load} with values ranging from 1MΩ to 1 GΩ for both types of NWs. For a given CNF and R_{load}, the power values are spread under a histogram having a bi-modal distribution. The average power values for each distribution are then extracted from the Gaussian fitting of these histograms.

From the analysis of these curves, we primarily observe that the average power values are of the order of a few nW for both sets of NWs. In addition, we note that the average power values of the 3rd distribution are systematically higher than the 2nd one, irrespective of the doping type of the NWs and the applied CNF. This behaviour is in agreement with the higher O.V. generated by the more flexible NWs of the 3rd distribution than the 2nd distribution.

If the shapes of the curves are compared to the theoretical curve (Fig. 7), we observe a non-classical behaviour, and the curves can be divided into two regimes. At higher R_{load} values (Regime 2 or R2), the classical bell-shape of the power curve is quasi-systematically obtained, while at lower R_{load} values (Regime 1 or R1) a sudden increase of the average power values is observed.

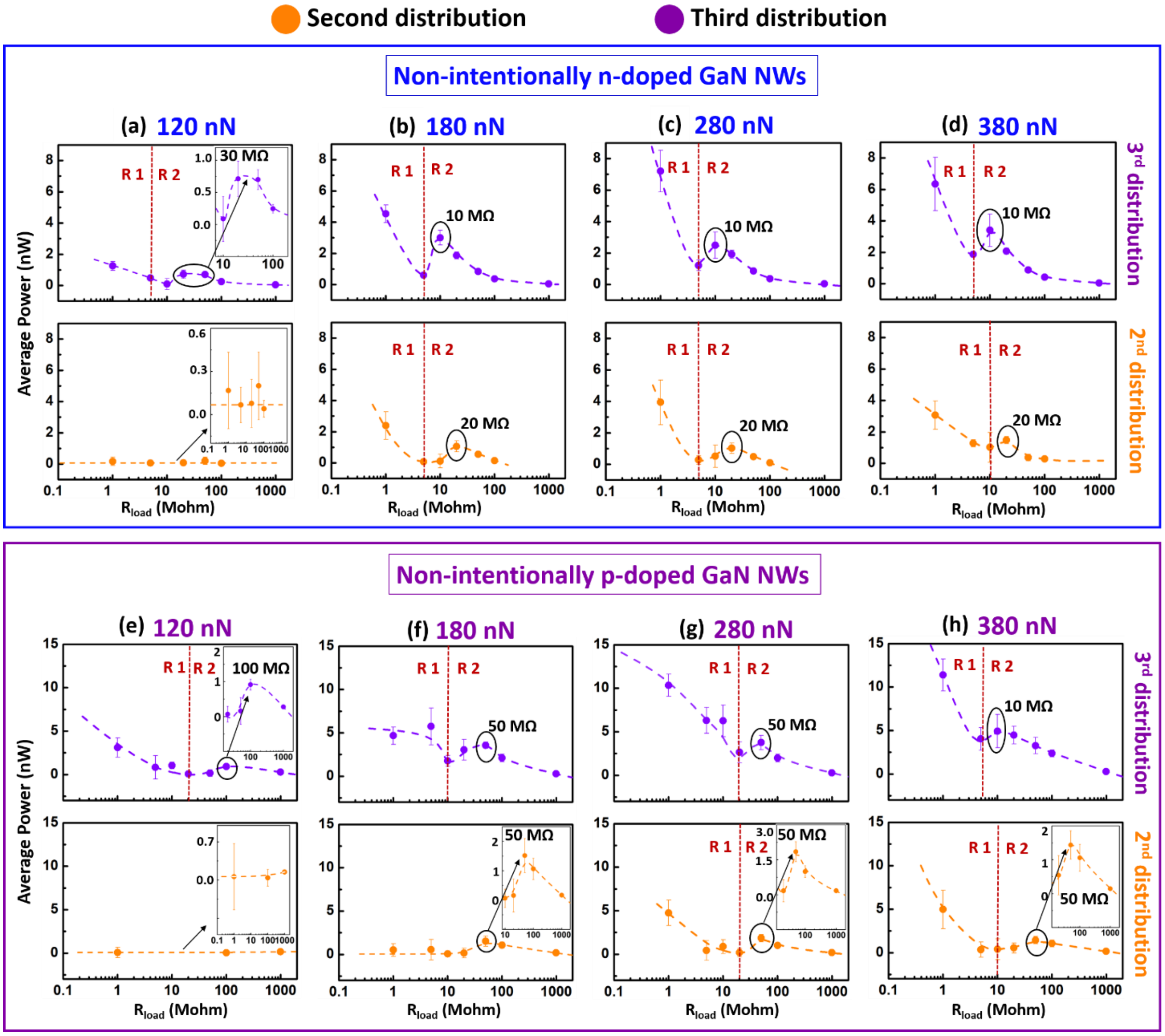

Figure 8. Evolution of the average power generated by non-intentionally (a-d) n- type doped and (e-h) p-type doped GaN NWs as a function of R_{load} and for CNF values of 120 nN, 180 nN, 280 nN and 380 nN. The images in the inset, when presented, show the zoom-in view of the maxima of the power curves. The dashed lines separates the two regimes of the power curves: the non-classical regime R1 and the classical regime R2.

Regime 1 (R1)

This 'non-classical' regime demonstrates a strong deviation from the theoretical power curves found in the literature. One might attribute this unclassical behaviour to the poor collection efficiency of the measurement system at lower R_{load} values. However, we can observe from Fig. 6 that significant O.V. up to several tens of mV were obtained for lower R_{load} values. Even though a stagnation of O.V. is seen at lower R_{load} values for certain CNFs and NW type, it is clearly not the case throughout the measurements. The O.V. increases with the increment of CNF at lower R_{load} values and is not a part of the background noise. Therefore, we can overrule this phenomenon to be the cause of the observed unclassical behaviour in our curves. This behaviour is observed irrespective of the doping type and the deformation rate of the NWs under study. This suggests that there is another parameter principally driving these evolutions. To this date, we have not been able to elucidate this behaviour, and new measurements must be organized for its thorough understanding.

Regime 2 (R2)

This regime shows the maxima of the average power curves at an "optimal R_{load}" of the measurement system. From a theoretical point of view, this optimal value is presumed to be equal to the average R_g associated to the NGs for each distribution, which is of the order of several tens of MΩ, and hence non-negligible. We can observe that the optimal R_{load} values globally decrease with the increase of the deformation rate (CNF) for each doping type and the degree of flexibility of NWs (recapitulated in Table 9). Moreover, for equivalent applied CNFs, the optimal value varies as a function of the NW stiffness (higher for 2nd distribution than the 3rd one, for both sets of NWs). Finally, for a given CNF and NW distribution, the optimal R_{load} values depend on the NW doping (higher for p-doped NWs).

Table 9. Optimal R_{load} values for the 2nd and the 3rd distributions of non-intentionally n-type and p-type doped GaN NWs at the applied CNF values.

	Non-intentionally n-doped GaN NWs		***Non-intentionally p-doped GaN NWs***	
CNF (nN)	*2nd distribution*	*3rd distribution*	*2nd distribution*	*3rd distribution*
120	*-*	*30 MΩ*	*-*	*100 MΩ*
160	*30 MΩ*	*20 MΩ*	*100 MΩ*	*100 MΩ*
180	*20 MΩ*	*10 MΩ*	*50 MΩ*	*50 MΩ*
280	*20 MΩ*	*10 MΩ*	*50 MΩ*	*50 MΩ*
330	*20 MΩ*	*10 MΩ*	*50 MΩ*	*30 MΩ*
380	*20 MΩ*	*10 MΩ*	*50 MΩ*	*10 MΩ*

Fig. 9 represents the evolution of the optimal R_{load} as a function of the CNF, which corresponds to R_g from a theoretical point of view. We observe a global decrease of the optimal R_{load} on increasing the CNF irrespective of the NW doping and the applied deformation.

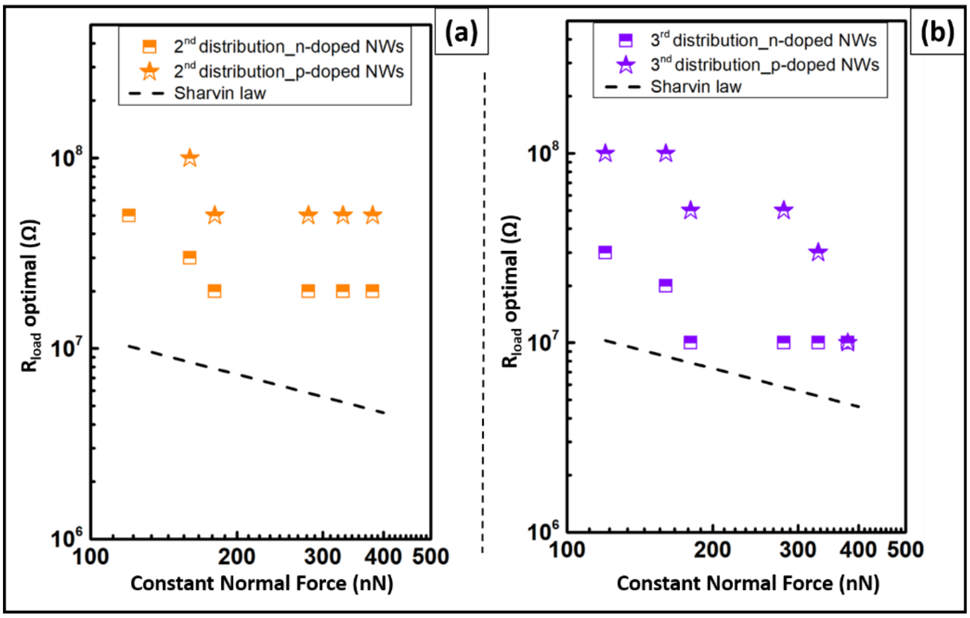

Figure 9. Optimal R_{load} values as a function of CNF for the (a) 2nd distribution (in orange) and (b) 3rd distribution (in purple), for both sets of NWs. The dashed line illustrates the evolution of contact resistance following the Sharvin's law (only the slope, not the values, should be considered).

At this point, to understand this particular trend, we are led to question what R_g represents. In the literature, R_g is considered to be solely the internal resistance of the NW. However, considering the O.V. measurement technique in our setup via the tip/NW Schottky contact, R_g can be expressed as the sum of three components: the tip/NW contact resistance (R_C), the Schottky diode resistance (R_D) associated to this contact and the intrinsic NW resistance (R_{NW}) (Eq. 3).

$$R_g = R_c + R_D + R_{NW} \tag{3}$$

However, it is very difficult to quantify the contribution of these components, thus, we limit ourselves to general considerations.

Here, we discuss each component individually:

Internal resistance of the NWs (R_{NW})

Amongst the three components, R_{NW} has no objective reason to vary with force. The R_{NW} depends on the doping levels [43]–[45] and the surface charges [43], [73], which do not vary while the measurements are being performed.

Contact resistance (R_C)

Firstly, we have employed the Hertz theory to estimate the contact size between an AFM tip and the summit of a NW, by assimilating the tip apex to a sphere. This theory describes a regime of purely elastic deformation between two ideally smooth solids, in the absence of adhesion and friction. Under these conditions, the mechanical contact surface between a sphere of radius R and a plane, which is a disc with radius 'a', is given by the expression:

$$a = \left(\frac{3}{4}\frac{F\,R}{E^{*}}\right)^{\frac{1}{3}} \tag{4}$$

where, *F* denotes the CNF and *E** is the reduced Young's modulus of the two materials defined by:

$$\frac{1}{E^{*}} = \left(\frac{1-\nu_1^2}{E_1}\right) + \left(\frac{1-\nu_2^2}{E_2}\right) \tag{5}$$

E_1, E_2 and ν_1, ν_2 being respectively the Young's modulus and Poisson's ratio of the two materials [74]. It can be seen from Eq. 4 that the Hertz contact radius varies with the applied force to the power 1/3. For a CrPt AFM tip of radius *R*=25 nm used in this study, the order of magnitude of '*a*' is a few nanometers for an applied force of a few hundred nN (Fig. 10).

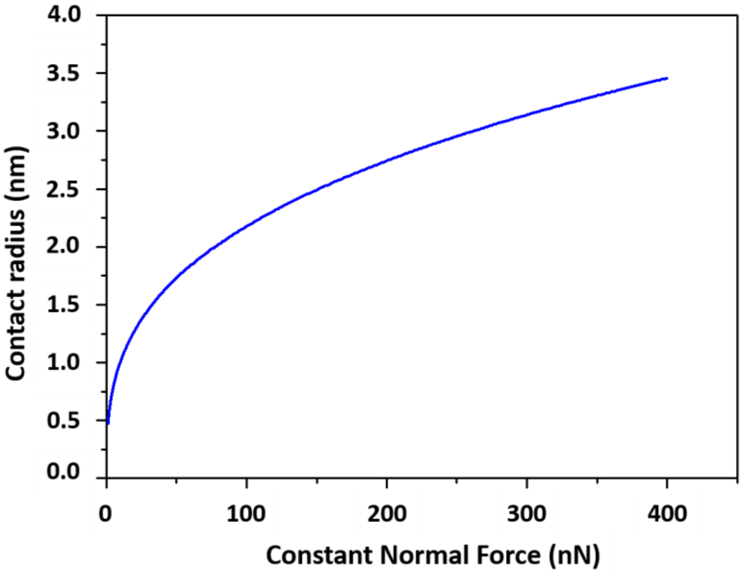

Figure 10. Calculated Hertzian contact radius for a CrPt tip (R=25nm) on a GaN sample.

Within such conditions, where the contact dimension is lower than the electron mean free path (of the order of a few tens of nm), the electrical transport regime is ballistic and the contact resistance can then be estimated using Sharvin's law:

$$R_C = \frac{4\,\rho\,\ell}{3\,\pi\,a^2} \tag{6}$$

where, ρ denotes the electrical resistivity and ℓ is the electron mean free path [75]. The combination of Eq. 4 and 6 leads to the expected variation of R_C with the applied force to the power -2/3. This evolution has been illustrated in Fig.9 by the dashed lines.

Hence, with the increase in the applied CNF, the contact resistance decreases and as a result the collection efficiency of the generated piezo-charges by the AFM tip increases.

Schottky diode resistance (R_D)

The Schottky diode resistance (R_D) is a function of the Schottky barrier height (SBH) (φ_B). We observe in Fig. 10 from the Hertz theory that the contact radius is of the order of a few nm only, which is smaller than the depletion width in the NWs (20-80 nm depending on the doping level of the NWs) [73], [76], [77]. Hence, the classical description of Schottky diode contact cannot be applied. Here, we are in the nano-contact regime, where the SBH becomes a function of the diode size [55] and the tunneling effect becomes predominant [78], [79]. Fig.10 shows that the contact radius increases with the increase of applied CNF, which in turn increases the thickness of the SBH [55]. Hence, the tunneling effect is less dominant and consequently leads to a less-efficient piezo-charges collection.

In Fig. 9, the optimal R_{load} values are in the range of 10^7-10^8 Ω. Considering the evolutions of the components of R_g, it can be discussed as follows:

1. For lower CNFs, we observe a decrease in the optimal R_{load} values, which is more pronounced than the behavior derived from Sharvin's law.
2. At higher CNFs, we observe a saturation of the R_{load} values, which can be related to the compensation of the decrease of the contact resistance (Sharvin's law) by the increase of the diode resistance.

Based on these observations, it is very difficult to explain the evolution of R_g as a function of CNF for both types of NWs. Hence, we propose another method to access the internal resistance of the nano-generator.

Alternative method to access NG's internal resistance 'R_g'

An alternative way to calculate the values of R_g would be to refer to the O.V. measurements (using Eq.7, derived from Eq. 1) performed in the open/short-circuit configuration, which is the classical method used in the literature [24], [48], [80], [81].

$$(R_g)_i = \frac{((V_g)_i - V_i) \times R_{load}}{V_i} \qquad (7)$$

Here, we choose an $R_{load} <<< R_g$ (nearly short-circuit configuration) and $(V_g)_i$ corresponds to O.V. value obtained in a nearly open circuit configuration (R_{load} = 1 GΩ) for an individual NW 'i'. Using the above equation, we have plotted in Fig. 11 the average values of R_g for an R_{load} of 1 MΩ, which is very small compared to the values obtained from the maxima of power curves.

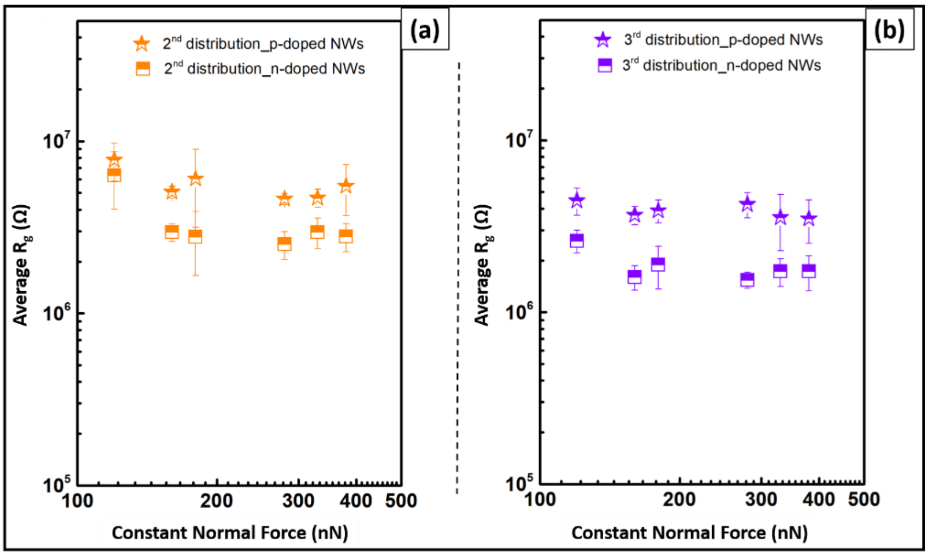

Figure 11. Calculated values of average R_g as a function of CNF for (a) the 2nd distribution and (b) the 3rd distribution, of non-intentionally n-doped and p-doped, GaN NWs, at 1 MΩ of R_{load}.

The evolution of R_g follows the same pattern as a function of CNF as observed in Fig. 9 (using the first method to quantify R_g). The R_g globally decreases and then saturates. This is compatible with the hypothesis proposed above, specifically, the compensation of different components of the resistance R_g (Eq. 3).

But we observe that the average R_g values are in the range of $10^6 - 10^7$ Ω, which is one decade smaller than the values deduced from power curves (Fig. 9). This very large discrepancy between the two calculation methods probably shows the limit of the simplification made by reasoning on model circuits involving only resistors.

However, these results allowed us to demonstrate that, contrary to what is found in the literature [1], [4], [8], [82], the resistance R_g is not to be neglected.

3.4. Towards a new method to quantify the piezo-conversion in NWs

In reality, the system must be described in an impedance framework, where the nanowire is represented by a generator V_g with a capacitance C_g and an internal resistance R_g, and this system flowing over a load represented by a resistance R_{load} and a parasitic capacitance C_{load} (Fig. 12). The latter comprises the capacitances of the input stages of the measurement system and the environmental capacitances (cables, AFM tip/nanowire interactions…).

So far, we have considered the description used for piezoelectric devices, which generally does not take into account the capacitance C_{load}.

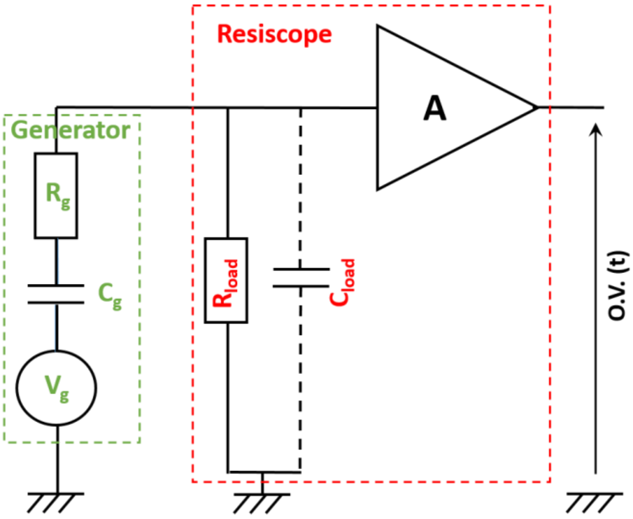

Figure 12. Electrical circuit involving stray capacitance of the load and internal capacitance of the nanowire.

In the context of measurements on single nanowires, the parasitic capacitance C_{load} can no longer be neglected. As the latter is generally close to or even greater than the C_g capacitance, it results in a significant reduction in the amplitude of the "peak" voltage, as well as in the time constants compared to what would be measured without the parasitic capacitance C_{load}. This effect is particularly important when the resistance R_{load} is large.

As an example, a simulation of the circuit in Fig. 12 with selected values of R_g = 50 MΩ, R_{load} = 1 GΩ and C_g = 1 pF, for three load capacitances, C_{load} of 0, 1 and 2 pF, respectively and a voltage step V_g = 1V, leads to drastically different transient responses (Fig. 13). We thus see a reduction of a factor of 3 in the maximum voltage measured when the C_{load} capacitance is twice as large as the C_g. In our case, we measured a time constant of about 3 ms for an R_{load} equal to 1 GΩ, which corresponds to a non-negligible value of the load capacitance (C_{load} of the order of several pF).

As each nanowire has a different morphology and internal electrical properties, this will result in a different resistance R_g and internal capacitance C_g for each nanowire. Attempting to measure the individual impedances of these nanowires is of no first interest here, because, in our case, we are rather interested in evaluating the energy that each nanowire can deliver. This could of course be obtained by considering the individual time signals $V_i(t)$, but it would represent a considerable amount of work in the context of statistical measurements involving the processing of several hundred nanowires to be reproduced on many samples. Moreover, this work would be difficult to perform in real-time during the scan.

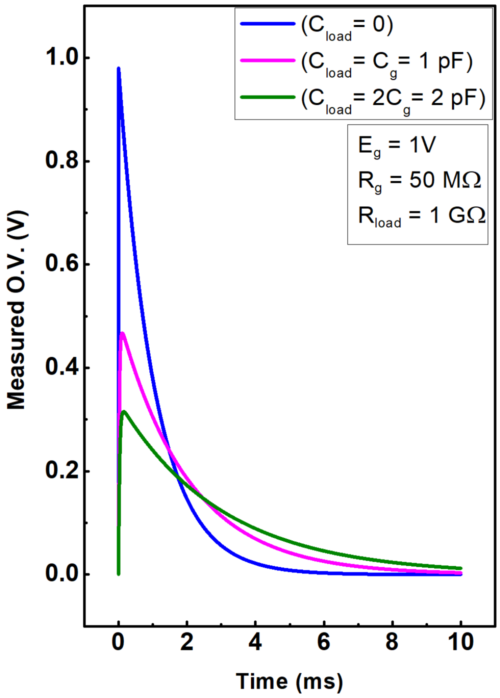

Figure 13. Simulated evolution of measured output voltage based on the electrical circuit of Fig. 12.

Proposed solution

Our simplified study based on the statistical observation of the maximum voltage measured for each peak corresponds to the method commonly used in the literature for the piezoelectric characterisation of individual NWs by AFM based techniques [1], [3], [6], [9], [11]. This methodology remains acceptable as long as it is a question of showing the evolution of electromechanical phenomena on the same sample under the effect of parameters such as the applied force or the tip scan rate.

In order to make absolute real-time measurements of the energy generated by each nanowire, and to make compatible measurements with the systems tested under device configuration, other methods must be employed. For example, some techniques, based on charge quantity measurements, have a structure that has the double advantage of being less sensitive to parasitic capacitances and of directly providing the total energy accumulated in each nanowire. Work is underway to follow this approach.

3.5. Conclusion

Using an AFM equipped with a modified Resiscope, we demonstrated that the piezo generation capacity of individual GaN NWs is highly influenced by the choice of the external R_{load} of the measurement circuit. We used the classical methods to obtain the optimal R_{load} values, however, we established a non-negligible participation of the internal resistance of the NGs. The quantification of the piezo-conversion efficiencies of the NWs via the conventional methods applied for piezo-generators, represent a strong limitation, which implies the consideration of parasitic capacitances. Hence new methods need to be explored such as the direct charge quantity measurements.

References

[1] Z. L. Wang and J. Song, ‘Piezoelectric Nanogenerators Based on Zinc Oxide Nanowire Arrays’, *Science*, vol. 312, no. 5771, pp. 242–246, Apr. 2006, doi: 10.1126/science.1124005.

[2] Y.-F. Lin, J. Song, Y. Ding, S.-Y. Lu, and Z. L. Wang, ‘Piezoelectric nanogenerator using CdS nanowires’, *Appl. Phys. Lett.*, vol. 92, no. 2, p. 022105, Jan. 2008, doi: 10.1063/1.2831901.

[3] Y. S. Zhou *et al.*, ‘Vertically Aligned CdSe Nanowire Arrays for Energy Harvesting and Piezotronic Devices’, *ACS Nano*, vol. 6, no. 7, pp. 6478–6482, Jul. 2012, doi: 10.1021/nn3022074.

[4] C.-Y. Chen *et al.*, ‘Electricity generation based on vertically aligned PbZr0.2Ti0.8O3 nanowire arrays’, *Nano Energy*, vol. 1, no. 3, pp. 424–428, May 2012, doi: 10.1016/j.nanoen.2012.01.003.

[5] P. A. Alekseev *et al.*, ‘Piezoelectric Current Generation in Wurtzite GaAs Nanowires’, *Phys. Status Solidi RRL - Rapid Res. Lett.*, vol. 12, no. 1, p. 1700358, Jan. 2018, doi: 10.1002/pssr.201700358.

[6] C.-T. Huang *et al.*, ‘GaN Nanowire Arrays for High-Output Nanogenerators’, *J. Am. Chem. Soc.*, vol. 132, no. 13, pp. 4766–4771, Apr. 2010, doi: 10.1021/ja909863a.

[7] C.-T. Huang *et al.*, ‘Single-InN-Nanowire Nanogenerator with Upto 1 V Output Voltage’, *Adv. Mater.*, vol. 22, no. 36, pp. 4008–4013, Sep. 2010, doi: 10.1002/adma.201000981.

[8] W. S. Su, Y. F. Chen, C. L. Hsiao, and L. W. Tu, ‘Generation of electricity in GaN nanorods induced by piezoelectric effect’, *Appl. Phys. Lett.*, vol. 90, no. 6, p. 063110, Feb. 2007, doi: 10.1063/1.2472539.

[9] N. Gogneau *et al.*, ‘GaN nanowires for piezoelectric generators: GaN nanowires for piezoelectric generators’, *Phys. Status Solidi RRL - Rapid Res. Lett.*, vol. 8, no. 5, pp. 414–419, May 2014, doi: 10.1002/pssr.201409105.

[10] N. Jegenyes *et al.*, ‘2 High piezoelectric conversion properties of axial 3 InGaN/GaN nanowires’, p. 13, 2018.

[11] X. Xu *et al.*, ‘An improved AFM cross-sectional method for piezoelectric nanostructures properties investigation: application to GaN nanowires’, *Nanotechnology*, vol. 22, no. 10, p. 105704, Mar. 2011, doi: 10.1088/0957-4484/22/10/105704.

[12] T.-C. Hou *et al.*, ‘Nanogenerator based on zinc blende CdTe micro/nanowires’, *Nano Energy*, vol. 2, no. 3, pp. 387–393, May 2013, doi: 10.1016/j.nanoen.2012.11.004.

[13] A. Koka, Z. Zhou, and H. A. Sodano, ‘Vertically aligned BaTiO $_3$ nanowire arrays for energy harvesting’, *Energy Env. Sci*, vol. 7, no. 1, pp. 288–296, 2014, doi: 10.1039/C3EE42540A.

[14] B. Moorthy *et al.*, ‘Piezoelectric energy harvesting from a PMN–PT single nanowire’, *RSC Adv.*, vol. 7, no. 1, pp. 260–265, 2017, doi: 10.1039/C6RA24688E.

[15] C. Chang, V. H. Tran, J. Wang, Y.-K. Fuh, and L. Lin, ‘Direct-Write Piezoelectric Polymeric Nanogenerator with High Energy Conversion Efficiency’, *Nano Lett.*, vol. 10, no. 2, pp. 726–731, Feb. 2010, doi: 10.1021/nl9040719.

[16] X. Chen, S. Xu, N. Yao, and Y. Shi, ‘1.6 V Nanogenerator for Mechanical Energy Harvesting Using PZT Nanofibers’, *Nano Lett.*, vol. 10, no. 6, pp. 2133–2137, Jun. 2010, doi: 10.1021/nl100812k.

[17] G. Zhu, A. C. Wang, Y. Liu, Y. Zhou, and Z. L. Wang, ‘Functional Electrical Stimulation by Nanogenerator with 58 V Output Voltage’, *Nano Lett.*, vol. 12, no. 6, pp. 3086–3090, Jun. 2012, doi: 10.1021/nl300972f.

[18] G. Zhu, R. Yang, S. Wang, and Z. L. Wang, ‘Flexible High-Output Nanogenerator Based on Lateral ZnO Nanowire Array’, *Nano Lett.*, vol. 10, no. 8, pp. 3151–3155, Aug. 2010, doi: 10.1021/nl101973h.

[19] S. N. Cha *et al.*, ‘Sound-Driven Piezoelectric Nanowire-Based Nanogenerators’, *Adv. Mater.*, vol. 22, no. 42, pp. 4726–4730, Nov. 2010, doi: 10.1002/adma.201001169.

[20] R. Yang, Y. Qin, L. Dai, and Z. L. Wang, ‘Power generation with laterally packaged piezoelectric fine wires’, *Nat. Nanotechnol.*, vol. 4, no. 1, pp. 34–39, Jan. 2009, doi: 10.1038/nnano.2008.314.

[21] N. Jamond *et al.*, ‘Piezo-generator integrating a vertical array of GaN nanowires’, *Nanotechnology*, vol. 27, no. 32, p. 325403, 2016.

[22] L. Lin *et al.*, ‘High output nanogenerator based on assembly of GaN nanowires’, *Nanotechnology*, vol. 22, no. 47, p. 475401, Nov. 2011, doi: 10.1088/0957-4484/22/47/475401.

[23] L. Lu *et al.*, ‘Nitride Nanowires: From Rigid to Flexible Piezo-generators’, *J. Phys. Conf. Ser.*, vol. 773, p. 012010, Nov. 2016, doi: 10.1088/1742-6596/773/1/012010.

[24] L. Lu, ‘Nanofils piézoélectriques de nitrure pour la récupération d’énergie et la détection de pression’, These de doctorat, Université Paris-Saclay (ComUE), 2018. Accessed: Oct. 13, 2021. [Online]. Available: http://www.theses.fr/2018SACLS436

[25] M. A. Johar *et al.*, ‘Facile growth of high aspect ratio c-axis GaN nanowires and their application as flexible p-n NiO/GaN piezoelectric nanogenerators’, *Acta Mater.*, vol. 161, pp. 237–245, Dec. 2018, doi: 10.1016/j.actamat.2018.09.030.

[26] A. Waseem *et al.*, ‘Enhanced performance of a flexible and wearable piezoelectric nanogenerator using semi-insulating GaN:Mg/ZnO coaxial nanowires’, *Nano Energy*, vol. 90, p. 106552, Dec. 2021, doi: 10.1016/j.nanoen.2021.106552.

[27] A. S. Dahiya *et al.*, ‘Zinc oxide nanowire-parylene nanocomposite based stretchable piezoelectric nanogenerators for self-powered wearable electronics’, *J. Phys.: Conf. Ser.*, vol. 1052, p. 012028, Jul. 2018, doi: 10.1088/1742-6596/1052/1/012028.

[28] K. Zheng *et al.*, ‘Orientation Dependence of Electromechanical Characteristics of Defect-free InAs Nanowires’, *Nano Lett.*, vol. 16, no. 3, pp. 1787–1793, Mar. 2016, doi: 10.1021/acs.nanolett.5b04842.

[29] S. Yang *et al.*, ‘The Piezotronic Effect of Zinc Oxide Nanowires Studied by In Situ TEM’, *Adv. Mater.*, vol. 24, no. 34, pp. 4676–4682, Sep. 2012, doi: 10.1002/adma.201104420.

[30] H. D. Espinosa, R. A. Bernal, and T. Filleter, ‘In Situ TEM Electromechanical Testing of Nanowires and Nanotubes’, *Small*, vol. 8, no. 21, pp. 3233–3252, Nov. 2012, doi: 10.1002/smll.201200342.

[31] Z. Wang, J. Hu, A. P. Suryavanshi, K. Yum, and M.-F. Yu, ‘Voltage Generation from Individual BaTiO $_3$ Nanowires under Periodic Tensile Mechanical Load’, *Nano Lett.*, vol. 7, no. 10, pp. 2966–2969, Oct. 2007, doi: 10.1021/nl070814e.

[32] X. Li, X. Wei, T. Xu, D. Pan, J. Zhao, and Q. Chen, ‘Remarkable and Crystal-Structure-Dependent Piezoelectric and Piezoresistive Effects of InAs Nanowires’, *Adv. Mater.*, vol. 27, no. 18, pp. 2852–2858, May 2015, doi: 10.1002/adma.201500037.

[33] M.-H. Zhao, Z.-L. Wang, and S. X. Mao, ‘Piezoelectric Characterization of Individual Zinc Oxide Nanobelt Probed by Piezoresponse Force Microscope’, *Nano Lett.*, vol. 4, no. 4, pp. 587–590, Apr. 2004, doi: 10.1021/nl035198a.

[34] M. Minary-Jolandan, R. A. Bernal, I. Kuljanishvili, V. Parpoil, and H. D. Espinosa, ‘Individual GaN Nanowires Exhibit Strong Piezoelectricity in 3D’, *Nano Lett.*, vol. 12, no. 2, pp. 970–976, Feb. 2012, doi: 10.1021/nl204043y.

[35] Y. Calahorra, M. Smith, A. Datta, H. Benisty, and S. Kar-Narayan, ‘Mapping piezoelectric response in nanomaterials using a dedicated non-destructive scanning probe technique’, *Nanoscale*, vol. 9, no. 48, pp. 19290–19297, 2017, doi: 10.1039/C7NR06714C.

[36] A. Gebrekrstos, G. Madras, and S. Bose, ‘Piezoelectric Response in Electrospun Poly(vinylidene fluoride) Fibers Containing Fluoro-Doped Graphene Derivatives’, *ACS Omega*, vol. 3, no. 5, pp. 5317–5326, May 2018, doi: 10.1021/acsomega.8b00237.

[37] X. Wang, ‘Piezoelectric nanogenerators—Harvesting ambient mechanical energy at the nanometer scale’, *Nano Energy*, vol. 1, no. 1, pp. 13–24, Jan. 2012, doi: 10.1016/j.nanoen.2011.09.001.

[38] N. Gogneau *et al.*, ‘Electromechanical conversion efficiency of GaN NWs: critical influence of the NW stiffness, the Schottky nano-contact and the surface charge effects’, *Nanoscale*, vol. 14, no. 13, pp. 4965–4976, 2022, doi: 10.1039/D1NR07863A.

[39] N. Gogneau *et al.*, ‘Impact of the GaN nanowire polarity on energy harvesting’, *Appl. Phys. Lett.*, vol. 104, no. 21, p. 213105, May 2014, doi: 10.1063/1.4880101.

[40] G. Liu *et al.*, ‘Nanogenerators based on vertically aligned InN nanowires’, *Nanoscale*, vol. 8, no. 4, pp. 2097–2106, 2016, doi: 10.1039/C5NR06841J.

[41] S. Ahoulou, E. Perret, and J.-M. Nedelec, ‘Functionalization and Characterization of Silicon Nanowires for Sensing Applications: A Review’, *Nanomaterials*, vol. 11, no. 4, p. 999, Apr. 2021, doi: 10.3390/nano11040999.

[42] C. Jin, H. Kim, S.-W. Choi, S. S. Kim, and C. Lee, ‘Synthesis, Structure, and Gas-Sensing Properties of Pt-Functionalized TiO₂ Nanowire Sensors’, *J. Nanosci. Nanotechnol.*, vol. 14, no. 8, pp. 5833–5838, Aug. 2014, doi: 10.1166/jnn.2014.8454.

[43] R. Tao, M. Mouis, and G. Ardila, ‘Unveiling the Influence of Surface Fermi Level Pinning on the Piezoelectric Response of Semiconducting Nanowires’, *Adv. Electron. Mater.*, vol. 4, no. 1, p. 1700299, Jan. 2018, doi: 10.1002/aelm.201700299.

[44] C.-H. Wang *et al.*, ‘Optimization of the Output Efficiency of GaN Nanowire Piezoelectric Nanogenerators by Tuning the Free Carrier Concentration’, *Adv. Energy Mater.*, vol. 4, no. 16, p. 1400392, Nov. 2014, doi: 10.1002/aenm.201400392.

[45] C.-H. Wang *et al.*, ‘Effects of Free Carriers on Piezoelectric Nanogenerators and Piezotronic Devices Made of GaN Nanowire Arrays’, *Small*, vol. 10, no. 22, pp. 4718–4725, Nov. 2014, doi: 10.1002/smll.201400768.

[46] Y. Su, C. Dagdeviren, and R. Li, ‘Measured Output Voltages of Piezoelectric Devices Depend on the Resistance of Voltmeter’, *Adv. Funct. Mater.*, vol. 25, no. 33, pp. 5320–5325, Sep. 2015, doi: 10.1002/adfm.201502280.

[47] O. Graton, G. Poulin-Vittrant, A. S. Dahiya, N. Camara, L.-P. T. H. Hue, and M. Lethiecq, ‘Equivalent circuit model of a nanogenerator based on a piezoelectric nanowire-polymer composite: Equivalent circuit model of a nanogenerator based on a piezoelectric nanowire-polymer composite’, *Phys. Status Solidi RRL - Rapid Res. Lett.*, vol. 7, no. 10, pp. 915–918, Oct. 2013, doi: 10.1002/pssr.201308017.

[48] M. A. Johar *et al.*, ‘Highly Durable Piezoelectric Nanogenerator by Heteroepitaxy of GaN Nanowires on Cu Foil for Enhanced Output Using Ambient Actuation Sources’, *Adv. Energy Mater.*, vol. 10, no. 47, p. 2002608, Dec. 2020, doi: 10.1002/aenm.202002608.

[49] A. Waseem *et al.*, ‘GaN/Al2O3 core-shell nanowire based flexible and stable piezoelectric energy harvester’, *J. Alloys Compd.*, vol. 860, p. 158545, Apr. 2021, doi: 10.1016/j.jallcom.2020.158545.

[50] A. S. Dahiya, F. Morini, S. Boubenia, K. Nadaud, D. Alquier, and G. Poulin-Vittrant, 'Organic/Inorganic Hybrid Stretchable Piezoelectric Nanogenerators for Self-Powered Wearable Electronics', *Adv. Mater. Technol.*, vol. 3, no. 2, p. 1700249, 2018, doi: 10.1002/admt.201700249.

[51] A. E. Kacimi, 'Capteurs piézoélectriques souples à base de microfils de GaN en structure capacitive', p. 169.

[52] L. Serairi, 'Elaboration et conception des dispositifs de la récupération d'énergie à base de nanofils de ZnO et de microfibres de PVDF-TrFE', p. 165.

[53] L. Serairi, L. Gu, Y. Qin, Y. Lu, P. Basset, and Y. Leprince-Wang, 'Flexible piezoelectric nanogenerators based on PVDF-TrFE nanofibers', *Eur. Phys. J. Appl. Phys.*, vol. 80, no. 3, p. 30901, Dec. 2017, doi: 10.1051/epjap/2017170288.

[54] S. Xu, Y. Wei, J. Liu, R. Yang, and Z. L. Wang, 'Integrated Multilayer Nanogenerator Fabricated Using Paired Nanotip-to-Nanowire Brushes', *Nano Lett.*, vol. 8, no. 11, pp. 4027–4032, Nov. 2008, doi: 10.1021/nl8027813.

[55] N. Jamond *et al.*, 'Energy harvesting efficiency in GaN nanowire-based nanogenerators: the critical influence of the Schottky nanocontact', *Nanoscale*, vol. 9, no. 13, pp. 4610–4619, 2017, doi: 10.1039/C7NR00647K.

[56] L. Largeau, E. Galopin, N. Gogneau, L. Travers, F. Glas, and J.-C. Harmand, 'N-Polar GaN Nanowires Seeded by Al Droplets on Si(111)', *Cryst. Growth Des.*, vol. 12, no. 6, pp. 2724–2729, Jun. 2012, doi: 10.1021/cg300212d.

[57] K. A. Bertness, A. Roshko, L. M. Mansfield, T. E. Harvey, and N. A. Sanford, 'Nucleation conditions for catalyst-free GaN nanowires', *J. Cryst. Growth*, vol. 300, no. 1, pp. 94–99, Mar. 2007, doi: 10.1016/j.jcrysgro.2006.10.209.

[58] M. D. Brubaker *et al.*, 'Effect of AlN buffer layer properties on the morphology and polarity of GaN nanowires grown by molecular beam epitaxy', *J. Appl. Phys.*, vol. 110, no. 5, p. 053506, Sep. 2011, doi: 10.1063/1.3633522.

[59] R. Songmuang, O. Landré, and B. Daudin, 'From nucleation to growth of catalyst-free GaN nanowires on thin AlN buffer layer', *Appl. Phys. Lett.*, vol. 91, no. 25, p. 251902, Dec. 2007, doi: 10.1063/1.2817941.

[60] L. Largeau, D. L. Dheeraj, M. Tchernycheva, G. E. Cirlin, and J. C. Harmand, 'Facet and in-plane crystallographic orientations of GaN nanowires grown on Si(111)', *Nanotechnology*, vol. 19, no. 15, p. 155704, Apr. 2008, doi: 10.1088/0957-4484/19/15/155704.

[61] 'Schneegans O, Chrétien P and Houzé F 2011 French Patent Specification FR 10 01940 International PCT WO 2011/ 138738'

[62] J. Liu, P. Fei, J. Zhou, R. Tummala, and Z. L. Wang, 'Toward high output-power nanogenerator', *Appl. Phys. Lett.*, vol. 92, no. 17, p. 173105, Apr. 2008, doi: 10.1063/1.2918840.

[63] G. Jacopin *et al.*, 'Interplay of the photovoltaic and photoconductive operation modes in visible-blind photodetectors based on axial p-i-n junction GaN nanowires', *Appl. Phys. Lett.*, vol. 104, no. 2, p. 023116, Jan. 2014, doi: 10.1063/1.4860968.

[64] P. Shirazi *et al.*, 'Size-Dependent Piezoelectric Properties of Electrospun BaTiO3 for Enhanced Energy Harvesting', *Adv. Sustain. Syst.*, vol. 1, no. 11, p. 1700091, 2017, doi: 10.1002/adsu.201700091.

[65] S. S. Lin, J. H. Song, Y. F. Lu, and Z. L. Wang, 'Identifying individual n- and p-type ZnO nanowires by the output voltage sign of piezoelectric nanogenerator', *Nanotechnology*, vol. 20, no. 36, p. 365703, Sep. 2009, doi: 10.1088/0957-4484/20/36/365703.

[66] Y. Gao and Z. L. Wang, 'Electrostatic Potential in a Bent Piezoelectric Nanowire. The Fundamental Theory of Nanogenerator and Nanopiezotronics', *Nano Lett.*, vol. 7, no. 8, pp. 2499–2505, Aug. 2007, doi: 10.1021/nl071310j.

[67] B. Pérez-García, J. Zúñiga-Pérez, V. Muñoz-Sanjosé, J. Colchero, and E. Palacios-Lidón, 'Formation and Rupture of Schottky Nanocontacts on ZnO Nanocolumns', *Nano Lett.*, vol. 7, no. 6, pp. 1505–1511, Jun. 2007, doi: 10.1021/nl070238m.

[68] D. J. Leo, *Engineering analysis of smart material systems*. Hoboken, N.J: John Wiley & Sons, 2007.

[69] M.-Y. Lu, J. Song, M.-P. Lu, C.-Y. Lee, L.-J. Chen, and Z. L. Wang, 'ZnO−ZnS Heterojunction and ZnS Nanowire Arrays for Electricity Generation', *ACS Nano*, vol. 3, no. 2, pp. 357–362, Feb. 2009, doi: 10.1021/nn800804r.

[70] P. X. Gao, J. Song, J. Liu, and Z. L. Wang, 'Nanowire Piezoelectric Nanogenerators on Plastic Substrates as Flexible Power Sources for Nanodevices', *Adv. Mater.*, vol. 19, no. 1, pp. 67–72, Jan. 2007, doi: 10.1002/adma.200601162.

[71] Z. Zhou, H. Tang, and H. A. Sodano, 'Scalable Synthesis of Morphotropic Phase Boundary Lead Zirconium Titanate Nanowires for Energy Harvesting', *Adv. Mater.*, vol. 26, no. 45, pp. 7547–7554, Dec. 2014, doi: 10.1002/adma.201403286.

[72] R. Tao *et al.*, 'Performance of ZnO based piezo-generators under controlled compression', *Semicond. Sci. Technol.*, vol. 32, no. 6, p. 064003, Jun. 2017, doi: 10.1088/1361-6641/aa691f.

[73] R. Calarco, T. Stoica, O. Brandt, and L. Geelhaar, 'Surface-induced effects in GaN nanowires', *J. Mater. Res.*, vol. 26, no. 17, pp. 2157–2168, Sep. 2011, doi: 10.1557/jmr.2011.211.

[74] K. L. Johnson, *Contact Mechanics*, 1st ed. Cambridge University Press, 1985. doi: 10.1017/CBO9781139171731.

[75] Y. V. Sharvin, 'A POSSIBLE METHOD FOR STUDYING FERMI SURFACES', p. 2.

[76] B. S. Simpkins, M. A. Mastro, C. R. Eddy, and P. E. Pehrsson, 'Surface depletion effects in semiconducting nanowires', *J. Appl. Phys.*, vol. 103, no. 10, p. 104313, May 2008, doi: 10.1063/1.2932072.

[77] P. Tchoulfian, F. Donatini, F. Levy, A. Dussaigne, P. Ferret, and J. Pernot, 'Direct Imaging of p–n Junction in Core–Shell GaN Wires', *Nano Lett.*, vol. 14, no. 6, pp. 3491–3498, Jun. 2014, doi: 10.1021/nl5010493.

[78] G. D. J. Smit, S. Rogge, and T. M. Klapwijk, ‘Scaling of nano-Schottky-diodes’, *Appl. Phys. Lett.*, vol. 81, no. 20, pp. 3852–3854, Nov. 2002, doi: 10.1063/1.1521251.

[79] G. D. J. Smit, S. Rogge, and T. M. Klapwijk, ‘Enhanced tunneling across nanometer-scale metal–semiconductor interfaces’, *Appl. Phys. Lett.*, vol. 80, no. 14, pp. 2568–2570, Apr. 2002, doi: 10.1063/1.1467980.

[80] N. Gogneau, N. Jamond, P. Chrétien, F. Houzé, E. Lefeuvre, and M. Tchernycheva, ‘From single III-nitride nanowires to piezoelectric generators: New route for powering nomad electronics’, *Semicond. Sci. Technol.*, vol. 31, no. 10, p. 103002, Oct. 2016, doi: 10.1088/0268-1242/31/10/103002.

[81] N. Jalali *et al.*, ‘Passivation of Zinc Oxide Nanowires for Improved Piezoelectric Energy Harvesting Devices’, *J. Phys. Conf. Ser.*, vol. 476, p. 012131, Dec. 2013, doi: 10.1088/1742-6596/476/1/012131.

[82] M.-P. Lu *et al.*, ‘Piezoelectric Nanogenerator Using p-Type ZnO Nanowire Arrays’, *Nano Lett.*, vol. 9, no. 3, pp. 1223–1227, Mar. 2009, doi: 10.1021/nl900115y.

Chapter 4

Surface charges for piezo-generation enhancement of GaN nanowires

Contents

1D-nanostructures such as nanowires, nanorods, nanowhiskers, nanofibers… are the building blocks of new-generation micro-electronics such as sensors [1]–[5], opto-electronic devices [6]–[9]... and piezoelectric generators [10]–[15]. For the optimisation of device performances, it is highly important to fundamentally understand the different physical mechanisms at play, which become predominant in the nanoscale regime. One such phenomenon is the surface charge effect (SCE), which manifests itself strongly in semiconductor NWs with sub-100 nm diameters. The origin of these surface charges might vary from one system to another. For example, in GaN NWs they originate mainly from covalent dangling bonds [16], bistable defects [17], nitrogen antisites or Ga vacancies [18]–[20]… whereas in ZnO NWs, surface charges appear due to the stabilisation processes including reconstruction, impurities and chemical adsorbates incorporation… [21]. In this Chapter, we experimentally demonstrate that the surface charges can be modulated as a function of the NWs diameter as well as its immediate environment. While these surface charges are considered detrimental for opto-electronic devices, we highlight their advantageous side in enhancing the piezo-generation capacity of GaN NWs.

4.1 Surface charges and Surface Fermi level pinning in semiconductors

4.1.1 Fermi level pinning in bulk materials

The abrupt interruption of the atomistic structure of a material results in the creation of surfaces, where the absence of neighbouring atoms result in a different electron density as compared to the bulk. In the case of semiconductors, this leads to the creation of new electronic states or surface states within the semiconductor bandgap. These surfaces states might carry charges, commonly known as surface charges (SC) [22].

SC may have various origins such as incomplete covalent bonds (i.e. dangling bonds), impurities, chemical adsorbates or stabilization processes (*e.g.* charge transfer, atomic re-arrangements following a relaxation or reconstructions).

However, the presence of these surface charges creates an energetically unfavourable situation, where a charge neutrality is required to achieve stabilization of the Fermi level [22]. Consequently, a charge transfer occurs between the surface and the bulk of the material resulting in the creation of a space-charge region at the interface, also called the ‘depletion layer’. The width of the latter is a direct function of the doping level of the material [18]. Thus, a built-in electric field is created at the interface and consequently a strong Fermi level band bending occurs [18], [23]–[26]. This phenomenon is defined as surface Fermi level pinning (SFLP) [23].

Using schematic diagrams, we illustrate the band structures for intrinsic, n-type and p-type doped semiconductors. We shall assume that the neutrality level, $E_F^{Surface}$, of the surface states is at midgap, meaning that there is no charge in the surface states if the Fermi level is at midgap.

For an ideal intrinsic semiconductor (undoped with no surface charges), the bulk Fermi level (E_F^{Bulk}) is aligned with $E_F^{Surface}$ and no charge transfer occurs. The bands thus remain flat up to the surface, as shown in Fig. 1.

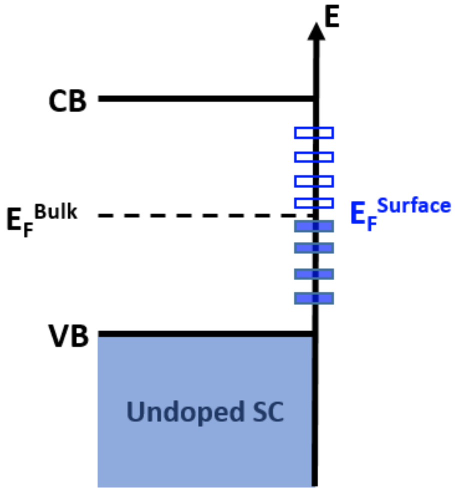

Figure 1. Flat bands of an ideal intrinsic (undoped) semiconductor where the Fermi level of the bulk (E_F^{Bulk}) and the surface ($E_F^{Surface}$) are aligned and no charge transfer occurs at the interface.

For an n-type semiconductor, E_F^{Bulk} is close to the conduction band (CB) and is thus positioned higher than $E_F^{Surface}$, as shown in Fig. 2a. To achieve overall electrical neutrality, a transfer of electrons from the bulk to the surface takes place which results in an upward band bending, as shown in Fig. 2b. A positive space charge is thus created at the semiconductor side, while the surface states will carry an opposite net negative charge. This space-charge region in the semiconductor is termed as the (electron) depletion layer (shown in green in Fig. 2b), since this region is depleted of free electrons, leaving a positive charge due to the immobile positively charged donor impurities.

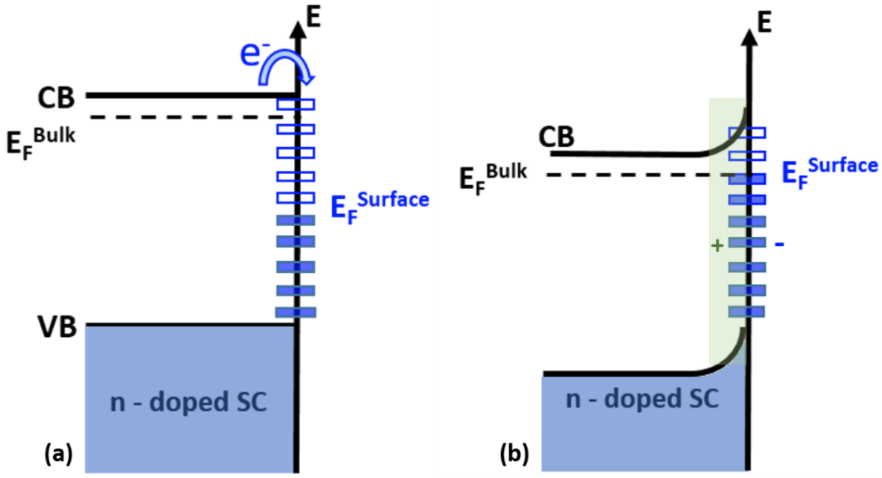

Figure 2. (a) For an n-type semiconductor, E_F^{Bulk} is positioned higher than the $E_F^{Surface}$, resulting in an un-equilibrium state. (b) Electron charge transfer takes place from the bulk to the surface to align the two Fermi levels. A positive space charge layer is created at the interface, called the 'electron' depletion layer.

On the other hand, for a p-type semiconductor, E_F^{Bulk} is located closer to the valence band, below the $E_F^{Surface}$ (Fig. 3a) and thus the electrons flow from the surface to the bulk (or holes from the bulk to the surface) in order to achieve electrical neutrality at equilibrium, causing a downward band bending (Fig. 3b). In this case, a negatively charged space-charge region occurs in the semiconductor, while positive charges lie on the surface and the created space-charge region is called the (hole) depletion layer (shown in orange in Fig. 3b).

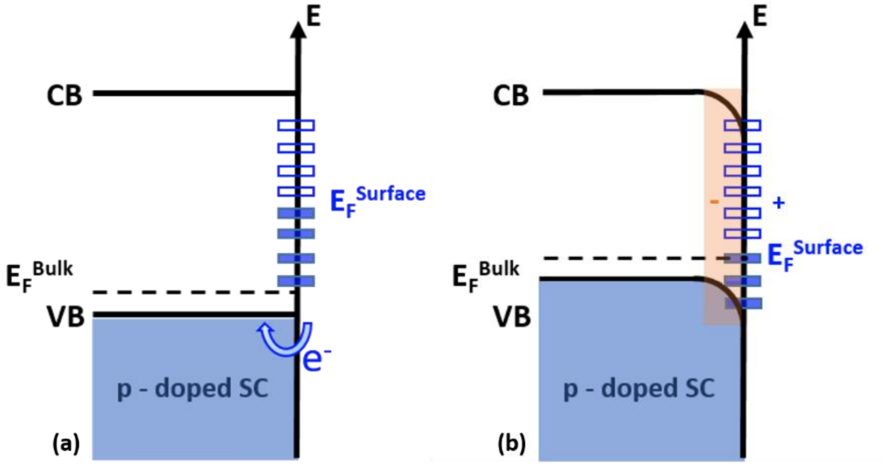

Figure 3. (a) The $E_F^{Surface}$ is positioned above the E_F^{Bulk} in the case of p-type doped semiconductors. (b) Electrons will flow from the surface to the bulk or holes in the counter direction until the Fermi levels are aligned, resulting in a downward band bending and the creation of a 'hole' depletion layer.

4.1.2 Fermi level pinning in 1D-nanostructures

Considering the low surface-to-volume ratio of 2D-films or bulk materials, the creation of a depletion layer presents limited effects on their material properties. However, for 1D-nanostructures, such as nanowires, nanorods, nanofibers… especially with a sub-100 nm diameter, the surface charge effect (SCE) is strongly pronounced [16], [22], [27]. In fact, due to an increase of their surface-to-volume ratio [28], 1D-nanostructures are characterized with a significant increase in the density of surface states [29]–[32]. This can lead to a strong modulation of the nanostructure's properties. The relationship between the SCE and the NW diameter has been experimentally demonstrated in GaN and ZnO NWs, both exhibiting a highly pronounced SCE. For instance, L. Polenta et al. [18] and M. Spies et al. [33] have used photoconductivity measurements to evidence localized surface states and the variation of the depletion width as a function of NW diameter for GaN NWs and AlN/GaN/AlN heterostructures, respectively.

Fig. 4 illustrates the relationship between surface charges and the NW diameter.

As a result of the surface charges, a strong SFLP takes place, creating a depletion layer of width 'w' (fixed by the doping of the material). Here, the critical diameter (d_{crit}) is defined as twice the depletion width and corresponds to a full depletion of the NW. When the NW diameter (d) is larger than d_{crit}, a conduction channel exists in the NW core whereas the depletion region is confined to the NW sidewalls only, leading to a partial depletion of the nanostructure (Fig. 4a). By contrast, when the NW diameter is equivalent to d_{crit}, the nanostructure is fully depleted with unchanged surface barrier height (SBH), ϕ, for the electrons in the conduction band to participate in the recombination mechanism at the surface (Fig. 4b). Further shrinking the diameter below the critical level ($d < d_{crit}$) leads to an overlapping of the depletion layer (Fig. 4c). In this case, the SBH decreases leading to a faster electron-hole recombination at the surface. The charge carrier concentration and lifetime are thus highly affected by the severity of the SFLP [34]–[37], thus directly affecting the NW conductance [18], [34], [38], [39], and consequently, the efficiencies of 1D-nanostructure based devices.

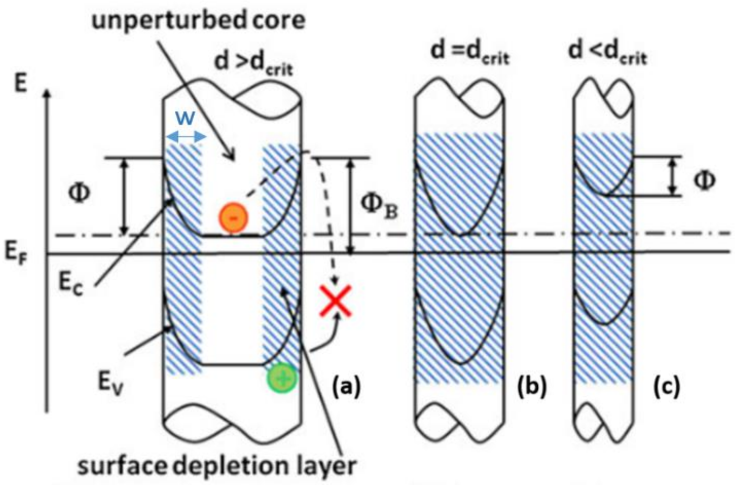

Figure 4. (Image taken from [38]). Fermi level pinning and the depletion width as a function of the NW diameter: (a) d > d$_{crit}$, (b) d = d$_{crit}$ and (c) d < d$_{crit}$. The valence band energy (E$_V$) and the conduction band energy (E$_C$) are shown along with the surface barrier height φ and the height φ$_B$ at which the Fermi level is pinned at the surface.

The potential detrimental or advantageous roles of the surface-related effects have already been pointed out but still remain unaddressed to a large extent. While in nanoscale electronic and optoelectronic devices, SCE have undesirable consequences [40]–[44], they open new perspectives for piezoelectric devices [45]–[47].

4.2 Impact of SCE in 1D-nanostructures and devices

For 1D-nanostructures characterized by sub-100 nm wide diameter, the expression of the surface charges strongly modulate their conductance [18].Thus, the role played by the surface charges can be detrimental or advantageous, depending on the targeted application.

4.2.1 Surface charge effects: A disadvantage for opto-electronic applications

As explained in Fig.4, a partial or full depletion of 1D-nanostructures due to the SFLP can induce a local decreasing of the free charge carrier diffusivity. This reduction is detrimental for the opto-electronic device performances, which strongly depend on the conductive properties of the material.

Calarco et al. in 2005 [39] are the first to present a model describing the interplay of SCE and the NW size for GaN nanowhiskers (Fig. 4) and supported it by investigating the influence of SCE on photocurrent measurements and I-V characteristics, performed on single nanowhiskers. A critical diameter of the order of 80 nm was identified below which a strong photocurrent decay was observed (Fig. 5a), suggesting a decrease in the size of the conduction channel (Fig. 4a). The insulating behaviour of the smaller NWs, due to the complete depletion of the column, was observed in the I-V characteristics with a V^2 to V^3 dependence of the dark currents at an applied bias above 0.1 V (Fig. 5b).

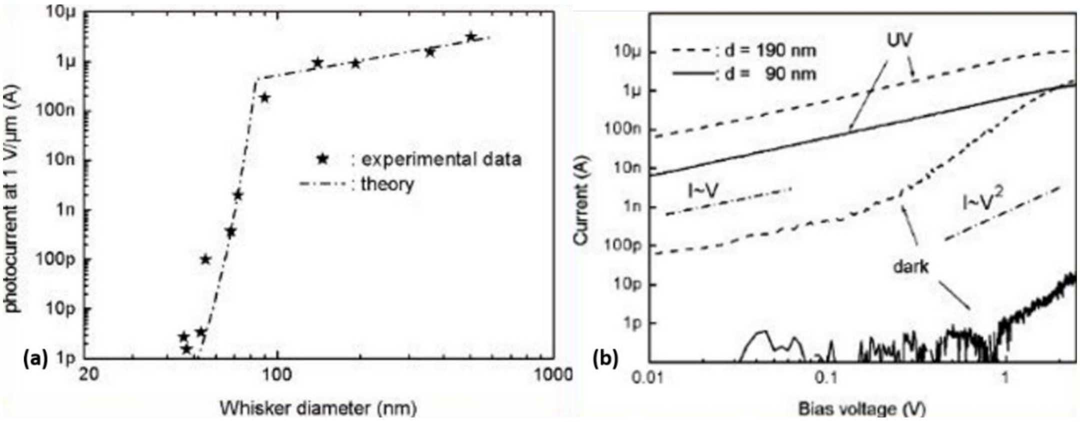

Figure 5. (Images taken from [39]). (a) Photocurrents as a function of the GaN nanowhisker diameter. A sharp decrease in the photocurrent is observed below a d_{crit} of 80 nm. (b) For smaller NWs, the dark currents at a bias above 0.1 V is no longer Ohmic and has a quadratic dependence similar to insulators.

Persistent photocurrents (PPC) decay in thin GaN NWs was also observed due to the decreased surface barrier height and a faster electron-hole recombination [38], as shown in Fig. 6.

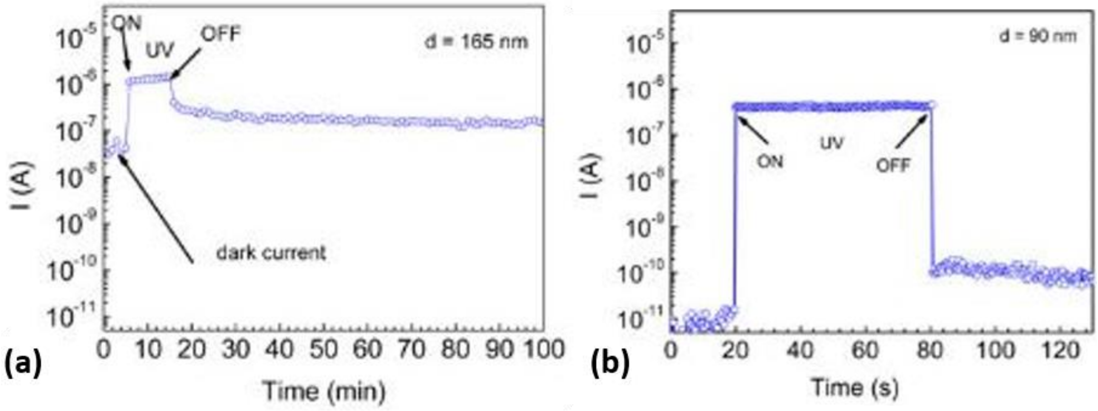

Figure 6. (Image taken from [38]). (a) Persistent photocurrents (PPC) observed for NW with a diameter of 165 nm, (b) a rapid decrease in the PPC for smaller diameter of the NW due to a faster charge carrier recombination.

Conductivity, mobility and charge-carrier lifetime measurements were also performed by Chen et al. in 2009 on m-axial GaN NWs [34], further supporting the model proposed by Calarco in 2005 [39]. The conductivity decreased when the NW size became smaller than a d_{crit} (30-40 nm in this case) as a result of a strong FLP (Fig. 7a). Smaller sizes of the NWs also resulted in the diminution of the product of mobility (µ) and carrier lifetime (T) of the free-charge carriers because of increased surface recombination (Fig. 7b).

The size-dependence of SCE on the opto-(electrical) properties has been experimentally reported in several 1D-semiconductor nanostructures such as Si NWs [48], III-V NWs such as GaAs, InAs, InP [35] and GaN NWs [18], [49], [50].

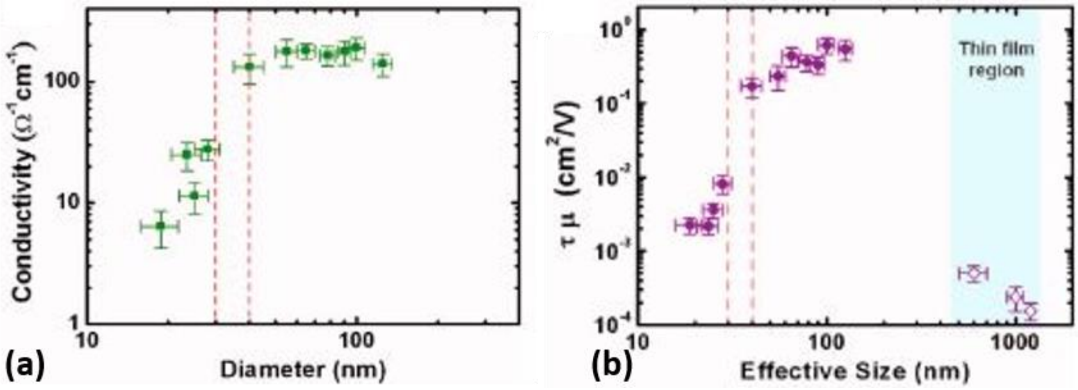

Figure 7. (Image taken from [34]). (a) Size-dependent dark conductivity and (b) the product of carrier lifetime and mobility for single GaN NWs as a function of diameter.

Surface charges are also responsible for the reduction in the emitter efficiency of optical devices by limiting their internal quantum efficiency, shorter laser operation lifetime, shift of the optical transition energy or an early degradation of electronic devices [41]–[44]. Finally, the SCE have also been reported to be detrimental for other systems, such as FETs [51], [52], LEDs, water splitting systems [53] (Fig. 8a), solar cells [54] (Fig. 8b)…

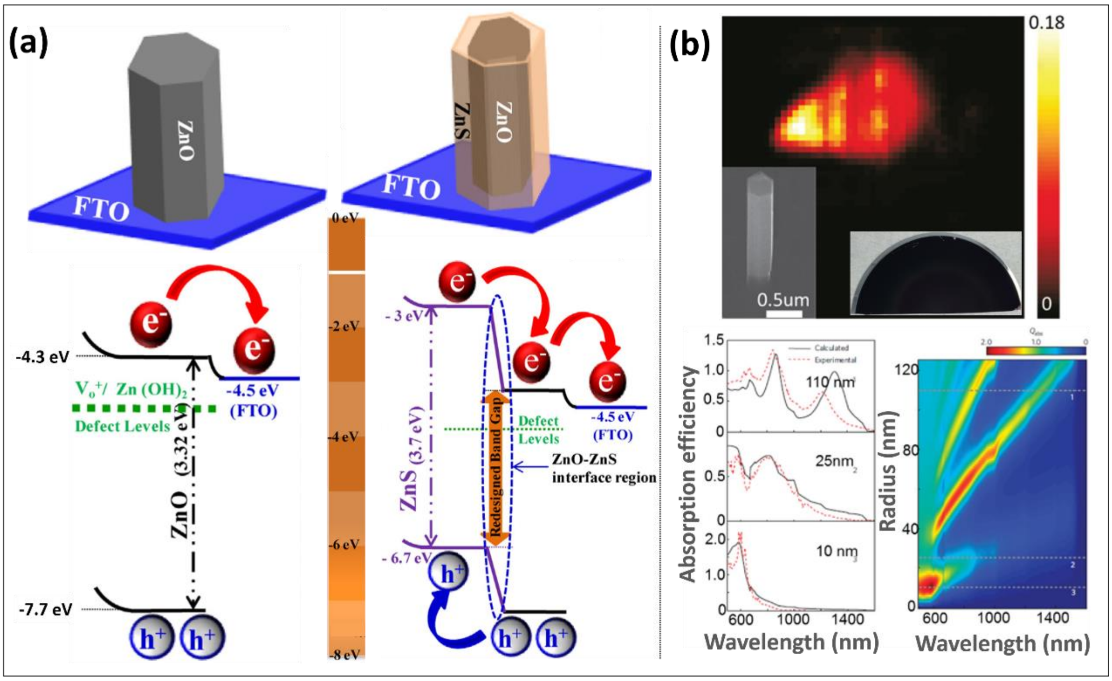

Figure 8. (Images taken from [53], [54]). Schematic diagram showing as-grown ZnO (left) and ZnO-ZnS core-shell NWs (right) on FTO coated glass slides. The photoelectrons generated at ZnS are transferred to ZnO resulting in a higher concentration of charge carriers. Moreover, the ZnS core-shell reduces the surface trap density of ZnO and a higher photocurrent is generated due to a lower electron-hole recombination. (b) (Top) Scanning photocurrent measurements performed on a single vertically oriented GaAsP NW device excited by a, 800 nm laser. Experimental and calculated absorption spectra for horizontal NWs with a radius of 110 nm, 25 nm, and 10 nm, respectively. Right: Two-dimensional plot of calculated absorption efficiency as a function of wavelength and radius of the nanowire.

4.2.2 Surface charge effects: An advantage for piezoelectric applications

While the SCE has undesired consequences for the electrical and optoelectronic properties due to an effective reduction in the charge carrier concentration, they can appear as an advantage for NW-based piezoelectric applications. In these nano-systems, free charge carriers are known to degrade the piezoelectric response, by screening the generated piezo-charges [6-8]. This phenomenon has been experimentally demonstrated in ZnO [55]–[58] and GaN [45] NWs. Fig. 9b clearly illustrates the deterioration of the piezo-response of GaN NW-based PZ, as the doping level of the NWs is increased.

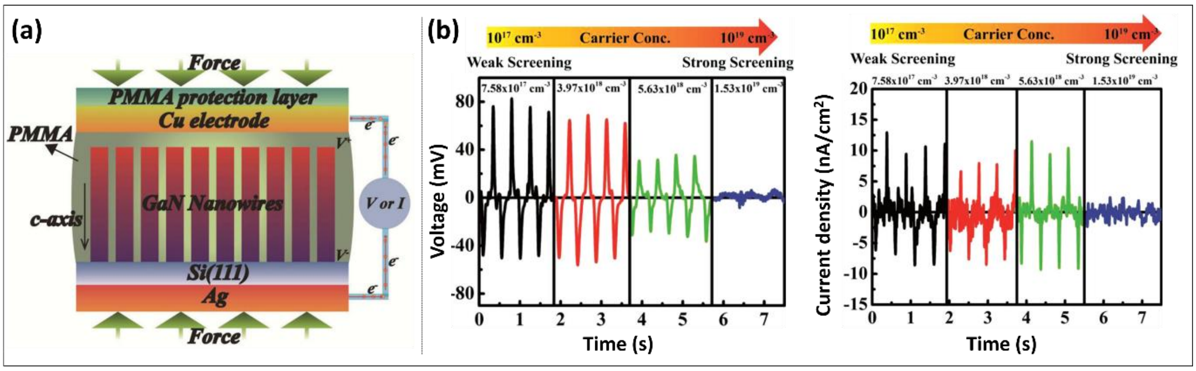

Figure 9. (Image taken from [45]). (a) Schematic diagram of the PZ integrating vertically oriented GaN NWs. (b) The voltage and the current density generated by the PZ under external deformation decreases as a function of the increased doping levels. The latter leads to an increased concentration of free-charge carriers, which effectively screens the generated piezo-charges inside the NW volume.

However, the reduction of free charge carrier concentration by taking advantage of the SCE appears promising for the exaltation of the piezo-potential inside the NWs, and thus, their electromechanical coupling efficiency.

This advantageous role of the SCE is clearly illustrated for chemically synthesized ZnO NWs. In fact, ZnO NWs growth by hydrothermal-based synthesis method are generally characterized by a strong intrinsic doping [59], [60], sufficiently high to screen the quasi-totality of the piezo-charges. However, a non-negligible piezo-response has been reported by several groups [61]–[64] [refs]. This unexpected response results from the presence of surface charges, strongly pronounced in ZnO NWs. The surface traps and thus the resulting SFLP leads to a limitation of the free carriers diffusion and hence to a lower piezo-charge screening. In consequence, the internal piezoelectric field within the NWs increases and a high piezoelectric response can be harvested.

However, only a few papers integrate the crucial role of the SCE and thus, surface Fermi level pinning, on the piezoelectric properties of 1D-nanostructures. The first consideration of these effects dates since 2018 with theoretical simulations, reported by Tao et al. [12]. In this paper, the piezo potential variation in the NWs was simulated as a function of the charge carrier concentration, NW morphology and the pinning conditions. Considering the SFLP on NW top and lateral surfaces as boundary conditions, an increment of the NW's piezo-potential by 10 to 16 times was observed as compared to NWs without SFLP (Fig. 10). These results demonstrated the positive impact of SFLP in enhancing the performances of piezoelectric nanowires by significantly reducing the screening effect.

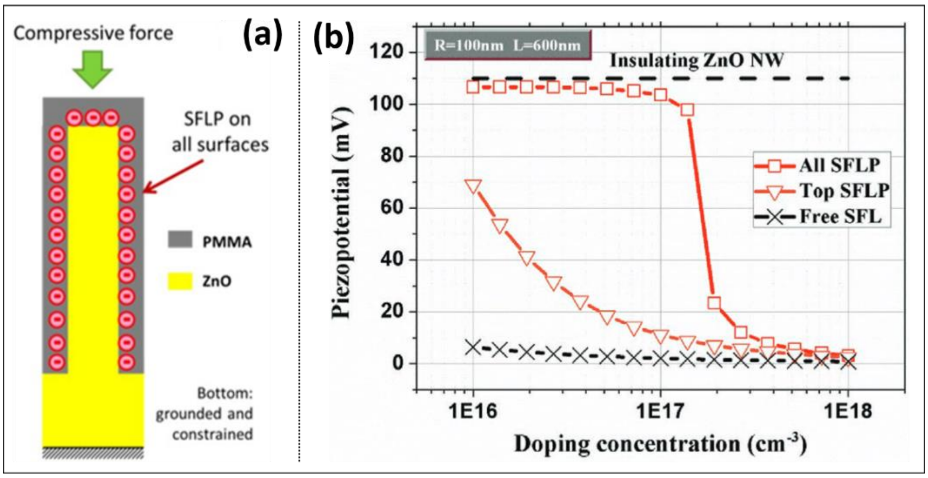

Figure 10. (Image taken from *[12]*). (a) Schematic diagram of a single ZnO NW with SFLP on all surfaces and PMMA encapsulation, subjected to compressive deformation, (b) Piezo-potential of a single ZnO NW with no SFLP (crosses), pinning only on NW top (triangles) and pinning on all interfaces (squares), as function of doping.

From an experimental point of view, even fewer teams have investigated the role of the SCE on the piezoelectric properties of 1D-nanostructures. Very recently the group of G. Ardila [64] has shown, via piezo-response measurements on ZnO NWs, the variations of the piezoelectric coefficient 'd_{33}' as a function of the NW diameter, and thus, as a function of the surface charges. Other groups have taken advantage of the SCE by functionalizing the NWs: X. Xue et al. [46] and S. Lu et al. [65] have demonstrated that by adsorbing gases or depositing nanoparticles on the NW surface, the surface trap density can be enhanced. In the first study, the depletion width inside the NWs was modulated as a function of the gas concentration, which directly influenced the voltage generated by the NWs under external strain, due to an effective screening (Fig. 11a). In the latter report, the screening in the NWs was supressed by introducing Au particles on the ZnO surfaces to form Schottky junctions. This led to an improvement of the piezoelectric response of the ZnO NW-based PZ (Fig. 11b).

These few examples unambiguously demonstrate the potential of the surface charges for enhancing the piezo-response of the NW-based PZs. However, to take full advantage of SC, it is important to identify the factors, which modulate them.

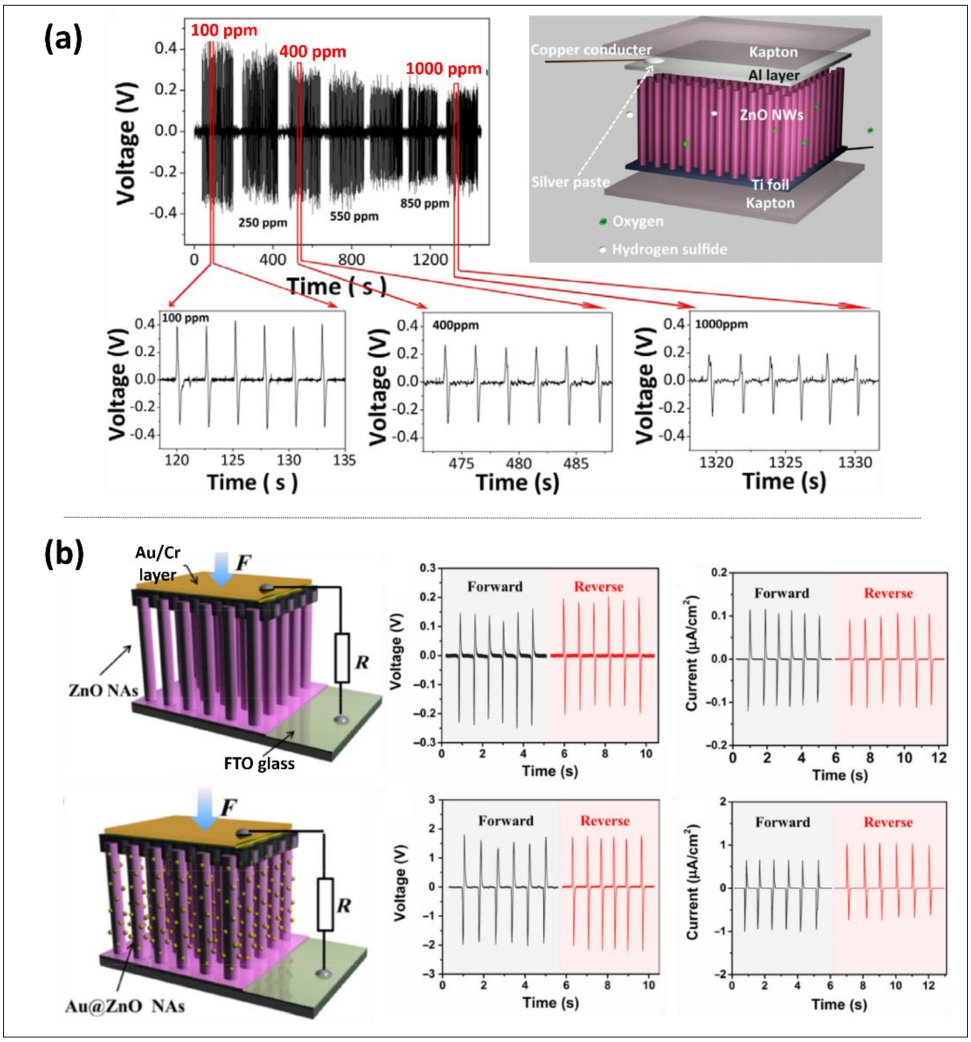

Figure 11. (Image taken from [46], [65]). (a) Schematic diagrm of the ZnO NWs-based PZ for gas sensing applications. The voltage generated by the NWs decreases with increasing the concentration of adsorbed gas in ppm. The depletion thickness decreases and screening becomes effective leading to the decreased piezo-response of NWs. (b) The presence of Au nanoparticles on the surface of ZnO NW-based PZ suppresses the screening. The voltage and the current generated by the PZ thus increases (bottom) as compared to the ZnO NWs without Au particles (top).

4.2.3 Factors responsible for surface charge modulation in 1D-nanostructures

Due to the large surface-to-volume ratio of 1D-nanostructures, the surface trap density is strongly pronounced. Especially in GaN and ZnO NWs, they have been reported to be of the order of 10^{12} - 10^{13} cm^{-2} by electrical and optical characterization techniques [32], [66], [67]. The SCE firstly depends on the inherent characteristics of the material itself. But, in 1D-nanostructures, their synthesis method as well as their immediate environment also plays a very crucial role.

Here we discuss the parameters influencing the surface charges and thus, the severity of the pinning of the Fermi level.

a) NW characteristics linked to the synthesis methods

For the synthesis of NWs, several growth techniques, with or without the use of catalysts, have been reported in the literature. These include Chemical Bath Deposition (CBD), Chemical Vapour Deposition (CVD), Metal Organic Vapour Phase Epitaxy (MOVPE), Molecular beam Epitaxy (MBE) [49], [68]–[73]… Fig. 12 highlights the inter-connected NW characteristics that can be modulated by the growth method, thus directly influencing their piezoelectric properties.

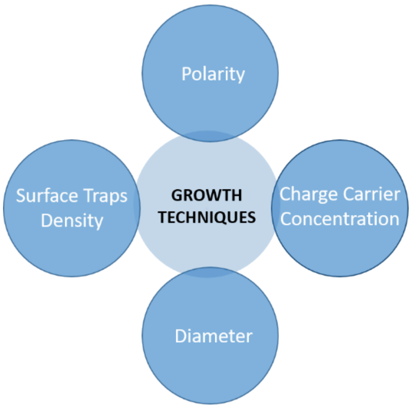

Figure 12. Schematics of the interplay between the growth techniques and the NW characteristics which can modulate their piezo-response.

Diameter and charge carrier concentration

Depending on the growth conditions (the growth axis and technique), the NW diameter can be varied from a few tens of nm to few hundreds of nm. For instance, it has been reported that the critical diameter, d_{crit} = 2w (with w defining the depletion width), below which the nanostructure will be fully depleted, of MBE grown c-axial GaN NWs is of the order of 60-80 nm [39]. By contrast, m-axial GaN NWs grown by CVD present critical diameters around 30-40 nm [34]. This difference in d_{crit} is due to a higher intrinsic dopant concentration in CVD, leading to a small depletion width inside the nanostructures. The d_{crit} can also be voluntarily decreased by intentionally doping the nanostructures. Hence, PA-MBE grown GaN NWs report a d_{crit} of 50 nm and below [74], [75], depending on the doping level. Concerning the ZnO NWs, Garcia et al. in 2021 [76] presented a detailed overview of the evolution of their charge carrier concentrations depending on the different growth methods (Fig. 13).

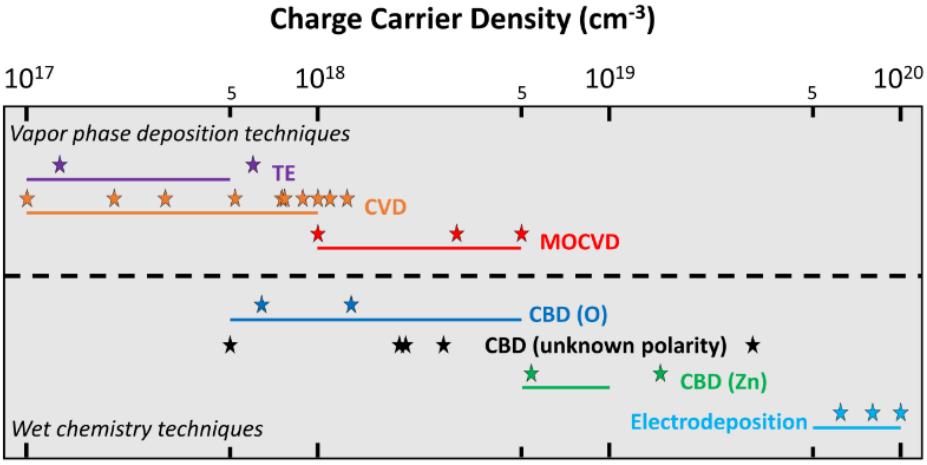

Figure *13*. (Image taken from *[76]*). Schematic diagram summarizing the variation of charge carrier concentration in cm $^{-3}$ as a function of the growth mode for ZnO nanowires.

As previously mentioned, the variation of the doping concentration of the NWs leads to a modulation of the d_{crit} and thus the expression of the surface charge effects. As a consequence, the piezoelectric properties are affected as simulated by Garcia et al. [76]. As illustrated in Fig. 14a, for lesser-doped (highly doped) NWs with d_{crit} higher than 120 nm (40 nm), the piezo-responses are almost negligible due to the high screening effect originating from the free charge-carriers. By contrast, for diameters lower than d_{crit}, the piezo-response is enhanced due to immobilisation of free carriers. Fig. 14b qualitatively maps the free carrier distribution inside the NW volume for NWs with 140 nm and 80 nm diameter, having an equivalent doping level of $N_d = 10^{17}$ cm^{-3}. Higher piezoelectric response was obtained for fully depleted NWs ($d_{NW} < d_{crit}$) due to the reduction of charge carriers.

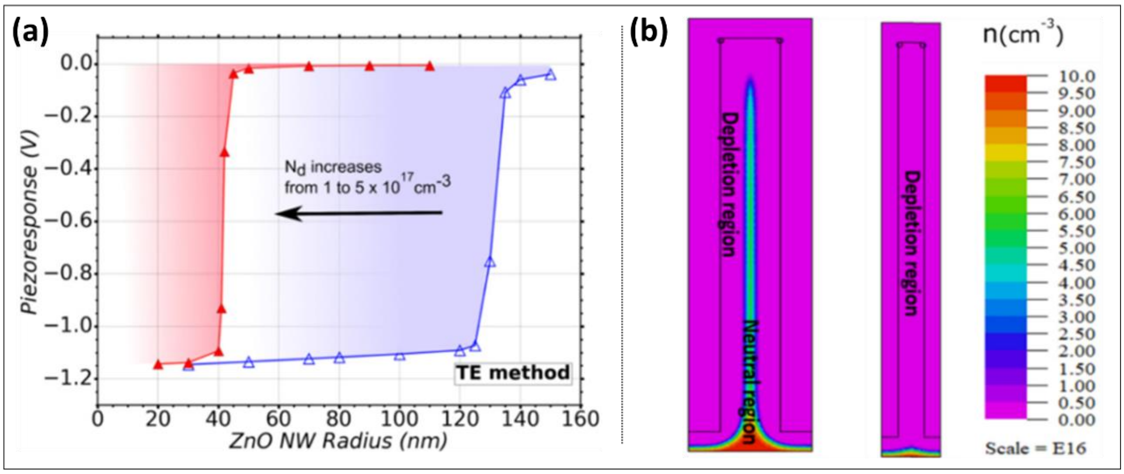

Figure 14. (Image taken from [76]). (a) Evolution of the piezo-resonse of ZnO NWs as a function of the NW diameter for a range of doping level N_d from 1 to 5 × 10^{17} cm^{-3}. (b) Quantitative maps of free carrier distribution within ZnO NWs with 140 nm and 80 nm diameter with a doping concentration of 10^{17} cm^{-3}.

Facet/polarity and surface trap density

It has been reported in the literature that a catalyst-free growth of GaN NWs via PA-MBE [69], [70], [77]–[82] or MOCVD [71] results in the [000-1] orientation of the NWs (C-axis), while the sidewalls are formed by non-polar M-planes. In contrast, catalyst-induced MOCVD-grown GaN NWs are oriented along the a-axis, whereas the sidewalls are formed by polar {0001} and semipolar $\{1\bar{1}01\}$ facets [72], [83], [84]. Moreover, CVD grown GaN NWs are aligned along the m-axis [49], [85].

It is worth mentioning that polar and non-polar planes do not have the same density of surface states. Hence we can expect that the expression of the surface charges as well as their distribution varies from one system to another depending on their growth technique, as reported for ZnO NWs [30], [31], [66], [86], [87]. Thus, the interplay between the surface polarity and the surface charges cannot be neglected [21], [38], [88].

Despite the strong influence of the growth conditions on the above described parameters affecting the piezoelectric properties of 1D-nanostructures, a comprehensive study of their impact remains today under investigation in the literature.

b) Environmental factors

The surface charges are also highly sensitive to all kinds of surface passivation treatments as highlighted in Fig. 15.

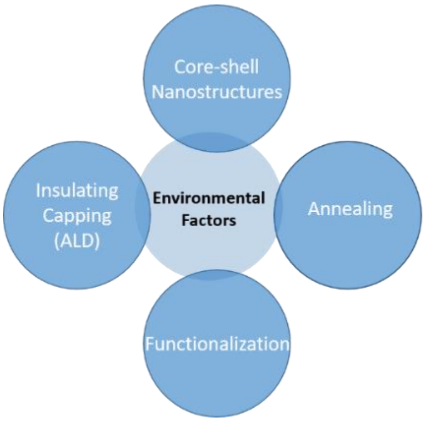

Figure 15. Schematics of the interplay between the NW surface trap density and their surrounding environment.

Several core-shell nanowire structures can be found in the literature, reporting a modification in the surface-related scattering, charge carrier lifetime and mobility along with the density of surface traps [89]–[95]. Simpkins et al. in 2009 [96] demonstrated that the surface traps density can be reduced by a factor of 4 using SiN passivation layer on GaN NWs. Other methods of surface passivation, including the deposition of an insulating Al_2O_3 layer on the NW surface via atomic layer deposition (ALD) [32], [97]–[101] or adsorption of chemical species [102]–[106], have shown a modulation of the surface trap density. Moreover, annealing treatments have also been observed to de-passivated the dangling bonds in Si NWs [107], [108] and in ZnO NWs [109].

Finally, the surface traps density of 1D-nanostructures can also been modulated by the soft matrices used to fabricate the NW-based devices. Studies have been carried out by few groups on the influence of the mechanical coupling between various matrices and NWs, on the performances of

GaN and ZnO NWs-based PZs [56], [110], [111]. However, the influence of these matrices on the surface trap density remains non-investigated to the best of our knowledge.

> *Surface engineering to modulate/control the surface trap densities opens up new pathways to enhance the piezoelectric conversion efficiency of NWs and thus improve the device performances integrating these 1D-nanostructures. However, fundamental questions regarding the effect of the surface charges on the piezoelectric properties of sub-100 nm wide NWs, remain open. Therefore, in-depth investigations must be carried out, amongst them, the experimental investigation of the surface trap density on the piezo-conversion efficiency of NWs as well as the coupling between the active NWs and their environment.*
>
> *In the following parts, we experimentally investigate these two points and validate the importance of surface charges in enhancing the piezo-generation capacity of NWs via statistical piezoelectric measurements performed on arrays of intrinsically p-doped GaN NWs.*

4.3 Critical influence of the surface charge effects: effect of the NW diameter

In this part, to investigate the influence of the surface charges on the piezo-response of GaN NWs, we characterized them by using an AFM system equipped with the modified Resiscope module in axial compression configuration (discussed in Chapter 2). This experimental configuration allows a direct correlation of the mechanical deformation of the 1D-nanostructures with their piezoelectric properties and thus, we can quantify their electromechanical coupling coefficient.

We experimentally demonstrate that the modulation of the surface charges as a function of the NW diameter can lead to a strong enhancement of the coupling coefficient. We thus establish that, optimising the diameter of the GaN NWs is a possible way to enhance their conversion efficiency.

4.3.1 Experimental section

a) Synthesis and morphology of GaN NWs

Intrinsically p-doped GaN NWs grown via PA-MBE on an oxide-free Si(111) n+ substrate were investigated. Due to the catalyst-free self-assembled growth mode, the nanostructures are characterized by a small dispersion of their height and diameter, which results in a dispersion of their stiffness. This dispersion can be seen here as an advantage, since it allows spanning a large range of diameters within a same sample. Fig. 16 shows the SEM images of the non-intentionally p-doped GaN NWs in tilted-view and the cross-section view, respectively.

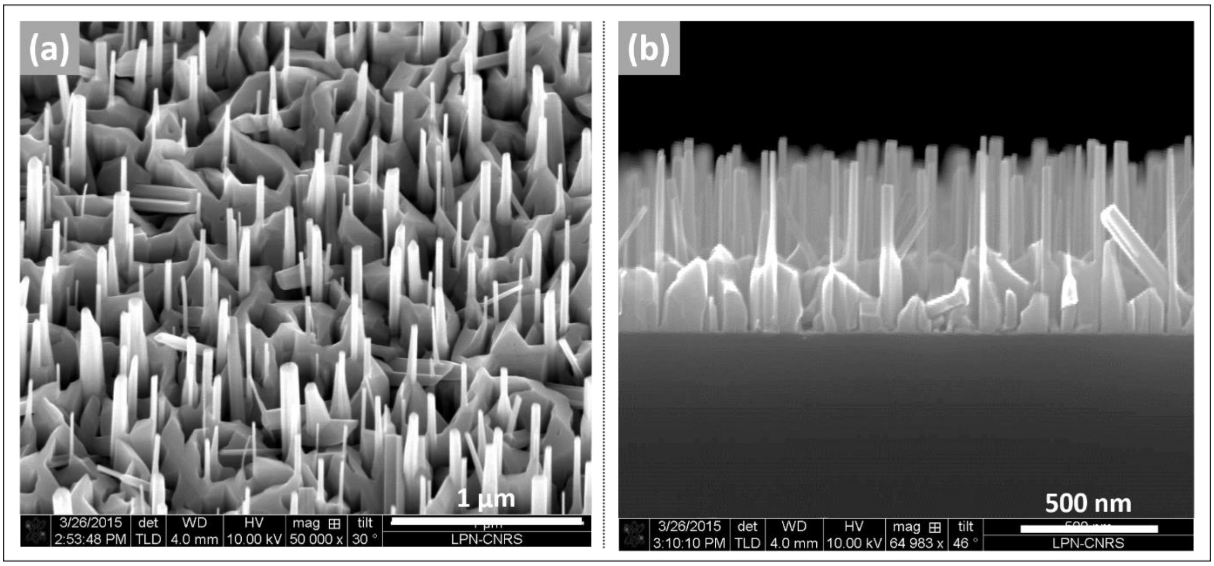

Figure 16. (a) Cross-section view and (b) tilted-view, of non-intentionally p-doped GaN NWs via PA-MBE.

Table 1 presents the NWs characteristics extracted from SEM images.

Table 1. Average height, diameter and density of the as-grown GaN NWs measured from SEM images in cross-section and top views respectively. The un-encapsulated NW height emerging out of PMMA matrix is also given.

	Height (nm)	***Diameter (nm)***	***Density (NW/cm^2)***
As-grown	1050 ± 200	50 ± 30	8×10^8
With PMMA matrix	*100 ± 200*	*50 ± 30*	*8×10^8*

b) AFM measurement principle and sample preparation

The piezoelectric conversion capacity of GaN NWs has been investigated by using an AFM equipped with the modified Resiscope module working in axial compression configuration. As a reminder, under this experimental configuration, the GaN NWs are vertically compressed along their piezoelectric c-axis. As a result, a positive piezo-potential is created within the NW volume (*cf.* Chapter 2, section 2.3.4). The GaN nanostructures investigated here are slightly p-doped. The Schottky diode, formed at the NW/AFM tip interface is thus positively biased and allows the collection of positive output voltages. Since, the topographic and electrical signals are simultaneously recorded, we can establish a direct relation between the mechanical deformation of the NWs and their piezo-conversion properties.

However, in order to perform reliable piezo-electric measurements under this axial compression, the GaN NW sample has been mechanically consolidated and electrically connected.

Mechanical consolidation

Since the GaN NWs are very flexible, it is essential to mechanically consolidate them, especially, when they are axially compressed. In fact, when the AFM tip enters into contact with the NW and axially compresses it, the 1D-nanostructure can undergo an additional deformation by bending or buckling [75]. To avoid this, the NW bases were embedded into a poly(methyl methacrylate)

(PMMA) resist layer, which has been etched-back by using reactive ion etching (RIE) with oxygen plasma to uncover the top portion of the NWs. Then, a diluted-HF etching was performed in order to remove the residual Ga_2O_3 oxide layer formed on the NWs top during the plasma treatment. Following this technological process, the GaN NWs emerging from the resist were characterized by a height equal to 100 ± 200 nm and an unchanged diameter as detailed in Table 1.

Electrical connections

Under the fast conditions of scanning met in the axial compression configuration (the tip interacts with the surface under intermittent mode), it is not easy to establish a stable electrical contact at the NW/AFM tip interface, ensuring an optimal collection of the output signals generated by the NW in response to its deformation. To guarantee a good electrical stability, we have directly deposited a 5 nm-Cr/20 nm-Pt metallic layer (playing the role of the Schottky diode) on the previously deoxidized tops of the NWs. With this "*deported*" electrode (NW-metal interface rather than NW-AFM tip interface), when the AFM tip enters in contact with the nanostructure, a metal/metal contact is established, thus ensuring a stable contact even under fast AFM scanning conditions. Fig. 17 illustrates the substrate preparation method.

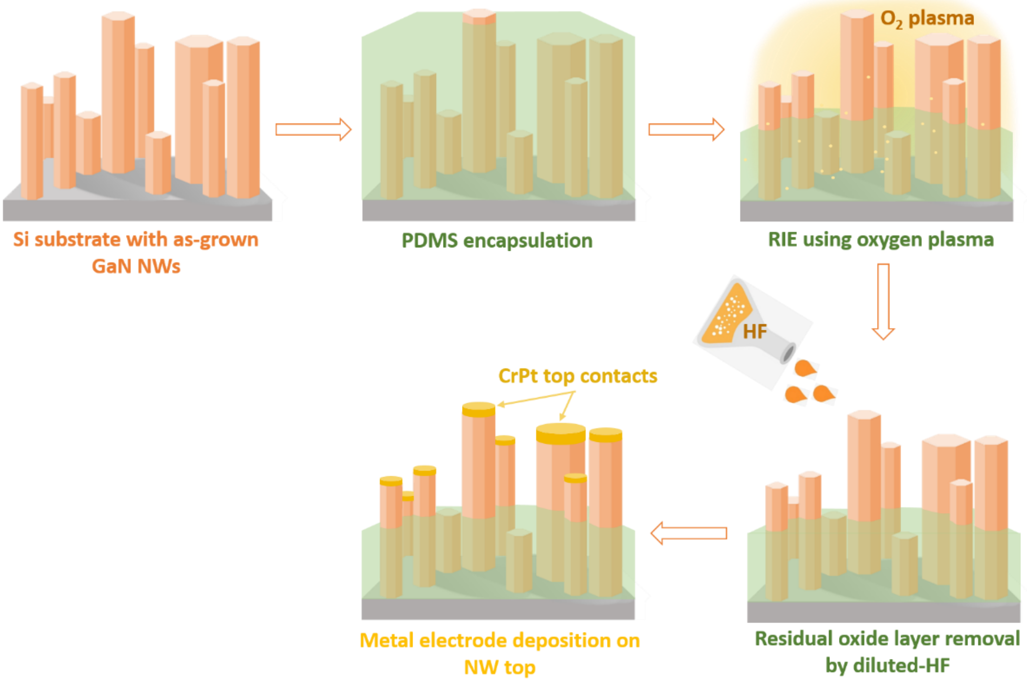

Figure 17. Schematic representation illustrating the substrate preparation method of the samples for piezo-electrical measurements under axial configuration.

Fig. 18 presents a cross-section view and titled-view of the prepared sample. We can distinguish the bottom portion of the NWs embedded into PMMA resist, as well as their metallised top portions emerging from the resist. We note that a Cr/Pt residual layer is also formed at the top of the PMMA resist. However, there is no continuity between this residual metallic layer and the one presents at the top of the NWs. This discontinuity thus ensures a diode-like behaviour of the Cr/Pt layer localized on the top of each NW.

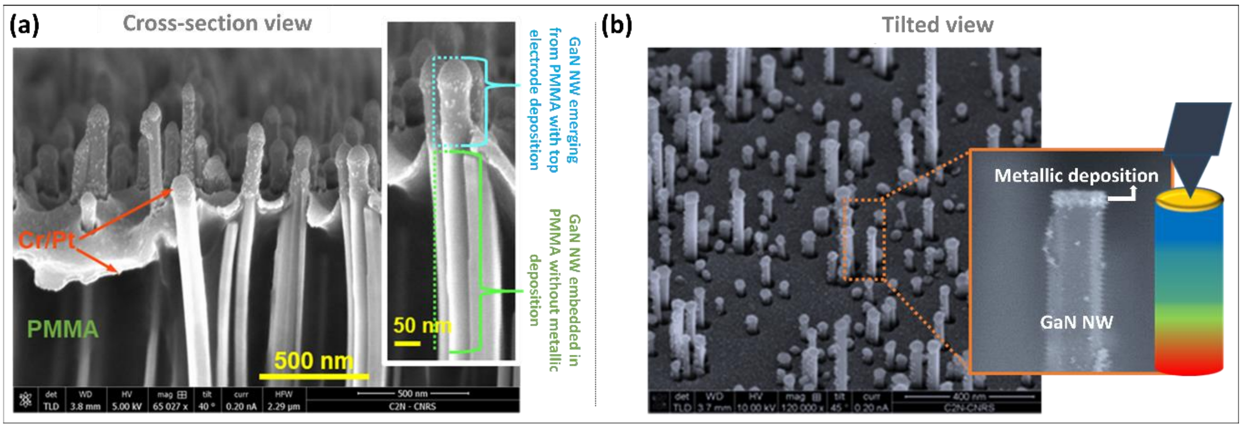

Figure 18. (a) Cross-section and (b) tilted-view, of PA-MBE grown GaN NWs partially embedded in PMMA resist. A Cr/Pt metal contact is deposited on the top of each NW to ensure electrical stability.

4.3.2 Results and Discussion

a) Piezoelectric response of GaN NWs

The piezoelectric response of the GaN NWs has been investigated under a well-controlled axial compressive force (the constant normal force, CNF) evolving between 40 and 220 nN. As observed in the 2D-electrical mappings presented in Fig. 19, the piezoelectric response of each deformed NW increases with the CNF, demonstrating the direct piezoelectric effect.

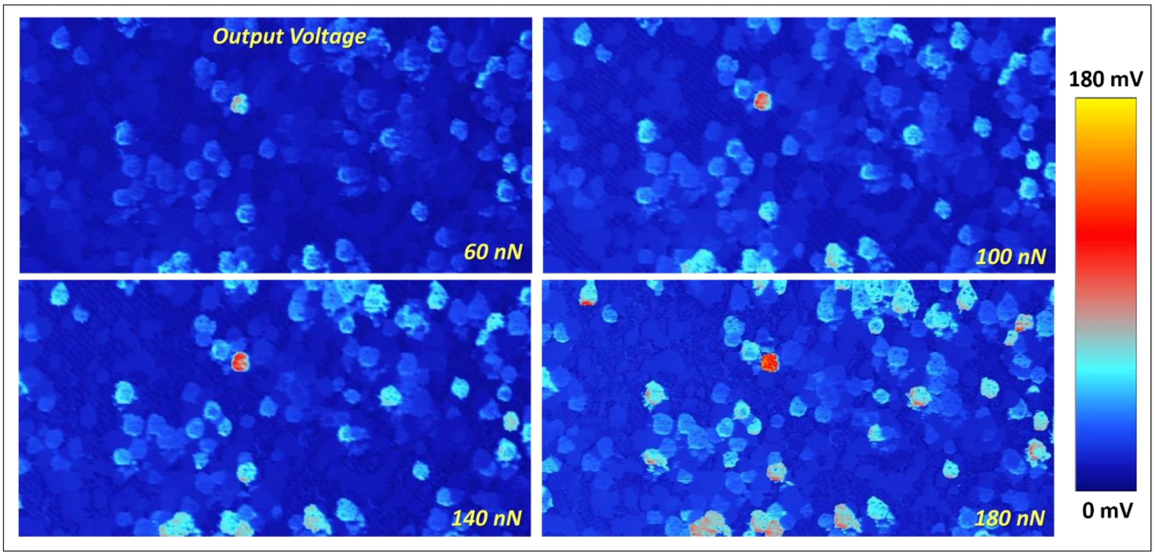

Figure 19. (10 µm × 5 µm) 2D-electrical mappings of the piezoelectric response of GaN NWs as a function of CNF. By increasing the applied CNF from 60 nN to 180 nN, the piezo-response of active NWs also increases.

The statistical analysis of these 2D electrical mappings is shown in Fig. 20. The average O.V. values follow a Gaussian distribution and evidence a bimodal distribution of the GaN NWs.

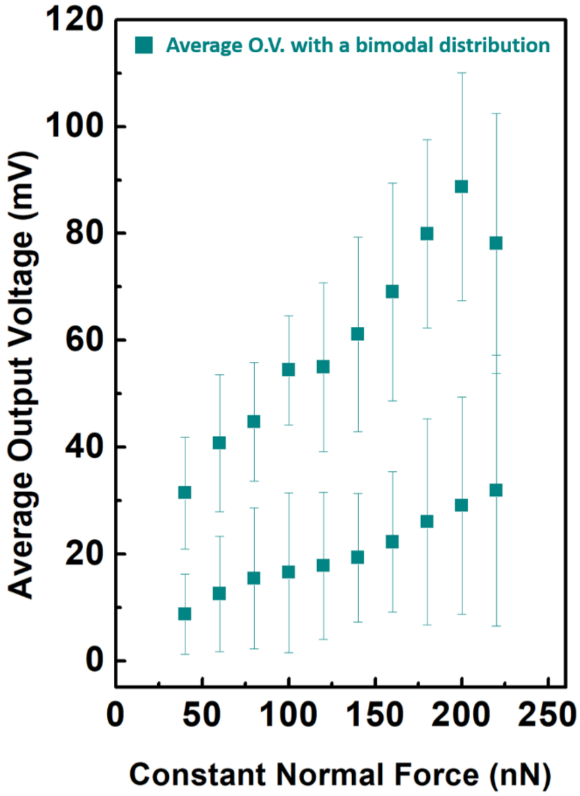

Figure 20. Average output voltage as a function of the applied constant normal force. A dispersion in the NW dimensions leads to a bi-modal distribution of the output voltage.

The piezo-response of NWs is directly related to their degree of deformation and thus to their dimensions. Due to the self-assembled growth mode used here to synthesize the NWs, they are characterized by a dispersion in their heights and diameters, and thus have different stiffness values. Thus, under an equivalent axial force, the NWs exhibit a different deformation rate, leading to a dispersion of their output signals. In our case, the first distribution corresponds to the most rigid set of NWs, which are only compressed axially, while the second distributions refers to more flexible NWs, combining axial compression and slightly buckling deformation as discussed in [75].

b) Conversion efficiency of GaN NWs and role of the surface charges

In the literature, and as we have done in chapter 3, the O.V. values generated by the NWs in response to an external mechanical input are considered to quantify their piezo-conversion capacity. However, this is not a rigorous methodology, especially if we want to compare the results. In fact, the O.V. is affected by several parameters such as the deformation mode, the applied force [112], the R_{load} through which O.V. are collected (Chapter 3)…

One solution to rigorously evaluate the conversion capacity of the 1D-nanostructures is to quantify their electromechanical coupling coefficient, defined by:

$$\eta = \frac{output\ electrical\ energy}{input\ mechanical\ energy} \qquad (1)$$

The AFM system equipped with a modified Resiscope module employed in this study, allows this kind of quantification by allowing a direct correlation between the mechanical deformation of the NWs and their piezoelectric response. In order to be in these experimental conditions, only the NWs from the first distribution, *i.e.* the rigid NWs presenting a stiffness (k) ≥ 5 N/m (elastic modulus lower than 3.5 GPa), have been considered here.

We can define the electromechanical coupling coefficient (η) as the ratio between (Annex 1):

- the output electric energy generated by an individual NW in one piezoelectric discharge, given by:

$$\Delta W_{Piezo} = \frac{1}{2}\frac{\tau}{R_L + R_{Total}} V^2 \tag{2}$$

and,

- the input mechanical energy, corresponding to the elastic deformation energy for axially compressing/releasing the NW, given by:

$$\Delta W_{Elast.} = F\Delta l \tag{3}$$

Here, F is the applied CNF; Δl is the NW height variation (Fig. 21a); V is the piezo-generated O.V.; $\tau\ (3\ ms)$ is the measured decay time of the system; $R_L\ (1\ G\Omega)$ is the load resistance of the measurement system; and finally, R_{Total} (144 MΩ) is evaluated from the I(V) characteristics (Fig. 21b) performed on various single GaN NWs and includes the series resistance (R_S), the contact resistance (R_C) of the Schottky diode, and the NW resistance (R_{NW}) (Annex 2).

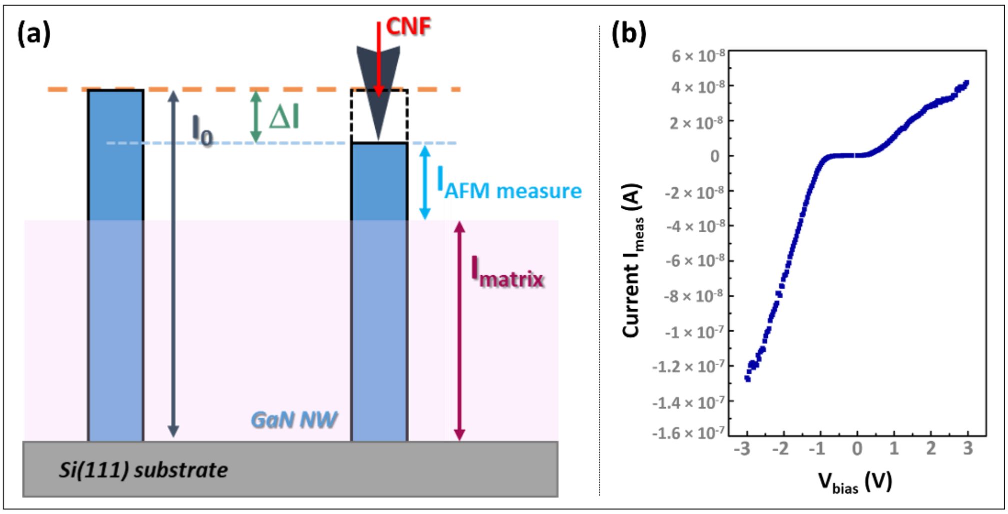

Figure 21. (a) Schematics of the GaN NWs partially embedded in PMMA matrix with thickness 'l_{matrix}'. The applied CNF axially compresses the NW, resulting in a height variation of Δl, as compared to non-compressed NW. (b) I-V characteristics performed on a series of GaN NWs in the bias range of -3 V to 3 V.

We have estimated the electromechanical coupling for NWs (k > 5 N/m) deformed under a pure axial compression and presenting a deformation degree of about 1%. Fig. 22 presents the variation of the coupling coefficient (η, otherwise known as the piezo-conversion efficiency) as a function of the NW stiffness. We show that η varies in the 5.9 - 43.4 % range and presents a correlation with the NW stiffness. This first observation could appear surprising in first approximation. In fact, all the NWs in this study present an equivalent compression strain of 1%. We should thus obtain an approximately constant 'η', since the piezo-conversion firstly depends on the material deformation.

This evolution demonstrates that η is not only driven by the mechanical characteristics of the NWs. And therefore, another parameter plays a non-negligible role. This leads us to the surface charge effects.

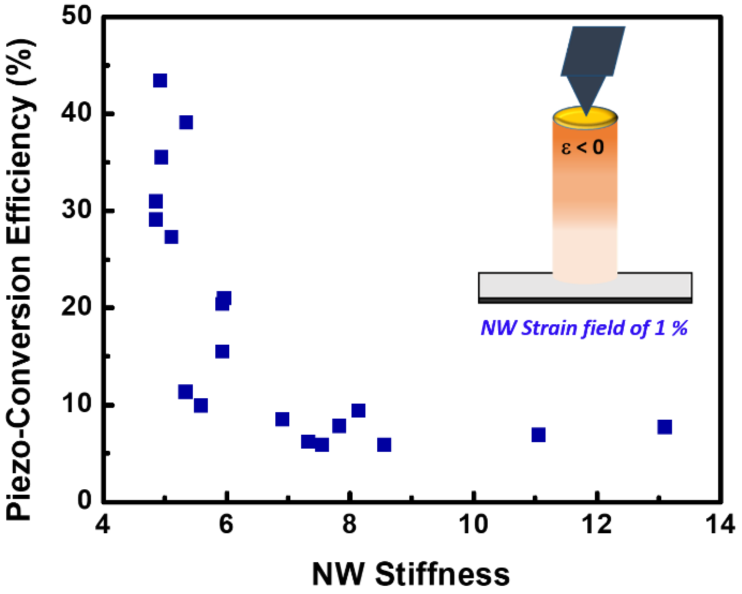

Figure 22. Variation of the electromechanical coupling coefficient,η, as a function of the NW stiffness for a deformation degree of 1%.

To investigate the influence of the surface charges on the piezo-conversion efficiency of our GaN NWs, we have plotted the coupling coefficient as a function of the NW radius/diameter (Fig. 23). In fact, here, all tested nanowires present the same surface trap density (NWs from the same sample) but they are characterized by a small variation of their diameter. As we have seen in the first part of this chapter, the expression of the surface charges can strongly evolve depending on the NW diameter.

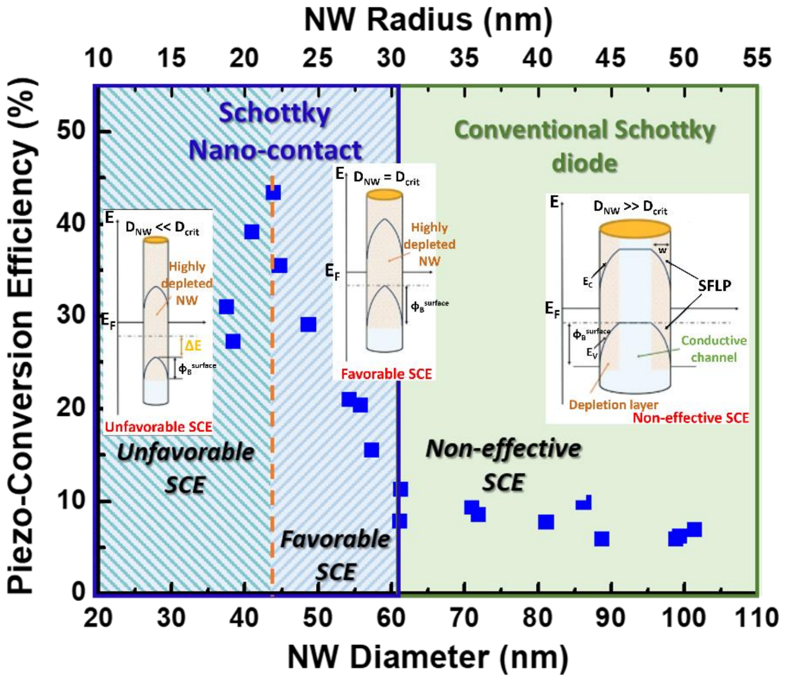

Figure 23. Evolution of the piezo-conversion efficiency as a function of the NW diameter/radius. The Schottky behavior of the nano-contacts for smaller diameters can highly influence the O.V. collection efficiency. Three NWs with different diameters have been integrated into the image with a different SFLP severity.

For NW diameter, D_{NW}, larger than 60 nm, the coupling coefficient is approximately constant. This means that only the deformation of the NWs controls their coupling efficiency. We can thus consider that, here, the surface charges do not affect the free charge carrier concentration within the NWs. We are thus in the configuration where $D_{NW} >> D_{crit}$, and, the depletion zone surrounds a conduction channel.

For D_{NW} approximately equivalent to the D_{crit} (diameter in the 44-60 nm range), the coupling coefficient abruptly increases up to 43.4%. Here, we assume that the NW is fully depleted with a surface barrier height, $\Phi_B^{Surface}$, of the order of the SFLP. The free carrier density and thus the screening effect are significantly reduced [34], [38], enhancing the O.V. generation of NWs and thus their coupling coefficient. Consequently, we can say that, here, the SCE played a favorable role in the enhancement of the piezo-conversion capacity of the NWs.

Finally, for $D_{NW} << D_{crit}$, a decreasing of the coupling coefficient is observed. For this diameter range, we assume that the NWs are strongly depleted. A strong SFLP leads to a reduction in the $\Phi_B^{Surface}$ and the carrier density is strongly decreased due to an increased electron-hole recombination at the surface. Consequently, the NWs becomes extremely resistive and induce also a limitation of the piezo-charge circulation in the external electrical circuit. Thus, the O.V. generation is highly degraded. Here we can say that the SCE turns unfavorable for the piezo-conversion.

These experimental results are a clear demonstration of the impact of the surface charges on the piezo-conversion capacities of GaN NWs and support the theoretically predicted behavior [34], [38], [47].

4.4 Critical influence of the surface charge effects: effect of the NW environment

To give a further push to our experimental investigations, we have analysed the influence of SCE on the piezo-generation capacity of our GaN NWs, by changing their immediate environment with an Al_2O_3 shell encapsulation. The Al_2O_3 is known to strongly decrease the surface trap density. To quantify this influence, we measure the piezo-response of the GaN NWs by using an AFM system equipped with the modified Resiscope module, working under 'bending in scanning configuration' (*cf*. Chapter 2, section 2.3.4). With this experimental configuration, we can access the strong O.V. values generated by our GaN NWs and observe the role of the surface charge on their generation capabilities. We thus establish a second possible way to adjust the GaN NW conversion efficiency.

4.4.1 Experimental section

a) Synthesis and morphology of GaN NWs

Intrinsically p-doped GaN NWs have been considered in this study to analyse the influence of surface charges on their piezoelectric response. These NWs are characterised with a bimodal height distribution owing to their self-assembled growth mode, whereas the diameter stays approximatively constant (~ 36 nm), at which a fully depletion of the NW takes place. The average height distributions (h_1 and h_2), diameter and density of the as-grown NWs are given in Table 2, as extracted from the SEM analysis (cross-section view of the NWs in *Fig. 24a*).

Table 2. Average height distributions h_1 and h_2, average diameter and density of the as-grown GaN NWs measured from SEM images in cross-section and top views respectively.

Average height h_1 (nm)	***Average height h_2 (nm)***	***Average diameter (nm)***	***Density (nWs/cm^3)***
553 ± 93	*755 ± 85*	*36 ± 9*	*3.4 x 10^9*

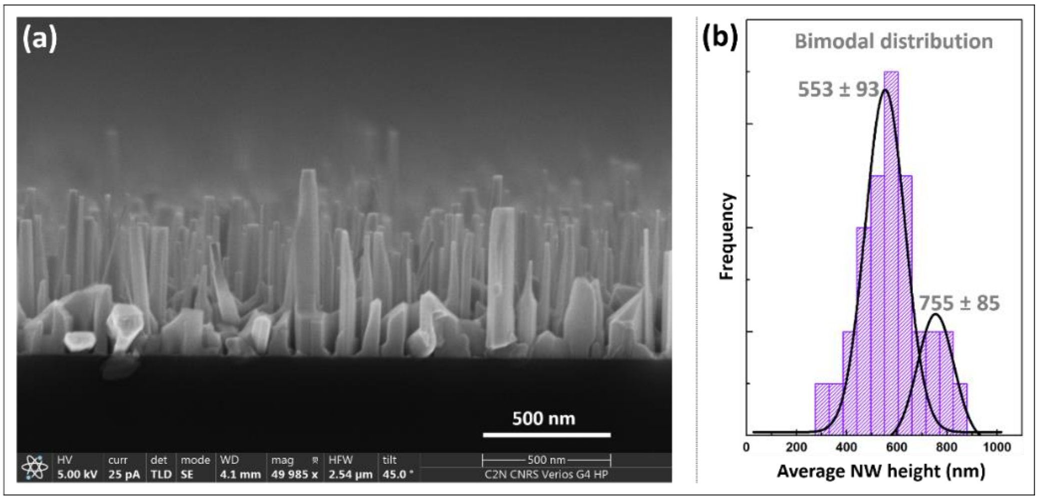

Figure 24. (a) SEM image of the intrinsically p-doped GaN NWs in the cross-section view. (b) Histogram showing the bimodal distribution of the NW heights with respective Gaussian fittings.

b) Sample preparation and piezo-electrical measurements

To demonstrate the importance of SCE on the O.V. generation capacity of intrinsically p-doped GaN NWs, the samples were prepared following different ways. Fig. 25 shows a schematic diagram illustrating the preparatory steps for the samples. For both, due to the high flexibility of the NWs and in order to perform reliable electrical measurements, the NWs were mechanically consolidated with a soft matrix.

The type 1 sample (A1) consists of as-grown GaN NWs embedded in a PDMS matrix, which has been etched-back using RIE to uncover the top portion of the NWs. Here, the un-encapsulated NW height is about 200 ± 50 nm. With a diameter of 36 ± 9 nm, the top portion of the NWs is characterized by an aspect ratio of 5.5.

The type 2 sample includes additional preparatory steps prior to PDMS coating. Firstly, a 10 nm thick Al_2O_3 shell is deposited on the NWs using atomic layer deposition (ALD), which acts as a passivation layer [97], [100], [101], [113] . Secondly, the NWs with the insulating shell are exposed to oxygen plasma for 30 seconds to enhance the wettability of PDMS with the NW sidewalls. Then, PDMS matrix is spin-coated and etched-back to uncover the top portion of the NWs. Finally, the Al_2O_3 capping the top facet of the NWs is removed by ion beam etching (IBE). Based on this preparation process, two different samples have investigated:

- **Type 2 sample B2:** The un-encapsulated NW height was adjusted to be of the order of 200 ± 50 nm, equivalent to the sample A1. However, it must be noted that the Al_2O_3 shell increases the diameter of the NWs. The diameter being 56 nm now for the NWs (initial NWs diameter of 36 nm plus the Al_2O_3 shell of 10 nm), they are characterized by a lower aspect ratio of 3.6. The NWs are thus more rigid compared to A1. As the deformation rate of the NWs strongly depends on their aspect ratios, for a given CNF value, the samples A1 and B2 do not have an equivalent deformation degree and thus their piezoelectrical performances cannot be properly compared.
- **Type 2 sample C2**: The un-encapsulated NW height has been adjusted to about 310 ± 50 nm. In these conditions, they present an aspect ratio of 5.5, equivalent to type 1 sample, A1.

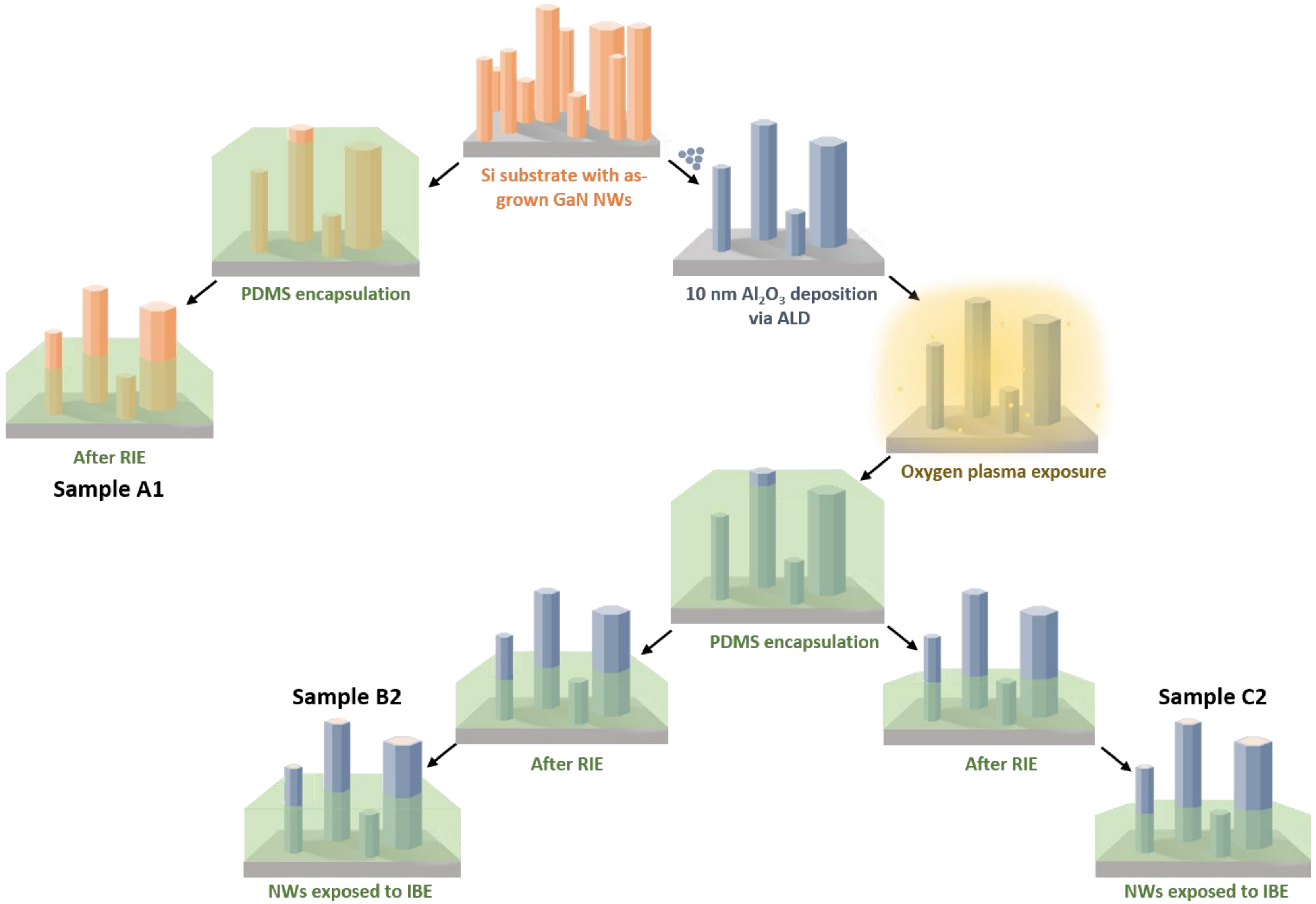

Figure 25. Schematic diagram with preparatory steps of the two types of samples for piezo-electrical measurements using AFM with modified Résiscope.

The three sample characteristics with their chosen nomenclature are recapitulated in Table 3.

Table3. Average un-encapsulated height and the average diameter of the NWs for the three samples with their type and nomenclature.

Sample Type (Intrinsically p-doped GaN NWs)	***Nomenclature***	***Emerging avg. height (h_{avg}) (nm)***	***Relative avg. diameter (d_{avg}) (nm)***	***Aspect ratio (AR) (h_{avg}/d)***
Type 1	*A1*	*200 ± 50*	*36 ± 9*	*5.5*
Type 2	*B2*	*200 ± 50*	*56 ± 9*	*3.6*
Type 2	*C2*	*310 ± 50*	*56 ± 9*	*5.5*

The piezoelectric conversion capacity of the prepared samples was investigated by using the AFM equipped with the modified Resiscope module, working in 'bending in scanning configuration' (also employed in Chapter 3). Due to the lateral NW deformation induced by the AFM tip, a piezoelectric potential is created within the NW, evolving from a negative piezo-potential on the stretched side of the NWs to a positive one on the compressive side (Fig. 15 Chapter 1). The GaN nanostructures investigated here are slightly p-doped. The Schottky diode, formed at the NW/AFM tip interface is thus positively biased when the AFM tip enters in contact with the compressive side of the NW. Since, the topographic and electrical signals are simultaneously recorded, we can easily establish a correlation between the positive O.V. generated by the NW and its localization.

4.4.2 Results and discussions

In this chapter, several examples have been provided to demonstrate that SCE are highly predominant in 1D-nanostructures. Especially, we have shown that these surface charges have a strong influence on the piezo-conversion efficiency of GaN NWs [75].

The prepared samples A1, B2 and C2 were characterized by our AFM-adapted Resiscope system. The topographical and output voltage maps were simultaneously registered at CNFs ranging between 120 nN and 380 nN for an R_{load} of 1 Gohm. The 3D-electrical mappings are shown in Fig. 26 for the aforementioned samples, and the corresponding statistical analysis is presented in Table 4.

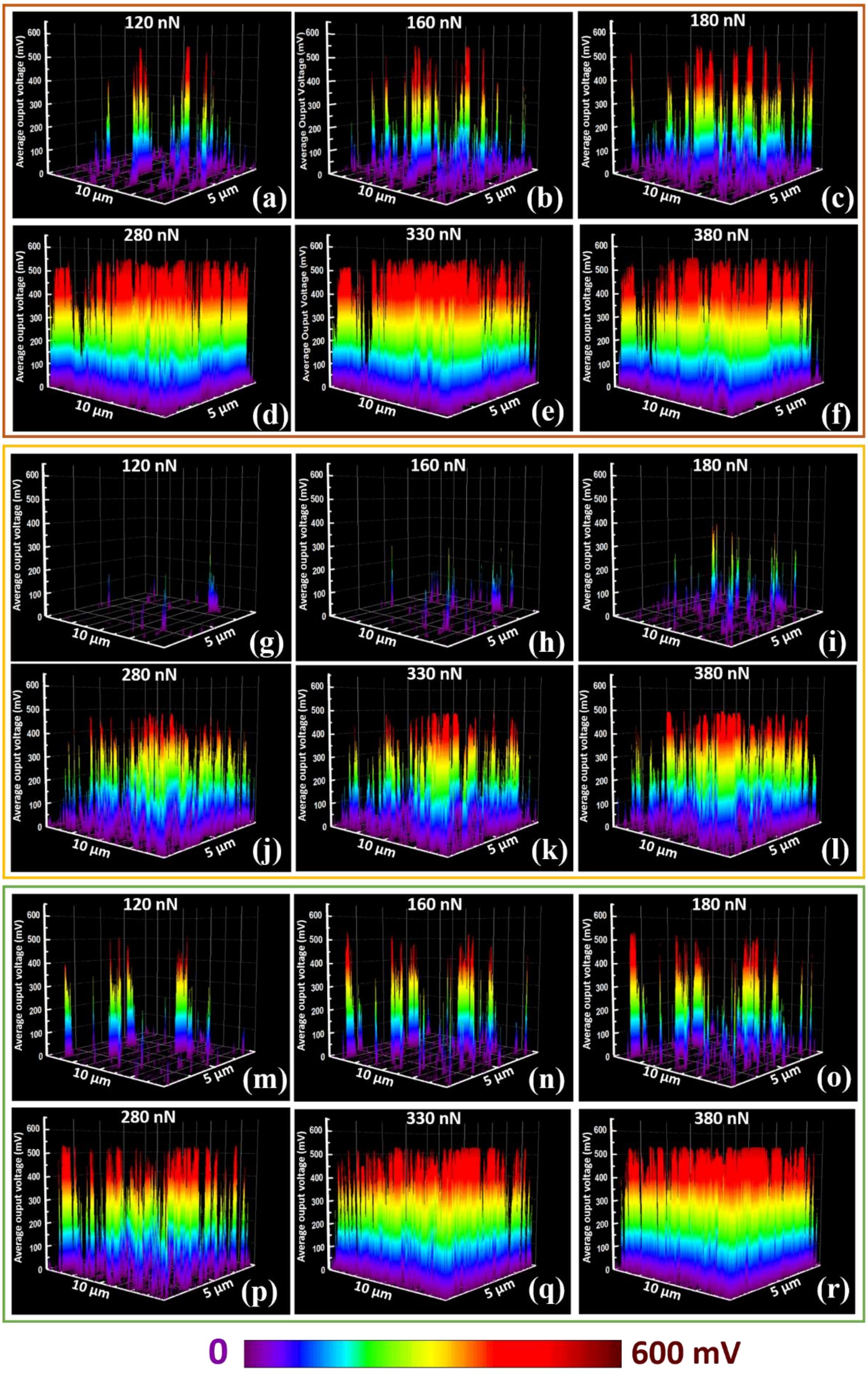

Figure 26. 3D representations of the electrical mappings (10 µm × 5 µm) for (a)-(f) sample A1, (g)-(l) sample B2 and (m)-(r) sample C2 at CNF ranging from 120 nN to 380 nN, respectively. All maps have an equivalent scale bars ranging from 0-600 mV.

Table 4. Average O.Vs obtained for the 1st, 2nd and 3rd distributions respectively, for samples A1, B2 and C2 respectively.

Constant Normal Force (CNF) (nN)	**First Distribution (mV)**	**Second Distribution (mV)**	**Third Distribution (mV)**
120	*58 ± 75*	*242 ± 58*	*509 ± 54*
160	*100 ± 89*	*373 ± 55*	*528 ± 37*
180	*123 ± 88*	*306 ± 88*	*499 ± 48*
280	*211 ± 71*	*407 ± 58*	*529 ± 31*
330	*--*	*335 ± 82*	*526 ± 39*
380	*250 ± 42*	*383 ± 57*	*517 ± 40*
120	*24 ± 19*	*117 ± 20*	*195 ± 26*
160	*28 ± 27*	*171 ± 44*	*289 ± 36*
180	*56 ± 54*	*259 ± 37*	*375 ± 38*
280	*114 ± 58*	*273 ± 61*	*417 ± 54*
330	*104 ± 69*	*271 ± 65*	*434 ± 49*
380	*135 ± 62*	*302 ± 56*	*446 ± 66*
120	*49 ± 33*	*182 ± 53*	*446 ± 86*
160	*67 ± 55*	*289 ± 74*	*481 ± 52*
180	*55 ± 53*	*243 ± 67*	*476 ± 61*
280	*127 ± 69*	*318 ± 63*	*472 ± 74*
330	*87 ± 68*	*332 ± 60*	*504 ± 62*
380	*--*	*302 ± 63*	*503 ± 57*

The average output voltages are also plotted as a function of CNF in Fig. 27. The three sets of samples present similar traits:

1. Positive output voltages are generated by the GaN NWs irrespective of their stiffness and the applied CNF. This result is in agreement with the intrinsic p-type doping of the GaN NWs achieved with our growth conditions [10], [75].

2. The average output voltages follow a Gaussian distribution and evidence a multi-modal distribution. It originates from the self-assembled growth mode of the NWs [75], [114]. The piezo-response of NWs being directly related to their degree of deformation and thus to their dimensions, their stiffness dispersion results in an O.V. dispersion. In the present case, the first distribution corresponds to the most rigid set of NWs, while the second and third distributions refers to more flexible NWs.

3. All three distributions show an increase in the average output voltages on increasing the applied CNF due to the direct piezoelectric effect and the increased stability of the Schottky contact [115], [116].

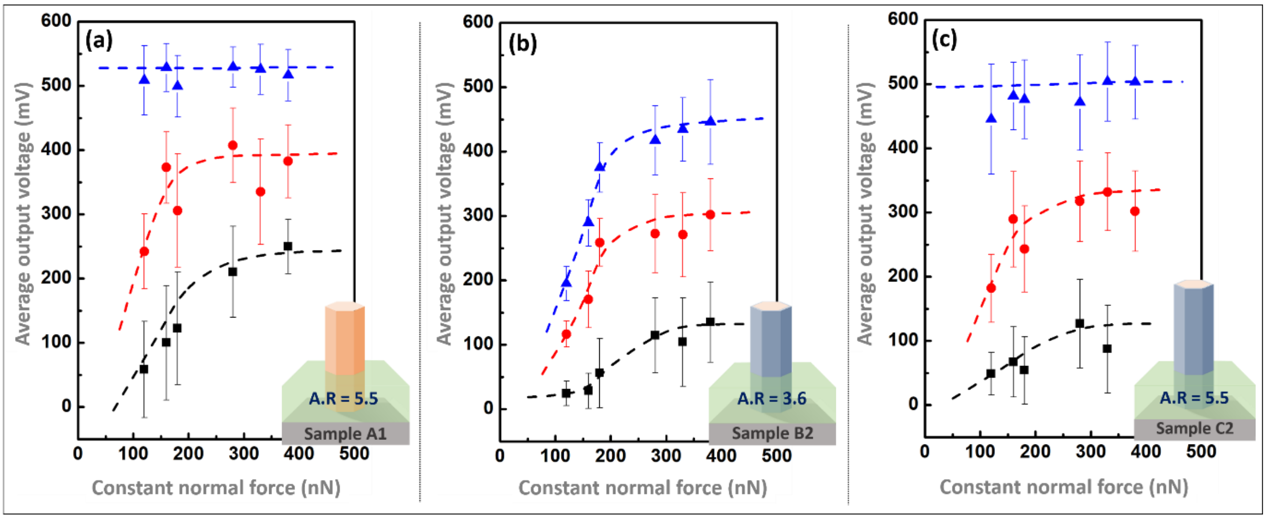

Figure 27. Statistical analysis of the evolution of average output voltages w.r.t. CNF for (a) sample A1, (b) sample B2, and, (c) sample C2. Three O.V distributions are observed, namely the 1st distribution (black squares), 2nd distribution (red circles) and 3rd distribution (blue triangles) for rigid NWs and comparably flexible NWs, respectively. Inset shows schematic representations of a single NW for each sample type with their corresponding aspect ratios.

Now, we analyse the O.V. variations for each sample:

- <u>Sample A1</u>: the first distribution increases continuously from ~ 58 mV to ~ 250 mV, while the second one achieves a saturation around 350 ± 50 mV for CNF ≥ 160 nN. The third distribution is characterized by approximatively constant O.V. values around 515 ± 15 mV, irrespective of the applied CNF. This means that the corresponding NWs are very flexible and attained their maxima of piezo-conversion at smaller forces.
- <u>Sample B2</u>: the first distribution increases continuously from ~ 25 mV to ~ 135 mV, while the second and third ones tend to saturate around 285 ± 15 mV and 430 ± 15 mV for CNF ≥ 280 nN. This behaviour clearly indicates that the maxima of piezo-conversion can only be attained at higher CNFs.
- <u>Sample C2</u>: the three distributions follow equivalent traits as the sample A1 but have smaller O.V. values. For this sample, the first distribution increases continuously from ~ 48 mV to ~ 100-130 mV, while the second one reaches a saturation around 290 ± 50 mV for CNF ≥ 160 nN. As sample A1, the third distribution is also characterized by approximatively constant O.V. values, but only around 475 ± 30 mV, whatever the applied CNF.

In order to understand and explain the O.V. variations presented by the three sets of NWs, it is important to consider different parameters controlling the capacity of the NWs to convert the mechanical deformation into a direct electrical signal.

- **The piezo-conversion firstly depends on the deformation degree of the material.** According to the direct piezoelectric effect, as the deformation increases, the output signal increases. This means that under an equivalent mechanical input, two GaN NWs presenting a different stiffness/aspect ratio will generate different internal piezoelectric fields and thus different output signals. This mechanism in play is illustrated in Fig. 27 by the multi-modal distribution of the O.V. values related to different NW stiffness. This mechanism is also schematized in Fig. 28.

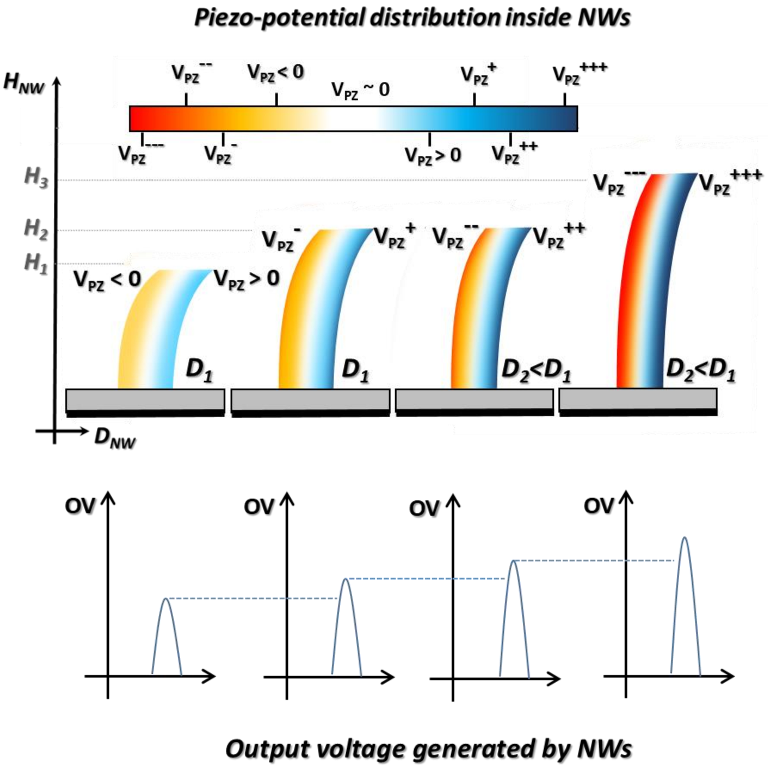

Figure 28. Schematic representation of the piezoelectric field distribution inside the NWs and the corresponding output voltage generated in response to an equivalent lateral force applied by the AFM tip as a function of the NW's stiffness (linked to the NW diameter D and height H).

- **The piezo-conversion is directly related to the conductivity/resistivity of the NWs.** It is well known that the free carriers tend to screen the piezo-charges. As a result, the internal piezoelectric field within the NW decreases and thus, the output signal degrades. The free charge carrier concentration is driven by the doping level of the NWs, but also by the surface charges. As explained in the beginning of this chapter, the surface charges lead to a pinning of the Fermi level in the depletion region. As a function of the diameter (see Fig. 4 and results presented in Fig. 23) or the surface trap density, the NW can be partially or fully depleted (insets of Fig. 23). This leads to a modulation of the free carrier density within the NW volume and thus, of the piezoelectric field.

The deposition of the Al_2O_3 shell induces an increase of the NW diameter and thus of the aspect ratio. It also induces a passivation of the NW edges with a strong reduction of the surface trap density [117]. In order to identify its influence on the piezo-conversion properties of our GaN NWs, we compare samples B2 and C2 with the sample A1, which is our reference sample.

Comparison between samples A1 (GaN NWs with AR = 5.5) and B2 (GaN/Al_2O_3 core/shell NWs with AR = 3.6)

In Fig. 27 and Table 4, the output voltages generated by sample B2 increase slowly for equivalent CNF and reach saturation (for distributions 2 and 3) at higher CNF. This behaviour is firstly due to the smaller aspect ratio of the NWs emerging from the PDMS matrix. Thus, higher forces are required to reach deformation degrees equivalent to A1. We can also note that the O.V. obtained for all three distributions at each CNF value are systematically lower for sample B2. This result evidences a limitation of the piezo-generation capacity of the NWs and can also be assigned to a smaller influence of the surface charges due to the Al_2O_3 shell.

In our reference sample A1, the NW diameter is around 36 ± 9 nm. Referring to our results in the previous section, we can assume that the NWs are fully depleted due to the SCE (Fig. 29a). As there is no conduction channel available, the screening of the piezo-potential by the free-charge carriers is extremely limited. This condition is highly favourable, leading to the creation of a strong internal electric field within the NWs, and therefore, resulting in the generation of higher O.V. values. In the sample B2, the presence of the passivation layer, i.e. the Al_2O_3 shell deposited at the NW sidewalls significantly reduces the surface trap density. As a result, the space charge region decreases and a narrow conduction channel is created in the core of the NWs (Fig. 29b). The generated piezo-charges are thus screened by the freely diffusing charge carriers in the conduction channel. Consequently, the internal piezoelectric field created within the NWs is smaller and collected O.V. values are lower.

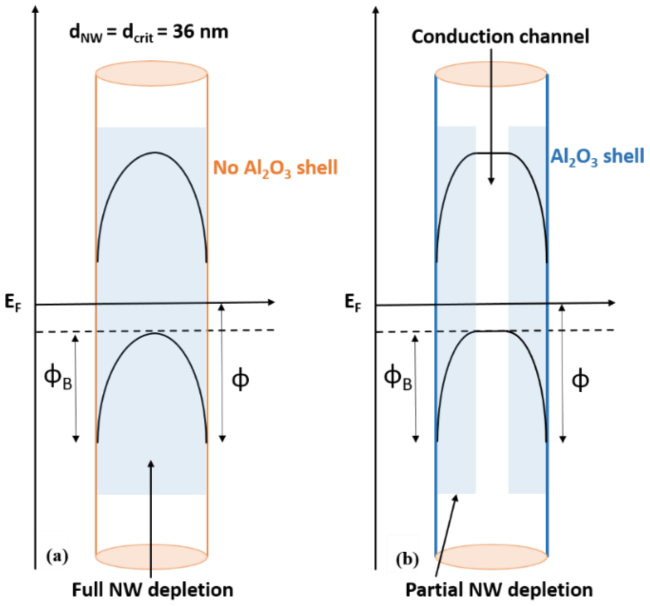

Figure 29. Surface Fermi level pinning in (a) GaN NW (sample A1), fully depleted due to the strong SFLP; and (b) partially depleted GaN/Al_2O_3 core/shell NW (sample B2), with the presence of a conduction channel in the NW core due to a less pronounced SFLP.

We can therefore conclude that for sample B2, two convoluted effects, namely the aspect ratio and the suppression of SCE in the presence of Al_2O_3, are responsible for the overall degradation of its generation capacity.

In order to de-convolute these two effects and investigate the sole effect of the SCE on the piezo-performances, we consider the sample C2.

<u>Comparison between samples A1 (GaN NWs) and C2 (GaN/Al2O3 core/shell NWs), both samples being characterized by an aspect ratio of 5.5</u>

Once again referring to Fig. 27 and Table 4, we can observe that sample C2 presents an equivalent evolution of generated output voltages as a function of CNF, as the sample A1. This phenomenon is justified as both samples have an equivalent aspect ratio of 5.5 and thus have similar deformation rates. This configuration thus permits a direct comparison of the output voltages obtained by sample C2 with the sample A1 and perform an evaluation of the surface charge effects.

The evolution of the average O.V. of individual distributions for the two samples is represented in Fig. 30, as a function of the applied CNF.

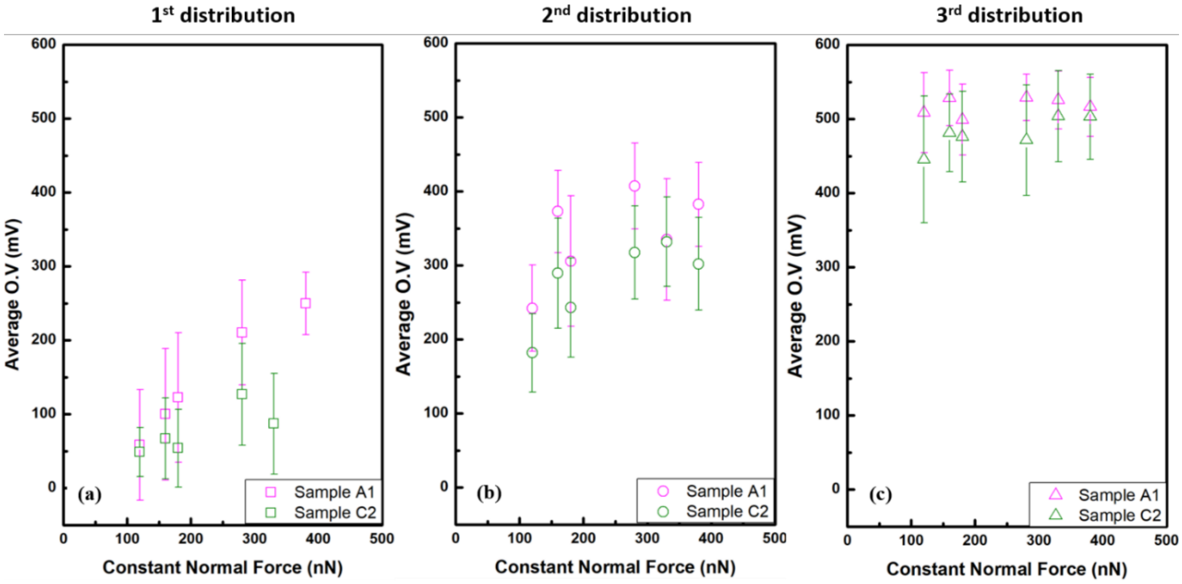

Figure 30. Average O.V. as a function of CNF for (a) 1st distribution (squares), (b) 2nd distribution (circles) and (c) 3rd distribution (triangles), for samples A1 (in pink) and C2 (in green), respectively.

On comparison, we clearly observe that the average output voltages of sample A1 are methodically higher than the ones of sample C2, irrespective of the distribution. For both samples, the saturation of the average O.V. for the most flexible NWs (3rd distribution) is observed and can be assigned to the complete rotation of the electric dipoles [118], [119]. Nevertheless, the average O.V. generated by sample C2 remains lower in comparison with the sample A1.

This diminution of the O.V. values for sample C2 can be solely attributed to the reduction of surface charges density due to the effective surface passivation via the Al_2O_3 shell. An enhancement of the screening effect thus takes place in the NW core due to the reduced severity of the FLP and the creation of a conduction channel as described in Fig. 29b. Whereas in sample A1, the surface charges lead to a fully depleted NW volume, thus limiting the screening effect. These experimental results establish once again the favourable role of surface charges on the piezo-electric responses of non-intentionally p-doped GaN NWs.

4.5 Conclusion

In this chapter, the role and the influence of the surface charges have been discussed. The results presented in this chapter demonstrate experimentally that the surface charges can play a favourable role in increasing the piezo-generation capacity of non-intentionally p-type doped GaN NWs and are an important parameter for the optimisation of device performances based on such nanostructures. We have identified two different ways for taking advantage of the SCE:

1) By adjusting the NW diameter, it is possible to strongly improve the electro-mechanical conversion efficiency of GaN NWs. The preponderance of favourable surface charges in the 44 nm to 60 nm diameter range significantly suppresses the screening effect and thus enhances the output voltage generation.
2) By modulating the NW environment. With the deposition of an Al_2O_3 shell, the absence of surface charges results in a significant decrease of the output voltages due to the enhanced screening effect. By avoiding surface passivation of our GaN NWS, or increasing their surface trap density, it is possible to obtain a high piezo-response of the NWs.

Although these results have been established with intrinsically p-doped GaN NWs, they can also be translated to GaN NWs with a residual n-type doping as well as other intrinsically doped 1D nanostructures such as ZnO NWs.

The surface charges being strongly linked to the free carrier density, the effect of doping on the piezo-responses of GaN NWs appears thusly as a new subject of investigation.

Finally, we would like to highlight here that GaN NWs taking advantage of the surface charges (as-grown GaN NWs with diameter around 36 nm) delivered average output voltages reaching ~ 529 mV per NW, which is the highest recorded O.V. in the literature for GaN NWs to the best of our knowledge. This piezoelectric response exceeds the ones generated by other piezoelectric 1D-nanostructures, especially ZnO NWs, which remains the most widely investigated nanostructures for developing a new generation of piezoelectric energy harvesters.

REFERENCES

[1] F. Patolsky, G. Zheng, and C. M. Lieber, ‘Nanowire sensors for medicine and the life sciences’, *Nanomedicine*, vol. 1, no. 1, pp. 51–65, Jun. 2006, doi: 10.2217/17435889.1.1.51.

[2] N. S. Ramgir, Y. Yang, and M. Zacharias, ‘Nanowire-Based Sensors’, *Small*, vol. 6, no. 16, pp. 1705–1722, Aug. 2010, doi: 10.1002/smll.201000972.

[3] G. Zheng, F. Patolsky, Y. Cui, W. U. Wang, and C. M. Lieber, ‘Multiplexed electrical detection of cancer markers with nanowire sensor arrays’, *Nat Biotechnol*, vol. 23, no. 10, pp. 1294–1301, Oct. 2005, doi: 10.1038/nbt1138.

[4] Y. Geng *et al.*, ‘Integration of ZnO nanorods with MOS capacitor for self-powered force sensors and nanogenerators’, *Nanotechnology*, vol. 32, no. 45, p. 455502, Nov. 2021, doi: 10.1088/1361-6528/ac19d7.

[5] Z. Chen *et al.*, ‘Flexible Piezoelectric-Induced Pressure Sensors for Static Measurements Based on Nanowires/Graphene Heterostructures’, *ACS Nano*, vol. 11, no. 5, pp. 4507–4513, May 2017, doi: 10.1021/acsnano.6b08027.

[6] F. Qian, S. Gradečak, Y. Li, C.-Y. Wen, and C. M. Lieber, ‘Core/Multishell Nanowire Heterostructures as Multicolor, High-Efficiency Light-Emitting Diodes’, *Nano Lett.*, vol. 5, no. 11, pp. 2287–2291, Nov. 2005, doi: 10.1021/nl051689e.

[7] R. Chen *et al.*, ‘On-Chip Fabrication of Well-Aligned and Contact-Barrier-Free GaN Nanobridge Devices with Ultrahigh Photocurrent Responsivity’, *Small*, vol. 4, no. 7, pp. 925–929, Jul. 2008, doi: 10.1002/smll.200701184.

[8] X. Duan, Y. Huang, R. Agarwal, and C. M. Lieber, ‘Single-nanowire electrically driven lasers’, *Nature*, vol. 421, no. 6920, pp. 241–245, Jan. 2003, doi: 10.1038/nature01353.

[9] Z. Wang *et al.*, ‘Polytypic InP Nanolaser Monolithically Integrated on (001) Silicon’, *Nano Lett.*, vol. 13, no. 11, pp. 5063–5069, Nov. 2013, doi: 10.1021/nl402145r.

[10] N. Jamond *et al.*, ‘Piezo-generator integrating a vertical array of GaN nanowires’, *Nanotechnology*, vol. 27, no. 32, p. 325403, Aug. 2016, doi: 10.1088/0957-4484/27/32/325403.

[11] L. Lu *et al.*, ‘Nitride Nanowires: From Rigid to Flexible Piezo-generators’, *J. Phys.: Conf. Ser.*, vol. 773, p. 012010, Nov. 2016, doi: 10.1088/1742-6596/773/1/012010.

[12] R. Tao *et al.*, ‘Performance of ZnO based piezo-generators under controlled compression’, *Semicond. Sci. Technol.*, vol. 32, no. 6, p. 064003, Jun. 2017, doi: 10.1088/1361-6641/aa691f.

[13] G. Zhu, A. C. Wang, Y. Liu, Y. Zhou, and Z. L. Wang, ‘Functional Electrical Stimulation by Nanogenerator with 58 V Output Voltage’, *Nano Lett.*, vol. 12, no. 6, pp. 3086–3090, Jun. 2012, doi: 10.1021/nl300972f.

[14] M. A. Johar *et al.*, ‘Highly Durable Piezoelectric Nanogenerator by Heteroepitaxy of GaN Nanowires on Cu Foil for Enhanced Output Using Ambient Actuation Sources’, *Adv. Energy Mater.*, vol. 10, no. 47, p. 2002608, Dec. 2020, doi: 10.1002/aenm.202002608.

[15] Y. Hu, Y. Zhang, C. Xu, L. Lin, R. L. Snyder, and Z. L. Wang, ‘Self-Powered System with Wireless Data Transmission’, *Nano Lett.*, vol. 11, no. 6, pp. 2572–2577, Jun. 2011, doi: 10.1021/nl201505c.

[16] C. G. Van de Walle and D. Segev, ‘Microscopic origins of surface states on nitride surfaces’, *Journal of Applied Physics*, vol. 101, no. 8, p. 081704, Apr. 2007, doi: 10.1063/1.2722731.

[17] C. H. Park and D. J. Chadi, ‘Stability of deep donor and acceptor centers in GaN, AlN, and BN’, *Phys. Rev. B*, vol. 55, no. 19, pp. 12995–13001, May 1997, doi: 10.1103/PhysRevB.55.12995.

[18] L. Polenta *et al.*, ‘Investigation on Localized States in GaN Nanowires’, *ACS Nano*, vol. 2, no. 2, pp. 287–292, Feb. 2008, doi: 10.1021/nn700386w.

[19] C. H. Qiu and J. I. Pankove, ‘Deep levels and persistent photoconductivity in GaN thin films’, *Appl. Phys. Lett.*, vol. 70, no. 15, pp. 1983–1985, Apr. 1997, doi: 10.1063/1.118799.

[20] T. Y. Lin, H. C. Yang, and Y. F. Chen, ‘Optical quenching of the photoconductivity in *n* -type GaN’, *Journal of Applied Physics*, vol. 87, no. 7, pp. 3404–3408, Apr. 2000, doi: 10.1063/1.372358.

[21] G. Kresse, O. Dulub, and U. Diebold, ‘Competing stabilization mechanism for the polar ZnO(0001)-Zn surface’, *Phys. Rev. B*, vol. 68, no. 24, p. 245409, Dec. 2003, doi: 10.1103/PhysRevB.68.245409.

[22] H. Lüth, *Solid Surfaces, Interfaces and Thin Films*. Berlin, Heidelberg: Springer Berlin Heidelberg, 2010. doi: 10.1007/978-3-642-13592-7.

[23] Z. Zhang and J. T. Yates, ‘Band Bending in Semiconductors: Chemical and Physical Consequences at Surfaces and Interfaces’, *Chem. Rev.*, vol. 112, no. 10, pp. 5520–5551, Oct. 2012, doi: 10.1021/cr3000626.

[24] P. D. C. King, T. D. Veal, D. J. Payne, A. Bourlange, R. G. Egdell, and C. F. McConville, ‘Surface Electron Accumulation and the Charge Neutrality Level in In 2 O 3’, *Phys. Rev. Lett.*, vol. 101, no. 11, p. 116808, Sep. 2008, doi: 10.1103/PhysRevLett.101.116808.

[25] I. Mahboob, T. D. Veal, C. F. McConville, H. Lu, and W. J. Schaff, ‘Intrinsic Electron Accumulation at Clean InN Surfaces’, *Phys. Rev. Lett.*, vol. 92, no. 3, p. 036804, Jan. 2004, doi: 10.1103/PhysRevLett.92.036804.

[26] M. Noguchi, K. Hirakawa, and T. Ikoma, ‘Intrinsic electron accumulation layers on reconstructed clean InAs(100) surfaces’, *Phys. Rev. Lett.*, vol. 66, no. 17, pp. 2243–2246, Apr. 1991, doi: 10.1103/PhysRevLett.66.2243.

[27] V. Chakrapani, C. Pendyala, K. Kash, A. B. Anderson, M. K. Sunkara, and J. C. Angus, ‘Electrochemical Pinning of the Fermi Level: Mediation of Photoluminescence from Gallium Nitride and Zinc Oxide’, *J. Am. Chem. Soc.*, vol. 130, no. 39, pp. 12944–12952, Oct. 2008, doi: 10.1021/ja710999r.

[28] S. Min Kim, H. Kim, Y. Nam, and S. Kim, ‘Effects of external surface charges on the enhanced piezoelectric potential of ZnO and AlN nanowires and nanotubes’, *AIP Advances*, vol. 2, no. 4, p. 042174, Dec. 2012, doi: 10.1063/1.4770314.

[29] M. Nehra *et al.*, ‘1D semiconductor nanowires for energy conversion, harvesting and storage applications’, *Nano Energy*, vol. 76, p. 104991, Oct. 2020, doi: 10.1016/j.nanoen.2020.104991.

[30] M. den Hertog *et al.*, ‘*In situ* biasing and off-axis electron holography of a ZnO nanowire’, *Nanotechnology*, vol. 29, no. 2, p. 025710, Jan. 2018, doi: 10.1088/1361-6528/aa923c.

[31] A. Soudi, C.-H. Hsu, and Y. Gu, ‘Diameter-Dependent Surface Photovoltage and Surface State Density in Single Semiconductor Nanowires’, *Nano Lett.*, vol. 12, no. 10, pp. 5111–5116, Oct. 2012, doi: 10.1021/nl301863e.

[32] D. M. Zhernokletov, M. A. Negara, R. D. Long, S. Aloni, D. Nordlund, and P. C. McIntyre, ‘Interface Trap Density Reduction for Al2O3/GaN (0001) Interfaces by Oxidizing Surface Preparation prior to Atomic Layer Deposition’, *ACS Appl. Mater. Interfaces*, vol. 7, no. 23, pp. 12774–12780, Jun. 2015, doi: 10.1021/acsami.5b01600.

[33] M. Spies *et al.*, ‘Effect of the nanowire diameter on the linearity of the response of GaN-based heterostructured nanowire photodetectors’, *Nanotechnology*, vol. 29, no. 25, p. 255204, Jun. 2018, doi: 10.1088/1361-6528/aab838.

[34] H.-Y. Chen, R.-S. Chen, F.-C. Chang, L.-C. Chen, K.-H. Chen, and Y.-J. Yang, ‘Size-dependent photoconductivity and dark conductivity of m-axial GaN nanowires with small critical diameter’, *Appl. Phys. Lett.*, vol. 95, no. 14, p. 143123, Oct. 2009, doi: 10.1063/1.3213556.

[35] H. J. Joyce *et al.*, ‘Electronic properties of GaAs, InAs and InP nanowires studied by terahertz spectroscopy’, *Nanotechnology*, vol. 24, no. 21, p. 214006, May 2013, doi: 10.1088/0957-4484/24/21/214006.

[36] F. L. A. Cruz, A. C. M. Carvalho, and H. W. L. Alves, ‘Theoretical study of the structural and electronic properties of impurities in non-passivated silicon thin nanowires’, *Solid State Communications*, vol. 290, pp. 1–6, Mar. 2019, doi: 10.1016/j.ssc.2018.12.010.

[37] B. S. Simpkins, M. A. Mastro, C. R. Eddy, and P. E. Pehrsson, ‘Surface depletion effects in semiconducting nanowires’, *Journal of Applied Physics*, vol. 103, no. 10, p. 104313, May 2008, doi: 10.1063/1.2932072.

[38] R. Calarco, T. Stoica, O. Brandt, and L. Geelhaar, ‘Surface-induced effects in GaN nanowires’, *J. Mater. Res.*, vol. 26, no. 17, pp. 2157–2168, Sep. 2011, doi: 10.1557/jmr.2011.211.

[39] R. Calarco *et al.*, ‘Size-dependent Photoconductivity in MBE-Grown GaN−Nanowires’, *Nano Lett.*, vol. 5, no. 5, pp. 981–984, May 2005, doi: 10.1021/nl0500306.

[40] G. Jacopin *et al.*, ‘Interplay of the photovoltaic and photoconductive operation modes in visible-blind photodetectors based on axial p-i-n junction GaN nanowires’, *Appl. Phys. Lett.*, vol. 104, no. 2, p. 023116, Jan. 2014, doi: 10.1063/1.4860968.

[41] J. Treu *et al.*, ‘Lattice-Matched InGaAs–InAlAs Core–Shell Nanowires with Improved Luminescence and Photoresponse Properties’, *Nano Lett.*, vol. 15, no. 5, pp. 3533–3540, May 2015, doi: 10.1021/acs.nanolett.5b00979.

[42] H. Sun, F. Ren, K. W. Ng, T.-T. D. Tran, K. Li, and C. J. Chang-Hasnain, ‘Nanopillar Lasers Directly Grown on Silicon with Heterostructure Surface Passivation’, *ACS Nano*, vol. 8, no. 7, pp. 6833–6839, Jul. 2014, doi: 10.1021/nn501481u.

[43] M. H. M. van Weert *et al.*, ‘Large redshift in photoluminescence of p-doped InP nanowires induced by Fermi-level pinning’, *Appl. Phys. Lett.*, vol. 88, no. 4, p. 043109, Jan. 2006, doi: 10.1063/1.2168255.

[44] L. Rigutti *et al.*, ‘Correlation of optical and structural properties of GaN/AlN core-shell nanowires’, *Phys. Rev. B*, vol. 83, no. 15, p. 155320, Apr. 2011, doi: 10.1103/PhysRevB.83.155320.

[45] C.-H. Wang *et al.*, ‘Optimization of the Output Efficiency of GaN Nanowire Piezoelectric Nanogenerators by Tuning the Free Carrier Concentration’, *Adv. Energy Mater.*, vol. 4, no. 16, p. 1400392, Nov. 2014, doi: 10.1002/aenm.201400392.

[46] X. Xue, Y. Nie, B. He, L. Xing, Y. Zhang, and Z. L. Wang, ‘Surface free-carrier screening effect on the output of a ZnO nanowire nanogenerator and its potential as a self-powered active gas sensor’, *Nanotechnology*, vol. 24, no. 22, p. 225501, Jun. 2013, doi: 10.1088/0957-4484/24/22/225501.

[47] R. Tao, M. Mouis, and G. Ardila, ‘Unveiling the Influence of Surface Fermi Level Pinning on the Piezoelectric Response of Semiconducting Nanowires’, *Adv. Electron. Mater.*, vol. 4, no. 1, p. 1700299, Jan. 2018, doi: 10.1002/aelm.201700299.

[48] N. Elfström, R. Juhasz, I. Sychugov, T. Engfeldt, A. Eriksson, and J. Linnros, ‘Surface charge sensitivity of silicon nanowires: Size dependence’, p. 18, Aug. 2007, doi: 10.1021/nl0709017.

[49] R.-S. Chen *et al.*, ‘Ultrahigh photocurrent gain in m-axial GaN nanowires’, *Appl. Phys. Lett.*, vol. 91, no. 22, p. 223106, Nov. 2007, doi: 10.1063/1.2817595.

[50] H.-Y. Chen *et al.*, ‘Size-dependent persistent photocurrent and surface band bending in m -axial GaN nanowires’, *Phys. Rev. B*, vol. 84, no. 20, p. 205443, Nov. 2011, doi: 10.1103/PhysRevB.84.205443.

[51] L.-C. Li *et al.*, ‘Low-Frequency Contact Noise of GaN Nanowire Device Detected by Cross-Spectrum Technique’, *Jpn. J. Appl. Phys.*, vol. 50, no. 6, p. 06GF21, Jun. 2011, doi: 10.1143/JJAP.50.06GF21.

[52] J. Yoon, F. Huang, K. H. Shin, J. I. Sohn, and W.-K. Hong, ‘Effects of Applied Voltages on the Charge Transport Properties in a ZnO Nanowire Field Effect Transistor’, *Materials*, vol. 13, no. 2, p. 268, Jan. 2020, doi: 10.3390/ma13020268.

[53] A. Kushwaha and M. Aslam, ‘ZnS shielded ZnO nanowire photoanodes for efficient water splitting’, *Electrochimica Acta*, vol. 130, pp. 222–231, Jun. 2014, doi: 10.1016/j.electacta.2014.03.008.

[54] Y. Zhang and H. Liu, ‘Nanowires for High-Efficiency, Low-Cost Solar Photovoltaics’, *Crystals*, vol. 9, no. 2, p. 87, Feb. 2019, doi: 10.3390/cryst9020087.

[55] J. Liu *et al.*, ‘Carrier Density and Schottky Barrier on the Performance of DC Nanogenerator’, *Nano Lett.*, vol. 8, no. 1, pp. 328–332, Jan. 2008, doi: 10.1021/nl0728470.

[56] R. Hinchet, S. Lee, G. Ardila, L. Montès, M. Mouis, and Z. L. Wang, ‘Performance Optimization of Vertical Nanowire-based Piezoelectric Nanogenerators’, *Adv. Funct. Mater.*, vol. 24, no. 7, pp. 971–977, Feb. 2014, doi: 10.1002/adfm.201302157.

[57] J. I. Sohn *et al.*, ‘Engineering of efficiency limiting free carriers and an interfacial energy barrier for an enhancing piezoelectric generation’, *Energy Environ. Sci.*, vol. 6, no. 1, pp. 97–104, 2013, doi: 10.1039/C2EE23404A.

[58] K. C. Pradel, W. Wu, Y. Zhou, X. Wen, Y. Ding, and Z. L. Wang, ‘Piezotronic Effect in Solution-Grown p-Type ZnO Nanowires and Films’, *Nano Lett.*, vol. 13, no. 6, pp. 2647–2653, Jun. 2013, doi: 10.1021/nl400792w.

[59] J. Gao, X. Zhang, Y. Sun, Q. Zhao, and D. Yu, ‘Compensation mechanism in N-doped ZnO nanowires’, *Nanotechnology*, vol. 21, no. 24, p. 245703, Jun. 2010, doi: 10.1088/0957-4484/21/24/245703.

[60] K. Y. Lee *et al.*, ‘Depletion width engineering via surface modification for high performance semiconducting piezoelectric nanogenerators’, *Nano Energy*, vol. 8, pp. 165–173, Sep. 2014, doi: 10.1016/j.nanoen.2014.06.008.

[61] P. X. Gao, J. Song, J. Liu, and Z. L. Wang, ‘Nanowire Piezoelectric Nanogenerators on Plastic Substrates as Flexible Power Sources for Nanodevices’, *Adv. Mater.*, vol. 19, no. 1, pp. 67–72, Jan. 2007, doi: 10.1002/adma.200601162.

[62] Y. Hu, L. Lin, Y. Zhang, and Z. L. Wang, ‘Replacing a Battery by a Nanogenerator with 20 V Output’, *Adv. Mater.*, vol. 24, no. 1, pp. 110–114, Jan. 2012, doi: 10.1002/adma.201103727.

[63] S. Xu *et al.*, ‘Ordered Nanowire Array Blue/Near-UV Light Emitting Diodes’, *Adv. Mater.*, vol. 22, no. 42, pp. 4749–4753, Nov. 2010, doi: 10.1002/adma.201002134.

[64] A. J. L. Garcia *et al.*, ‘Size and Semiconducting Effects on the Piezoelectric Performances of ZnO Nanowires Grown onto Gravure-Printed Seed Layers on Flexible Substrates’, *Nanoenergy Advances*, vol. 2, no. 2, pp. 197–209, May 2022, doi: 10.3390/nanoenergyadv2020008.

[65] S. Lu *et al.*, ‘The enhanced performance of piezoelectric nanogenerator via suppressing screening effect with Au particles/ZnO nanoarrays Schottky junction’, *Nano Res.*, vol. 9, no. 2, pp. 372–379, Feb. 2016, doi: 10.1007/s12274-015-0916-6.

[66] F. Donatini *et al.*, ‘Comparison of Three E-Beam Techniques for Electric Field Imaging and Carrier Diffusion Length Measurement on the Same Nanowires’, *Nano Lett.*, vol. 16, no. 5, pp. 2938–2944, May 2016, doi: 10.1021/acs.nanolett.5b04710.

[67] M. Siva Pratap Reddy, K.-S. Im, J.-H. Lee, R. Caulmione, and S. Cristoloveanu, ‘Trap and 1/f-noise effects at the surface and core of GaN nanowire gate-all-around FET structure’, *Nano Res.*, vol. 12, no. 4, pp. 809–814, Apr. 2019, doi: 10.1007/s12274-019-2292-0.

[68] L. Largeau, D. L. Dheeraj, M. Tchernycheva, G. E. Cirlin, and J. C. Harmand, ‘Facet and in-plane crystallographic orientations of GaN nanowires grown on Si(111)’, *Nanotechnology*, vol. 19, no. 15, p. 155704, Apr. 2008, doi: 10.1088/0957-4484/19/15/155704.

[69] E. Calleja *et al.*, ‘Luminescence properties and defects in GaN nanocolumns grown by molecular beam epitaxy’, *Phys. Rev. B*, vol. 62, no. 24, pp. 16826–16834, Dec. 2000, doi: 10.1103/PhysRevB.62.16826.

[70] K. A. Bertness, A. Roshko, N. A. Sanford, J. M. Barker, and A. V. Davydov, ‘Spontaneously grown GaN and AlGaN nanowires’, *Journal of Crystal Growth*, vol. 287, no. 2, pp. 522–527, Jan. 2006, doi: 10.1016/j.jcrysgro.2005.11.079.

[71] S. D. Hersee, X. Sun, and X. Wang, ‘The Controlled Growth of GaN Nanowires’, *Nano Lett.*, vol. 6, no. 8, pp. 1808–1811, Aug. 2006, doi: 10.1021/nl060553t.

[72] T. Kuykendall, P. Pauzauskie, S. Lee, Y. Zhang, J. Goldberger, and P. Yang, ‘Metalorganic Chemical Vapor Deposition Route to GaN Nanowires with Triangular Cross Sections’, *Nano Lett.*, vol. 3, no. 8, pp. 1063–1066, Aug. 2003, doi: 10.1021/nl034422t.

[73] N. Gogneau *et al.*, ‘GaN nanowires for piezoelectric generators: GaN nanowires for piezoelectric generators’, *Phys. Status Solidi RRL*, vol. 8, no. 5, pp. 414–419, May 2014, doi: 10.1002/pssr.201409105.

[74] T. Richter, H. L. R. Meijers, R. Calarco, and M. Marso, ‘Doping Concentration of GaN Nanowires Determined by Opto-Electrical Measurements’, *Nano Lett.*, vol. 8, no. 9, pp. 3056–3059, Sep. 2008, doi: 10.1021/nl8014395.

[75] N. Gogneau *et al.*, ‘Electromechanical conversion efficiency of GaN NWs: critical influence of the NW stiffness, the Schottky nano-contact and the surface charge effects’, *Nanoscale*, vol. 14, no. 13, pp. 4965–4976, 2022, doi: 10.1039/D1NR07863A.

[76] A. J. L. Lopez Garcia, M. Mouis, V. Consonni, and G. Ardila, ‘Dimensional Roadmap for Maximizing the Piezoelectrical Response of ZnO Nanowire-Based Transducers: Impact of Growth Method’, *Nanomaterials*, vol. 11, no. 4, p. 941, Apr. 2021, doi: 10.3390/nano11040941.

[77] R. Calarco, R. J. Meijers, R. K. Debnath, T. Stoica, E. Sutter, and Hans. Lüth, ‘Nucleation and Growth of GaN Nanowires on Si(111) Performed by Molecular Beam Epitaxy’, *Nano Lett.*, vol. 7, no. 8, pp. 2248–2251, Aug. 2007, doi: 10.1021/nl0707398.

[78] V. Consonni, M. Knelangen, L. Geelhaar, A. Trampert, and H. Riechert, ‘Nucleation mechanisms of epitaxial GaN nanowires: Origin of their self-induced formation and initial radius’, *Phys. Rev. B*, vol. 81, no. 8, p. 085310, Feb. 2010, doi: 10.1103/PhysRevB.81.085310.

[79] T. Gotschke, T. Schumann, F. Limbach, T. Stoica, and R. Calarco, ‘Influence of the adatom diffusion on selective growth of GaN nanowire regular arrays’, *Appl. Phys. Lett.*, vol. 98, no. 10, p. 103102, Mar. 2011, doi: 10.1063/1.3559618.

[80] M. Yoshizawa, A. Kikuchi, M. Mori, N. Fujita, and K. Kishino, ‘Growth of Self-Organized GaN Nanostructures on $\bf Al_{2}O_{3}(0001)$ by RF-Radical Source Molecular Beam Epitaxy’, *Jpn. J. Appl. Phys.*, vol. 36, no. Part 2, No. 4B, pp. L459–L462, Apr. 1997, doi: 10.1143/JJAP.36.L459.

[81] L. Largeau, D. L. Dheeraj, M. Tchernycheva, G. E. Cirlin, and J. C. Harmand, ‘Facet and in-plane crystallographic orientations of GaN nanowires grown on Si(111)’, *Nanotechnology*, vol. 19, no. 15, p. 155704, Apr. 2008, doi: 10.1088/0957-4484/19/15/155704.

[82] L. Largeau, E. Galopin, N. Gogneau, L. Travers, F. Glas, and J.-C. Harmand, ‘N-Polar GaN Nanowires Seeded by Al Droplets on Si(111)’, *Crystal Growth & Design*, vol. 12, no. 6, pp. 2724–2729, Jun. 2012, doi: 10.1021/cg300212d.

[83] F. Qian, Y. Li, S. Gradečak, D. Wang, C. J. Barrelet, and C. M. Lieber, ‘Gallium Nitride-Based Nanowire Radial Heterostructures for Nanophotonics’, *Nano Lett.*, vol. 4, no. 10, pp. 1975–1979, Oct. 2004, doi: 10.1021/nl0487774.

[84] G. T. Wang *et al.*, ‘Highly aligned, template-free growth and characterization of vertical GaN nanowires on sapphire by metal–organic chemical vapour deposition’, *Nanotechnology*, vol. 17, no. 23, pp. 5773–5780, Dec. 2006, doi: 10.1088/0957-4484/17/23/011.

[85] C.-C. Chen *et al.*, ‘Catalytic Growth and Characterization of Gallium Nitride Nanowires’, *J. Am. Chem. Soc.*, vol. 123, no. 12, pp. 2791–2798, Mar. 2001, doi: 10.1021/ja0040518.

[86] A. M. Lord *et al.*, ‘Factors that determine and limit the resistivity of high-quality individual ZnO nanowires’, *Nanotechnology*, vol. 24, no. 43, p. 435706, Nov. 2013, doi: 10.1088/0957-4484/24/43/435706.

[87] Q. X. Zhao, L. L. Yang, M. Willander, B. E. Sernelius, and P. O. Holtz, ‘Surface recombination in ZnO nanorods grown by chemical bath deposition’, *J. Appl. Phys.*, vol. 104, no. 7, p. 073526, 2008, doi: 10.1063/1.2991151.

[88] S. Dai and H. S. Park, ‘Surface effects on the piezoelectricity of ZnO nanowires’, *Journal of the Mechanics and Physics of Solids*, vol. 61, no. 2, pp. 385–397, Feb. 2013, doi: 10.1016/j.jmps.2012.10.003.

[89] H. J. Joyce, J. L. Boland, C. L. Davies, S. A. Baig, and M. B. Johnston, ‘A review of the electrical properties of semiconductor nanowires: insights gained from terahertz conductivity spectroscopy’, *Semicond. Sci. Technol.*, vol. 31, no. 10, p. 103003, Oct. 2016, doi: 10.1088/0268-1242/31/10/103003.

[90] J. W. W. van Tilburg, R. E. Algra, W. G. G. Immink, M. Verheijen, E. P. A. M. Bakkers, and L. P. Kouwenhoven, 'Surface passivated InAs/InP core/shell nanowires', *Semicond. Sci. Technol.*, vol. 25, no. 2, p. 024011, Feb. 2010, doi: 10.1088/0268-1242/25/2/024011.

[91] M. A. Seo, J. Yoo, S. A. Dayeh, S. T. Picraux, A. J. Taylor, and R. P. Prasankumar, 'Mapping Carrier Diffusion in Single Silicon Core–Shell Nanowires with Ultrafast Optical Microscopy', *Nano Lett.*, vol. 12, no. 12, pp. 6334–6338, Dec. 2012, doi: 10.1021/nl303502f.

[92] M. Heurlin, O. Hultin, K. Storm, D. Lindgren, M. T. Borgström, and L. Samuelson, 'Synthesis of Doped InP Core–Shell Nanowires Evaluated Using Hall Effect Measurements', *Nano Lett.*, vol. 14, no. 2, pp. 749–753, Feb. 2014, doi: 10.1021/nl404039d.

[93] J. L. Boland *et al.*, 'Modulation Doping of GaAs/AlGaAs Core–Shell Nanowires With Effective Defect Passivation and High Electron Mobility', *Nano Lett.*, vol. 15, no. 2, pp. 1336–1342, Feb. 2015, doi: 10.1021/nl504566t.

[94] P. Parkinson *et al.*, 'Carrier Lifetime and Mobility Enhancement in Nearly Defect-Free Core−Shell Nanowires Measured Using Time-Resolved Terahertz Spectroscopy', *Nano Lett.*, vol. 9, no. 9, pp. 3349–3353, Sep. 2009, doi: 10.1021/nl9016336.

[95] A. Armstrong, Q. Li, Y. Lin, A. A. Talin, and G. T. Wang, 'GaN nanowire surface state observed using deep level optical spectroscopy', *Appl. Phys. Lett.*, vol. 96, no. 16, p. 163106, Apr. 2010, doi: 10.1063/1.3404182.

[96] B. S. Simpkins, M. A. Mastro, C. R. Eddy, and P. E. Pehrsson, 'Surface-Induced Transients in Gallium Nitride Nanowires', *J. Phys. Chem. C*, vol. 113, no. 22, pp. 9480–9485, Jun. 2009, doi: 10.1021/jp901122k.

[97] L. E. Black, A. Cavalli, M. A. Verheijen, J. E. M. Haverkort, E. P. A. M. Bakkers, and W. M. M. Kessels, 'Effective Surface Passivation of InP Nanowires by Atomic-Layer-Deposited Al_2O_3 with PO_x Interlayer', *Nano Lett.*, vol. 17, no. 10, pp. 6287–6294, Oct. 2017, doi: 10.1021/acs.nanolett.7b02972.

[98] M. Knez, K. Nielsch, and L. Niinistö, 'Synthesis and Surface Engineering of Complex Nanostructures by Atomic Layer Deposition', *Adv. Mater.*, vol. 19, no. 21, pp. 3425–3438, Nov. 2007, doi: 10.1002/adma.200700079.

[99] S. Kato *et al.*, 'Improvement of carrier diffusion length in silicon nanowire arrays using atomic layer deposition', *Nanoscale Res Lett*, vol. 8, no. 1, p. 361, Dec. 2013, doi: 10.1186/1556-276X-8-361.

[100] A. Ghods, C. Zhou, and I. T. Ferguson, 'Enhancement in electrical and optical properties of field-effect passivated GaN blue light emitting diodes', *Semicond. Sci. Technol.*, vol. 36, no. 11, p. 115018, Nov. 2021, doi: 10.1088/1361-6641/ac1b12.

[101] D. K. Simon, P. M. Jordan, T. Mikolajick, and I. Dirnstorfer, ‘On the Control of the Fixed Charge Densities in Al $_2$ O $_3$ -Based Silicon Surface Passivation Schemes’, *ACS Appl. Mater. Interfaces*, vol. 7, no. 51, pp. 28215–28222, Dec. 2015, doi: 10.1021/acsami.5b06606.

[102] G. Kwak and K. Yong, ‘Adsorption and Reaction of Ethanol on ZnO Nanowires’, *J. Phys. Chem. C*, vol. 112, no. 8, pp. 3036–3041, Feb. 2008, doi: 10.1021/jp7103819.

[103] Q. Zhang, J. Qi, Y. Huang, X. Li, and Y. Zhang, ‘Negative differential resistance in ZnO nanowires induced by surface state modulation’, *Materials Chemistry and Physics*, vol. 131, no. 1–2, pp. 258–261, Dec. 2011, doi: 10.1016/j.matchemphys.2011.09.036.

[104] A. Mohammadpour *et al.*, ‘100-Fold Improvement in Carrier Drift Mobilities in Alkanephosphonate-Passivated Monocrystalline TiO2 Nanowire Arrays’, *ERA*, Jan. 06, 2017. https://era.library.ualberta.ca/items/f9fbdde3-9911-49ae-af8c-be9fe52f9fda (accessed May 09, 2022).

[105] N. Fukata and R. Rurali, Eds., *Fundamental Properties of Semiconductor Nanowires*. Singapore: Springer Singapore, 2021. doi: 10.1007/978-981-15-9050-4.

[106] S. Ahoulou, E. Perret, and J.-M. Nedelec, ‘Functionalization and Characterization of Silicon Nanowires for Sensing Applications: A Review’, *Nanomaterials*, vol. 11, no. 4, p. 999, Apr. 2021, doi: 10.3390/nano11040999.

[107] R. Ulbricht, R. Kurstjens, and M. Bonn, ‘Assessing Charge Carrier Trapping in Silicon Nanowires Using Picosecond Conductivity Measurements’, *Nano Lett.*, vol. 12, no. 7, pp. 3821–3827, Jul. 2012, doi: 10.1021/nl3017835.

[108] M. R. Bergren *et al.*, ‘Ultrafast Electrical Measurements of Isolated Silicon Nanowires and Nanocrystals’, *J. Phys. Chem. Lett.*, vol. 5, no. 12, pp. 2050–2057, Jun. 2014, doi: 10.1021/jz500863a.

[109] J. B. Baxter and C. A. Schmuttenmaer, ‘Conductivity of ZnO Nanowires, Nanoparticles, and Thin Films Using Time-Resolved Terahertz Spectroscopy’, *J. Phys. Chem. B*, vol. 110, no. 50, pp. 25229–25239, Dec. 2006, doi: 10.1021/jp064399a.

[110] N. Doumit and G. Poulin-Vittrant, ‘Effect of the Dielectric and Mechanical Properties of the Polymer Matrix on ZnO-Nanowire-Based Composite Nanogenerators Performance’, *Adv. Theory Simul.*, vol. 3, no. 9, p. 2000128, Sep. 2020, doi: 10.1002/adts.202000128.

[111] L. Lu, ‘Nanofils piézoélectriques de nitrure pour la récupération d’énergie et la détection de pression’, These de doctorat, Université Paris-Saclay (ComUE), 2018. Accessed: Oct. 13, 2021. [Online]. Available: http://www.theses.fr/2018SACLS436

[112] N. Gogneau, N. Jamond, P. Chrétien, F. Houzé, E. Lefeuvre, and M. Tchernycheva, ‘From single III-nitride nanowires to piezoelectric generators: New route for powering nomad electronics’, *Semicond. Sci. Technol.*, vol. 31, no. 10, p. 103002, Oct. 2016, doi: 10.1088/0268-1242/31/10/103002.

[113] A. Ek, C. Reichel, A. Richter, and J. Benick, ‘Influence of layer thickness on passivation properties in SiO_x/Al_2O_3 stacks’, *Journal of Applied Physics*, vol. 127, no. 23, p. 235303, Jun. 2020, doi: 10.1063/1.5135391.

[114] N. Jegenyes *et al.*, ‘High Piezoelectric Conversion Properties of Axial InGaN/GaN Nanowires’, *Nanomaterials*, vol. 8, no. 6, p. 367, May 2018, doi: 10.3390/nano8060367.

[115] N. Jamond *et al.*, ‘Energy harvesting efficiency in GaN nanowire-based nanogenerators: the critical influence of the Schottky nanocontact’, *Nanoscale*, vol. 9, no. 13, pp. 4610–4619, 2017, doi: 10.1039/C7NR00647K.

[116] B. Pérez-García, J. Zúñiga-Pérez, V. Muñoz-Sanjosé, J. Colchero, and E. Palacios-Lidón, ‘Formation and Rupture of Schottky Nanocontacts on ZnO Nanocolumns’, *Nano Lett.*, vol. 7, no. 6, pp. 1505–1511, Jun. 2007, doi: 10.1021/nl070238m.

[117] U. Saleem, M. D. Birowosuto, N. Gogneau, P. Coquet, M. Tchernycheva, and H. Wang, ‘Yellow and green luminescence in single-crystal Ge-catalyzed GaN nanowires grown by low pressure chemical vapor deposition’, *Opt. Mater. Express*, vol. 7, no. 6, p. 1995, Jun. 2017, doi: 10.1364/OME.7.001995.

[118] X. Xu *et al.*, ‘An improved AFM cross-sectional method for piezoelectric nanostructures properties investigation: application to GaN nanowires’, *Nanotechnology*, vol. 22, no. 10, p. 105704, Mar. 2011, doi: 10.1088/0957-4484/22/10/105704.

[119] D. J. Leo, *Engineering analysis of smart material systems*. Hoboken, N.J: John Wiley & Sons, 2007.

Conclusion & perspectives

The abundant use of smart objects (IoTs), and amongst them, of micro-devices, is on a constant rise, both in our daily lives as well as in high-tech applications. However, today, their energetic autonomy is a key worldwide challenge. Primarily, to deal with the critical increase of their associated energy consumption, but also, to enhance their condition for usage, especially, in remote working environments with restricted or no electrical grid infrastructure. To tackle these fundamental issues, 'small-scale energy harvesting' has emerged amongst the prominent solutions in the past decade to develop self-powering micro/nano-electronic devices, thus allowing the possibility to replace short-lived and bulky components such as batteries.

The integration of nanostructured materials, such as the nanowires (NWs), is a promising technique to fabricate a new generation of ultra-compact and high-efficient piezoelectric generators to meet the energy demands of the micro-devices (with energy consumption in the µW-mW range). In fact, thanks to their large aspect ratio, quasi-perfect crystalline quality and their nanometric dimensions, the NWs are characterized by high mechanical and piezo-electric properties, in comparison to their bulk and 2D-film counterparts. These properties confer to them several advantages to fundamentally improve the electro-mechanical conversion efficiency of the micro-systems.

Since the first demonstration of piezoelectric conversion properties of ZnO NWs in 2006, and the emergence of the concept of nanogenerators, several other 1D-nanostructures have demonstrated their ability to convert a mechanical deformation into direct electrical energy. Based on these demonstrations, numerous piezoelectric devices have been fabricated in the past decade. Moreover, during these years, various aspects have been investigated to enhance the energy conversion capacity of these new harvesters. To this date, the mechanism of piezoelectricity generation in 1D-nanostrcutures, the impact of dopant incorporation, the functionalization of the NWs as well as different piezo-generator designs have been thoroughly investigated. Based on these studies, power densities of the order of a few µW/cm^2 to several tens of µW/cm^2 (few mW/cm^3 to several tens of mW/cm^3 range) have been reported.

However, these results are obtained under laboratory conditions, which are not equivalent to the mechanical deformations and vibrations found in the vicinity of the micro-devices, that we target to supply. In addition, the strong dimensional constraints linked to the reduction in the size of the micro-devices are *quasi-never* taken into account.

Today it is of crucial importance to develop high-efficient and ultra-compact piezoelectric generators working under *environmental conditions*. To reach this ambitious objective, which is the first building block towards a future technological transfer, it is required to integrate an active media presenting a strong electro-mechanical conversion efficiency per unit surface area.

The III-Nitride NWs have demonstrated their high conversion capacities both at the nanometer scale with the generation of several hundreds of mV per NW, and at micrometer scale with the generation of an average power density of the order of 0.6 mW/cm^2, under mechanical inputs compatible with environmental conditions. However, it remains limited for powering micro-devices and a further enhancement in their electro-mechanical conversion capacity is required. This PhD project has investigated new solutions in order to reach this goal.

In a first time, we have highlighted the importance of the impedance of the external read-out circuit and of the internal resistance of the nanogenerator (NG), in order to well apprehend the electromechanical properties of our GaN NWs. Although, the performances of the final piezo-(nano)generator devices firstly depend on the piezo-conversion capacity of the GaN NWs based active layer, the measuring circuit used to harvest the piezo-generated energies has an equal importance. In this thesis, we have studied the piezoelectric response of arrays of intrinsically doped GaN NWs via an atomic force microscope (AFM) equipped with a home-made modified Resiscope. It must be noted that these results have been obtained by considering only the purely resistive elements of the NG (NW) and the measurement load, while in reality, capacitive components are also present.

We have experimentally demonstrated that the choice of the external load resistance (R_{load}) of the measurement circuit directly influences the output voltage collection efficiency for equivalent applied deformations. Hence, for the first time in the nanoscale regime, we established the direct dependence of the piezo-response measurement of GaN NWs on R_{load}. We also highlighted the non-negligible participation of the internal resistance of individual NGs (here NWs), which in reality is the sum of the internal resistance of each nanowire of the ensemble $(R_{NW})_i$, the contact resistance (R_C) and the diode resistance (R_D), and is strongly dependent on the nanowire characteristics. To quantify the NG's resistance, two different methods have been employed:

a- The *classical method* employed for microsystems in the literature, which consists in plotting the evolution of instantaneous power values (P_i), as a function of R_{load}. Based on this method, the maximum read-out power (P_{max}) is obtained only at an optimal value of R_{load}, which theoretically corresponds to the internal resistance (R_g) of the system. In our case, on plotting the average instantaneous power values as a function of the R_{load} (from 1 MΩ to 1 GΩ), two regimes were observed: a classical regime with the similar power evolution as for microsystems and a non-classical one. The latter has not yet been fully understood and requires additional measurements. A *quasi-optimal* value of R_{load} was extracted from the classical regime of the power curve, giving an estimation of the internal resistance of the NG in the range of 10^7-10^8 Ω.

b- An alternative method was employed as well to calculate the values of R_g directly from the O.V. measurements performed in the open/short-circuit configuration. An average R_g in the range of $10^6 – 10^7$ Ω has been estimated, which is a decade smaller than the ones obtained using the first method.

Despite the difference in the obtained values of R_g, these results clearly demonstrated that the internal resistance of the system is non-negligible and cannot be overlooked as is often the case in the literature.

These results also emphasized the limitations of the simple approach by reasoning on model circuits involving only resistors, as we have done here and as it is applied in the literature. Nevertheless, this methodology remains acceptable as long as it is a question of presenting the evolution of the electro-mechanical phenomena on the same sample under the effect of parameters such as the applied force or the tip scan rate. If we want to carry out real time absolute measurements of the energy generated by each nanowire, and to make compatible measurements with the systems tested under device configuration, other methods must be employed, such as the ones based on charge quantity measurements.

A second solution consists in taking advantage of the specific nanoscale properties exhibited by 1D-nanostructures, which remain either non-existent or non-significant at micrometric scales. These properties can lead to a strong modification of the NW characteristics, which is the case of our GaN NWs. An exaltation of the piezoelectric coefficients or the formation of a Schottky nano-contact at the NW/electrode interface are examples of these nanoscale phenomena. Amongst these specific properties, we can cite the modulation of the free charge-carrier concentration in the NW volume, due to the presence of the surface charges (SC), which are strongly pronounced in sub-100 nm wide GaN NWs. These surface charges are known to induce a surface Fermi level pinning and can lead to a partial or complete depletion of the NWs. Although these effects are detrimental for device performances in nano-photonics and nano-electronics, they can be seen as an advantage for the piezoelectric applications. In fact, it is well known that the free carriers degrade the piezoelectric response by screening the piezoelectric charges. Hence, a modulation of their concentration in the NW volume by tuning the surface charges appears as a promising solution. To verify this hypothesis, we led an experimental investigation by considering two approaches.

a- We have analyzed the piezoelectric response and more precisely the evolution of the electro-mechanical coupling coefficient of the NWs, as a function of their diameter, by using an AFM system equipped with the adapted Resiscope module working under a well-controlled axial compressive force. We have thus demonstrated that the conversion efficiency can be exalted up to 43% when the NW diameter is approximately equivalent to two times the depletion width (critical diameter), thus leading to fully depleted nanostructures, thanks to the presence of surface charges.

b- We have also analyzed the piezoelectric response of our GaN NWs as a function of their immediate environment in the 'bending in scanning configuration' of the AFM system equipped with the modified Resiscope module. We have demonstrated a degradation of the piezo-response of the GaN NWs by encapsulating them in an Al_2O_3 shell, which is known to strongly reduce the surface charges.

Both these results clearly demonstrate that the presence of surface charges can be advantageous for improving the electro-mechanical conversion efficiency of our GaN NWs.

Finally, by taking into account these surface effects, and by properly choosing the diameter of our non-intentionally p-type doped GaN NWs (about 36 nm), we have obtained an average output voltage reaching up to 529 mV per NW. This is the highest recorded O.V. in the literature for GaN NWs to the best of our knowledge, and largely exceeds the ones generated by other piezoelectric 1D-nanostructures, especially ZnO NWs, which remain the most widely investigated nanostructures for developing piezoelectric energy harvesters.

Although these new solutions presented in this PhD manuscript have been investigated via an AFM system and are being studied at macroscopic scales (devices), they undeniably open the way towards the development of a new generation of piezo-electric devices based on GaN NWs, working under ambient conditions.

In order to delve further into the development of piezoelectric devices for energy harvesting solutions, I propose some perspectives, which address two different but intrinsically linked objectives.

1- The Exaltation of the electromechanical coupling of the generators integrating nano-materials via the investigation of several fundamental aspects and solutions:

a- The investigation of the NW doping effect on the piezoelectric response of the NWs. The increase in the generator performances requires taking into account the internal resistance of the NWs and therefore their doping. As a matter of fact, the free carriers are known to screen the piezoelectric charges and thus decrease the response of the generators. Despite the importance of this effect, the concentration of carriers is often neglected in the design of piezo-generators. It is thus of vital importance to establish the close relationship between the doping level of the NWs and their piezo-conversion properties. By understanding this relation, optimized GaN NWs with the ability to exalt the mechanical-electrical energy conversion will prove fruitful for the development of high-efficient piezoelectric generator devices.

b- The integration of pre-strained hetero-structures. This second axis aims to nano-engineer the active material by integrating pre-strained axial heterostructures in the NW volume to further enhance the energy generation. When a NW hetero-structure consists of a vertical stacking of materials with different lattice constants and layer thicknesses, an axial elastic strain is created inside the NW. The latter modifies the built-in electric fields, and thus the initial state of the NW. So that when an external force is applied, the operation range is shifted. This approach is analogous to the already existing one in piezo-actuators, using pre-strained materials to achieve symmetrical voltage response and to improve linearity. Despite the demonstration of the usefulness of this strategy, it has never been considered for NW-based piezo-conversion. Axial InGaN/GaN NW heterostructures with compressive InGaN disks are under investigation both at the nanometer and micrometer scales.

c- The development of a new AFM-based module for charge quantification. Until now, the piezo-generated energies by the NWs are evaluated by considering the output voltage evolution across a defined resistive charge (R_{load}). To quantify more realistically the harvested energy, our team at laboratory GeePs is developing a new electronic structure integrated to the Resiscope module. The objective is to collect the amount of charges generated in the NW volume in response to the mechanical deformations. This new AFM-Resiscope will allow characterization of the electro-mechanical coupling properties of NWs, but also composites integrating other nanomaterials such as nanoparticles.

2- The realization of a complete piezoelectric generator:

The development of efficient generators requires the definition of each building block constituting the autonomous power supply system, in accordance with the conditions of usage and the specificities of the targeted application, while taking into account aspects of cost and sustainability, which are important parameters in the implementation of such alternative solutions.

In addition, the transductor based on our GaN NWs embedded into a soft matrix with electrical contacts, which is also termed as the piezo-generator by misuse of language, must be:

a- Integrated to a mechanical module, which will ensure the adequation between the vibration fund present in the surrounding environment and what is required for activating the system. This module must also regulate the optimal frequency for which the transductor (PG) can efficiently convert the deformation into an electrical signal.

b- Coupled to an electrical module. The electric circuit, in terms of load resistance and coupled capacitance, must be adjusted to ensure the best harvesting and optimum storage of the generated energy.

Finally, the robustness, fatigue and durability of the harvester must be investigated. In fact, the study of the generator’s behavior with time is essential for their future technological transfer.

ANNEX

Electromechanical coupling coefficient and current-voltage measurements

Annex A: Electromechanical coupling coefficient

The electromechanical coupling coefficient is given by:

$$\eta = \frac{output\ electrical\ energy}{input\ mechanical\ energy} = \frac{\Delta W_{PZT}}{\Delta W_{ELD}} \qquad (1)$$

The input mechanical energy corresponds to the elastic deformation energy for compressing/releasing the 1D-nanostructure.

The deformation of a NW under an axial force is expressed by Eq. 2, defining the Young's modulus *E*:

$$E = \frac{Stress}{Strain} = \frac{F/A_0}{\Delta l/l_0} \qquad (2)$$

or using the (x, y, z) coordinates:

$$E = \frac{F/A_0}{Z_m/Z_0} \qquad (3)$$

where *F* is the applied CNF, A_0 is the NW section supposed unchanged, l_0 is the initial NW height, and Δl is the NW height variation measured from topographic images in response to its compression under the action of *F*. Fig. A-1 illustrates these defined parameters.

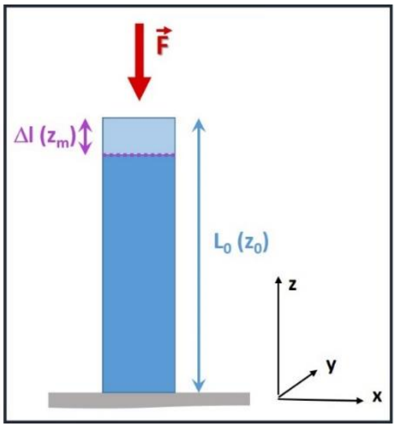

Figure. A-1: Schematic representation of the NW under mechanical deformation.

For each cycle, during the compression phase, the applied force *f*, increasing from *0* to *F*, may be expressed as:

$$f = \frac{E\ A_0\ Z}{Z_0} \qquad (4)$$

The mechanical work done by this external force for axially compressing the NW is given by:

$$W_{ELD} = \int_{f=0}^{f=F} f dl = \int_{0}^{Z_m} f(Z) dZ \tag{5}$$

$$W_{ELD} = \frac{EA_0}{Z_0} \int_{0}^{Z_m} Z\, dZ \tag{6}$$

$$\boldsymbol{W_{ELD} = \frac{1}{2} \frac{EA_0}{Z_0} Z_m^2} \tag{7}$$

After one cycle of pure axial mechanical input, including, along the z-axis, the mechanical compression of the NW under the AFM tip applied force, and the mechanical decompression of the NW at the AFM tip releasing, we assume that the elastic energy loss is given by:

$$\boldsymbol{\Delta W_{ELD} = 2 * W_{ELD} = \frac{EA_0}{Z_0} Z_m^2 = \frac{EA_0}{l_0} \Delta l^2 = F \Delta l} \tag{8}$$

Output piezoelectric energy: The capacitance associated to the charges generated by an individual NW in one piezoelectric discharge is given by:

$$C = \frac{\tau}{R} = \frac{\tau}{R_L + R_S + R_C + R_{NW}} \tag{9}$$

where τ is the decay time of the system and R is the resistance of the system corresponding to the sum of the load resistance (R_L), the series resistance (R_S), the contact resistance (R_C), of the Schottky diode, through which the O.V. is harvested and the NW resistance (R_{NW}).

According to the discharge of an RC circuit [1], the output electric energy generated by an individual NW in one piezoelectric discharge is given by:

$$\Delta W_{PZT} = \frac{1}{2} C V^2 \tag{10}$$

Using Eq. 9, and by considering that with our measurement method, the R_{Total} value includes the sum of the resistances, this gives:

$$\boldsymbol{\Delta W_{PZT} = \frac{1}{2} \frac{\tau}{R_L + R_{Total}} V^2} \tag{11}$$

where V is the piezo-generated O.V. and R_L ($1\ G\Omega$) is the load resistance. The convolution of the resistances, R_S, R_C and R_{NW} (R_{total} = 144 MΩ) has been evaluated from I(V) characteristics performed on various single NWs. By fitting the curve $\frac{dV}{dLnI} = f(I)$ to a straight line and by using the following equation, $\frac{dV}{dLnI} = n\frac{k_B T}{q} + IR_{Total}$, R_{Total} can be determined from the slope of the line. Finally, the measured decay time (τ) of the system is 3ms.

Annex B: Current-voltage measurements

To perform I(V) measurements, the AFM-Resiscope is used in the axial configuration (Fig. B-1). In this experimental system, the classical configuration of the Resiscope module is used.

The AFM tip is brought into contact with the NW top, which induces a vertical compression of the nanostructures under a controlled and constant normal force. The voltage is applied via the substrate and the current is collected through the conductive AFM tip. We have thus a negative representation of the diode characteristic. When the contact is negatively polarized ($V_{Bias} = V_{GaN\ NWs} - V_{Tip} < 0$), the forward current is able to cross the interface. By contrast, when the AFM tip - GaN NW contact is submitted to positive polarization ($V_{Bias} = V_{GaN\ NWs} - V_{Tip} > 0$), the reverse current is blocked by the diode, leading to a weak current.

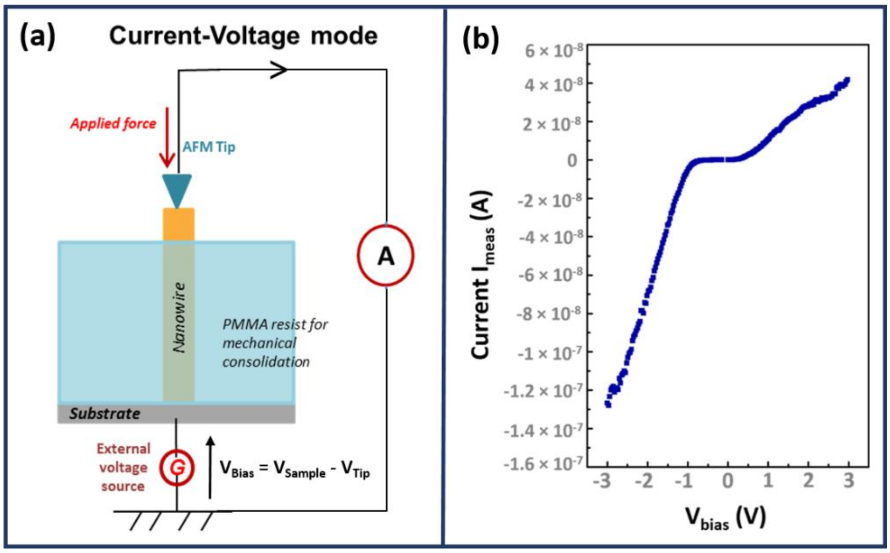

Figure. B-1: (a) Schematic representation of the AFM system equipped with the Resiscope module in current-voltage configuration; (b) I(V) curve of the Cr/Pt AFM tip/GaN NW Schottky diode.

The quantification of the total resistance ($R_S + R_C + R_{NW}$) has been done by using the Cheung-Cheung theory [2]. This approach has been favorited to the thermionic emission theory [3] in order to take into account the deviations from ideal behavior. Then, R_{Total} can be expressed by Cheung functions given by Eq. 12 and 13:

$$\frac{dV}{dLnI} = n\frac{k_B T}{q} + IR_{Total} \tag{12}$$

$$H(I) = n\Phi_B + IR_{Total} \tag{13}$$

where, in our case, V is $-V_{Bias}$ and I is $-I_{mes}$, q is the electronic charge, k_B the Boltzmann constant, T the absolute temperature, n the ideality factor and Φ_B the Schottky barrier height.

By fitting the curve $\frac{dV}{dLnI} = f(I)$ to a straight line and by using Eq. 8, R_{Total} can be determined from the slope of the line. Then by fitting the curve H(I) = g(I) which gives a straight line, we can also determine R_{Total} from the y-axis intercept.

We note here that the calculations of the diode characteristics have been performed for several single NWs and for loading forces higher than the threshold ones, i.e. when the stable electric contact has already been formed.

REFERENCES

[1] Z. L. Wang and J. Song, ‘Piezoelectric Nanogenerators Based on Zinc Oxide Nanowire Arrays’, *Science*, vol. 312, no. 5771, pp. 242–246, Apr. 2006, doi: 10.1126/science.1124005.

[2] S. K. Cheung and N. W. Cheung, ‘Extraction of Schottky diode parameters from forward current-voltage characteristics’, *Appl. Phys. Lett.*, vol. 49, no. 2, pp. 85–87, Jul. 1986, doi: 10.1063/1.97359.

[3] ‘Frontmatter’, in *Semiconductor Material and Device Characterization*, Hoboken, NJ, USA: John Wiley & Sons, Inc., 2005, pp. i–xv. doi: 10.1002/0471749095.fmatter.

Résumé en Français

Aujourd'hui, les micro-dispositifs sont devenus pléthoriques au travers de leur intégration dans l'électronique personnelle (montres connectées, ordinateurs portables, tablettes…), les implants médicaux, les capteurs ou bien encore les actionneurs. Cependant, leur utilisation a conduit à une augmentation drastique de la demande d'approvisionnement en énergie à une époque où les ressources naturelles s'épuisent. Les batteries et micro-batteries constituent jusqu'à présent la principale source d'énergie pour alimenter les microsystèmes. Malgré de nombreuses études menées pour augmenter leurs performances, leurs durées de vie représentent un réel défi pour l'autonomie des micro-dispositifs. De plus, pour l'alimentation de systèmes travaillant dans des environnements difficiles d'accès, le remplacement des batteries est extrêmement compliqué et coûteux. Par ailleurs, l'intégration de telles sources d'énergie dans les micro-nano-systèmes entraîne aujourd'hui une augmentation de leurs dimensions ou de leur poids, limitant ainsi l'utilisation des dispositifs.

La récente miniaturisation des micro-dispositifs, associée aux progrès dans les domaines de la micro-nano-fabrication, a permis de réduire considérablement leurs besoins énergétiques (mW-µW). Cela ouvre la voie vers le développement de micro-systèmes auto-alimentés utilisant la récupération des énergies renouvelables. Ces récupérateurs d'énergies convertissent les énergies trouvées dans l'environnement direct du micro-dispositif en une énergie électrique directement utilisable pour son alimentation, soit en assistant, soit en remplaçant la batterie existante. Parmi les énergies renouvelables, les déformations mécaniques et les vibrations présentent l'avantage d'être omniprésentes et de pouvoir être converties grâce à l'utilisation de matériaux piézoélectriques.

Depuis une quinzaine d'années, les nanostructures 1D, telles que les nanofils, sont apparues comme des candidats prometteurs pour la réalisation de générateurs piézoélectriques à la fois compacts et performants. En effet, en raison de leur rapport surface sur volume élevé, de leur quasi perfection cristalline (absence de dislocations) et de leurs dimensions nanométriques, les nanostructures 1D présentent des propriétés mécaniques et piézoélectriques supérieures à celles de leurs homologues massifs ou sous forme de couches minces. Ainsi les nanofils se caractérisent par des propriétés mécaniques supérieures, des coefficients piézoélectriques exaltés ainsi que par un degré de flexibilité plus élevé et donc une plus grande sensibilité aux forces environnantes. De surcroît, dans le cas des nanostructures 1D présentant des diamètres inférieurs à 100 nm, celles-ci sont caractérisées par des propriétés uniques qui ne s'exprimaient pas aux échelles macrométriques. Ainsi, parmi ces propriétés devenant prédominantes aux échelles nanométriques, nous pouvons citer la formation de nano-contacts Schottky permettant une meilleure collecte des charges piézoélectriques ou encore l'influence des effets de charges de surface (SCE).

Bien que les dispositifs piézoélectriques à base de nanostructures 1D puissent générer des densités de puissance de l'ordre de quelques µW-mW/cm^3, leur utilisation en tant que sources d'énergie pour des microsystèmes reste aujourd'hui limitée en raison de leur faible efficacité de conversion lorsqu'ils sont soumis à des déformations équivalentes à celles trouvées dans l'environnement. Il est aujourd'hui indispensable d'augmenter les efficacités de conversion électromécanique de ces systèmes piézo-générateurs pour permettre leur futur transfert technologique.

Cette thèse se concentre sur l'amélioration de la conversion piézoélectrique des nanofils de GaN. Ces derniers sont synthétisés sur des substrats de silicium (111) dopés de type n en utilisant l'épitaxie par jets moléculaire assistée par plasma et caractérisés à l'aide d'un système AFM équipé d'un module Résiscope qui a été spécifiquement adapté pour réaliser des mesures de conversion piézoélectrique directe sur les nanofils. Le manuscrit s'organise autour de deux grands axes d'étude : l'influence du système de mesure sur la collection des tensions générées en réponse à une déformation et l'étude des effets de charges de surface sur l'efficacité de conversion des nanofils.

Optimisation du système de mesure : défis et limites de la méthode de mesure

Les capacités de piézo-conversion des nanostructures 1D sont généralement caractérisées soit via un système AFM équipé d'un module électrique spécifique, auquel cas nous mesurons ici la réponse de chaque nanofil constituant le réseau, soit au travers de la réponse d'une couche transductrice intégrant les nanofils via un système de sollicitations mécaniques tel qu'un shaker. Dans les deux cas, l'efficacité de conversion est mesurée par les valeurs de la tension de sortie obtenues, et ce, malgré les différentes conditions de test des systèmes de mesure ou bien encore de la valeur de la résistance de charge (R_{load}) du système de collecte externe. Il est donc très difficile de comparer les performances des différentes nanostructures 1D trouvées dans la littérature. Malgré la forte influence de R_{load} sur les performances des transducteurs "classiques", son effet sur les efficacités de conversion des piézo-générateurs à base de nanostructures 1D n'a attiré l'attention que récemment. Seules quelques équipes ont démontré que l'impédance du circuit externe est un important facteur limitant (tout comme dans les systèmes macroscopiques), et ont déterminé les valeurs optimales de R_{load} (au regard des spécificités de leur système) pour obtenir un maximum de puissance générée. Cependant, aucune étude de ce type n'a été réalisée pour les nanofils seuls (aussi appelés nanogénérateurs) sous AFM. Or celle-ci est aujourd'hui indispensable pour pleinement comparer les résultats publiés qui sont le plus souvent obtenus pour des R_{load} différentes variant de 100 MΩ à 1 GΩ.

Pour la première fois, nous avons réalisé une étude systématique permettant de démontrer l'influence des valeurs de R_{load} sur les signaux de tension de sortie générés par des nanofils de GaN dopés non intentionnellement de type n (hauteurs des nanofils non encapsulés - $H_{n\text{-}GaN} = 90 \pm 30$ nm et diamètres - $D_{n\text{-}GaN} = 88 \pm 21$ nm) ou de type p (hauteurs de nanofils non encapsulés - $H_{p\text{-}GaN} = 200 \pm 50$ nm et diamètres - $D_{p\text{-}GaN} = 36 \pm 9$ nm). Le système AFM utilisé est équipé d'un module Résiscope qui a été spécifiquement modifié pour réaliser des mesures de conversion piézoélectrique sur des nanofils qui sont latéralement déformés par la pointe AFM qui scanne la surface en mode contact (initialement ils sont verticalement orientés sur leur substrat). La réponse piézoélectrique des échantillons est enregistrée dans des conditions de sollicitation équivalentes (force normale constante, FNC, variant entre 120 nN et 380 nN) et pour des valeurs de R_{load} comprises entre 1 MΩ et 1 GΩ en utilisant une pointe AFM conductrice de CrPt. Une représentation schématique du système AFM et du circuit électrique équivalent, simplifié, sont présentés sur la *Figure 1*. Nous entendons par circuit simplifié que le nanogénérateur (ici le nanofil) et la charge de mesure sont décrits par des éléments purement résistifs, R_g et R_{load}, respectivement.

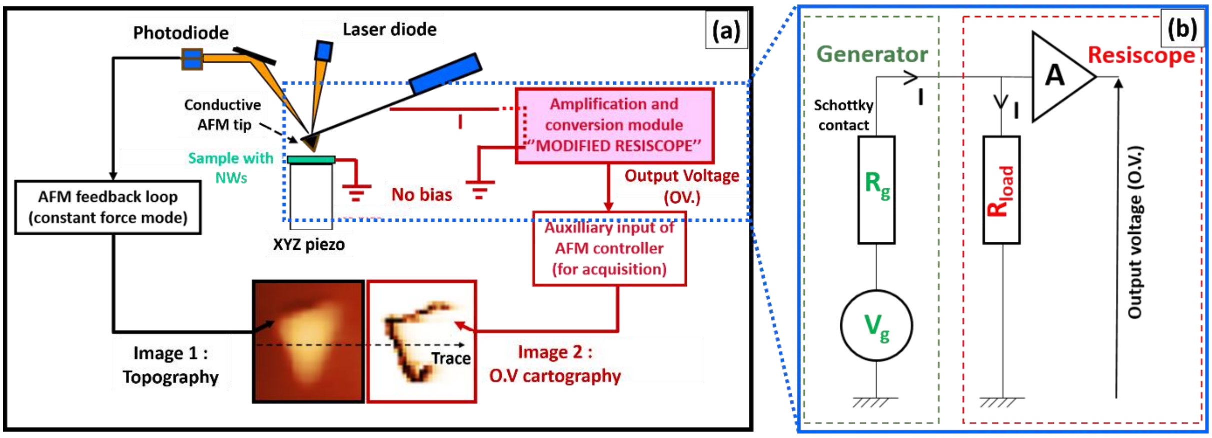

Figure 1. Représentation schématique (a) du montage AFM conducteur avec le Résiscope modifié ; et (b) du circuit électrique simplifié représentant le nanogénérateur (un nanofil ayant une résistance interne R_g) et le Résiscope modifié (avec une résistance de charge R_{load}). Aucune polarisation externe n'est appliquée pendant les mesures.

Réponse piézoélectrique de nanofils de GaN dopés non-intentionnellement de type n et de type p en fonction de la charge de mesure

La *Figure 2* présente, pour les deux types d'échantillons, l'évolution de la tension de sortie moyenne générée par les nanofils en fonction de la FNC appliquée pour chaque valeur de R_{load}. Pour les deux types d'échantillons, nous observons les comportements classiques de la piézo-génération tels que :

(i) les nanofils de GaN dopés de type n et de type p génèrent respectivement des tensions de sortie négatives et positives, ce qui est en accord avec leur dopage non-intentionnel obtenu avec nos conditions de croissance ;

(ii) la présence d'une distribution multi-modale liée à la dispersion des valeurs de rigidité des nanofils. Ainsi pour une FNC donnée, les nanofils présentant un degré de rigidité différent présenteront un taux de déformation différent, conduisant à une dispersion de la tension générée ;

(iii) les valeurs de tension de sortie augmentent avec la FNC (en raison de l'effet piézoélectrique direct ajouté à l'amélioration de la stabilité du contact métal-semiconducteur) jusqu'à atteindre des valeurs maximales à cause de la saturation du champ piézoélectrique interne des nanofils ;

(iv) les tensions de sortie générées par les nanofils de GaN dopés de type p sont systématiquement plus élevées que celles générées par les nanofils dopés de type n en raison de leur hauteur non encapsulée plus grande, ainsi que de leur différent niveau de dopage intrinsèque.

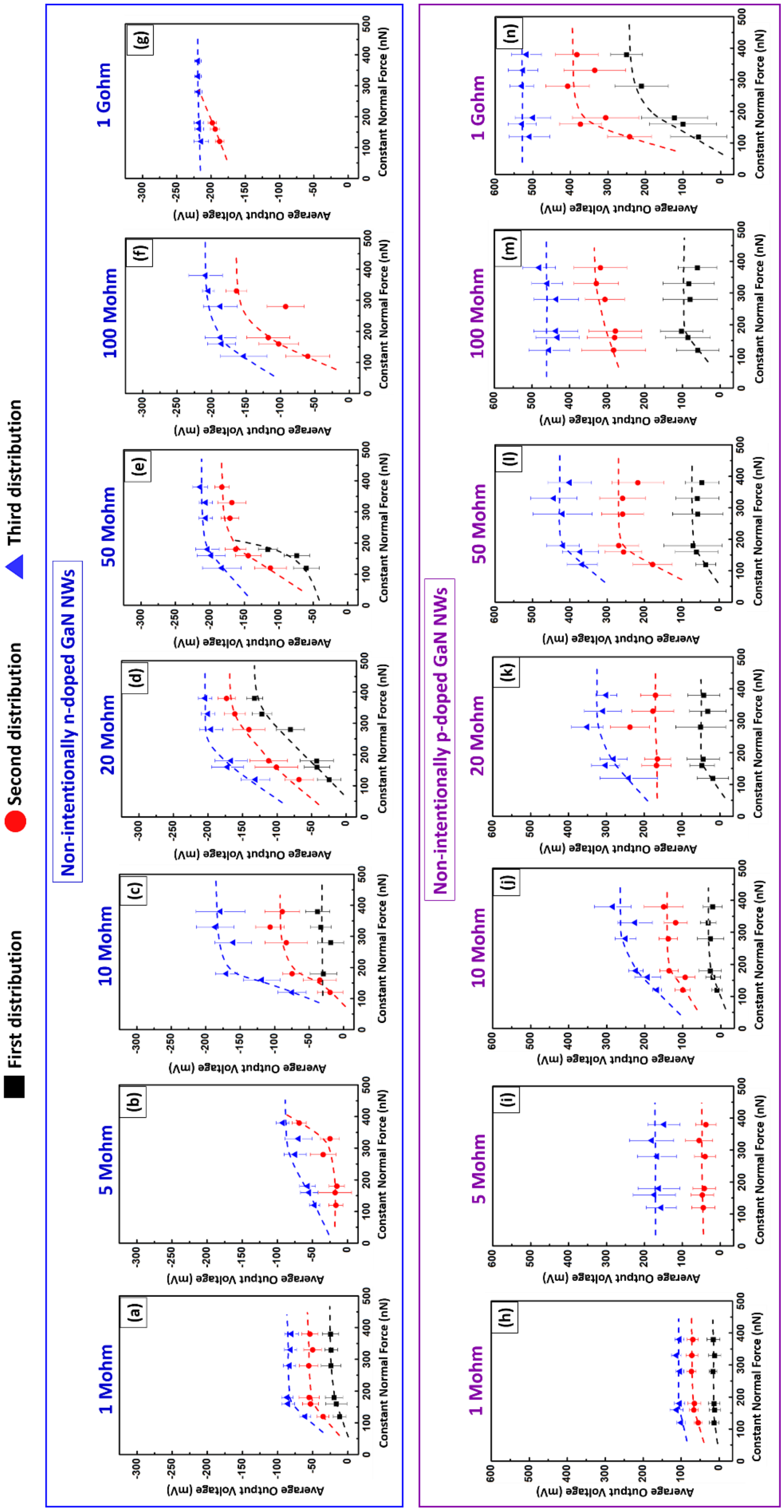

Figure 2. Évolution des tensions de sortie moyennes générées par des nanofils de GaN dopés non intentionnellement (a-g) de type n et (h-n) de type p, en fonction de la FNC pour différentes valeurs de R_{load}.

Dans les deux cas, la tension de sortie moyenne générée par les deux ensembles de nanofils de GaN évolue entre plusieurs dizaines et centaines de mV. Malgré le type de dopage dans les nanofils et la R_{load} employée, les valeurs de tension de sortie sont équivalentes ou dépassent celles générées par d'autres nanostructures 1D trouvées dans la littérature. En particulier, pour les nanofils de GaN dopés p, les valeurs moyennes obtenues par le système AFM peuvent atteindre plus de 442 ± 62 mV pour une valeur de R_{load} de 50 Mohm et jusqu'à 529 ± 30 mV à 1 Gohm. Ces valeurs établissent un nouvel état de l'art pour la conversion piézoélectrique des nanostructures 1D. À partir de cette expérience, nous démontrons clairement le fort impact de la R_{load} sur les valeurs moyennes de tensions de sortie mesurées, et ce pour les deux échantillons. La réponse piézoélectrique diminue lorsque la valeur de R_{load} diminue, ceci résultant de la présence du pont de résistances formé par R_g et R_{load} (comme le montre la *Figure 1b*), ce qui implique que la résistance interne des nanogénérateurs (R_g) est non-négligeable contrairement à ce qui est considéré dans la littérature.

Méthodes de calcul de la résistance interne (R_g) des nanofils de GaN

Afin d'obtenir la valeur de R_g, nous avons tracé les valeurs moyennes de puissance calculées pour chaque ensemble de nanofils en fonction de R_{load} pour différentes valeurs de FNC. Il s'agit d'une méthode conventionnelle utilisée lors de l'optimisation de R_{load} des microsystèmes où la valeur de la résistance interne du système est obtenue au maximum de la courbe de puissance en forme de cloche, comme le montre la *Figure 3*.

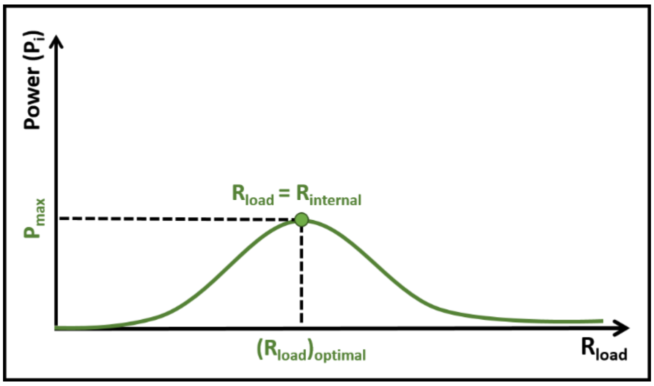

Figure 3. Représentation théorique de la courbe de puissance en fonction de R_{load}. Le maximum de la courbe est obtenu lorsque la R_{load} est égale à la résistance interne du système mesuré.

La *Figure 4* présente l'évolution de la puissance moyenne en fonction de R_{load} pour quelques FNC représentatives. Pour des raisons de mesures, seules les $2^{ème}$ et $3^{ème}$ distributions sont présentées. Il est important de noter ici que la troisième distribution est à associer à des nanofils plus flexibles (moins rigides) que ceux attribués à la seconde distribution.

Indépendamment du type de dopage des échantillons, les valeurs de puissance moyenne obtenues pour la $3^{ème}$ distribution sont plus élevées que celles de la $2^{ème}$ distribution, ce qui est cohérent avec les valeurs de tension de sortie plus élevées générées par les nanofils plus flexibles de la $3^{ème}$ distribution par rapport à la $2^{ème}$ distribution. De plus, deux différents régimes peuvent être observés : le régime R1 observé pour des faibles valeurs de R_{load}, et le régime R2 obtenu pour des grandes valeurs de R_{load}. Le régime R1 présente un comportement non classique (en comparaison avec la courbe de puissance théorique de la *Figure 3*) avec une puissance moyenne qui augmente lorsque les valeurs de R_{load} diminuent. À ce jour, nous n'avons pas été en mesure d'élucider ce comportement et de nouvelles mesures doivent être mises en œuvre pour une compréhension approfondie de ce régime. Par contre, dans le régime R2, la forme classique en cloche de la courbe de puissance est obtenue de manière quasi-systématique. Les valeurs de R_g obtenues à partir des maximums des courbes de puissance affichées sont de l'ordre de $(10^7 - 10^8)\ \Omega$. Elles ne sont donc pas négligeables. De plus, nous observons une évolution dynamique de la valeur de R_g en fonction de la FNC pour chaque ensemble d'échantillons quel que soit le type de dopage, puisque cette valeur de R_g dépend de la force appliquée et donc de leur déformation.

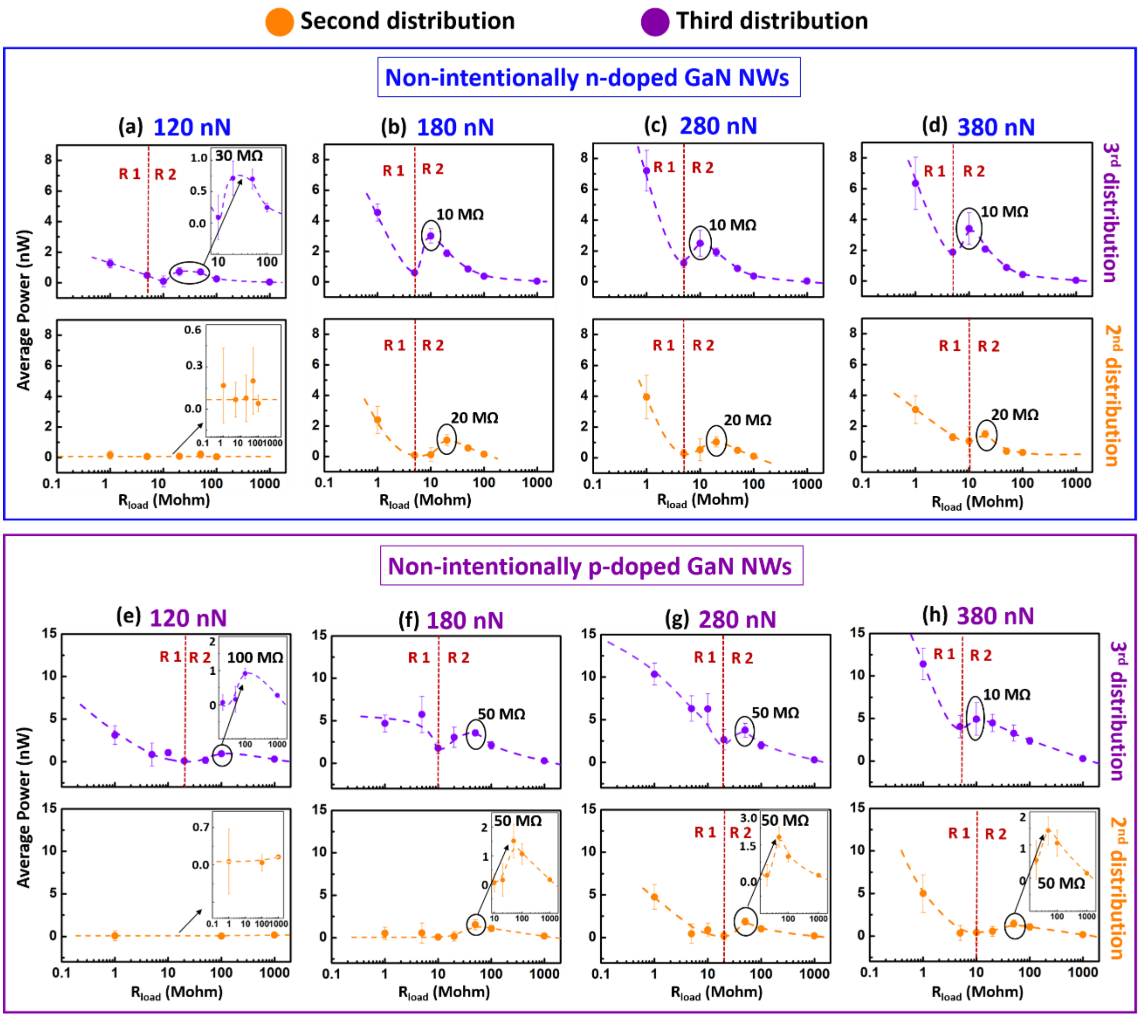

Figure 4. Évolution de la puissance moyenne générée par des nanofils de GaN dopés non intentionnellement (a-d) de type n et (e-h) de type p en fonction de R_{load} et pour des valeurs de FNC de 120 nN, 180 nN, 280 nN et 380 nN. Les images en encarts, lorsque celles-ci sont présentées, montrent le zoom des maximums des courbes de puissance. Les lignes pointillées séparent les deux régimes des courbes de puissance : le régime non-classique R1 et le régime classique R2.

Cependant, l'évolution de R_g est très difficile à expliciter. En effet, R_g est définie comme une somme de plusieurs composantes, à savoir la somme de la résistance interne du nanofil ($R_{nanofil}$), de la résistance de la diode Schottky (R_D) et de la résistance de contact pointe AFM-nanofil (R_C). Même en étudiant le comportement individuel de chacune de ces composantes, il n'est pas aisé d'établir le comportement global R_g.

Par conséquent, nous avons proposé une seconde méthode pour déterminer la valeur de R_g en nous référant aux mesures de tensions de sortie effectuées dans la configuration de circuit ouvert/court-circuit, à l'aide de l'équation suivante :

$$(R_g)_i = \frac{((V_g)_i - V_i) \times R_{load}}{V_i} \qquad (1)$$

Nous choisissons ici une R_{load} <<< R_g pour nous situer dans une configuration de quasi court-circuit, alors que $(V_g)_i$ correspond à la valeur de tension de sortie obtenue dans une configuration de quasi circuit ouvert (dans ce cas, V_g est mesurée avec R_{load} = 1 GΩ) pour un nanofil individuel 'i'.

La *Figure 5* montre l'évolution des valeurs moyennes de R_g pour une R_{load} de 1 MΩ, qui est très faible par rapport aux valeurs obtenues à partir des maximums des courbes de puissance (de l'ordre de 10^7 - 10^8 Ω).

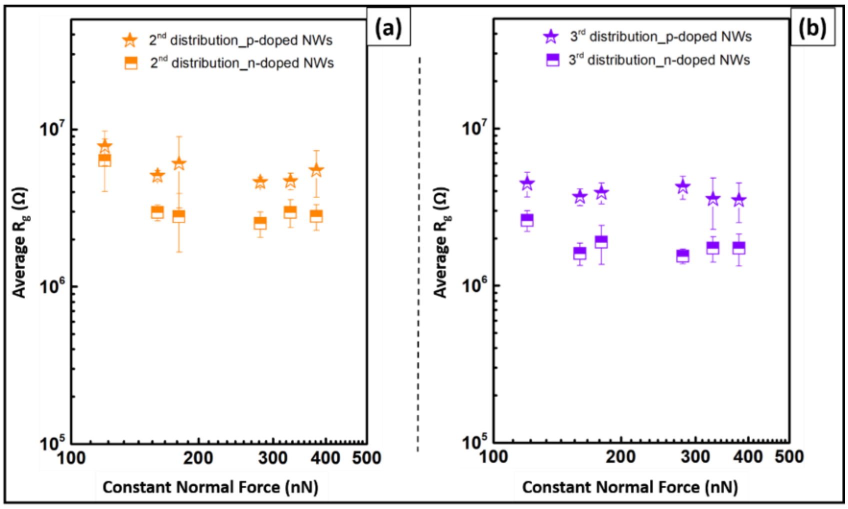

Figure 5. Valeurs calculées de R_g moyen en fonction du FNC pour (a) la $2^{ème}$ distribution et (b) la $3^{ème}$ distribution, de nanofils de GaN dopés non intentionnellement de type n et de type p, avec R_{load} = 1 MΩ.

En utilisant cette seconde méthode de mesure, nous obtenons des valeurs moyennes de R_g de l'ordre de 10^6 - 10^7 Ω, soit un facteur 10 plus bas que les valeurs déduites des courbes de puissance (*Figure 4*). L'une des raisons possibles de cet écart très important entre les deux méthodes de calcul peut être attribuée à la simplification opérée lors du raisonnement sur des circuits modèles ne considérant que des résistances (*Figure 1b*). En réalité, le système doit être décrit dans un cadre d'impédance, où le nanofil est représenté par un générateur V_g avec une capacité C_g et une résistance interne R_g, ce système se déchargeant au travers de R_{load} et de la capacité parasite associée C_{load} (comme le montre la *Figure 6a*). En effet, à l'aide d'une simulation, nous démontrons que dans le cadre de mesures sur des nanofils uniques, la capacité parasite C_{load} ne peut plus être négligée et qu'une augmentation de C_{load} peut entraîner une réduction significative de l'amplitude de la tension maximale mesurée (*Figure 6b*).

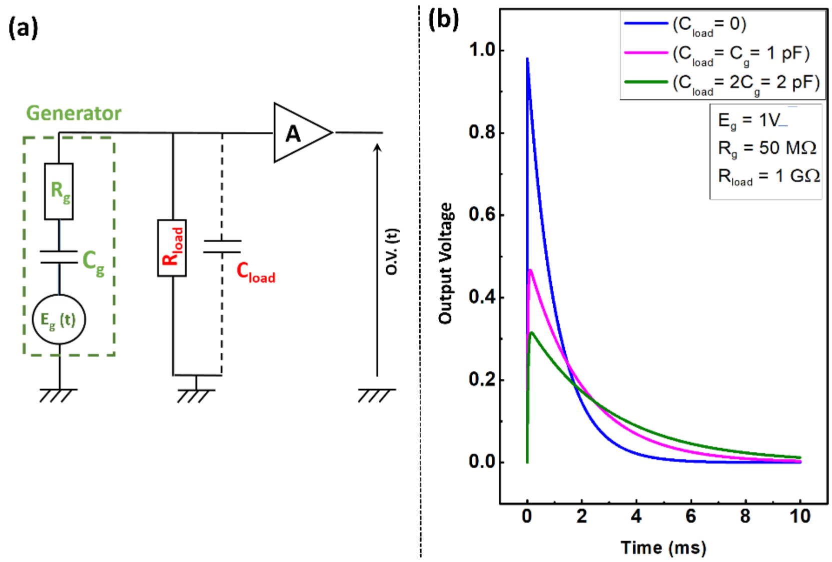

Figure 6. (a) Circuit électrique impliquant la capacité parasite C_{load} et la capacité interne du nanofil C_g, et (b) évolution simulée de la tension de sortie mesurée en faisant varier la valeur de C_{load}.

Ainsi, nous avons établi que la quantification des efficacités de la conversion piézoélectrique des nanofils via les méthodes conventionnelles (applicables aux générateurs piézoélectriques) considérées ici et dans la littérature présente certaines limitations. Il est aujourd'hui nécessaire de pleinement prendre en compte les capacités parasites et l'utilisation de techniques plus adaptées afin de surmonter ces limitations et donc aboutir à des mesures pleinement comparatives dans la littérature.

Charges de surface : une solution pour améliorer la conversion piézoélectrique des nanofils

Les matériaux III-Nitrures sont caractérisés par une forte densité de pièges de surface. Dans le cas des nanostructures 1D (en raison de leur rapport surface sur volume important) et notamment présentant des diamètres inférieurs à 100 nm, l'influence de ces densités de pièges de surface est très importante. Dans les nanofils de GaN, elles sont de l'ordre de 10^{13} cm^{-2}. De la présence de ces charges de surface résulte un fort pinning du niveau de Fermi (FLP) et ainsi la création d'une zone de déplétion dont la largeur est liée au dopage du nanofil. Selon les dimensions des nanofils, ces derniers peuvent être partiellement ou complètement déplétés. Ceci a pour conséquence directe une modulation de la conductivité des nanofils et donc des effets d'écrantage des charges piézoélectriques par les porteurs libres circulant dans le matériau. L'écrantage étant connu pour abaisser les capacités de piézo-conversion des nanosystèmes, la réduction de ce dernier via les effets des charges de surface apparait donc comme une voie prometteuse pour accroitre la réponse piézoélectrique des nanofils de GaN.

Bien que les charges de surface soient inhérentes aux propriétés du matériau, leur densité peut être modulée en modifiant l'environnement immédiat des nanofils, et leur influence peut être ajustée au regard du diamètre des nanofils. Lors de cette étude, ces deux facteurs ont été étudiés individuellement afin de démontrer le rôle positif joué par la présence des charges de surface dans l'optique d'améliorer l'efficacité de la conversion piézoélectrique de nos nanofils de GaN.

Influence de l'environnement immédiat des nanofils

Pour cette expérience, nous avons utilisé des nanofils de GaN intrinsèquement dopés de type p qui présentent une dispersion en hauteur (553 ± 50 nm ; 755 ± 80 nm) tandis que leur diamètre reste approximativement constant (36 ± 9 nm). Ainsi ici les diamètres des nanofils n'influenceront pas l'expression des charges de surfaces. Ces caractéristiques morphologiques des nanofils ont été obtenues en ajustant soigneusement les paramètres de croissance des nanofils en PA-MBE. Ces nanofils ont ensuite été préparés de deux façons différentes. Tout d'abord, les nanofils ont été simplement encapsulés partiellement dans une matrice PDMS afin de les consolider mécaniquement, tandis que selon la seconde méthode, les nanofils ont d'abord été soumis à un dépôt de couche atomique (ALD) afin d'obtenir une coquille d'Al_2O_3 de 10 nm d'épaisseur sur les parois latérales des nanofils (procédé connu pour abaisser la densité des états de surface de 10^{13} cm^{-2} à 10^{10-11} cm^{-2}) et ont ensuite été partiellement encapsulés dans du PDMS. La coquille d'Al_2O_3 induisant un élargissement du diamètre des nanofils, nous avons fait très attention que les deux échantillons présentent un rapport d'aspect équivalent de 5,5. Pour cela, la hauteur des nanofils non encapsulés a été ajustée (*Figure 7*). Garder un même rapport d'aspect des nanofils dépassant de la matrice nous assure ainsi qu'ils sont soumis à des taux de déformation équivalents.

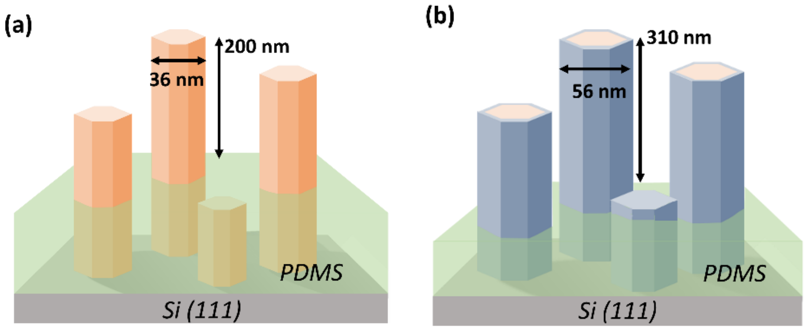

Figure 7. Représentation schématique de (a) nanofils de GaN as-grown et (b) nanofils de GaN avec une coquille d'Al_2O_3 de 10 nm d'épaisseur, partiellement encapsulés dans une matrice de PDMS. Les deux échantillons ont un rapport d'aspect (hauteur/diamètre) équivalent de 5,5 assurant qu'ils présentent un même taux de déformation sous l'action de leur déformation par la pointe AFM.

La réponse piézoélectrique des nanofils a été étudiée à l'aide d'un système de microscope à force atomique (AFM) équipé d'un module Résiscope qui a été spécifiquement modifié. Dans la configuration considérée ici, les nanofils sont déformés latéralement par la pointe AFM qui balaye la surface en restant en contact avec celle-ci. Grâce à cette configuration expérimentale, nous pouvons accéder aux fortes valeurs de tensions de sortie générées par nos nanofils de GaN et ainsi observer l'influence des charges de surface sur la réponse piézoélectrique de ces derniers mesurée aux bornes d'une résistance de charge externe (R_{load}) de 1 GΩ. Les tensions de sortie moyennes générées pour chaque échantillon sont représentées en fonction de la force normale constante (FNC) appliquée sur la *Figure 8*.

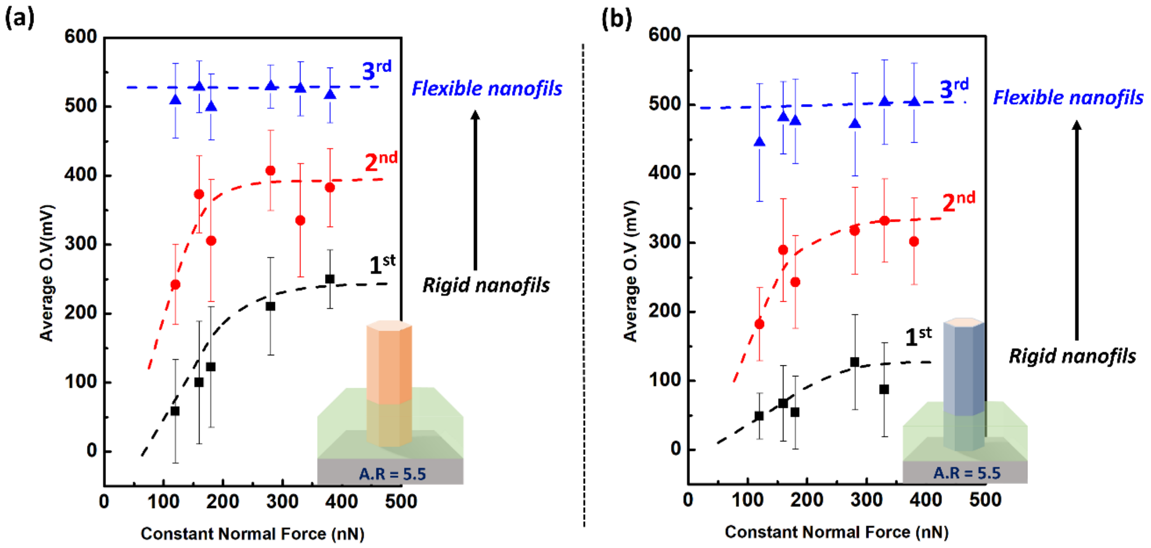

Figure 8. Analyse statistique de l'évolution des tensions de sortie moyennes en fonction de la FNC pour (a) des nanofils de GaN as-grown, et, (b) des nanofils de GaN avec une coquille d'Al_2O_3 de 10 nm d'épaisseur. Les nanofils sont partiellement encapsulés dans une matrice de PDMS. Trois distributions de tensions de sortie sont observées, à savoir la 1ère distribution (carrés noirs), la 2ème distribution (cercles rouges) et la 3ème distribution (triangles bleus) correspondant respectivement à des nanofils rigides et les nanofils comparativement plus flexibles. L'encart schématise un seul nanofil. Pour chaque type d'échantillon, la hauteur des nanofils non encapsulée a été ajustée pour garder un même rapport d'aspect et ainsi assurer que les nanostructures présentent le même degré de déformation sous l'action de la pointe AFM.

Les deux séries d'échantillons présentent des caractéristiques similaires :

(i) Des tensions de sortie positives sont générées par les nanofils de GaN indépendamment de leurs valeurs de rigidité et de la FNC appliquée. Ce résultat est en accord avec le dopage intrinsèque de type p des nanofils de GaN obtenu dans nos conditions de croissance.
(ii) Les tensions de sortie moyennes suivent une distribution gaussienne et mettent en évidence une distribution multimodale résultant du mode de croissance auto-assemblé des nanofils. La réponse piézoélectrique des nanofils étant directement liée à leur degré de déformation, et donc à leurs dimensions, la dispersion de leur rigidité se traduit par une dispersion de la tension de sortie. Dans le cas présent, la première distribution correspond à l'ensemble des nanofils les plus rigides, tandis que les deuxième et troisième distributions correspondent à des nanofils plus flexibles.
(iii) Les trois distributions présentent une augmentation des tensions de sortie moyennes avec l'augmentation de la FNC appliquée. Cet effet est typique de l'effet piézoélectrique direct, mais résulte, en second ordre, d'une stabilité accrue du contact Schottky formé entre le sommet du nanofil mesuré et la pointe AFM qui joue le rôle d'électrode de collecte.

Avant de comparer les réponses piézoélectriques respectives des deux échantillons, il faut se rappeler que les deux échantillons présentent des taux de déformation équivalents pour une FNC donnée (même rapport d'aspect de 5,5) et, par conséquent, une réponse piézoélectrique analogue est attendue. Néanmoins, les valeurs moyennes de tensions de sortie obtenues pour les nanofils de GaN *as-grown* sont systématiquement plus élevées pour chaque distribution en comparaison avec les nanofils de GaN présentant une coquille d'Al_2O_3. La diminution des valeurs moyennes des tensions de sortie pour ces derniers peut être exclusivement attribuée à la réduction de la densité des pièges de surface ($10^{10-11}/cm^2$) due à la passivation efficace de la surface par la coquille en Al_2O_3.

En effet, une densité de pièges de surface moindre se traduit par un pinning du niveau de Fermi plus faible et donc une déplétion des nanofils plus faible. Il en résulte un effet d'écrantage des charges piézoélectriques qui est plus marqué dans le cœur du nanofil via notamment la création d'un canal de conduction comme schématisé sur la *Figure 9b*. À l'opposé, pour les nanofils *as-grown* (c'est-à-dire présentant une densité de charges de surface plus grande ($10^{13}/cm^2$)), la zone de déplétion couvre l'ensemble du volume des nanofils. Le pinning du niveau de Fermi est plus fort, ce qui se traduit par une déplétion des nanofils plus marquée et donc une limitation plus forte des effets d'écrantage (*Figure 9a*).

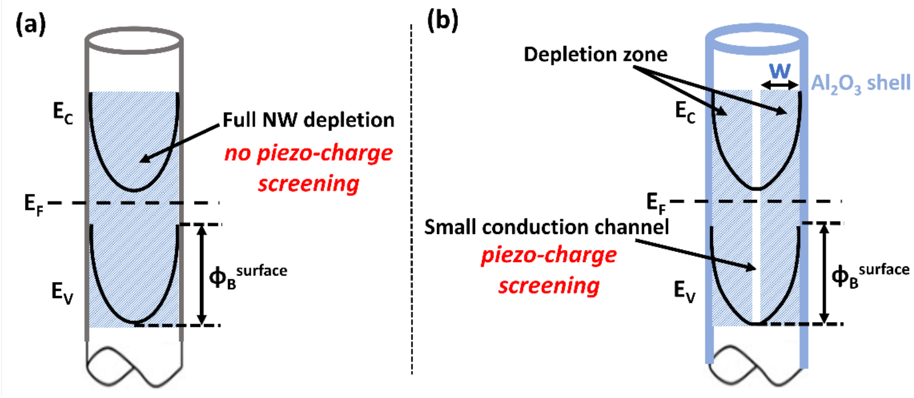

Figure 9. Schématisation de pinning du niveau de Fermi de surface dans (a) un nanofil de GaN as-grown, totalement déplété ; et (b) un nanofil de GaN/Al_2O_3 partiellement déplété avec la présence d'un canal de conduction dans le cœur du nanofil.

Ces résultats sont les premières démonstrations expérimentales du rôle favorable des charges de surface sur la conversion piézoélectrique des nanofils de GaN. Ainsi en optimisant ces effets, nous avons pu mesurer des valeurs moyennes de tensions de sortie de l'ordre de 529 mV par nanofil. Cette valeur est, à notre connaissance, la plus élevée jamais enregistrée dans la littérature pour des nanofils de GaN. Cette réponse piézoélectrique dépasse également largement celles générées par d'autres nanostructures 1D piézoélectriques, notamment les nanofils de ZnO qui sont les nano-objets les plus employés dans la littérature pour la fabrication de générateurs piézoélectriques à base de nanostructures 1D.

Influence du diamètre du nanofil

Pour donner une impulsion supplémentaire à nos investigations expérimentales, nous avons analysé l'influence des charges de surface sur la capacité de conversion piézoélectrique de nos nanofils de GaN en modifiant leur diamètre. Pour ce faire, nous avons épitaxié des nanofils de GaN intrinsèquement dopés de type p caractérisés par une hauteur approximativement constante d'environ 1050 ± 200 nm mais présentant néanmoins une forte dispersion de diamètre dans la gamme de 20 à 100 nm. Ces nanofils présentent une densité équivalente de pièges de surface ainsi que de concentration de dopant.

Pour quantifier la réponse piézoélectrique des nanofils en fonction de leur diamètre, nous avons utilisé un système AFM équipé du module Résiscope modifié permettant cette fois de déformer axialement des nanofils sous l'application d'une force extrêmement bien contrôlée. Cette configuration expérimentale permet une corrélation directe entre la déformation mécanique des nanostructures 1D et leurs propriétés piézoélectriques, nous donnant ainsi la faculté de quantifier leur coefficient de couplage électromécanique.

Pour réaliser des mesures de piézo-conversion sous une déformation axiale, il est nécessaire de consolider mécaniquement les nanofils. Pour ce faire, une encapsulation partielle des nanofils dans du PMMA a été réalisée de façon à ce que la hauteur des nanofils émergeant de la matrice soit d'environ 100 nm. Tous les nanofils utilisés pour cette étude présentaient une rigidité ≥ 5 N/m. Ce choix était impératif afin d'assurer une déformation uniquement axiale et donc de s'affranchir du possible flambage ou de la courbure locale des nanofils. Par ailleurs, pour assurer une collecte efficace des charges piézoélectriques, une couche métallique de 5 nm-Cr/20 nm-Pt a été déposée sur les sommets des nanofils. Cela conduit à l'établissement d'un contact métal-métal entre la pointe AFM et l'électrode déposée. Ce dernier est particulièrement stable même dans les conditions de balayage AFM rapide utilisées dans le mode de compression axiale. La *Figure 10* montre une image MEB prise en vue transverse de l'échantillon préparé.

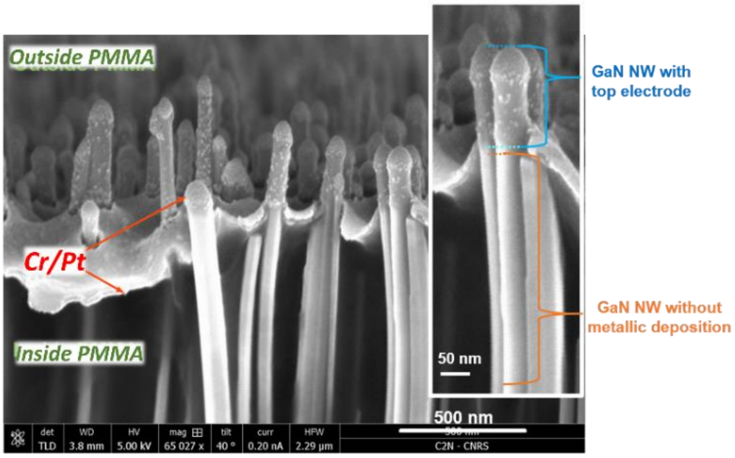

Figure 10. Image MEB en vue transverse des nanofils de GaN synthétisés par PA-MBE et partiellement encapsulés dans une résine de PMMA. Un contact métallique Cr/Pt est déposé sur le dessus de chaque nanofil pour assurer une bonne collecte des charges générées.

Dans la configuration de compression axiale, la tension de sortie 'V' a été mesurée en fonction de la force appliquée 'F'. Pour un champ de déformation de chaque nanofil équivalent à 1%, le coefficient de couplage électromécanique, η, a été calculé à l'aide de l'équation suivante :

$$\eta = \frac{\acute{e}nergie\ \acute{e}lectrique\ de\ sortie}{\acute{e}nergie\ \acute{e}lectrique\ d'entr\acute{e}e} = \frac{\frac{1}{2}\,CV^2}{F\,\Delta l}$$

où C est la capacité associée aux charges générées par un nanofil unique lors d'une décharge piézoélectrique et Δl est la variation de hauteur du nanofil comme schématisé sur la *Figure 11*.

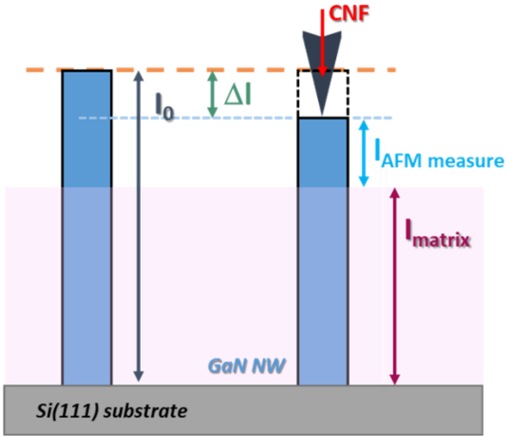

Figure 11. Schématisation des nanofils de GaN partiellement encapsulés dans la matrice de PMMA avec une épaisseur 'l_{matrix}'. La FNC appliquée comprime axialement le nanofil, ce qui entraîne une variation de sa hauteur de Δl par rapport au nanofil non comprimé.

La *Figure 12* présente l'évolution du coefficient de couplage électromécanique en fonction de la rigidité des nanofils. Nous montrons que η varie dans la gamme de 5,9 à 43,4 % et présente une corrélation directe avec la rigidité des nanofils. Cette observation est surprenante. En effet, comme tous les nanofils présentent une contrainte de compression équivalente de 1%, nous devrions obtenir un 'η' approximativement équivalent puisque la conversion piézoélectrique dépend en premier lieu de la déformation du matériau.

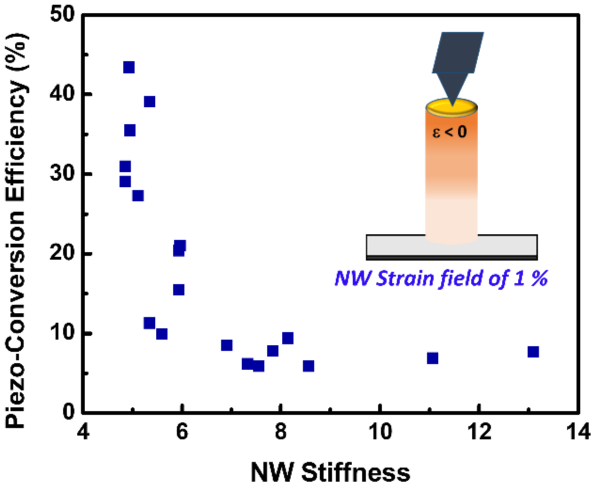

Figure 12. Variation du coefficient de couplage électromécanique, η, en fonction de la rigidité des nanofils pour un degré de déformation de 1%.

Cette évolution de η démontre que celui-ci n'est pas seulement gouverné par les caractéristiques mécaniques des nanofils, mais qu'un autre paramètre joue un rôle non négligeable. Ce paramètre est la présence des charges de surface dont les effets sont connus pour évoluer en fonction du diamètre des nanofils.

Pour étudier l'influence des charges de surface sur l'efficacité de la conversion piézoélectrique de nos nanofils de GaN, nous avons tracé le coefficient de couplage en fonction du rayon/diamètre des nanofils (*Figure 13*). Ici nous pouvons observer une relation étroite entre le coefficient de couplage des nanofils et leurs diamètres.

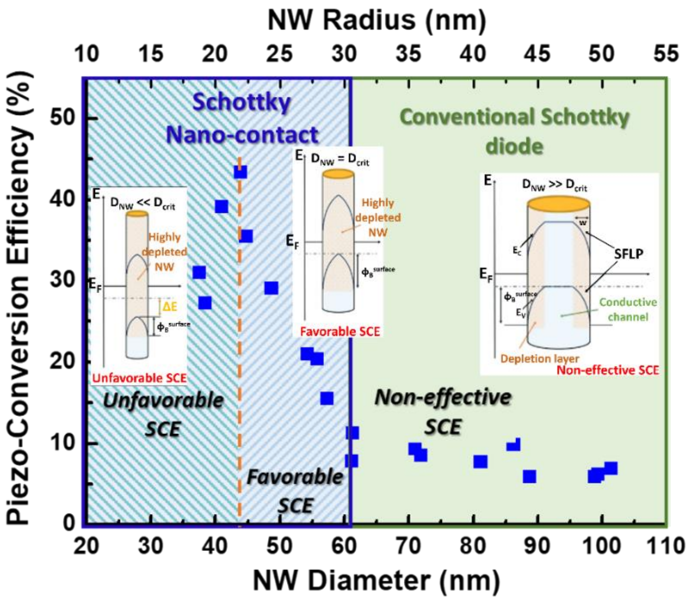

Figure 13. Évolution de l'efficacité de la conversion piézoélectrique en fonction du diamètre/rayon des nanofils. L'encart schématise les courbures de bandes de trois nanofils de différents diamètres avec diverses intensités de pinning du niveau de Fermi.

Pour un diamètre de nanofil, D_{NW}, supérieur à 60 nm, le coefficient de couplage est approximativement constant. Cela indique que le nanofil n'est que partiellement déplété. Nous sommes de ce fait dans la configuration où $D_{NW} >> D_{crit}$, et où la zone de déplétion entoure un canal de conduction. Les porteurs libres peuvent donc aisément circuler et écranter les charges piézoélectriques générées. Nous pouvons donc considérer ici que les charges de surface n'affectent pas la capacité de piézo-conversion des nanofils et que celle-ci est seulement contrôlée par la déformation des nanofils.

Pour un D_{NW} approximativement équivalent au D_{crit} (diamètre dans la gamme de 44 à 60 nm), le coefficient de couplage augmente brusquement jusqu'à 43,4 %. Nous supposons ici que les nanofils sont complètement déplétés avec une hauteur de barrière de surface, $\Phi_B^{Surface}$, de l'ordre du pinning du niveau de Fermi. Plus les nanofils sont déplétés (réduction de leur diamètre), plus l'écrantage dû aux porteurs libres est réduit, permettant ainsi pour un même taux de déformation de générer des tensions de sortie des nanofils plus grandes et ainsi accroître leur coefficient de couplage. Dans cette gamme de diamètre des nanofils, nous pouvons conclure que les charges de surface jouent un rôle favorable dans l'amélioration de la capacité de conversion piézoélectrique des nanofils.

Enfin, pour $D_{NW} << D_{crit}$, une diminution du coefficient de couplage est observée. Pour cette gamme de diamètres, les nanofils sont fortement déplétés, conduisant à la fois à une réduction de la barrière de surface $\Phi_B^{Surface}$ et une augmentation de la recombinaison électron-trou aux surfaces. Par conséquent, les nanofils deviennent extrêmement résistifs et induisent également une limitation de la circulation des charges piézoélectriques dans le circuit électrique externe. Ainsi, la génération de tension de sortie est fortement dégradée, ce qui se traduit par une baisse des efficacités de conversion comme observé. Nous pouvons dire ici que les charges de surface deviennent défavorables pour la conversion piézoélectrique.

Ainsi, nous avons démontré qu'en ajustant soigneusement le diamètre de nos nanofils de GaN dans la gamme de 44 à 60 nm, nous pouvons tirer parti de la présence des charges de surface pour augmenter l'efficacité de la conversion piézoélectrique jusqu'à 43,4 %.

Dans cette étude de l’influence des effets de charges de surface sur la réponse piézoélectrique des nanofils, nous avons démontré expérimentalement pour la première fois toute l’influence de ces effets. En architecturant soigneusement les dimensions et l’environnement des nanofils, il nous est possible d’augmenter la conversion piézoélectrique de nos nanofils de GaN. De tels résultats ouvrent la voie vers la réalisation de générateurs piézoélectriques à base de nanofils plus efficaces, ce qui est aujourd’hui un prérequis pour espérer dans les années futures un transfert de technologie.